

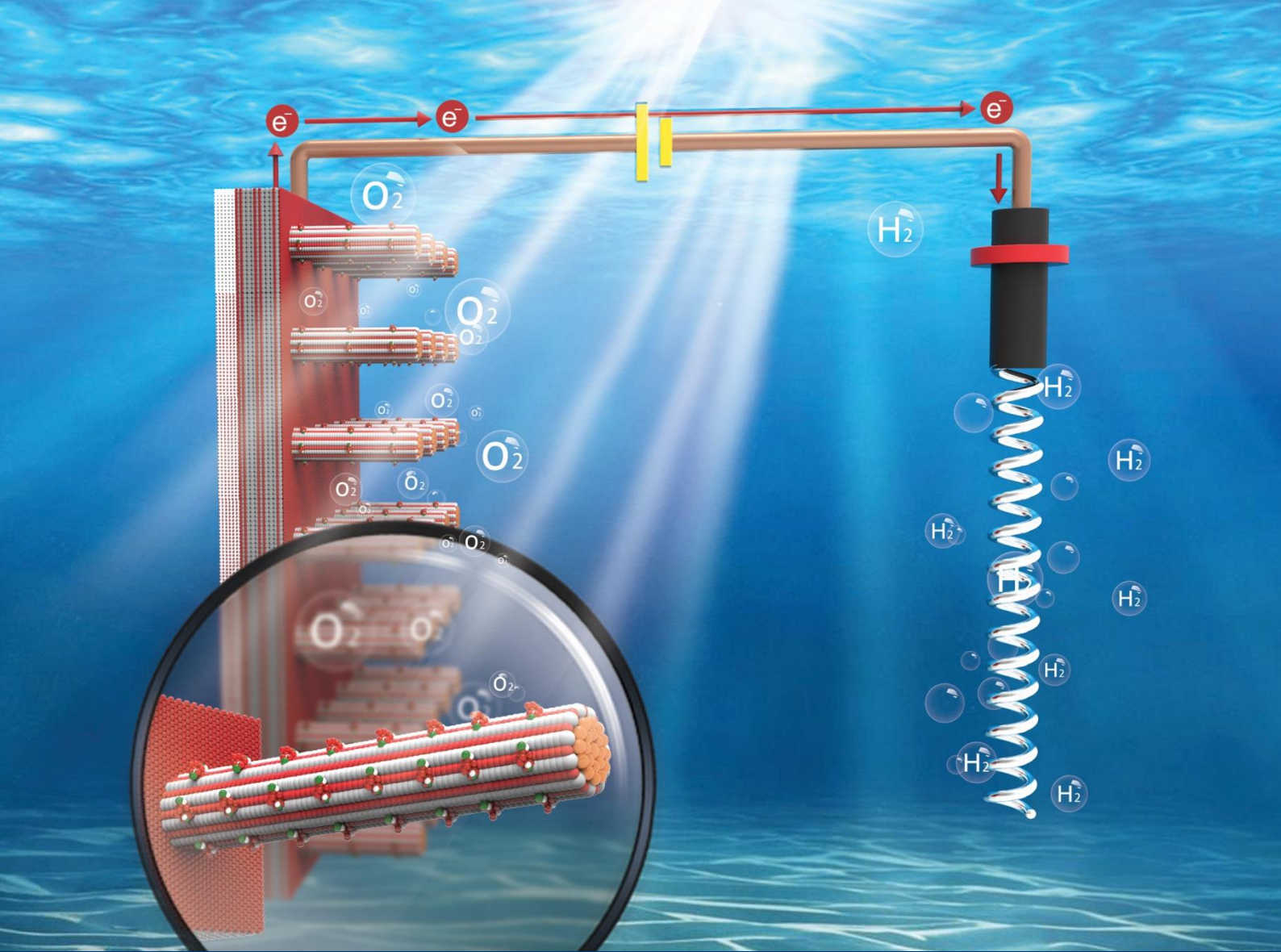


Universitat Autònoma de Barcelona

ADVERTIMENT. L'accés als continguts d'aquesta tesi queda condicionat a l'acceptació de les condicions d'ús establertes per la següent llicència Creative Commons:  http://cat.creativecommons.org/?page_id=184

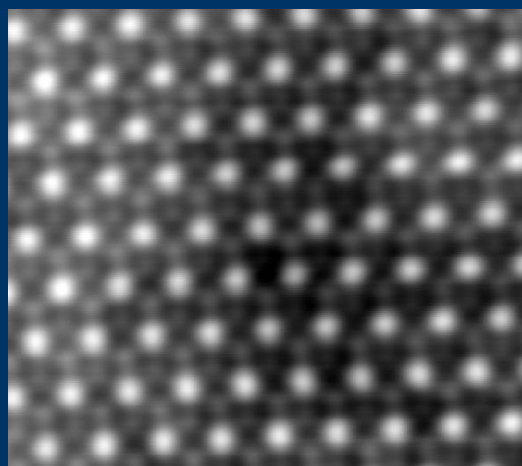
ADVERTENCIA. El acceso a los contenidos de esta tesis queda condicionado a la aceptación de las condiciones de uso establecidas por la siguiente licencia Creative Commons:  <http://es.creativecommons.org/blog/licencias/>

WARNING. The access to the contents of this doctoral thesis it is limited to the acceptance of the use conditions set by the following Creative Commons license:  <https://creativecommons.org/licenses/?lang=en>



Semiconductor Composite Materials for Energy Storage and Conversion Applications

PengYi Tang



Doctorate Program in Materials Science

Semiconductor Composite Materials for Energy Storage and Conversion Applications

PengYi Tang

Director: Prof. Jordi Arbiol i Cobos

Co-Director: Prof. Joan Ramón Morante i Lleonart

Tutor: Prof. Jordi Sort i Viñas

Institut Català de Nanociència i Nanotecnologia (ICN2), CSIC & BIST

Institut de Recerca en Energia de Catalunya (IREC)

Department of Physics, Faculty of Sciences

Universitat Autònoma de Barcelona (UAB)



Barcelona Institute of
Science and Technology



Jordi Arbiol i Cobos, ICREA Research Professor at Institut Català de Nanociència i Nanotecnologia (ICN2), CSIC & BIST, **Joan Ramón Morante i Lleonart**, Professor and Director at Institut de Recerca en Energia de Catalunya (IREC) and **Jordi Sort i Viñas**, ICREA Research Professor at Department of Physics, Universitat Autònoma de Barcelona (UAB)

CERTIFY

that Mr. **PengYi Tang**, MSc in Physical Chemistry, carried out the work entitled “**Semiconductor Composite Materials for Energy Storage and Conversion Applications**” under their direction and qualifies for the degree of Doctor in Materials Science.

And for that record, sign this certificate.

Prof. Jordi Arbiol i Cobos,

Prof. Joan Ramón Morante i Lleonart,

Prof. Jordi Sort i Viñas,

PengYi Tang

Bellaterra, May 2018

Table of Contents

Acknowledgments	1
Abstract	3
Resum	5
Introduction: Materials for Energy Storage and Energy Conversion Applications	8
1.1 The Energy Landscape	9
1.2 Fundamentals Concept of Supercapacitors.....	9
1.2.1 Background of Supercapacitors.....	9
1.2.2 The Energy Storage Mechanism of EDLCs	11
1.2.3 The Energy Storage Mechanism of Pseudo-capacitance.....	15
1.2.4 The Evaluated Criteria of Supercapacitor Devices and the Progress of Supercapacitor Electrodes	18
1.3 Fundamental Concepts of Photoelectrochemical Water Splitting	21
1.3.1 Fundamental Concepts of Photoelectrochemistry	21
1.3.2 Physics of Semiconductor Materials	22
1.3.3 Semiconductor Materials for Photoanodes	26
1.3.4 Electrocatalysts for OER and HER in Water Splitting	27
1.3.5 The Semiconductor/Electrolyte Interface and the Concept of Surface State	28
References.....	33
Methodology	40
2.1 Fundamental Concepts in Transmission Electron Microscopy	41
2.1.1 The Concept of Resolution	41
2.1.2 Aberration Correctors	45
2.1.3 TEM and STEM Modes	47
2.1.4 HAADF and ABF Images.....	48
2.1.5 Electron Energy-Loss Spectrum (EELS).....	51
2.1.6 Atomic Modelling and TEM/STEM Image Simulations via Rhodius, Eje-Z and STEM Cell.....	53
2.2 The Fundamental Concepts in Electrochemistry.....	55
2.2.1. Cyclic Voltammetry	55
2.2.2 Electrochemical Impedance Spectroscopy.....	58
References.....	62
Hematite-Polypyrrole Based Nanoflakes as Negative Electrodes for Asymmetric Supercapacitors	65
3.1 Introduction	66
3.2 Experimental Section	69
3.2.1 Synthesis of MnO ₂ Nanosheets on Nickel Foam	69
3.2.2 Synthesis of Honeycomb-like Fe ₂ O ₃ Nanoflakes on NF	69
3.2.3 Synthesis of PPy Nanoleaves Decorated Honeycomb-like Hematite Nanoflakes on NF	70
3.2.4 Assembly of the ASC.....	70
3.2.5 Characterization of Microstructural Properties	70
3.2.6 Measurement of Electrochemical Properties.....	71

3.3 Results and Discussion	71
3.3.1 Optimization of the Hydrothermal Reaction Time of Fe ₂ O ₃ Samples	72
3.3.2 Optimization of PPy Deposition Charges in Core-Shel Fe ₂ O ₃ @PPy Samples	73
3.3.3 Investigation of PPy Growth Mechanism in Core-shell Fe ₂ O ₃ @PPy Samples	77
3.3.4 The Structural and Electrochemical Characterization of Representative MnO ₂ , Fe ₂ O ₃ and Fe ₂ O ₃ @PPy Nanoflake Samples	82
3.3.5 The Electrochemical Properties of Fabricated ASCs.....	89
3.4 Summary	93
References.....	94
ITO/Hematite/Fe₂TiO₅/FeNiOOH Composite Nanowires as Photoanodes for Water Splitting in Alkaline Electrolyte	99
4.1 Introduction	100
4.2 Experimental Section	102
4.2.1 Chemicals and Materials	102
4.2.2 Electrode Preparation	103
4.2.3 Optical, Structural and Morphological Characterization	105
4.2.4 Photo-electrochemical Measurements.....	106
4.2.5 Incident Photon to Current Efficiency (IPCE)	106
4.3 Result and Discussion.....	107
4.3.1 Structure of the Pristine Hematite Electrode	107
4.3.2 Optimization of the ITO Thickness in the ITO/Fe ₂ O ₃ Electrodes.....	109
4.3.3 The Optimization of the Sintering Conditions and ALD TiO ₂ Thickness of ITO/Fe ₂ O ₃ /Fe ₂ TiO ₅ Electrodes	114
4.3.4 Optimization of the FeNiOOH Deposition Charge in the ITO/Fe ₂ O ₃ / Fe ₂ TiO ₅ /FeNiOOH Electrodes.....	117
4.3.5 Optimization of the Sintering Conditions in the Fe ₂ O ₃ /Fe ₂ TiO ₅ Electrodes	119
4.3.6 Systematically Structural, PEC Performance Comparison of Optimized Fe ₂ O ₃ , ITO/Fe ₂ O ₃ , ITO/Fe ₂ O ₃ /Fe ₂ TiO ₅ and ITO/Fe ₂ O ₃ /Fe ₂ TiO ₅ /FeNiOOH Electrodes	120
4.3.7 Mechanism Investigation of Optimized Fe ₂ O ₃ , ITO/Fe ₂ O ₃ , ITO/Fe ₂ O ₃ / Fe ₂ TiO ₅ and ITO/Fe ₂ O ₃ /Fe ₂ TiO ₅ /FeNiOOH Electrodes via PEIS	134
4.4 Summary	146
References.....	147
Hematite/Fe₂TiO₅/CoFe Prussian Blue Analogues Composite Nanowires as Photoanodes for Water Splitting in Acidic Electrolyte	154
5.1 Introduction	155
5.2 Experimental Section	156
5.2.1 Chemicals and Materials	156
5.2.2 Electrode Preparation	156
5.2.3 Structural and Morphological Characterization	158
5.2.4 Photo-electrochemical Measurements.....	159
5.3 Result and Discussion.....	160
5.3.1 Pristine CoFe PBA for OER Processed by Chemical Etching Characterized by SEM and TEM	160
5.3.2 Optimization of the Chemical Bath Reaction Time in Fe ₂ O ₃ /CoFe PBA	

Electrodes	165
5.3.3 Optimization of the Chemical Bath Reaction Time in Fe ₂ O ₃ /Fe ₂ TiO ₅ / CoFe PBA Electrodes	166
5.3.4 Comparison between Structure and PEC Performance in Optimized Fe ₂ O ₃ , Fe ₂ O ₃ /Fe ₂ TiO ₅ and Fe ₂ O ₃ /Fe ₂ TiO ₅ /CoFe PBA Electrodes	168
5.3.5 PEC mechanism Investigation of the Optimized Fe ₂ O ₃ , Fe ₂ O ₃ /Fe ₂ TiO ₅ and Fe ₂ O ₃ /Fe ₂ TiO ₅ /CoFe PBA Electrodes via PEIS	177
5.4 Summary	186
References.....	187
Advanced TEM Characterization of 2D Materials for Water Splitting	191
6.1 Introduction	192
6.2 Experimental Section	194
6.3 Result and Discussion.....	195
6.3.1 Structural Defects in 2D MoS ₂	195
6.3.2 Core-Shell MoO ₂ /MoS ₂ Nanoflakes.....	203
6.3.3 Semiconductor and Metallic Phases of MoTe ₂	208
6.3.4 Vacancy Generation in PtSe ₂ by means of Argon Plasma Treatment.....	213
6.4 Summary	218
References.....	219
General Conclusions and Outlook	223
7.1 General Conclusions.....	224
7.2 Outlook.....	228
List of Publications	230

Acknowledgments

The research presented in this dissertation could not have been finished without the assistance, guidance and help of my outstanding colleagues. Herein, I would like to thank all the people for their invaluable help during the development of this PhD dissertation.

First of all, I would like to express my deepest gratitude to my supervisor, Professor Jordi Arbiol at Institut Català de Nanociència i Nanotecnologia (ICN2), for his excellent guidance and advices along this way, for his endless and contagious enthusiasm, as well as for his patience, support and confidence in me.

I would like to acknowledge Professor Joan Ramon Morante at Institut de Recerca en Energia de Catalunya (IREC). His novel ideas and wise guidelines broadens my horizons about the science and engineering world, and thanks to his financial support made this work possible.

Thanks to all GAeN group members at ICN2, where I always felt comfortable like at home in the past three years. I kindly appreciate the scientific environment sharing knowledge, and time spent together with Sara, Francisco, Maria, Aziz, Jérémy and Ting. I would express my thanks to my colleagues at IREC, HaiBing, Carles, Martí, Qin, Teresa, Sebastián, Nina, Félix, ZhiShan, Yu, JunFeng and Hemesh. Without their support, I could not start the fantastic chemical synthesis and water splitting experiments at IREC. I would like to express my thanks to the scientific help provided by LiJuan and Prof. José Ramón Galán-Mascarós from Institute of Chemical Research of Catalonia (ICIQ). I would like to thank all the technical staff working at the different facilities, for their support, especially from the Electron Microscopy Division at ICN2 (Francisco Belarre, Marcos Rosado and Dr. Belen Ballesteros) and Dr. Doris Cadavid at IREC. I also would like to express my thanks to the samples provided by YongMin and Professor Zheng Liu from Nanyang Technological University (Singapore), Xuan and Professor Jan Fransaer from KU Leuven (Belgium), Professor Alberto Vomiero from Luleå University of Technology (Sweden) as well as Dr.

Mauro Epifani from Consiglio Nazionale delle Ricerche-Istituto per la Microelettronica ed i Microsistemi (Italy).

Part of the atomic resolution TEM experiments was conducted at the Ernst Ruska-Centre (ER-C) for Microscopy and Spectroscopy with Electrons in Jülich (Germany) during my five months research stay. I would like to thank Professor Rafal E. Dunin-Borkowski for hosting me at ER-C. The experiments were conducted with great assistance provided by Dr. Paul Paciok, Dr. Marc Heggen, Dr. HongChu Du, Dr. XianKui Wei and Dr. Lei Jin. I would like to thank all the ER-C colleagues for their hospitality and fruitful discussions during the lunch or coffee break sessions and friendship activities outside of the institute. Finally, I would like to acknowledge the scholarship I received from the German Academic Exchange Service (DAAD) and ICN2 Severo Ochoa Mobility Program for my stay at ER-C.

Finally, thanks to my family, for their great support for me and to my dearest LiJuan for her love and understanding.

Abstract

The energy originated from fossil fuels has enabled the remarkable advancement of civilization over the past century. However, fossil fuels are not infinite in supply and they are a source of increasing atmospheric carbon dioxide and the associated abominable environmental effects. Improving the efficiency of the energy storage devices and conversion of solar energy into hydrogen energy via water splitting are key technologies to tackle the serious energy and environmental problems. Earth-abundant, environmental-friendly semiconductors for supercapacitor and water splitting applications have received great attention due to their specific characteristics.

It is well established that the capacitive properties of semiconductors are greatly affected by their nanostructure and poor conductivity, leading to a limited energy and power densities. Thus, understanding and manipulating the hierarchical structure at the nanoscale is essential to design composite materials for energy storage with enhanced charge transfer and electrolyte ions transportation abilities. On one hand, in photoelectrochemical water splitting (PEC), the electron-hole recombination in the bulk interfaces plays a determinative role in the catalytic performance. The investigation about modulation of the charge transfer kinetics as well as the energy level and density of surface state upon the modification of a second semiconductor or oxygen evolution catalysts (OEC) could be of great interest. On the other hand, for hydrogen evolution catalysts (HEC), as the identification of structural defects, phase transmission and vacancies presented in the 2D materials play a vital role in optimizing the catalyst for hydrogen evolution reaction (HER) in water splitting.

This dissertation is divided into 7 chapters:

Chapter 1 is the introduction part, which includes the background of supercapacitors and water splitting and reviews the limited factors affecting the electrochemical properties of semiconductors for supercapacitor and water splitting applications.

In **Chapter 2** summarizes the applied methodologies in this dissertation. This chapter includes the details about the TEM, STEM, EELS experimental setups, data

processing, simulations and general introductions to the electrochemical techniques, such as cyclic voltammetry, electrochemical impedance spectrum as well the electrical circuit model for illustrating the surface states.

Specific synthesis procedures and experimental results for every one of the studied nanosystems are presented in Chapters 3-6. **Chapter 3** deals with the fabrication of core-branch $\text{Fe}_2\text{O}_3/\text{PPy}$ nanocomposites as negative electrode for supercapacitor applications as well as the investigation of PPy nanoleaves growth mechanism onto the hematite nanoflakes.

In **Chapter 4**, we have optimized the synthesis conditions, including the ITO thickness, TiO_2 thickness, FeNiOOH deposition charge and the post-sintering temperature of $\text{ITO}/\text{Fe}_2\text{O}_3/\text{Fe}_2\text{TiO}_5/\text{FeNiOOH}$ nanowire-based photoanodes for water splitting in alkaline electrolyte. The detailed structure has been mainly investigated by TEM and STEM-EELS, while, the charge transfer and reaction kinetic mechanisms were systematically investigated by PEIS.

In **Chapter 5**, we have optimized the chemical bath conditions for synthesising CoFe PBA supported onto $\text{Fe}_2\text{O}_3/\text{Fe}_2\text{TiO}_5$ nanowire-based photoanodes for water splitting in acidic electrolyte. The detailed structure has been mainly investigated by TEM and STEM-EELS, while, the charge transfer and reaction kinetic mechanisms were investigated by PEIS.

In **Chapter 6**, we moved the characterization of structural defects, phase transmission, vacancies in 2D materials for HER in water splitting with advanced aberration-corrected dedicated STEM, including HAADF, ABF, EELS-STEM, GPA and HAADF simulation.

Finally, **Chapter 7** summarizes the general conclusions of this dissertation, along with a brief outlook.

Resum

L'energia que s'origina de combustibles fòssils ha permès avenços molt remarcables a la nostra civilització durant el segle passat. No obstant, els combustibles fòssils no són il·limitats i suposen una font d'increment del diòxid de carboni a l'atmosfera, amb els seus conseqüents efectes ambientals nocius. Millorar la eficiència dels dispositius d'emmagatzematge d'energia i la conversió d'energia solar a hidrògen mitjançant la dissociació de l'aigua són tecnologies clau per encarar problemes energètics i ambientals. Els semiconductors que es presenten en abundància i són beneficiosos pel medi ambient han estat en el punt de mira durant els últims anys donades les seves característiques específiques com a supercapacitors i dispositius per la dissociació de l'aigua.

És conegut que les propietats capacitives dels semiconductors estan molt afectades per la seva estructura a la nanoescala i la seva baixa conductivitat, limitant les densitats d'energia i potencia. Així doncs, entendre i manipular l'estructura jeràrquica a la nanoescala és essencial per dissenyar materials nanocompostos per l'emmagatzematge d'energia amb millores en la transferència de càrrega i habilitat de transportar ions electrolítics. Per la dissociació d'aigua fotoelectroquímica (PEC), la recombinació electró-forat al "bulk" i les interfícies juguen un paper molt determinant en l'actuació catalítica. La investigació sobre la modulació de la dinàmica de transferència de càrrega així com el nivell d'energia i la densitat d'estats de superfície sobre la modificació d'un segon semiconductor o catalitzadors per dissociació de l'oxígen (OEV) podrien ser de gran interès. Per altra banda, pels catalitzadors de evolució d'hidrògen (HEC), com la identificació de defectes estructurals, transmissió de fase i les vacants presents en materials 2D juguen un paper de vital interès per optimitzar els catalitzadors per la reacció d'evolució de l'hidrògen (HER) en la dissociació de l'aigua.

Aquest treball està dividit en 7 capítols:

El **Capítol 1** és la part introductòria, que inclou els principis bàsics dels supercapacitors i la dissociació de l'aigua i comenta els factors limitants de les propietats electroquímiques dels semiconductors per aplicacions en supercapacitors i dissociació de l'aigua.

El **Capítol 2** resumeix les metodologies emprades en aquest treball. Aquest capítol inclou els detalls sobre les configuracions experimentals del TEM, STEM i EELS, processament de dades, simulacions i una introducció a les tècniques electroquímiques com la voltimetria cíclica, espectre d'impedància electroquímica i els models de circuits electrònics per il·lustrar els estats de superfície.

La síntesi i els resultats experimentals es presenten en els **Capítols 3-6**. El **Capítol 3** tracta sobre la fabricació de nuclis embrancats de nanocompostos de $\text{Fe}_2\text{O}_3/\text{PPy}$ com a electrodes negatius per aplicacions en supercapacitors, així com la investigació dels mecanismes de creixement de nanofulles de PPy sobre flocs d'hematita.

Al **Capítol 4**, hem optimitzat les condicions de síntesi, incloent el gruix de ITO, gruix de TiO_2 , càrrega de dipòsit de FeNiOOH i la temperatura de post-sinterització dels nanofil·ls de $\text{ITO}/\text{Fe}_2\text{O}_3/\text{Fe}_2\text{TiO}_5/\text{FeNiOOH}$ com a fotoànodes per la dissociació de l'aigua en electrolits alcalins. Els detalls de l'estructura s'han investigat principalment mitjançant TEM i STEM-EELS, mentre que la transferència de càrrega i els mecanismes de la dinàmica de reacció han estat investigats sistemàticament per PEIS.

Al **Capítol 5** hem optimitzat les condicions del bany químic per sintetitzar CoFe PBA suportat sobre fotoànodes basats en nanofil·ls de $\text{Fe}_2\text{O}_3/\text{Fe}_2\text{TiO}_5$ per la dissociació de l'aigua en electrolits àcids. Els detalls de l'estructura han estat investigats principalment per TEM i STEM-EELS mentre que la transferència de càrrega i els mecanismes de la dinàmica de reacció han sigut investigats sistemàticament per PEIS.

Al **Capítol 6**, ens hem centrat en la caracterització de defectes estructurals, transmissió de fase, vacants en materials 2D per HER per la dissociació de l'aigua amb un STEM dedicat amb correcció d'aberracions, incloent HAADF, ABF, EELS-STEM, GPA i simulacions d'HAADF.

Finalment, al **Capítol 7** es resumeixen les conclusions generals d'aquest treball, juntament amb les projeccions futures d'aquests.

Chapter 1

**Introduction: Materials for Energy Storage and Energy
Conversion Applications**

1.1 The Energy Landscape

Energy originating from fossil fuels has enabled the remarkable advancement of civilization over the past century. Our current demand for food, housing, transport, and health maintenance for more than 7 billion people is considerably larger than the needed for the 1 billion people inhabiting the planet prior to the application of fossil fuel. The fundamental characteristics making fossil fuels unique are their abundance and relatively large energy surplus, based on the quantity of energy extracted versus that of energy used to perform the extraction. [1] However, fossil fuels are not infinite in supply and are a source of increasing atmospheric carbon dioxide and associated detrimental environmental effects. [2] It is debatable when these effects will become unacceptable in terms of climatic events, social or political conflicts, but their finite nature ensures that the days of fossil fuels are numbered. Accordingly, plenty of effort has been devoted to the development of efficient energy storage devices such as batteries, supercapacitors etc. and to ensure that alternative energy sources will provide the same opportunity for a high quality of life, as the one facilitated by the fossil fuels until now. However, these new alternative energies and energy storage devices must be built with earth abundant materials and possess energy surplus and environmental friendly characteristics.

1.2 Fundamentals Concept of Supercapacitors

1.2.1 Background of Supercapacitors

The demand for efficient, clean alternative energy and large capacitance storage is growing in order to meet the projected doubling of world energy consumption within the next half century. Intense research efforts have been made to develop efficient energy from renewable sources, such as solar and wind that offer great potential for the projected energy demands. Meanwhile, enormous attention has been paid to the development of large capacitance charge storage devices so that the electricity generated from these intermittent renewable sources can be effectively used and distributed on a large scale. These high capacitance energy storage devices can also

benefit hybrid electric vehicles and portable electronic devices.

Typically, there are two main types of charge storage devices: batteries and electrochemical capacitors, which have attracted a great deal of attention. [3-5] The fundamental difference between batteries and electrochemical capacitors is that batteries store energy in thick redox reactant layers that are capable of generating electricity through two separate half redox reactions. Electrochemical capacitors, on the other hand, store energy directly as ions or in thin redox layers that allow rapid charging and discharging. [6] Most often, batteries have high energy density but long recharge times while electrochemical capacitors have high power density (see **Figure 1.1**) with fast and safe charging and discharging times. [7] However, charge storage devices with high energy and power densities and fast recharge times are required to achieve the high energy density and power output required for applications such as all-electric/plug-in hybrid vehicles. For these types of applications, an electrochemical capacitor must have large capacitance (C) per gram of active material at high current density to satisfy the need for high power density.

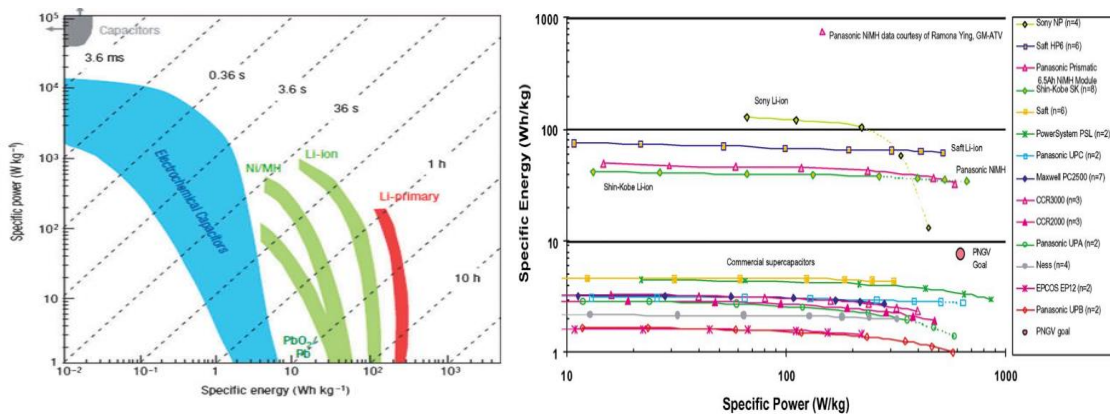


Figure 1.1 Left: Ragone plot (specific power vs. specific energy) for various electrochemical energy storage devices. Right: Ragone plot of measured data on commercial Li-ion batteries, NiMH batteries and supercapacitors, normalized to total cell weight. Adapted from ref. [6] and ref. [8].

Supercapacitors are electrochemical energy storage devices, whose stored energy is based, in principal, on two different types of capacitive behaviour: electrical double layer capacitance (EDLC) from the accumulation of the pure electrostatic charge at the electrode interface, and the pseudo-capacitance derived from fast and reversible

surface redox processes at characteristic potentials. [6, 9]

1.2.2 The Energy Storage Mechanism of EDLCs

Due to the limited charge storage areas and finite geometric constraints of the separation distance between the two charged plates, conventional capacitors generally store relatively little energy. However, supercapacitors based on the EDLC mechanism can store much more energy as they can benefit from the enhanced interfacial area and the atomic scale of charge separation distances.

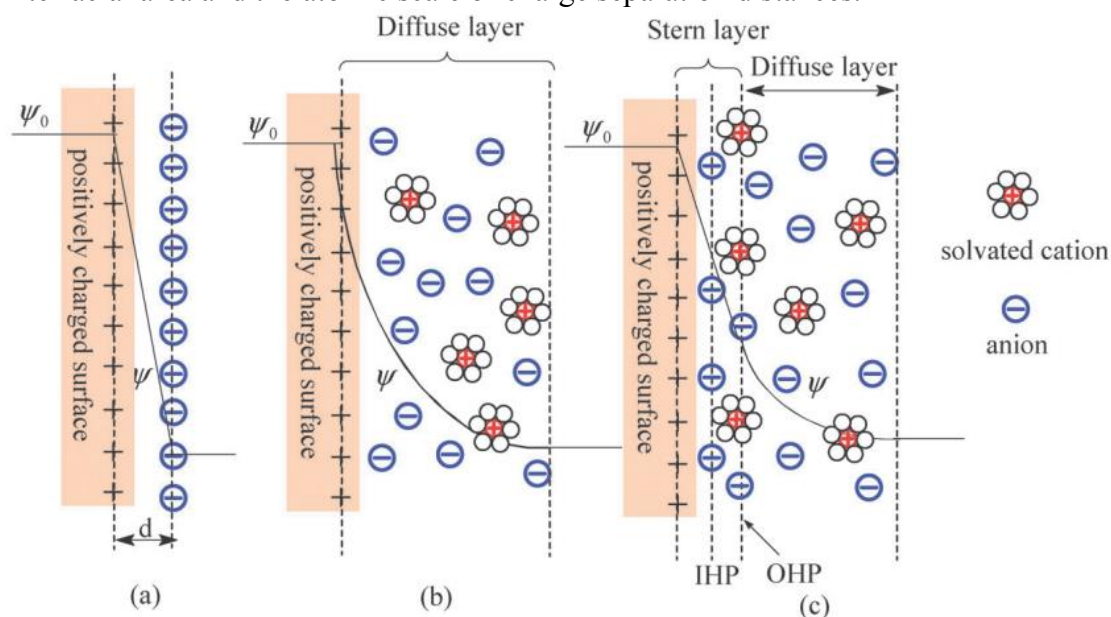


Figure 1.2 Models of the electrical double layer at a positively charged surface: (a) the Helmholtz model, (b) the Gouy-Chapman model, and (c) the Stern model, showing the inner Helmholtz plane (IHP) and outer Helmholtz plane (OHP). The IHP refers to the distance of closest approach of specifically adsorbed ions (generally anions) and OHP refers to that of the non-specifically adsorbed ions. The OHP is also the plane where the diffuse layer begins. d is the double layer distance described by the Helmholtz model. ψ_0 and ψ are the potentials at the electrode surface and the electrode/electrolyte interface, respectively. Adapted from ref. [9]

As schematically displayed in **Figure 1.2a**, H. V. Helmholtz first described and modelled the concept of the electrical double layer (EDL) in the 19th century during his investigation into the distribution of opposite charges presented at the interface of colloidal particles. [10] The Helmholtz EDL model reveals two layers of opposite charge presented at the electrode/electrolyte interface separated by an atomic distance,

which is similar to that of two-plate conventional capacitors. The simple Helmholtz EDL model was further developed by M. Gouy and D.L. Chapman, [12-13] in consideration of a continuous distribution of electrolyte cations and anions in the electrolyte solution, driven by thermal motion, termed the diffuse layer, as illustrated in **Figure 1.2b**. However, the Gouy-Chapman model results in the overestimation of the EDLC because the capacitance of two separated arrays of charges increases inversely with the separation distance. Thus, a very large capacitance would arise in the case of point charge ions close to the electrode surface. Later, Stern [14] combined the Helmholtz model with the Gouy-Chapman model to explicitly identify two regions of ion distribution: the inner region called the Stern layer and an outer region, termed the diffuse layer (**Figure 1.2c**). In the Stern layer, hydrated ions are strongly adsorbed by the electrode, which is thus named the compact layer. The compact layer also consists of specifically adsorbed ions and non-specifically adsorbed counterions. The inner Helmholtz plane (IHP) and outer Helmholtz plane (OHP) are employed to distinguish these two types of adsorbed ions. The diffuse layer region is the same as that defined by the Gouy-Chapman model. [14]

The capacitance in the EDL (C_{dl}) is a combination of the Stern type of compact double layer capacitance (C_H) and the diffusion region capacitance (C_{diff}). Therefore, C_{dl} can be expressed by the following equation: [9]

$$\frac{1}{C_{dl}} = \frac{1}{C_H} + \frac{1}{C_{diff}} \quad (1)$$

The critical factors that determine the EDL behaviour at a planar electrode surface include the electrolyte ion types, the electrical field distribution, the electrolyte solvent, and the chemical affinity of the adsorbed ions and the electrode surface. Since the porous electrode normally possess a high specific surface area, the EDL behaviour at the pore surface of the porous electrode is more complex than that of an infinite planar electrode because the ion transfer and transportation in a confined system can be drastically affected by a number of parameters, including the space constrain inside the pores, the mass transfer path, the ohmic resistance along with the electrolyte, and

the wetting behaviour of the pore surface by the electrolyte. [9]

The capacitance of an EDL-type supercapacitor is generally assumed to follow that of a parallel-plate capacitor: [15]

$$C = \frac{\epsilon_r \epsilon_0}{d} A, \quad (2)$$

where ϵ_r is the dielectric constant of electrolyte, ϵ_0 is the vacuum permittivity, A is the electrode's specific surface area accessible to the electrolyte ions, and d is the effective thickness of the EDL (the Debye length). According to equation (2), there is a linear relationship between specific capacitance (C) and specific surface area (A). However, some experimental results reveal that this simple linear relationship does not hold. [16-17] Typically, it was believed that the submicropores of the electrode materials did not contribute to the formation of the EDL because of the inaccessibility of the submicropore surface to the large solvated ion. However, Raymundo-Pinero et al. recently observed the vital contribution of micropores to the overall capacitance and revealed that the partial desolvation of hydrated ions contributed to the enhanced capacitance. [16] Recently, Simon et al. observed an anomalous capacitance increase in carbon electrodes with pore sizes less than 1 nm. [6] These results further demonstrated a capacitance contribution derived from pores with sizes smaller than the solvated ions.

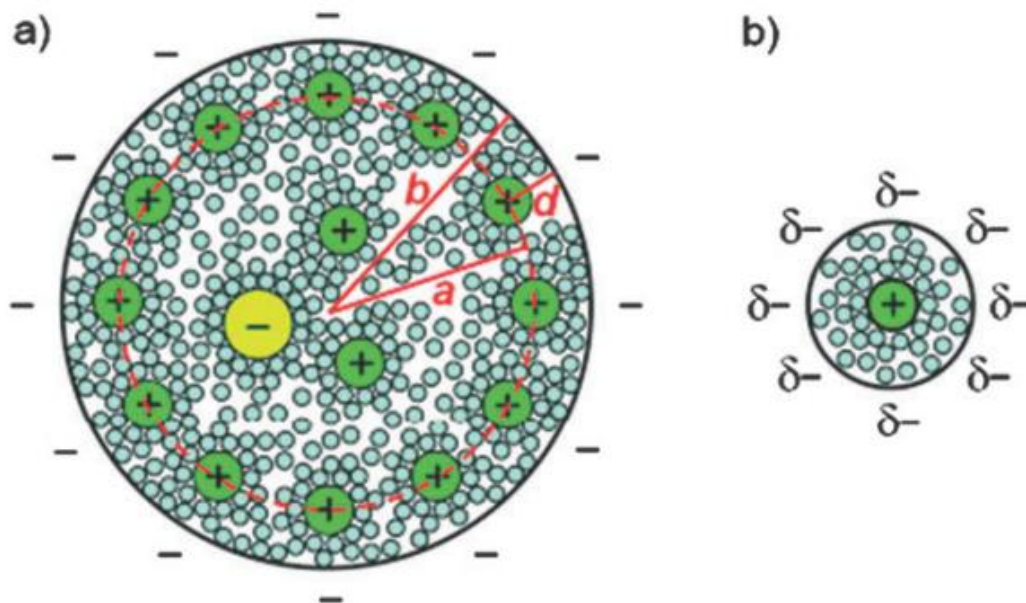


Figure 1.3 Schematic diagrams (top views) of (a) a negatively charged mesopore with solvated cations

approaching the pore wall to form an electric double-cylinder capacitor and (b) a negatively charged micropore of radius b with cations lining up along the pore axis to form an electric wire-in-cylinder capacitor. Adapted from ref. [18]

However, these new experimental results cannot be fully illustrated by the classic EDL theory because in such confined micropore spaces, there is not sufficient space to accommodate the compact layer and diffuse layer simultaneously. Recently, Huang et al. reported a heuristic method to describe supercapacitors based on nanoporous carbon. [18] They propose a different capacitive behaviour depending on the pore size, which also takes the pore curvature into consideration. An electric double-cylinder capacitor (EDCC) model is utilized for the interpretation of mesoporous carbon electrodes, whereas, an electric wire-in-cylinder capacitor (EWCC) model is employed for modelling microporous carbon electrodes, as illustrated in **Figure 1.3**.

The pore curvature is no longer significant when the pores are large enough and the EDCC model can be reduced naturally to the traditional planar EDL model, shown in equation (2). The capacitance estimation for the proposed EDCC and the EWCC models are given in equations (3) and (4), respectively:

$$C = \frac{\epsilon_r \epsilon_0}{b \ln[b/(b-d)]} A \quad (3)$$

$$C = \frac{\epsilon_r \epsilon_0}{b \ln(\frac{b}{a_0})} A \quad (4)$$

where b represents the pore radius, d represents the distance of approaching ions to the surface of the carbon electrode, and a_0 represents the effective size of the counterions.

With these models, the researchers were able to make good fits of theoretical results based on equations (3) and (4) on experimental data, regardless of the types of carbon materials and electrolytes employed.

There is no faradic reaction at EDLC electrodes because of the electrostatic charge storage mechanism. A supercapacitor electrode can be considered as a blocking

electrode from an electrochemical point of view and there is no limitation caused by the electrochemical kinetics through a polarization resistance. Additionally, its surface storage mechanism allows fast energy uptake and delivery, and better power performance. [6]

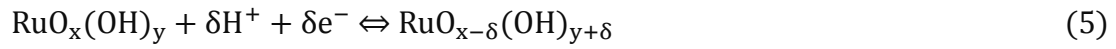
The absence of faradic reactions also reduces the swelling of the active material during charge/discharge cycles, which is often observed in the case of batteries. Thus, EDLCs can sustain millions of cycles, however, batteries survive a few thousand at best. Finally, the solvent of the electrolyte is not involved in the charge storage mechanism, unlike in Li-ion batteries, where it forms the solid-electrolyte interphase when graphite anodes or high-potential cathodes are used. This enables the utilization of solvents, and electrolytes with high power performances at low temperatures for EDLC applications. However, due to the electrostatic surface charging mechanism, the EDLC devices typically suffer from a limited energy density. Therefore, today's the EDLC research is largely focused on increasing their energy density performance and widening the temperature limits into the range where batteries cannot operate. [19]

1.2.3 The Energy Storage Mechanism of Pseudo-capacitance

In contrast to EDLC, pseudo-capacitance originates from thermodynamic factors and is derived from charge acceptance (Δq) and a change in potential (ΔV). [20] The derivative $C = d(\Delta q)/(d\Delta V)$ refers to a capacitance, which is defined as pseudo-capacitance. The main difference between EDLC and pseudo-capacitance lies in the fact that pseudo-capacitance originates from the faradic reaction, involving fast and reversible redox reactions between the electro-active materials and electrolyte on the electrode surface. Metal oxides, such as ruthenium oxide, iron oxide, tin oxide, manganese oxide, vanadium nitride as well as conducting polymers, have been extensively studied in the past decades. [21-26] The specific pseudo-capacitance exceeds that of carbon materials using a double layer charge storage mechanism, justifying the interest in the pseudo-capacitance systems. However, due to the utilization of redox reactions, pseudo-capacitors, similar to batteries, often suffer from

the lack of stability during cycling.

RuO_2 , has been widely investigated because of its intrinsic reversibility for various surface redox couples and high conductivity. [27] The electrochemical behaviour of both amorphous and crystalline types of ruthenium oxide has been widely investigated in acidic electrolyte over the past 30 years. [28] Its capacitance is attributed to the mixed proton-electron conductivity within $\text{RuO}_2 \cdot x\text{H}_2\text{O}$ because the superficial redox transitions of ruthenium oxide involve a proton and electron double injection/expulsion process according to the following reaction: [29]



in which $\text{RuO}_x(\text{OH})_y$ and $\text{RuO}_{x-\delta}(\text{OH})_{y+\delta}$ are the surface oxyruthenium materials at higher and lower oxidation states. Typically, in a proton-rich electrolyte environment, the faradic charges are reversibly stored and delivered through the redox reactions of oxyruthenium groups, such as Ru(IV)/Ru(III) and Ru(III)/Ru(II). Based on electron transfer numbers, the theoretical specific capacitance of RuO_2 is calculated to range from 1300 to 2200 F g^{-1} . [30] C.C. Hu et al. have reported a very high specific capacitance of 1300 F g^{-1} with a nanostructured RuO_2 electrode. [29] Its superior electrochemical performance is correlated to its tuned nanotubular arrayed architecture with metallic conductivity and its hydrous nature. According to equation (5), the reversible redox transitions depend on both proton exchange and electron-hopping processes. The tubular arrayed structure as well as metallic conductivity enable an effective pathway for electrolyte ions and electron transportation. Consequently, the designed nanostructure confirms a promising electrode material for energy storage applications. However, Ru-based aqueous supercapacitors are expensive, and the I-V voltage window limits their practical application to electronic devices.

Cheap oxides of vanadium, iron, cobalt and nickel have been investigated in aqueous electrolytes, but none of them has been tested as much as MnO_2 . [31] The charge

storage mechanism relies on surface adsorption of electrolyte cations, for example, K^+ , Na , etc., as well as proton incorporation according to the reaction:

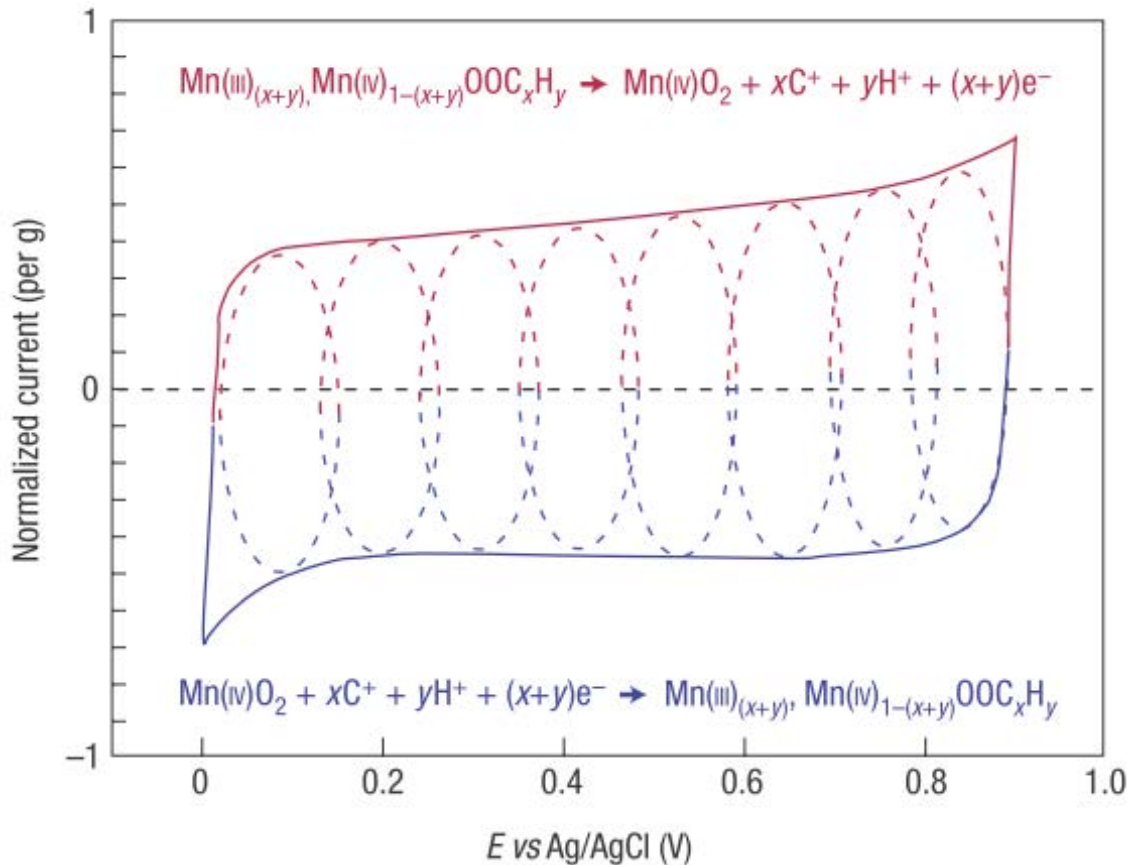


Figure 1.4 Schematic of cyclic voltammetry for a MnO_2 electrode cell in 0.1 M K_2SO_4 aqueous electrolyte showing the successive multiple surface redox reactions resulting in the pseudo-capacitive charge storage mechanism. The red (upper) part is related to the oxidation from Mn (iii) to Mn (iv) and the blue (lower) part refers to the reduction from Mn (iv) to Mn (iii). Adapted from ref. [6]

Figure 1.4 shows a cyclic voltammogram of a MnO_2 electrode in 0.1 M K_2SO_4 aqueous electrolyte. The fast, reversible successive surface redox reactions determine the behaviour of the voltammogram, whose shape is similar to that of the EDLC. MnO_2 microscale powders or films have a specific capacitance of 150 F g^{-1} in neutral aqueous electrolytes within a voltage window of less than 1 V. [6] Because there is no oxidation state available at less than 0 V, the interest in MnO_2 materials for symmetric supercapacitor devices is somehow limited. Notwithstanding, MnO_2 materials are still

suitable for a positive pseudo-capacitive electrode in hybrid systems.

Furthermore, many conducting polymers, such as polyaniline, polythiophene, polypyrrole and their derivatives have been investigated as pseudo-capacitive materials for electrochemical capacitance applications. [32-34] Both have high gravimetric and volumetric pseudo-capacitance in various nonaqueous electrolytes at operating voltages up to 3 V. When used as in the form of bulk materials, conducting polymers often suffer from a limited stability during cycling. [35] For this reason, research efforts devoted to metal oxides and conducting polymers for supercapacitor applications are nowadays directed towards hybrid materials.

1.2.4 The Evaluated Criteria of Supercapacitor Devices and the Progress of Supercapacitor Electrodes

The electrochemical performance of supercapacitors is evaluated based on the following criteria: (i) a power density much higher than batteries with relatively high energy densities (higher than 10 Wh kg⁻¹); (ii) an excellent cyclability (100 times higher than that of batteries); (iii) ultra-fast charge/discharge processes within several seconds; (iv) low self-discharging; (v) safe operation, and (vi) low cost. [9]

Typically, a supercapacitor device is composed of two electrodes separated by an ion-permeable membrane separator in the electrolyte and its cell capacitance (C) is calculated as follows: [36]

$$\frac{1}{C} = \frac{1}{C_+} + \frac{1}{C_-} \quad (7)$$

in which C₊ and C₋ are the specific capacitance of the positive and negative electrodes, respectively.

Its energy density and power density can be calculated based on equations (8) and (9): [37]

$$E = \frac{CU^2}{2m} \quad (8)$$

$$P = \frac{UI}{2m} \quad (9)$$

where C (F/g) is the specific capacitance of the supercapacitor device, U (V) is the potential window of discharge current, I (A) is the discharge current and m (g) is the total active material mass of positive and negative electrodes. Therefore, in order to increase energy density (E), it is necessary to enhance cell voltage (U) and the specific capacitance (C) of these electrodes.

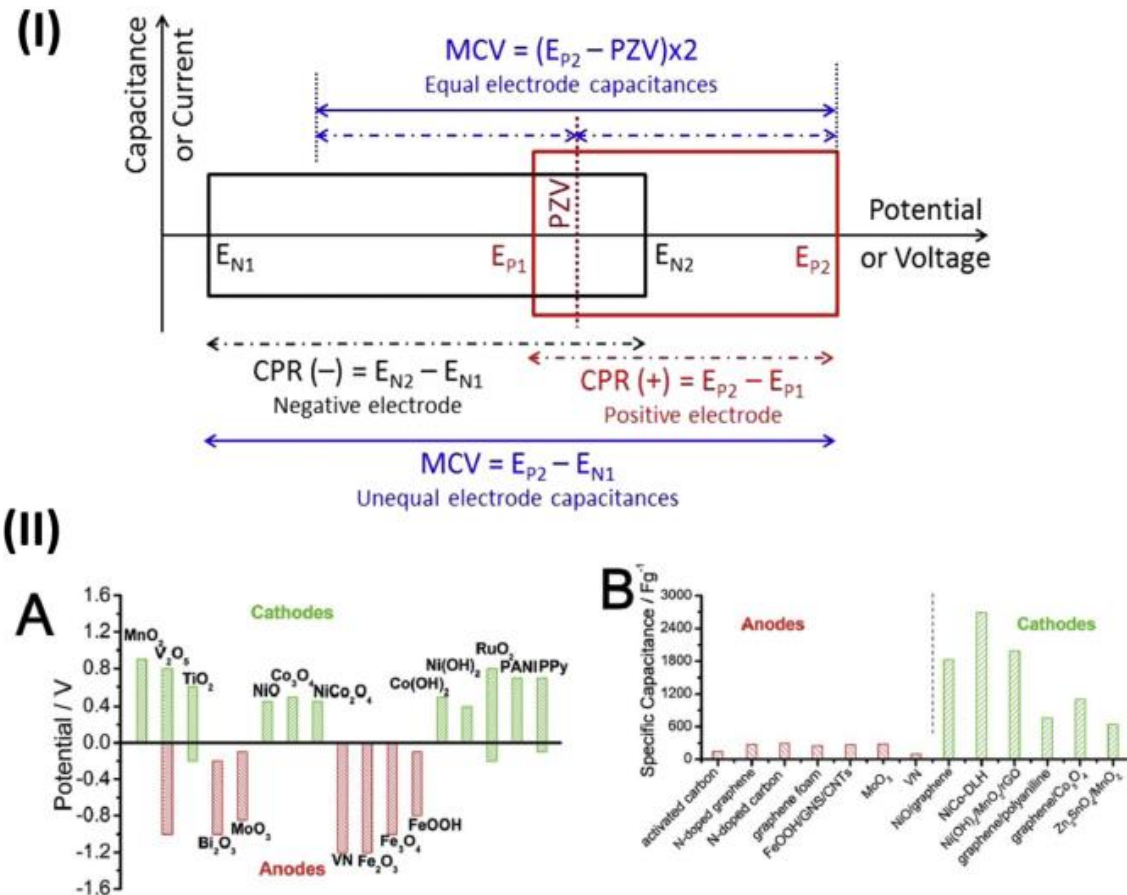


Figure 1.5 (I) Schematic illustration of supercapacitor maximum charging voltage, potential of zero voltage and electrode capacitive potential range for positive and negative electrode. (II) A. Potential window of various pseudocapacitive electrode materials in aqueous electrolyte B. Specific capacitance of selected anode and cathode materials. Adapted from ref. [36]

The assembly of a supercapacitor device can be either symmetric or asymmetric. The symmetric supercapacitor consists of similar positive and negative electrodes and the capacitance (C) of the symmetric cell is $C_+/4$, since $C_+ = C_-$, while the mass loading of the symmetric supercapacitor is twice that of the positive or negative electrodes. The asymmetric supercapacitors (ASCs) are composed of two distinct positive and negative electrodes separated by a porous membrane separator. The potential window

of ASCs is the overlay of the characteristic operating voltages of positive and negative electrodes. The positive and the negative electrode materials of ASCs can be either pseudo/EDLC or a pseudo/pseudo combination. Generally, the potential ranges of the positive and the negative electrodes are determined by the oxygen and the hydrogen evolution reactions, respectively. In the case of ASCs, it is essential to choose positive and negative materials which possess high hydrogen and oxygen evolution over potentials leading to a larger cell voltage (U) (**Figure 1.5 I**). The potential window of various positive and negative electrodes in aqueous electrolyte is displayed in **Figure 1.5 II (A)**. As the cell capacitance (C) is dependent on both positive and negative electrodes, the reported specific capacitance of the representative anode and the cathode electrodes is represented in **Figure 1.5 II (B)**. It can be seen that the achieved specific capacitance of the negative electrodes is usually much less than that of the positive electrodes. Therefore, this paves the way for further research to develop a negative electrode to achieve high energy density supercapacitors. [38-39]

Typical negative electrodes employed in supercapacitors are Fe_2O_3 , Fe_3O_4 , FeOOH , Bi_2WO_6 , Bi_2O_3 , MoO_3 , MoO_2 , WO_3 , VN, TiN etc.. [40-53] Among these negative electrodes, the $\alpha\text{-Fe}_2\text{O}_3$ (hematite) based negative electrode for supercapacitors has attracted plenty of attention because of its high theoretical specific capacitance (3625 F g^{-1}), low price, thermal stability, abundance in nature and environmental friendliness. [54] Typically, the pseudocapacitive performance of Fe_2O_3 is attributed to the reversible oxidation/reduction reaction between Fe^{3+} and Fe^{2+} . [55] Nevertheless, the electrochemical performance of hematite still suffers from its poor electrical conductivity ($10^{-14} \text{ S cm}^{-1}$), resulting in high charge transfer resistance between the electrolyte and the electrode. Another limitation of hematite is the capacitance decay due to its volume expansion during cycle stability testing. Thus, much effort has been devoted to increasing the number of active sites, reducing the diffusion length of the charge carriers, and minimizing the volume expansion by reducing the particle size. A detailed investigation on the pseudocapacitive performance of hematite-based supercapacitor electrodes will be presented in the third chapter of this dissertation.

1.3 Fundamental Concepts of Photoelectrochemical Water Splitting

1.3.1 Fundamental Concepts of Photoelectrochemistry

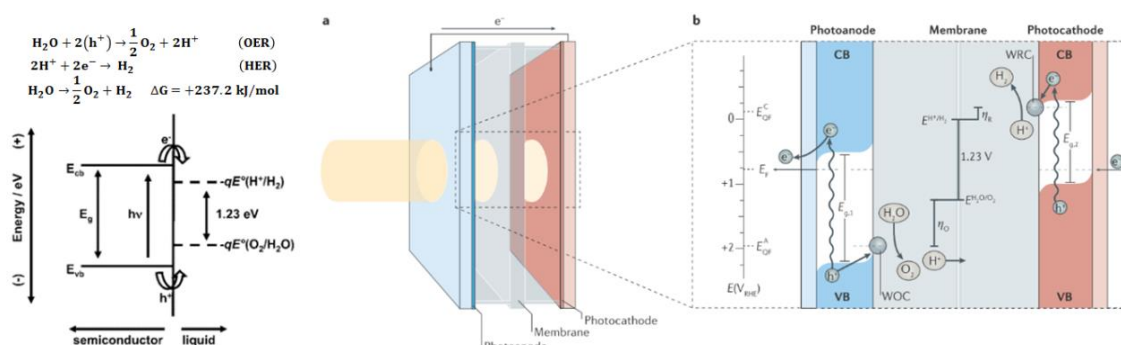


Figure 1.6 Left: Oxygen evolution reaction (OER) and hydrogen evolution reaction (HER) for water splitting under acidic conditions, where E° is the theoretical reduction potential for both (H^+/H_2) and ($\text{O}_2/\text{H}_2\text{O}$) redox couples. Right: Photoelectrochemical cell for whole water splitting. (a) Schematic of a ‘wired’-type tandem water splitting cell with incident solar illumination striking the photoanode and transmitting to the photocathode. (b) Working principle of the tandem cell for water splitting using a photoanode with bandgap energy $E_{g,1}$, and a photocathode with $E_{g,2}$ (where $E_{g,1} > E_{g,2}$). Briefly, on absorption of a solar photon, an electron (e^-) from the valence band (VB) is promoted to the conduction band (CB) leaving the corresponding electron hole (h^+). The electric field in the depletion layer physically separates these charges. Photogenerated electrons in the CB of the photoanode travel through the external circuit to recombine with the holes in the VB of the photocathode. E_F , Fermi energy; $E(V_{\text{RHE}})$, electronic potential with respect to the reversible hydrogen electrode; η_R , overpotential for reduction; η_O , overpotential for oxidation. Adapted from ref. [56-57]

The free energy change required for the conversion of 1 H_2O molecule to H_2 and $1/2$ O_2 molecule under standard conditions is $\Delta G = 237.2 \text{ kJ mol}^{-1}$. [56] According to Nernst's equation, it corresponds to $\Delta E^\circ = 1.23 \text{ V/transferred electron}$. To drive this reaction under illumination with a semiconductor, the semiconductor must absorb sunlight with photon energies of $> 1.23 \text{ eV}$ (corresponding to wavelengths less than 1000 nm) and transfer the solar energy into H_2 and O_2 . The corresponding process must generate two electron-hole pairs/ H_2 molecular ($2 \times 1.23 \text{ eV} = 2.46 \text{ eV}$) or four electron-hole pairs/ O_2 molecule ($4 \times 1.23 \text{ eV} = 4.92 \text{ eV}$). Theoretically, a semiconductor with a band gap energy (E_g) large than 1.23 eV can drive the HER and

OER using electrons/holes generated under illumination (**Figure 1.6**), provided it has a conduction band edge energy (E_{cb}) and valence band edge energy (E_{vb}) that straddles the electrochemical potentials of E° (H^+/H_2) and E° (O_2/H_2O). To drive these two reactions, photoinduced electrons or holes in the semiconductor bulk must travel to a semiconductor/electrolyte interfaces, and then react with electrolyte species directly at the semiconductor surface without recombination. The charge-transfer process at semiconductor/electrolyte interfaces results in losses because of the concentration and kinetic overpotentials for driving the HER and the OER. Therefore, the energy required for photoelectrochemical water splitting at a photoelectrode is usually reported as 1.6-2.4 eV/generated electron-hole pair. [58-59] Although it is possible to construct a PEC cell with one photoelectrode and another standard metallic (dark) electrode, developing a single photoelectrode that can produce sufficient photovoltage for OER and HER and also harvest a significant portion of the solar spectrum is still a huge challenge. As semiconductors can transmit photons with energy less than their E_g , a PEC cell can be constructed with two photoelectrodes. An example is a n-type photoanode and a p-type photocathode, in a tandem configuration that increases the photovoltage and the harvested light energy simultaneously, as shown in **Figure 1.6**. [60] The practical need for 1.6-2.4 eV to effectively drive water splitting motivates the use of semiconductor heterojunctions with different energy gaps, which will be discussed in the next section. The surface state presented at the semiconductor/electrolyte interface, and how these surface states affect the energetics of photoelectrochemical water splitting, will be explored in section **1.3.5**.

1.3.2 Physics of Semiconductor Materials

The motivation for research regarding the use of semiconductors for water splitting stems from the unique electronic and optical characteristics of semiconductors, such as the specified energy gap between their valence band and conduction band. The density of states distributions related to the valence and conduction bands are complicated energy functions (**Figure 1.7 a**). However, near the band edges they often approach to the simple parabolic forms shown in **Figure 1.7 b**. In this dissertation, we

will simplify the band diagram for semiconductors to the form shown in **Figure 1.7 c**. The critical energies are the energies of the conduction and valence band edges, E_C and E_V , which define the band gap energy.

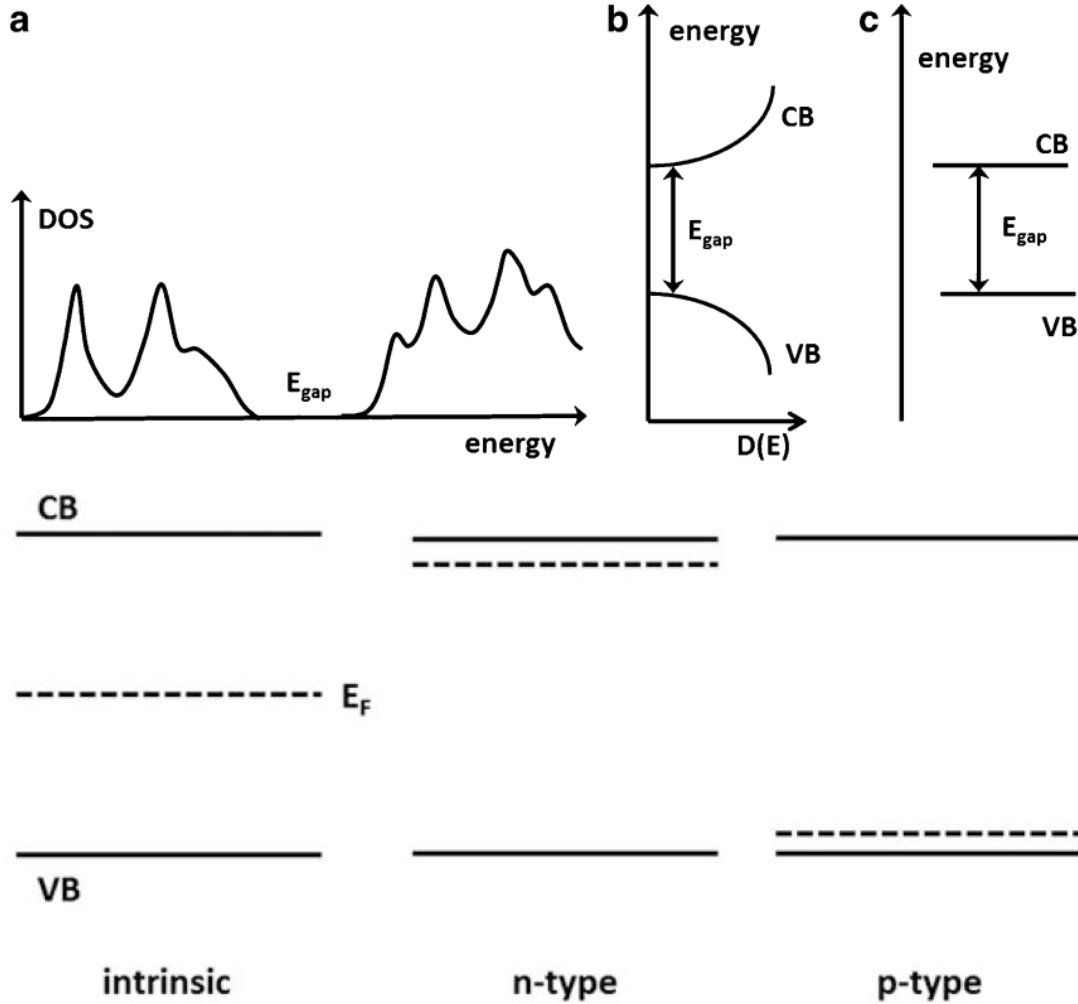


Figure 1.7 Top: (a) Density of states (DOS) for a typical semiconductor; (b) parabolic approximation near band edges; (c) simplified band diagram used in this dissertation. Bottom: Band diagrams intrinsic and doped semiconductors, showing the position of the Fermi energy E_F . Adapted from ref. [61]

Typically, the electron occupation probability for the energy level distributions of semiconductors is defined by the Fermi-Dirac function $f(E)$: [61]

$$f(E) = \frac{1}{1 + \exp\left(\frac{E - E_F}{k_B T}\right)} \quad (10)$$

in which E_F is the Fermi energy. For $E > E_F$, the occupation probability falls rapidly to zero over an energy range of a few $k_B T$, however, for $E < E_F$, it increases rapidly to 1.

For $E=E_F$, the occupation probability is 0.5. For a pure semiconductor material that has no doping impurities, electrons can be thermally excited across the forbidden gap, leaving holes in the valence band. The concentrations of electrons (n) and holes (p), which must be equal under these conditions, can be expressed in terms of the Fermi-Dirac probability function for the presence (f) or absence ($1-f$) of electrons: [61]

$$n = \int_{E_c}^{\infty} D_c(E)f(E)dE \quad (11)$$

$$p = \int_{-\infty}^{E_v} D_v(E)[1 - f(E)]dE \quad (12)$$

$$np = N_c N_v \exp\left(-\frac{E_{gap}}{k_B T}\right) \quad (13)$$

in which D_C and D_V represent the densities of states distributions, respectively. And N_C and N_V are the effective densities of states in the conduction and valence band, respectively. The equilibrium concentrations of electrons and holes are related to the mass balance equation. When N_C and N_V are equal, it follows that the Fermi energy E_F for an undoped semiconductor is situated at the mid-gap position because $n=p$.

Generally, we are dealing with doped semiconductors, like n-type or p-type semiconductors. They contain donor (n-type doping) or acceptor (p-type doping) atoms (or vacancies) in the lattice, which can create electrons or holes. The ionization energies for these reactions are normally of the order of $k_B T$. Thus, the free electron or hole concentrations at room temperature are directly determined by the doping level rather than by the excitation of electrons across the band gap. In this case, the E_F is determined by N_D or N_A , and if $n \ll N_C$ or $p \ll N_V$, where the Fermi Dirac function reduces to the Boltzmann function.

$$n = N_c \exp\left(-\frac{E_c - E_f}{k_B T}\right); \quad p = N_v \exp\left(-\frac{E_v - E_f}{k_B T}\right) \quad (14)$$

It is well established that different semiconductors have distinct energy band gaps, the corresponding valence band edge and conductance band edge, as displayed in **Figure 1.8** top. Constructing suitable heterojunctions with different semiconductors will enhance the charge separation efficiency. Herein, we will introduce the concepts of

three types of heterojunctions (**Figure 1.8** bottom) to describe the various band alignments normally found in heterojunctions for photoelectrochemical water splitting.

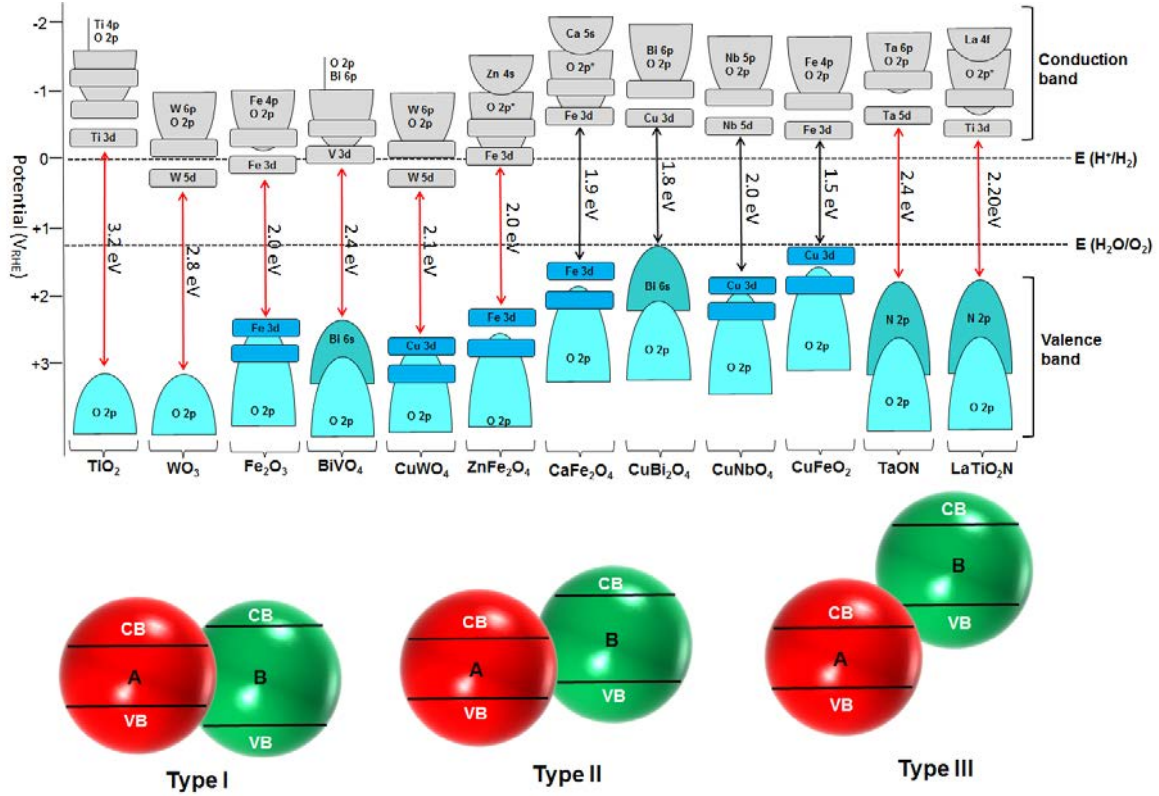


Figure 1.8 Top: bandgap structure of semiconductors for PEC water splitting applications. Contribution of metal cation and oxygen anion states to the conduction and valence bands. The bandgap energy (red for n-type, black for p-type) is shown with respect to the reversible hydrogen electrode and the water redox energy levels. Bottom: Band alignment in Type I, II, and III heterojunctions. [57, 62]

Letter A corresponds to semiconductor A, and letter B corresponds to semiconductor B (both A and B semiconductors can be either n-type or p-type). A Type I heterojunction is composed of two different semiconductors, in which the conduction band (CB) of semiconductor B is higher than that of A and the valence band (VB) of B is lower than that of A. In this way, the holes and electrons will transfer and accumulate on semiconductor A. A type II junction enables the transfer of photoexcited electrons from B to A because of the more negative CB position of B. In

contrast, holes will travel in the opposite direction from semiconductor A to semiconductor B, resulting in efficient charge separation and enhanced catalytic performance. Finally, the last possible situation, Type III, is identical to Type II except for a broken gap where there is no overlapping of the band gaps of both combined semiconductors. [62-63]

1.3.3 Semiconductor Materials for Photoanodes

A photoanode enabling OER is usually an n-type semiconductor material, in which the band bending generated electric field drives the photoinduced holes to the surface. The photoanode material should have a band gap, suitable band-edge positions as well as electrical properties, such as doping and resistivity that enable efficient charge carrier collection. In addition, the photoanodes should be stable under water oxidization conditions. As a result of these requirements, metal oxides, in pure, mixed, or doped forms have been extensively investigated as potential photoanode materials. Normally, the electronic structure of these metal oxides is that the VB is composed of O 2p orbitals, and CB consists of orbitals of the metal elements. [56] It has been revealed that, especially in ionic crystals, the potential of the VB remains almost unchanged at 3.0 (0.5 V vs. NHE for most metal oxides, like TiO₂, SrTiO₃, WO₃, Fe₂O₃ and ZnO (**Figure 1.8**)). [64] Thus, metal ions derived from bulk matrix or dopant materials work together to tune the CB edges as well as the band gap. Among these photoanodes, hematite based photoanodes have been intensively investigated because of several promising properties, such as high natural abundance, low cost, and environmental friendliness. More importantly, in terms of its applications in photoelectrochemical water splitting, hematite possesses high photoelectrochemical stability, a narrow band gap (1.9-2.2 eV), and a theoretical maximum solar-to-hydrogen (STH) efficiency of 15.4%, corresponding to 12.5 mA cm⁻² at Air-Mass 1.5 Global solar illumination, which exceeds the STH benchmark efficiency of 10% required for practical applications. [65] In this dissertation, a systematic investigation of Fe₂O₃ based photoanodes for photoelectrochemical water splitting will be presented in **chapters 4 and 5**.

1.3.4 Electrocatalysts for OER and HER in Water Splitting

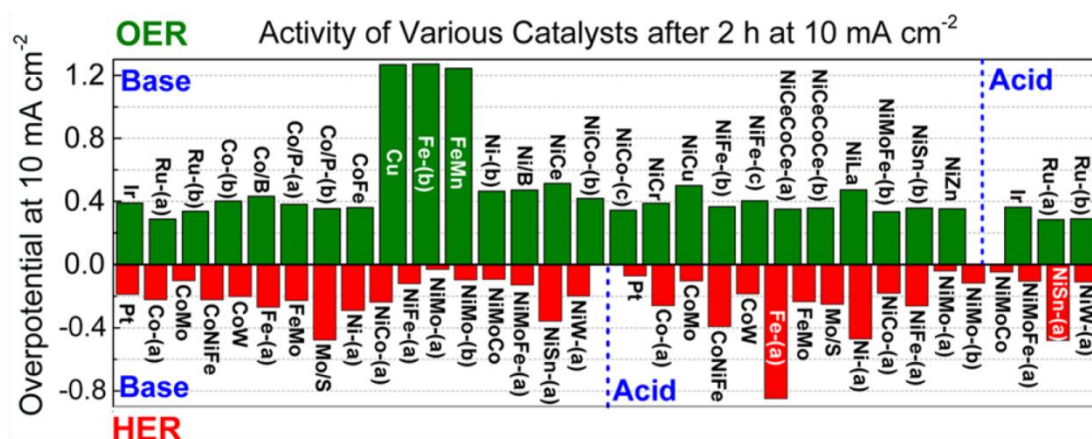


Figure 1.9 Activity of Various Catalysts after 2h at 10 mAcm⁻² electrochemical test. Adapted from ref. [66]

Table 1.1 Representative electrocatalyst surface-modified hematite for PEC water splitting.

Reference	Materials	Fabrication methods	Photocurrent at 1.23 V vs RHE
[70]	Fe ₂ O ₃ /IrOx	Photoelectrodeposition	0.66 mAcm ⁻² ; electrolyte: (pH = 1.01)
[71]	Fe ₂ O ₃ /Fe-Pt	Plasma enhanced-CVD and sputtering	0.638 mAcm ⁻² ; electrolyte: (pH = 13.7)
[72]	Fe ₂ O ₃ /RuO ₂	Spraypyrolysis	0.15 mAcm ⁻² ; electrolyte: (pH = 13)
[73]	Fe ₂ O ₃ /Ru(II) complex	Self-assembly	0.12 mAcm ⁻² ; electrolyte: (pH = 3)
[74]	Fe ₂ O ₃ :Ti/Ni(OH) ₂	Two-step hydrothermal method	0.39 mAcm ⁻² ; electrolyte: (pH = 13.3)
[75]	Fe ₂ O ₃ /Ni(OH) ₂ /IrO ₂	CBD and successive ion layer adsorption	1.7 mAcm ⁻² ; electrolyte: (pH = 13.6)
[76]	Fe ₂ O ₃ /NiOOH	Photoelectrodeposition	0.625 mAcm ⁻² ; electrolyte: (pH = 13.6)
[77]	Fe ₂ O ₃ /Ni-Bi	Photodeposition	0.55 mAcm ⁻² ; electrolyte: (pH = 13.6)
[78]	Fe ₂ O ₃ /Co ₃ O ₄	Hydrothermal growth	1.20 mAcm ⁻² ; electrolyte: (pH = 13.6)
[79]	Fe ₂ O ₃ /Co-Pi	Electrodeposition	0.60 mAcm ⁻² ; electrolyte: (pH = 13.6)

As the interfacial OER kinetics of the photoanodes is determined to be rate limiting, an oxygen evolution catalyst integrated with photoanodes is supposed to reduce the required overpotential and ultimately enhance PEC water splitting performance. [69] Several water oxidation electrocatalysts have been utilized to modify the hematite

photoanode surface and the results are summarized in **Table 1.1**.

On the other hand, among the HER electrocatalysts, two dimensional (2D) transition metal dichalcogenide materials (TMDs), like MoS₂, MoTe₂, PtSe₂ etc. have drawn plenty of researcher's attention due to its fascinating advantages such as low cost, earth abundance, and good stability. [80-81] Up to date, structural defects, such as edges, [82-86] doped heteroatoms, [87] defects [88] or basal planes [89-90] presented in the 2D materials have been intensively investigated for HER in water splitting and identified as the active sites.

1.3.5 The Semiconductor/Electrolyte Interface and the Concept of Surface State

A description of a semiconductor/electrolyte interface is usually similar to a semiconductor/metal interface (**Figure 1.10**). In this dissertation, our aim is not to provide an extended survey of the thermodynamics and kinetics of semiconductor-electrolyte interfaces. Instead, we just wish to focus on the electronic properties of photoelectrochemical interfaces of semiconductor/electrolyte that are important for understanding charge transfer reactions in water splitting devices. [61]

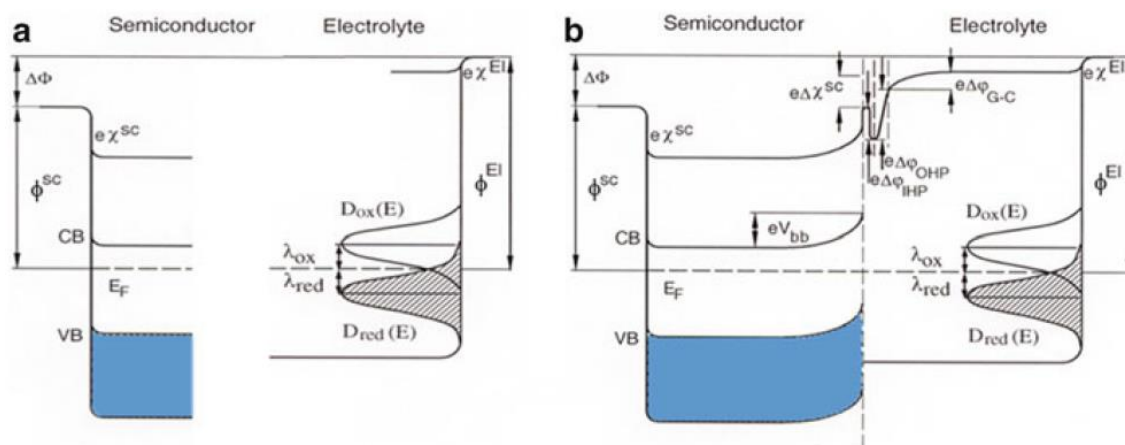


Figure 1.10 Contact formation of a semiconductor-electrolyte interface including a well-defined one-electron transfer reversible outer sphere redox couple with its redox potential $E_{\text{red/ox}}$ given by its work function ϕ^{El} . (a) Before contact: both work functions contain a surface dipole potential drop of $e\chi$. (b) after contact: as schematically shown as contributions of different dipolar or electrochemical double layers (semiconductor dipole, inner Helmholtz and outer Helmholtz). Subsequently, the original given difference in work function is divided into an extended space charge layer eV_{bb} and double layer

potential drops. Adapted from ref. [61]

At the surface of a semiconductor, the periodic crystal symmetry is broken and thus electronic states within the bandgap are produced, which are termed surface states/mid-gap states. The surface state derived residence at the surface of semiconductors can be intrinsic or extrinsic, when their existence relies on the environmental conditions of the semiconductors. In the field of semiconductor photoelectrochemistry, surface states play a vital role in the kinetics of interfacial reactions of illuminated semiconductor electrodes. Specifically, the importance of surface states for the kinetics of photoelectrochemical reactions involving holes has been highlighted in the system of III-V semiconductors and Fe_2O_3 . [91-92]

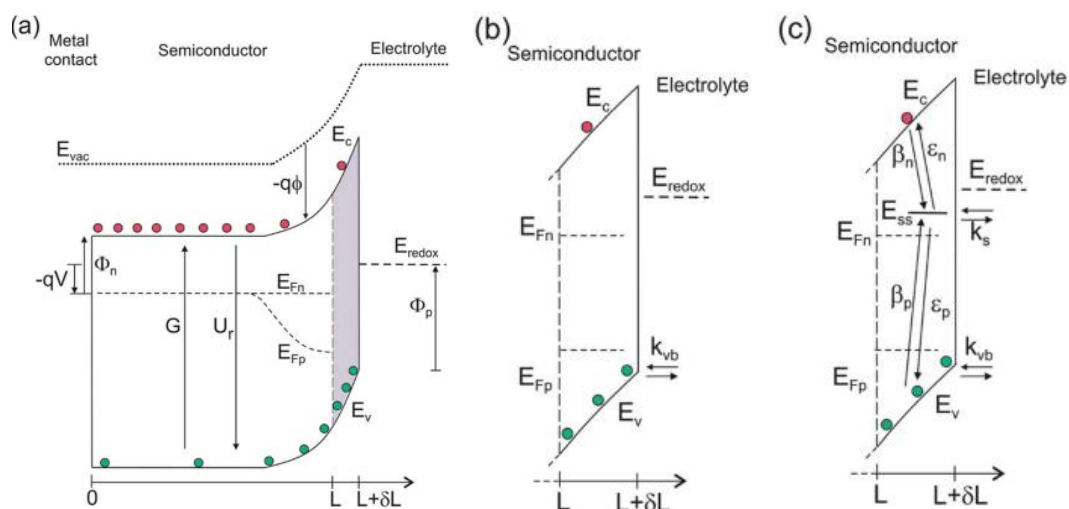


Figure 1.11 (a) Energy diagrams of a n-type semiconductor of thickness L where electrons and holes are generated at a rate G and recombine at a rate U_r . At the interface of length δL , hole transfer to the redox level E_{redox} can take place (b) directly from the valence band (kinetic constant k_{vb}) and (c) indirectly from surface states at low bias and directly from the valence band at higher bias. In this latter model, we consider trapping of electrons and holes (β_n and β_p) and detrapping (ϵ_n, ϵ_p) and hole transfer from surface states (k_s) at the energy level E_{ss} , in competition with direct hole transfer. In these schemes E_c and E_v are the energies of the lower edge of the conduction band and the higher edge of the valence band, respectively. E_{Fn} and E_{Fp} are the quasi Fermi levels, Φ_n and Φ_p are the injection barriers of electrons and holes, E_{vac} is the local vacuum level, ϕ is the local electrostatic potential and V is the applied voltage. [95]

Surface states can act as recombination centres for holes generated by light and surface recombination therefore competes intensively with charge transfer from the semiconductor to electrolyte. Under illumination, the valence band of a photoanode acquires an abundant excess of holes, which can be transferred to the electrolyte via a direct charge transfer mechanism to launch the solar fuel production reaction. However, with the presence of surface states, the localized bandgap states trap hole carriers and thus present another favourable pathway for indirect charge transfer and a new undesirable recombination pathway. [93-94]

A simple kinetic model neglecting any electrostatic influence, such as like the presence of an electric field, is presented in **Figure 1.11**. This model helps to understand the effect of the surface state-assisted electron-hole recombination and indirect charge transfer processes on photoelectrochemical water splitting. At low bias potentials, direct holes transferring from the valence band can be neglected and only three processes occur at this interface: trapping/detrapping of electrons, trapping/detrapping of holes and charge transfer of holes. Hence, from this simple picture, it is clear that surface state-assisted recombination and hole transfer to the solution have hole trapping/detrapping as a common factor. [96]

Specifically, the mechanism of photoelectrochemical oxygen evolution on hematite involves the 4-electron transfer/O₂ molecule. It is well established that the OER reaction steps involve higher-valence state iron formation at the surface by hole capture. Equations (14-17) illustrate the complications arising from the fact that the oxidation of water is a 4-electron process, so that holes need to be ‘stored’ in intermediate states. The Fe(IV) and Fe(V) intermediates in this scheme can also act as electron acceptors, so that surface recombination reactions of the kind shown in equations (18-19) are likely to take place. The Fe(IV) and Fe(V) states can also be thought of as ‘surface-trapped holes’, which may have sufficient surface mobility to allow second order reactions of the type illustrated by the last step shown in equations (14-17). [97]





Impedance spectroscopy allows probing the density of surface states by monitoring the surface state chemical capacitance (C_{μ}^{SS}) as a function of the applied bias (electron Fermi level). In dark conditions, majority carriers are in equilibrium with the transport band (conduction band for an n-type material) and this capacitance is termed the equilibrium chemical capacitance of surface states ($C_{\mu\text{eq}}^{\text{SS}}$) as [98]

$$C_{\mu\text{eq}}^{\text{SS}} = Aq^2N_{\text{SS}} \frac{\partial f_{\text{SS}}}{\partial E_{\text{Fn}}} = A \frac{q^2N_{\text{SS}}}{k_{\text{B}}T} f_{\text{SS}}(1 - f_{\text{SS}}), \quad (20)$$

where, N_{SS} is the density of the surface states, f_{SS} the fractional occupancy of the surface states, k_{B} the Boltzmann constant, and E_{Fn} the electron Fermi level. In the presence of a wide distribution of surface states such as the Gaussian distribution, the surface state capacitance is related to the density of surface states (DOS), $N_{\text{SS}}(E)$, as [98]

$$C_{\mu\text{eq}}^{\text{SS}} = A_s q N_{\text{SS}}(E_{\text{Fn}}) \quad (21)$$

It is well established that the Fermi level pinning results from surface states, in that changes in the surface brought about by deliberate surface chemistry will change the surface states and hence the photovoltage in solid-state and liquid-junction solar devices. [99]

A great deal of attention has been paid to the modification of semiconductor-electrolyte interfaces by coating of additional electronic/chemical passivation layers to avoid Fermi level pinning derived from surface states. In summary, for semiconductors used for photoelectrochemical water splitting, there are a few general remarks to be made:

(i) Intrinsic surface states of semiconductors are derived from the loss of translational bulk crystal symmetry influenced by surface orientation, surface relaxation and reconstruction.

(ii) The chemical bond formation/surface interaction with secondary phases results in extrinsic surface states, which modify the intrinsic surface states.

(iii) Normally, the concentration of surface/interface states is usually very high, if they are active for Fermi level pinning, which may enhance surface carrier recombination depending on its energy positions.

References

- [1] C.A.S. Hall, K.A. Klitgaard, Energy and the wealth of nations, Springer New York, New York, NY, **2012**.
- [2] B. Obama, The irreversible momentum of clean energy, *Science*, **2017**, 355, 126-129.
- [3] H. D. Abruña, K. Yasuyuki, J. C. Henderson, Batteries and electrochemical capacitors, *Physics Today*, **2008**, 61, 43-47.
- [4] N. S. Choi, Z.H. Chen, S. A. Freunberger, X.L. Ji, Y.K. Sun, K. Amine, G. Yushin, L. F. Nazar, J. Cho, Bruce P. G., Challenges facing lithium batteries and electrical double-layer capacitors, *Angew. Chem. Int. Ed.*, **2012**, 51, 9994-10024.
- [5] W. Martin, R. J. Brodd, What are batteries, fuel cells, and supercapacitors? *Chemical reviews*, **2004**, 104, 4245-4270.
- [6] P. Simon, Y. Gogotsi, Materials for electrochemical capacitors, *Nature materials*, **2008**, 7, 845-854.
- [7] W.F. Wei, X.W. Cui, W.X. Chen, D.G. Ivey, Manganese oxide-based materials as electrochemical supercapacitor electrodes, *Chem. Soc. Rev.*, **2011**, 40, 1697-1721.
- [8] A. Chu, P. Braatz, Comparison of commercial supercapacitors and high-power lithium-ion batteries for power-assist applications in hybrid electric vehicles: I. Initial characterization, *Journal of Power Sources*, **2002**, 112, 236-246.
- [9] L. L. Zhang, X. S. Zhao, Carbon-based materials as supercapacitor electrodes, *Chem. Soc. Rev.*, **2009**, 38, 2520-2531.
- [10] H. V. Helmholtz, Ueber einige gesetze der vertheilung elektrischer ströme in körperlichen leitern mit anwendung auf die thierisch-elektrischen versuche, *Ann. Phys.* **1853**, (Leipzig), 89, 21.
- [12] M. Gouy, Sur la constitution de la charge électrique à la surface d'un electrolyte, *J. Phys. Theor. Appl.* **1910**, 9, 457-468.
- [13] D. L. Chapman, A contribution to the theory of electrocapillarity, *Philos. Mag.*, **1913**, 6, 475-481.
- [14] O. Stern, Zur theorie der elektrolytischen doppelschicht, *Berichte der Bunsengesellschaft für physikalische Chemie*, **1924**, 30, 508-516.
- [15] E. Frackowiak, Carbon materials for supercapacitor application, *Phys. Chem. Chem. Phys.*, **2007**, 9, 1774-1785.
- [16] D. Qu and H. Shi, Studies of activated carbons used in double-layer capacitors, *J. Power Sources*, **1998**, 74, 99-107.
- [17] M. Endo, T. Maeda, T. Takeda, Y. J. Kim, K. Koshiba, H. Hara, M. S. Dresselhaus, Capacitance and pore-size distribution in aqueous and nonaqueous electrolytes using various activated carbon electrodes, *J. Electrochem. Soc.*, **2001**, 148, 910-914.
- [18] J. Huang, Bobby G. Sumpter and V. Meunier, A universal model for nanoporous carbon supercapacitors applicable to diverse pore regimes, carbon materials, and electrolytes, *Chem. Eur. J.*, **2008**, 14, 6614-6626.

- [19] R. Kötzt, M. Carlen, Principles and applications of electrochemical capacitors. *Electrochim. Acta*, **2000**, 45, 2483-2498.
- [20] B. E. Conway, Electrochemical supercapacitors: Scientific fundamentals and technological applications, *Kluwer Academic/Plenum Publisher*, **1999**, New York.
- [21] N.L.Wu, Nanocrystalline oxide supercapacitors. *Mater. Chem. Phys.* **2002**, 75, 6-11.
- [22] T. Brousse, M. Toupin, R. Dugas, L. Athouël, O. Crosnier, D. Bélanger, Crystalline MnO₂ as possible alternatives to amorphous compounds in electrochemical supercapacitors. *J. Electrochem. Soc.* **2006**, 153, 2171-2180.
- [23] A. Rudge, I. Raistrick, S. Gottesfeld, J. P. Ferraris, Conducting polymers as active materials in electrochemical capacitors. *J. Power Sources*, **1994**, 47, 89-107.
- [24] D. Choi, G. E. Blomgren, P. N. Kumta, Fast and reversible surface redox reaction in nanocrystalline vanadium nitride supercapacitors, *Adv. Mater.*, **2006**, 18, 1178-1182.
- [25] L. Z. Fan, Y. S. Hu, J. Maier, P. Adelhelm, B. Smarsly, M. Antonietti, High electroactivity of polyaniline in supercapacitors by using a hierarchically porous carbon monolith as a support, *Adv. Funct. Mater.*, **2007**, 17, 3083-3087.
- [26] M. Seredych, D. Hulicova-Jurcakova, G. Q. Lu and T. J. Bandosz, Surface functional groups of carbons and the effects of their chemical character, density and accessibility to ions on electrochemical performance, *Carbon*, **2008**, 46, 1475-1488.
- [27] T. C. Wen, C. C. Hu, Hydrogen and oxygen evolutions on Ru-Ir binary oxides, *J. Electrochem. Soc.*, **1992**, 139, 2158-2163.
- [28] B. E. Conway, Transition from “supercapacitor” to “battery” behavior in electrochemical energy storage, *J. Electrochem. Soc.* **1991**, 138, 6, 1539-1548.
- [29] C. C. Hu, K. H. Chang, M. C. Lin, Y. T. Wu, Design and tailoring of the nanotubular arrayed architecture of hydrous RuO₂ for next generation supercapacitors, *Nano Lett.*, **2006**, 6, 2690-2695.
- [30] C. C. Hu, W. C. Chen, K. H. Chang, How to achieve maximum utilization of hydrous ruthenium oxide for supercapacitors, *J. Electrochem. Soc.*, **2004**, 151, 281-290.
- [31] H.Y. Lee, J.B. Goodenough, Supercapacitor behavior with KCl electrolyte. *J. Solid State Chem.*, **1999**, 144, 220-223.
- [32] A. Rudge, I. Raistrick, S. Gottesfeld, J. P. Ferraris, Conducting polymers as active materials in electrochemical capacitors. *J. Power Sources*, **1994**, 47, 89-107.
- [33] A. Laforgue, P. Simon, J.F. Fauvarque, Chemical synthesis and characterization of fluorinated polyphenylthiophenes: application to energy storage. *Synth. Met.* **2001**, 123, 311-319.
- [34] K. Naoi, S. Suematsu, A. Manago, Electrochemistry of poly(1,5-diaminoanthraquinone) and its application in electrochemical capacitor materials. *J. Electrochem. Soc.* **2000**, 147, 420-426.
- [35] R. Kötzt, M. Carlen, Principles and applications of electrochemical capacitors. *Electrochim. Acta*, **2000**, 45, 2483-2498.
- [36] V. D. Nithya, N. S. Arul, Review on α -Fe₂O₃ based negative electrode for high performance Supercapacitors, *J. Power Sources*, **2016**, 327, 297-318.

- [37] P.Y. Tang, L.J. Han, L. Zhang, Facile synthesis of graphite/PEDOT/MnO₂ composites on commercial supercapacitor separator membranes as flexible and high-performance supercapacitor electrodes, *ACS Appl. Mater. Interfaces*, **2014**, 6, 10506-10515.
- [38] M. Yu, Z. Wang, Y. Han, Y. Tong, X. Lu, S. Yang, Recent progress in the development of anodes for asymmetric supercapacitors, *J. Mater. Chem. A*, **2016**, 4, 4634-4658.
- [39] X.F. Lu, G.R. Li, Y.X. Tong, A review of negative electrode materials for electrochemical supercapacitors, *Sci. China Tech. Sci.* **2015**, 58, 1799-1808.
- [40] M. Zhang, K. Chen, X. Chen, X. Peng, X. Sun, D. Xue, Ethylenediamine-assisted crystallization of Fe₂O₃ microspindles with controllable size and their pseudocapacitance performance, *Cryst. Eng. Comm.* **2015**, 17 1521-1525.
- [41] L. Wang, H. Ji, S. Wang, L. Kong, X. Jiang, G. Yang, Preparation of Fe₃O₄ with high specific surface area and improved capacitance as a supercapacitor, *Nanoscale*, **2013**, 5, 3793-3799.
- [42] K. Chen, X. Chen, D. Xue, Hydrothermal route to crystallization of FeOOH nanorods via FeCl₃·6H₂O: effect of Fe³⁺ concentration on pseudocapacitance of iron-based materials, *Cryst. Eng. Comm.*, **2015**, 17, 1906-1910.
- [43] V.D. Nithya, R. Kalai Selvan, D. Kalpana, L. Vasylechko, C. Sanjeeviraja, Synthesis of Bi₂WO₆ nanoparticles and its electrochemical properties in different electrolytes for pseudocapacitor electrodes, *Electrochim. Acta*, **2013**, 109, 720-731.
- [44] X. Li, J. Shao, J. Li, L. Zhang, Q. Qu, H. Zheng, Ordered mesoporous MoO₂ as a high-performance anode material for aqueous supercapacitors, *J. Power Sources*, **2013**, 237, 80-83.
- [45] X. Lu, G. Wang, T. Zhai, M. Yu, S. Xie, Y. Ling, C. Liang, Y. Tong, Y. Li, Stabilized TiN nanowire arrays for high-performance and flexible supercapacitors, *Nano Lett.* **2012**, 12, 5376-5381.
- [46] J. Balamurugan, G. Karthikeyan, T.D. Thanh, N.H. Kim, J.H. Lee, Facile synthesis of vanadium nitride/nitrogen-doped graphene composite as stable high performance anode materials for supercapacitors, *J. Power Sources*, **2016**, 308, 149-157.
- [47] J. Li, Q. Wu, G. Zan, A High-performance supercapacitor with well-dispersed Bi₂O₃ nanospheres and active-carbon electrodes, *Eur. J. Inorg. Chem.* **2015**, 5751-5756.
- [48] T. Zhai, X. Lu, H. Wang, G. Wang, T. Mathis, T. Liu, C. Li, Y. Tong, Y. Li, An electrochemical capacitor with applicable energy density of 7.4 Wh/kg at average power density of 3000 W/kg, *Nano Lett.* **2015**, 15, 3189-3194.
- [49] R. Wang, X. Yan, J. Lang, Z. Zheng, P. Zhang, A hybrid supercapacitor based on flower-like Co(OH)₂ and urchin-like VN electrode materials, *J. Mater. Chem. A*, **2014**, 2, 12724-12732.
- [50] X. Lu, M. Yu, T. Zhai, G. Wang, S. Xie, T. Liu, C. Liang, Y. Tong, Y. Li, High energy density asymmetric quasi-solid-state supercapacitor based on porous vanadium nitride nanowire anode, *Nano Lett.* **2013**, 13, 2628-2633.
- [51] L. Zhang, C.M.B. Holt, E.J. Luber, B.C. Olsen, H. Wang, M. Danaie, X. Cui, X.H. Tan, V.W. Lui, W.P. Kalisvaart, D. Mitlin, High rate electrochemical capacitors from three-dimensional arrays of vanadium nitride functionalized carbon nanotubes, *J. Phys. Chem. C*, **2011**, 115, 24381-24393.

- [52] P. Sun, Z. Deng, P. Yang, X. Yu, Y. Chen, Z. Liang, H. Meng, W. Xie, S. Tan, W. Mai, Freestanding CNT-WO₃ hybrid electrodes for flexible asymmetric supercapacitors, *J. Mater. Chem. A*, **2015**, 3, 12076-12080.
- [53] W. Tang, L. Liu, S. Tian, L. Li, Y. Yue, Y. Wu, K. Zhu, Aqueous supercapacitors of high energy density based on MoO₃ nanoplates as anode material, *Chem. Commun.* **2011**, 47, 10058-10060.
- [54] X. Chen, K. Chem, H. Wang, D. Xue, Composition design upon iron element toward supercapacitor electrode materials, *Mater. Focus*, **2015**, 4, 78-80.
- [55] Y. Gao, D. Wu, T. Wang, D. Jia, W. Xia, Y. Lv, Y. Cao, Y. Tan, P. Liu, One-step solvothermal synthesis of quasi-hexagonal Fe₂O₃ nanoplates/graphene composite as high performance electrode material for supercapacitor, *Electrochim. Acta*, **2016**, 191, 275-283.
- [56] M. G. Walter, E. L. Warren, J. R. McKone, S. W. Boettcher, Q. Mi, E. A. Santori, N. S. Lewis, Solar water splitting cells, *Chem. Rev.*, **2010**, 110, 6446-6473.
- [57] K. Sivula, R. V. D. Krol, Semiconducting materials for photoelectrochemical energy conversion, *Nat. Rev. Mater.*, **2016**, 1, 15010.
- [58] J. A. Turner, A realizable renewable energy future, *Science*, **1999**, 285, 687-689.
- [59] J. R. Bolton, S. J. Strickler, J. S. Connolly, Limiting and realizable efficiencies of solar photolysis of water, *Nature*, **1985**, 316, 495-500.
- [60] A. J. Nozik, Photochemical diodes. *Appl. Phys. Lett.* **1977**, 30, 567-569.
- [61] S. Giménez, J. Bisquert, Photoelectrochemical solar fuel production-from basic principles to advanced devices, **2016**, Springer.
- [62] S. J. A. Moniz, S. A. Shevlin, D. J. Martin, Z.X. Guo, J.W. Tang, Visible-light driven heterojunction photocatalysts for water splitting-a critical review, *Energy Environ. Sci.*, **2015**, 8, 731-759.
- [63] R. Marschall, Semiconductor composites: strategies for enhancing charge carrier separation to improve photocatalytic activity, *Adv. Funct. Mater.*, **2014**, 24, 2421-2440.
- [64] Y. Matsumoto, Energy positions of oxide semiconductors and photocatalysis with iron complex oxides, *J. Solid State Chem.* **1996**, 126, 227-234.
- [65] S. H. Shen, S. A. Lindley, X. Y. Chen and J. Z. Zhang, Hematite heterostructures for photoelectrochemical water splitting: rational materials design and charge carrier dynamics, *Energy Environ. Sci.*, **2016**, 9, 2744-2775.
- [66] C. C. L. McCrory, S. Jung, I. M. Ferrer, S. M. Chatman, J. C. Peters, T. F. Jaramillo, Benchmarking hydrogen evolving reaction and oxygen evolving reaction electrocatalysts for solar water splitting devices, *J. Am. Chem. Soc.* **2015**, 137, 4347-4357.
- [67] R. Subbaraman, D. Tripkovic, K.C. Chang, D. Strmcnik, A. P. Paulikas, P. Hirunsit, M. Chan, J. Greeley, V. Stamenkovic, N. M. Markovic, Trends in activity for the water electrolyser reactions on 3d M (Ni, Co, Fe, Mn) hydr(oxy)oxide catalysts, *Nat. Mater.*, **2012**, 11, 550-557.
- [68] M. W. Louie, A. T. Bell, An investigation of thin-film Ni-Fe oxide catalysts for the electrochemical evolution of oxygen, *J. Am. Chem. Soc.* **2013**, 135, 12329-12337.

- [69] K. M. H. Young, B. M. Klahr, O. Zandi and T. W. Hamann, Photocatalytic water oxidation with hematite electrodes, *Catal. Sci. Technol.*, **2013**, 3, 1660-1671.
- [70] W. Li, S. W. Sheehan, D. He, Y. He, X. Yao, R. L. Grimm, G. W. Brudvig and D. Wang, Hematite-based solar water splitting in acidic solutions: Functionalization by mono- and multilayers of iridium oxygen-evolution catalysts, *Angew. Chem., Int. Ed.*, **2015**, 54, 11428-11432.
- [71] M. E. A. Warwick, D. Barreca, E. Bontempi, G. Carraro, A. Gasparotto, C. Maccato, K. Kaunisto, T.P. Ruokozmo, H. Lemmetyinen, C. Sada, Y. Gonullu, S. Mathur, Pt-functionalized Fe₂O₃ photoanodes for solar water splitting: the role of hematite nano-organization and the platinum redox state, *Phys. Chem. Chem. Phys.*, **2015**, 17, 12899-12907.
- [72] S. A. Majumder and S. U. M. Khan, Photoelectrolysis of water at bare and electrocatalyst covered thin film iron oxide electrode, *Int. J. Hydrogen Energy*, **1994**, 19, 881-887.
- [73] X. Chen, X. Ren, Z. Liu, L. Zhuang and J. Lu, Promoting the photoanode efficiency for water splitting by combining hematite and molecular Ru catalysts, *Electrochem. Commun.*, **2013**, 27, 148-151.
- [74] Q. Li, J. Bian, N. Zhang and D. H. L. Ng, Loading Ni(OH)₂ on the Ti-doped hematite photoanode for photoelectrochemical water splitting, *Electrochim. Acta*, **2015**, 155, 383-390.
- [75] Z. Wang, G. Liu, C. Ding, Z. Chen, F. Zhang, J. Shi, C. Li, Synergetic Effect of conjugated Ni(OH)₂/IrO₂ cocatalyst on titanium-doped hematite photoanode for solar water splitting, *J. Phys. Chem. C*, **2015**, 119, 19607-19612.
- [76] F. Malara, A. Minguzzi, M. Marelli, S. Morandi, R. Psaro, V. D. Santo and A. Naldoni, α -Fe₂O₃/NiOOH: An effective heterostructure for photoelectrochemical water oxidation, *ACS Catal.*, **2015**, 5, 5292-5300.
- [77] Y. R. Hong, Z. Liu, S. F. B. S. A. Al-Bukhari, C. J. J. Lee, D. L. Yung, D. Chi and T. S. A. Hor, Effect of oxygen evolution catalysts on hematite nanorods for solar water oxidation, *Chem. Commun.*, **2011**, 47, 10653-10655.
- [78] L. Xi, P. D. Tran, S. Y. Chiam, P. S. Bassi, W. F. Mak, H. K. Mulmudi, S. K. Batabyal, J. Barber, J. S. C. Loo, L. H. Wong, Co₃O₄-decorated hematite nanorods as an effective photoanode for solar water oxidation, *J. Phys. Chem. C*, **2012**, 116, 13884-13889.
- [79] D. K. Zhong, J. Sun, H. Inumaru and D. R. Gamelin, Solar water oxidation by composite catalyst/ α -Fe₂O₃ photoanodes, *J. Am. Chem. Soc.*, **2009**, 131, 6086-6087.
- [80] S. Manzeli, D. Ovchinnikov, D. Pasquier, O. V. Yazyev, A. Kis, 2D transition metal dichalcogenides. *Nat. Rev. Mater.*, **2017**, 2, 17033.
- [81] D. Voiry, J. Yang, M. Chhowalla, Recent strategies for improving the catalytic activity of 2D TMD nanosheets toward the hydrogen evolution reaction. *Adv. Mater.* **2016**, 28, 6197-6206.
- [82] T. F. Jaramillo, K. P. Jørgensen, J. Bonde, J. H. Nielsen, S. Hørch, I. Chorkendorff, Identification of active edge sites for electrochemical H₂ evolution from MoS₂ nanocatalysts. *Science*, **2007**, 317, 100-102.
- [83] J. Kibsgaard, Z. Chen, B. N. Reinecke, T. F. Jaramillo, Engineering the surface structure of MoS₂ to preferentially expose active edge sites for electrocatalysis. *Nat. Mater.* **2012**, 11, 963-969.

- [84] Q. Ji, Y. Zhang, Y. Zhang, Z. Liu, Chemical vapour deposition of group-VIB metal dichalcogenide monolayers: engineered substrates from amorphous to single crystalline. *Chem. Soc. Rev.* **2015**, 44, 2587-2602.
- [85] G.Q. Li, D. Zhang, Q. Qiao, Y.F. Yu, D. Peterson, A. Zafar, R. Kumar, S. Curtarolo, F. Hunte, S. Shannon, Y.M. Zhu, W.T. Yang, L.Y. Cao, All the catalytic active sites of MoS₂ for hydrogen evolution. *J. Am. Chem. Soc.* **2016**, 138, 16632-16638.
- [86] J. F. Xie, H. Zhang, S. Li, R. X. Wang, X. Sun, M. Zhou, J. F. Zhou, X.W. Lou, Y. Xie, Defect-rich MoS₂ ultrathin nanosheets with additional active edge sites for enhanced electrocatalytic hydrogen evolution. *Adv. Mater.* **2013**, 25, 5807-5813.
- [87] X.P. Dai, K.L. Du, Z.Z. Li, M.Z. Liu, Y.D. Ma, H. Sun, X. Zhang, Y. Yang, Co-doped MoS₂ nanosheets with the dominant CoMoS phase coated on carbon as an excellent electrocatalyst for hydrogen evolution. *ACS Appl. Mater. Interfaces*, **2015**, 7, 27242-27253.
- [88] G. L. Ye, Y.J. Gong, J.H. Li, B. Li, Y.M. He, S. T. Pantelide, W. Zhou, R. Vajtai, P. M. Ajayan, Defects engineered monolayer MoS₂ for improved hydrogen evolution reaction. *Nano Lett.* **2016**, 16, 1097-1103.
- [89] H. Li, C. Tsai, A. L. Koh, L.L. Cai, A. W. Contryman, A. H. Fragapane, J.H. Zhao, H.S. Han, H. C. Manoharan, F. Abild-Pedersen, J. K. Nørskov, X. L. Zheng, Activating and optimizing MoS₂ basal planes for hydrogen evolution through the formation of strained sulphur vacancies. *Nat. Mater.* **2016**, 15, 48-53.
- [90] D. Voiry, R. Fullon, J. Yang, C. D. C. C. E. Silva, R. Kappera, I. Bozkurt, D. Kaplan, M. J. Lagos, P. E. Batson, G. Gupta, A. D. Mohite, L. Dong, D.Q. Er, V. B. Shenoy, T. Asefa, M. Chhowalla, The role of electronic coupling between substrate and 2D MoS₂ nanosheets in electrocatalytic production of hydrogen. *Nat. Mater.* **2016**, 15, 1003-1009.
- [91] J.J. Kelly, R. Memming, The influence of surface recombination and trapping on the cathodic photocurrent at p-type III-V electrodes. *J Electrochem Soc*, **1982**, 129, 730-738.
- [92] M.P. Dareedwards, J.B. Goodenough, A. D. Hamnett, P. R. Trevellick, Electrochemistry and photoelectrochemistry of Iron(III) oxide. *J Chem Soc Farad Trans I*, **1983**, 79, 2027-2041.
- [93] P. Salvador, C. Gutierrez, The nature of surface states involved in the photo- and electroluminescence spectra of n-titanium dioxide electrodes. *J. Phys Chem*, **1984**, 88, 3696-3698.
- [94] P. Salvador, C. Gutierrez, Mechanisms of charge transfer at the semiconductor-electrolyte interface. *J. Electrochem Soc*, **1984**, 131,326-336.
- [95] L. Bertoluzzi, P. Lopez-Varo, J. A. J. Tejada, J. Bisquert, Charge transfer processes at the semiconductor/electrolyte interface for solar fuel production: insight from impedance spectroscopy, *J. Mater. Chem. A*, **2016**, 4, 2873-2879.
- [96] J. Bisquert, Theory of the impedance of charge transfer via surface states in dye-sensitized solar cells. *J. Electroanal Chem*, **2010**, 646, 43-51.
- [97] K. G. Upul Wijayantha, S. Saremi-Yarahmadi, L. M. Peter, Kinetics of oxygen evolution at α -Fe₂O₃ photoanodes: a study by photoelectrochemical impedance spectroscopy, *Phys. Chem. Chem. Phys.*, **2011**, 13, 5264-5270.

[98] J. Bisquert, Nanostructured energy devices: equilibrium concepts and kinetics. *CRC Press*, **2014**, Boca Raton.

[99] A.J. Bard, A. B. Bocarsly, F.R.F. Fan, E. G. Walton, M. S. Wrighton, The Concept of Fermi Level Pinning at Semiconductor/Liquid Junctions. Consequences for Energy Conversion Efficiency and Selection of Useful Solution Redox Couples in Solar Devices, *J. Am. Chem. Soc.*, **1980**, 102, 3671-3677.

Chapter 2

Methodology

In this chapter, the basic concepts of transmission electron microscopy (TEM) and (photo)electrochemical techniques are summarized. In the TEM part (**section 2.1**), the concepts of limited factors of spatial resolution, aberration correctors, scanning transmission electron microscopy (STEM), the related Electron energy loss spectroscopy (EELS), atomic modelling and image simulation will be firstly introduced. In the electrochemical techniques part (**section 2.2**), the concepts of cyclic voltammetry, electrochemical impedance spectrum (EIS), equivalent series electrical circuit and the interpretation of surface state with fitted EIS data will be presented.

2.1 Fundamental Concepts in Transmission Electron Microscopy

2.1.1 The Concept of Resolution

Since the naked eye works only in the visible range of the electromagnetic spectrum, our ability to observe objects is limited by visible light wavelengths. Specifically, in optical microscopes, it is possible to magnify the observed objects by using different lenses; however, the maximum resolution is still harnessed by the wavelength of the light. The smallest resolvable distance between two points is defined as ‘resolution’ of the device. According to the classic Rayleigh criterion, the minimum distance that can be distinguished, δ , is given by: [1]

$$\delta = \frac{0.61\lambda}{\mu \sin\beta} \approx 0.61\lambda \quad (1)$$

in which, λ represents the radiation wavelength, μ is the refractive index of the viewing medium, and β is the collection semi-angle.

According to Louis de Broglie’s equation, the wavelength of the electron is related to the corresponding energy: [1]

$$\lambda = \frac{1.22}{\sqrt{E}} \quad (2)$$

in which, λ is in nm, while E is in electron volts (eV). Therefore, a higher resolution can be achieved by using spectral sources with high energies, equivalent to shorter wavelengths. By using electron beam energies in the range 40 to 300 keV we should

be able to achieve atomic resolution, at least theoretically, as displayed in **Table 2.1**. However, the presence of aberrations decreases the final resolution and the microscope performance. In this way, in 1960s, in order to achieve atomic resolution, a first approach used was designing ultra-high voltage microscopes. Ultrahigh voltage TEM (potentials ranging from 1 to 3 MeV) were produced in the 1960s but are not used nowadays because the utilization of ultrahigh voltage in these TEMs resulted in electron irradiation damage to most of the materials except in few exceptions as some ultra-hard materials.

Table 2.1 Electron Properties as a Function of Accelerating Voltage. [1]

Accelerating voltage (kV)	Non-relativistic wavelength (nm)	Relativistic wavelength (nm)	Mass ($\times m_0$)	Velocity ($\times 10^8$ m/s)
100	0.00386	0.00370	1.196	1.644
120	0.00352	0.00335	1.235	1.759
200	0.00273	0.00251	1.391	2.086
300	0.00223	0.00197	1.587	2.330
400	0.00193	0.00164	1.783	2.484
1000	0.00122	0.00087	2.957	2.823

Rayleigh criterion can give a rough estimation of the image resolution ability from an incoherent self-luminous source, which is not affected by any physical principles or factors. According to Abbe's theory, a more rigorous definition of the resolution based on the radius of the Airy disk can be established: [1]

$$r = 1.22 \frac{\lambda}{\beta} \quad (3)$$

where β is the lenses collection angle, λ is in nm, and r is the minimum resolvable spacing. The calculation needed to obtain the number 1.22 involves the use of Bessel functions because of the circular symmetry of the aperture. Based on equation (3), r increases with the decreasing of β , meaning that the resolution gets worse. This expression for the Airy disk diameter also confirms that r is proportional to λ . However, this determination is based on an ideal aplanatic lens, which does not exist

in practice, as shown in **Figure 2.1** Left. The spherical aberration (C_s) occurs when the lens field behaves differently for off-axis rays. For our electromagnetic lenses, the further off axis the electron is, the more strongly it is bent back towards the axis, as shown in **Figure 2.1** Right. As a result, a point object is imaged as a disc of finite size after crossing the lens, the radius (r_{sph}), is proportional to the collection angle and C_s , as follows: [1]

$$r_{\text{sph}} = C_s \beta^3 \quad (4)$$

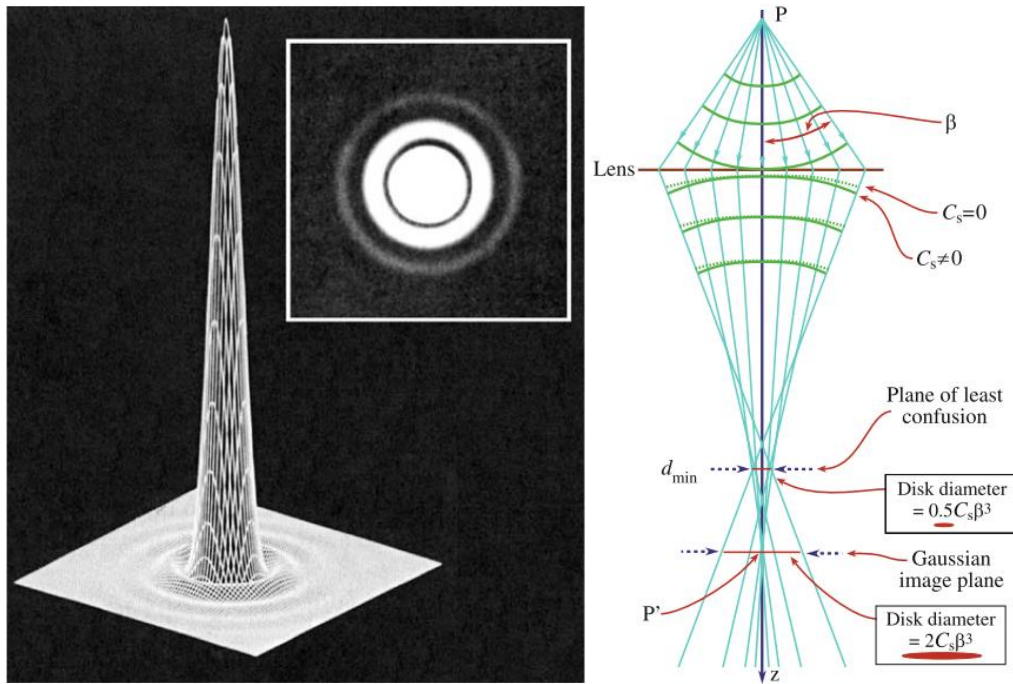


Figure 2.1 Left: The visible-light intensity produced by a 0.5-mm-diameter circular aperture and the observed Airy rings (inset). The width of the central intense region is $1.22\lambda/D$. Right: Spherical aberration in the lens resulting in wavefronts from a point object P to be spherically distorted by bending the rays at the outside of the lens more than those close to the axis. The point is thus imaged as a disk with a minimum radius in the plane of least confusion and a larger disk at P' in the Gaussian-image plane. The plane of least confusion is where the smallest image of the object is formed. Schematic intensity distributions at these two important planes are shown beside the ray diagram. Adapted from ref. [1].

Unfortunately, the objective lens bends lower energy electrons more strongly. As a result, electrons from a point in the object are once again blurred to form a disk in the Gaussian-image plane, which is derived from the chromatic aberration. The radius r_{chr}

of this disk is defined as follows: [1]

$$r_{\text{chr}} = C_c \frac{\Delta E}{E_0} \beta \quad (5)$$

where C_c represents the chromatic-aberration coefficient of the lens, ΔE represents the energy loss of the electrons, E_0 represents the initial beam energy, and β represents the collection angle of the lens. Chromatic aberration could be almost completely ignored when it is compared to the spherical one. The exception is that if a C_s corrector exists after compensating for C_s , then C_c is the next most-persistent aberration that needs to be corrected.

The distortion of an image induced by the lenses aberrations is mathematically represented by the Contrast Transfer Function (CTF), affected by spherical aberration (C_s), defocus (Δz), and astigmatism (C_a). For example, the phase-distortion function is described as follows: [1]

$$\chi = \pi \Delta f \lambda u^2 + \frac{1}{2} \pi C_s \lambda^3 u^4 \quad (6)$$

which will depend on the values of C_s (the lens quality), λ (the accelerating voltage), Δf (the defocus value used to form the image), and u (the spatial frequency). The phase signal transmitted to the real space is in the form of images, therefore, the information translated to the image is controlled by the CTF.

In 1949, Scherzer noticed that the CTF could be optimized by balancing the effect of spherical aberration with a specific negative value of Δf . This value is well known as ‘Scherzer defocus’, Δf_{Sch} which occurs at

$$\Delta f_{\text{Sch}} = -1.2(C_s \lambda)^{0.5} \quad (7)$$

At this defocus, all the beams will have nearly a constant phase out to the ‘first crossover’ of the zero axis. This crossover point is defined as the instrumental resolution limit, which is the fundamental principle of the phase-contrast imaging in high resolution TEM. The resolution at the Scherzer defocus can be defined as follows:

$$r_{\text{Sch}} = 0.66 C_s^{\frac{1}{4}} \lambda^{\frac{3}{4}}. \quad (8)$$

Therefore, the resolution is unquestionably limited by the lenses aberrations. Further details on TEM image formation and instrumentation can be found in reference. [1]

2.1.2 Aberration Correctors

The electromagnetic lenses used to direct the electrons inside the microscope column are intrinsically not perfect and somehow distort the image. The lowest order aberration, named defocus, is readily compensated by tuning the image to the corrected height of the optical axis. The correction of other aberrations can be achieved using dipoles, quadrupoles, hexapoles as well as octupoles etc., which combine in different ways to apply various magnetic fields perpendicular to the optical. It is worth noting that the electrons' travelling path inside the microscope column is helical, which is supervised by the magnetic field created by different lenses. When the electrons realize a non-uniform magnetic field as they spiral round the optic axis, astigmatism occurs. This occurs as a result of the fact that it is impossible to manufacture perfectly cylindrically symmetrical soft-iron polepieces and thus the lens cannot be precisely centred around the axis. Fortunately, astigmatism is readily corrected using stigmators, which are composed of octupoles. There are stigmators applied in both the condenser lenses and the objective lens. In short, spherical aberration, chromatic aberration and astigmatism are the three major defects presented in electromagnetic lenses, which need to be corrected. Additionally, there are several minor defects, such as barrel and pincushion distortion, field curvature, coma etc. The first system for compensating the spherical aberration of the objective lens was constructed and successfully implemented in a 200 kV microscope in 1998. [2] The objective lenses are indeed the most important lenses in microscopes because they form the TEM image. The aberration corrector for objective lenses is composed of two hexapoles and four lenses alternating in the following order: one hexapole/two dipoles/one hexapole/two dipoles. The point resolution in a 200 kV Philips CM200 was improved from 0.24nm to 0.14nm, and the contrast delocalization was

substantially reduced. [3]

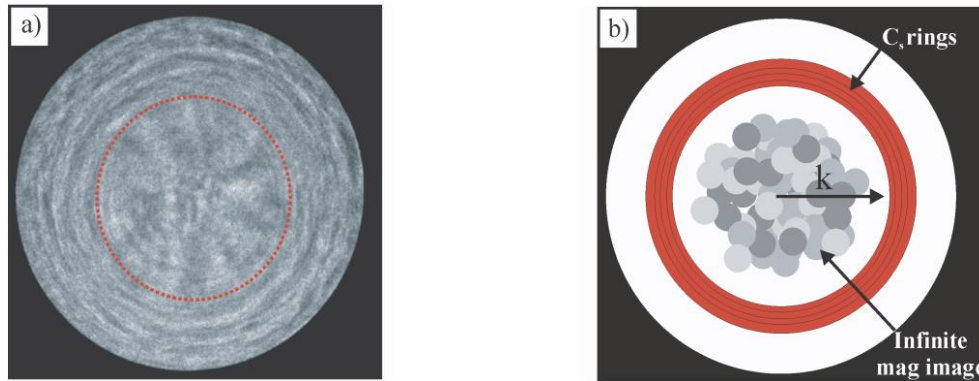


Figure 2.2 Description of the coherent electron ronchigram (formed from amorphous material). a) An experimental ronchigram, formed inside the largest probe forming aperture. b) A simplified conceptual “map” of the ronchigram showing the location of the rings caused by C_s , and the presence of the shadow image inside the rings. In the real case the “blobs” in the center of the ronchigram flash randomly due to the small movements of the incident probe and specimen. Adapted from ref. [4].

To perform the experiments in aberration-corrected TEM, the parameters of the actual aberrations in the TEM system must be measured firstly. Typically, this is done by acquiring diffractograms in HRTEM mode or images of the electron probe in STEM mode at varying beam tilts, under- and over focus value. Specifically, in STEM mode, the defocus, two-fold astigmatism (A1) and coma (B2) can be initially corrected by observing the Ronchigram (**Figure 2.2**), which is defined as the shadow image of the species or as the convolution of the aperture function with the diffraction pattern of the species.

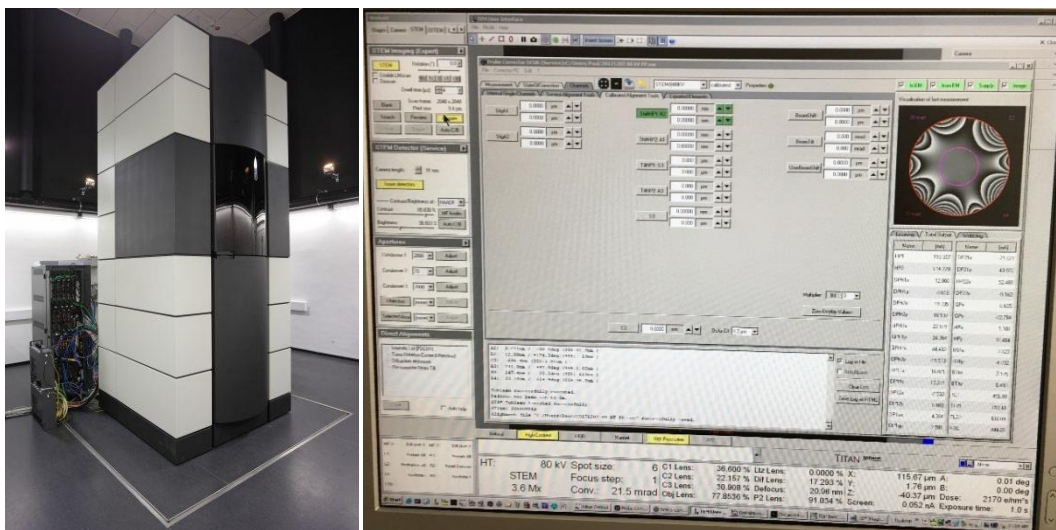


Figure 2.3 Digital picture of FEI titan 50-300 pico at Ernst Ruska-Centre (ER-C) for Microscopy and Nanoscience

Spectroscopy with Electrons and the corresponding controlled TIA software and probe corrector.

The precisely aberration evaluation and compensation are highly automatized and can be carried out using commercially available software, such as Probe corrector software (<http://www.ceos-gmbh.de/English/index.html>), [3] as displayed in **Figure 2.3**. The collection of resulting diffractograms is known as Zemlin's tableau. The evaluation of the resulted defocus and A1 as function of the illumination tilt allows the estimation of the rest of the aberrations, which can be compensated by the correction system automatically.

2.1.3 TEM and STEM Modes

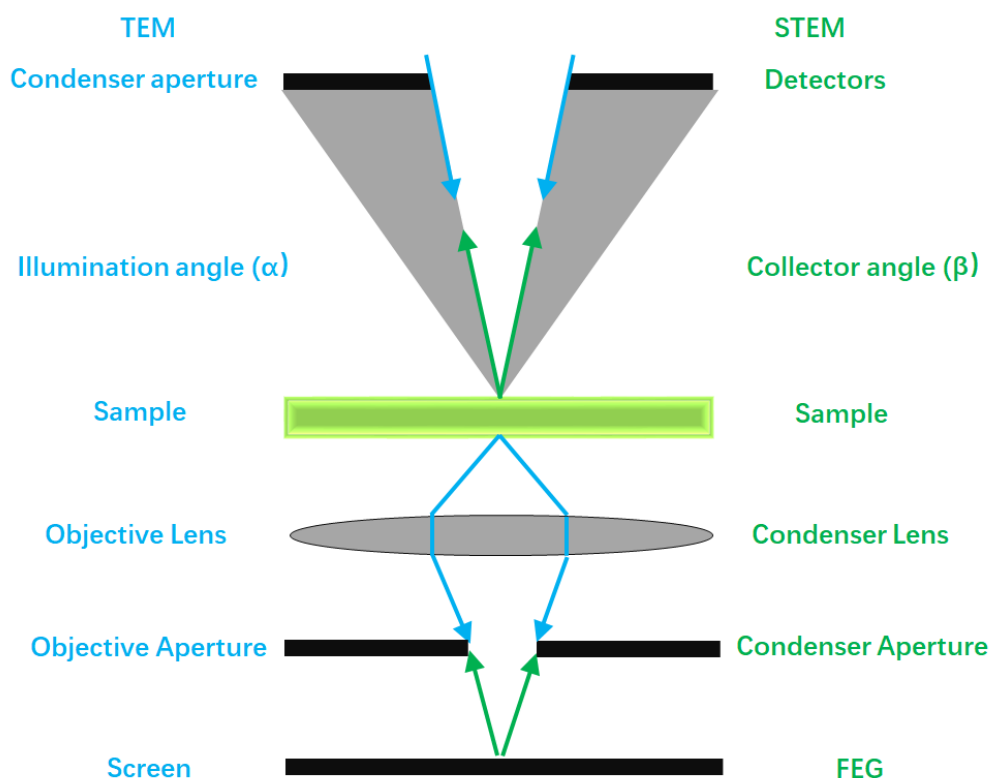


Figure 2.4 Schematic showing the principle of reciprocity between HRTEM (indigo) and STEM (green).

Electron transmission microscopes are versatile instruments, which can be used in different modes, including classic TEM and STEM modes. The fundamental principle for classifying the work modes of electron transmission microscopes is based on the illumination systems, such as, parallel illumination for conventional TEM and convergent illumination for STEM. It is worth mentioning that, based on the

helmholtz reciprocity theorem, Cowley confirmed that there is an equivalence relationship between TEM and BF-STEM. Specifically, the same intensity should be obtained by translating the source from A to P, if a point source-S placed at A results in an intensity I at the position P. In this case, the reciprocity is similar to that shown in the ray diagram of HRTEM and BF-STEM techniques in **Figure 2.4**, where the electron trajectory is the same but in an opposite direction.

In TEM modes, the phase contrast image is composed of the interference of the elastically scattered electrons passing the samples, which results in the phase difference of the scattered electrons. The obtained interference patterns provide the lattice information rather than the direct atomic structure of the sample. It is very difficult to illustrate the interference patterns obtained in TEM mode because the phase contrast is influenced by various factors, such as sample thickness, crystalline orientation, focus and astigmatism, which may be resolved by crystalline modelling and simulation.

In STEM mode, the electron beam is focused into a small probe, which can be scanned over the sample to induce multiple signals from it, such as incoherent elastically scattered electrons (high-angle annular dark-field: HAADF), incoherent inelastically scattered electrons (Electron energy loss spectroscopy: EELS, Energy filtered transmission electron microscopy: EFTEM) and coherent elastically scattered electrons (electron diffraction: ED, TEM, bright field: BF) etc. Furthermore, STEM mode enables these techniques at atomic resolution by the utilization of the aberration correctors in electron transmission microscopes.

2.1.4 HAADF and ABF Images

The utilization of annular detectors in STEM is popular nowadays and the classification of these image techniques in STEM modes is based on the angle ranges for collecting the scattered electrons, as displayed in **Figure 2.5**. The collected scattered electrons in special angular ranges is related to the corresponding interaction of electrons with the sample, which provides different information depending on the

angular range.

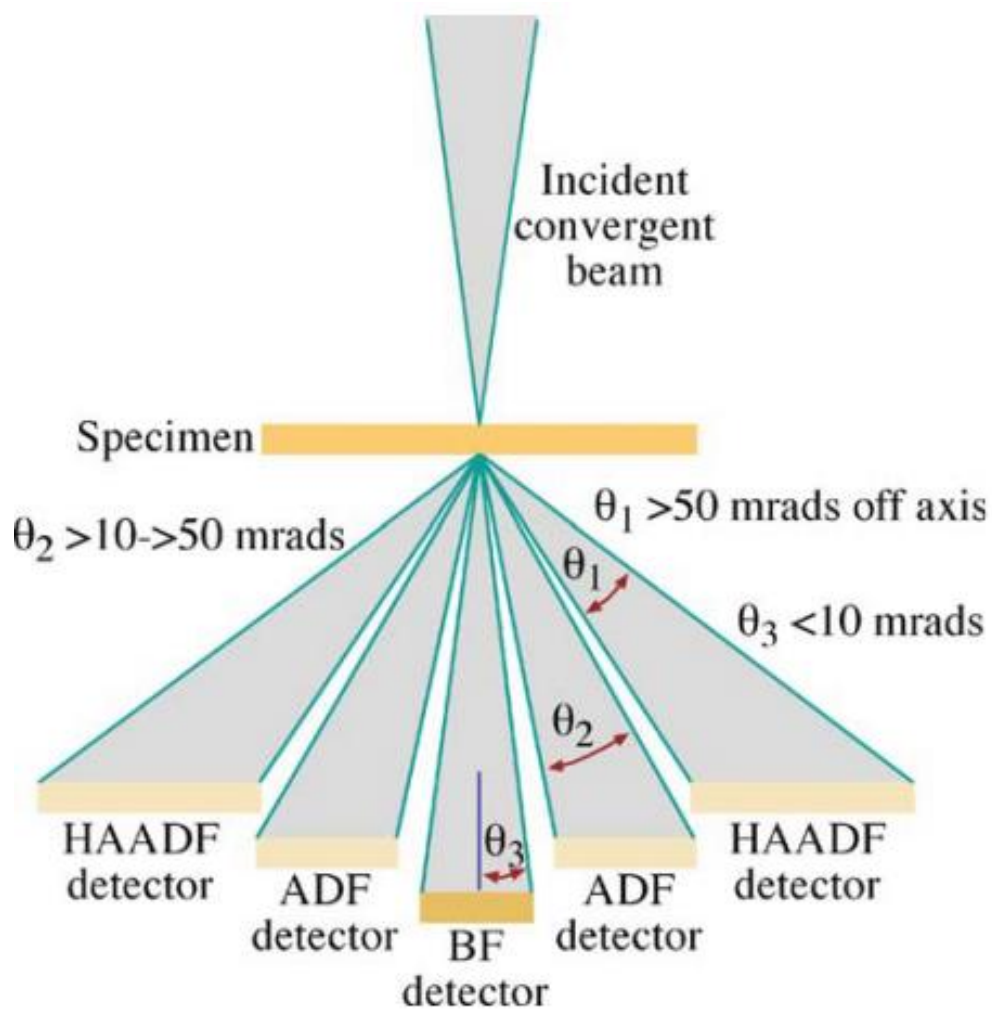


Figure 2.5 The various electron detectors in a STEM. Scintillator-PM detectors are invariably used for secondary electrons (SE) detection and semiconductor detectors for the backscattered electron (BSE). The on-axis and annular forward-scattered and high-angle dark field detectors may be either type, depending on the microscope. Adapted from ref. [1]

HAADF images are based on the collection of high angle scattered electrons, in which thermal diffuse scattering (TDS) dominates. Specifically, a HAADF detector at the high angle scattering region will collect the electrons after a process similar to Rutherford scattering, which enables their incoherent interference for HAADF images. The most important advantage of HAADF images, named as Z-contrast images, is that the observed contrast is proportional to the atomic number of the analyzed samples. It is well established the dependence of Z contrast on the detector geometry. In addition, an analytical expression for the Z dependence on the image intensity can

be approximated by an exponential function of the form I (signal intensity) $\sim Z^\alpha$, where α is smaller than 2 and in the range 1.6-1.9 for most of the cases. [5] The dependence of α with the inner collection angle θ is described by equation (9) (A and B are the fitting parameters):

$$\alpha = 2 - Ae^{B\theta} \quad (9)$$

Therefore, HAADF images can be mathematically related to the convolution of the illuminating probe ($P(r)$), and an object function of the specimen, $O(r)$ as

$$I_{\text{incoher}}(r) = P(r)^2 \otimes O(r) \quad (10)$$

Whereas, for HRTEM and BF images, the relationship between different scattered electrons interfering and the coherent intensity is expressed as

$$I_{\text{coher}} = |P(r) \otimes \phi(r)|^2 \quad (11)$$

in which $\phi(r)$ is the specimen transmission function.

According to the Z contrast rule, it is difficult for a HAADF detector to detect the weak scattering signal from the lightest atoms if the samples also contain heavier atoms. Therefore, it is necessary to set a suitable angular range without the contribution from TDS to identify the light element visualization, which rely on phase contrast images rather than in amplitude contrast. The imaging mode obtain with such an angular range is named Annular Bright Field (ABF). [6]

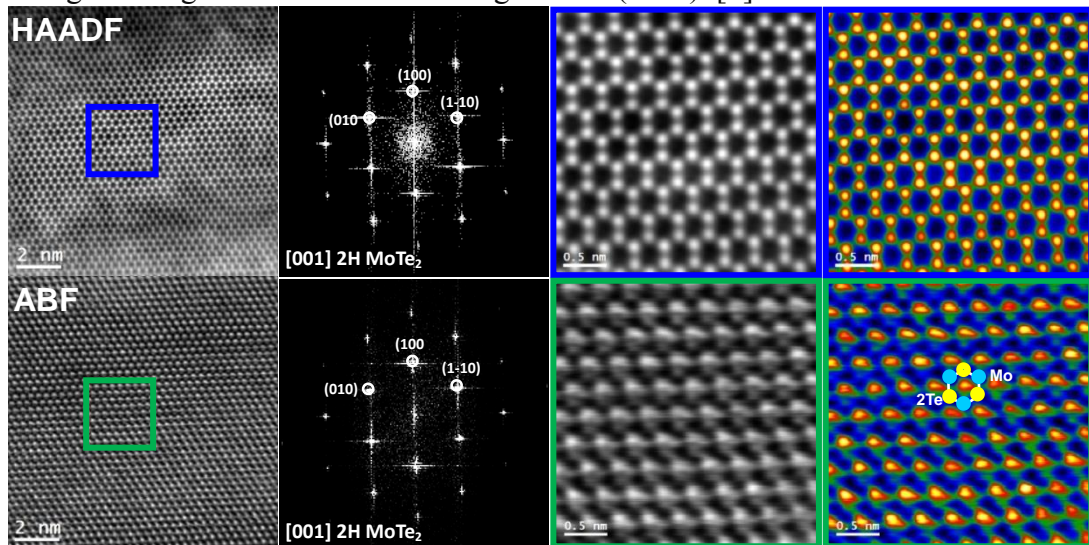


Figure 2.6 Top row: Left: atomic resolution HAADF image and its corresponding FFT spectrum

showing a hexagonal atomic ordering and indicating that the membrane crystallized in the hexagonal MoTe₂ crystal phase, [P63/MMC]-space group 194, with lattice parameters of $a=b=0.3521$ nm, $c=1.396$ nm and $\alpha=\beta=90^\circ$, $\gamma=120^\circ$ as visualized along the [001] direction. Right: HAADF STEM and temperature coloured atomic resolution HAADF images of the blue squared region showing the ordering of Mo and Te atoms. Bottom row: Left: atomic resolution ABF STEM image and its corresponding FFT spectrum showing a hexagonal atomic ordering and indicating that the membrane crystallized in the hexagonal MoTe₂ crystal phase, [P63/MMC]-space group 194, with lattice parameters of $a=b=0.3521$ nm, $c=1.396$ nm and $\alpha=\beta=90^\circ$, $\gamma=120^\circ$ as visualized along the [001] direction. Right: ABF STEM and temperature coloured ABF STEM atomic resolution images of the green squared region showing the ordering of Mo and Te atoms. (The inset shows the atomic model of Mo and Te atoms, Mo atoms marked as indigo and Te atoms marked as yellow).

As displayed in **Figure 2.6**, the atomic positions in the ABF STEM images present darker features on a bright background, which contrasts with the HAADF STEM images. The ABF STEM experiment uses an annular detector located at the adequate angular range by adjusting the camera length to get an 11-22 mrad angular range, which is dominated by the coherent interference of elastically scattered electrons, thus strongly enhancing the image intensity of the light elements. [7-8] Therefore, by controlling the utilization of different detectors as well as the collection angles, it is possible to precisely identify the atomic ordering in the samples. [9] The latest development of pixelated detectors allow the acquisition of the whole transmitted angular spectra and allows the selection of different angular ranges. [10]

2.1.5 Electron Energy-Loss Spectrum (EELS)

The detection of the inelastically scattered electrons after interactions with the sample is another valuable signal containing chemical information. The separation of the electrons based on the electron kinetic energy after crossing the specimen results in EELS. Typically, EELS is divided into two different regions, including the low-loss and the core-loss region in the spectrum. Energy losses in the low-loss region range from 0 eV to 40 eV, including elastically scattered electrons, unscattered electrons and electron-phonon interactions etc. A zero-loss peak located at the low-loss region

accounts for all elastic events, which is much stronger than any other peak in the spectrum. The core-loss region includes the contribution from the inner-shell excitations, ranging from 40 eV to several thousand eV. The EELS recorded in the core-loss region contains the ionization edges of the elements in the samples, which is characteristic of the excited elements.

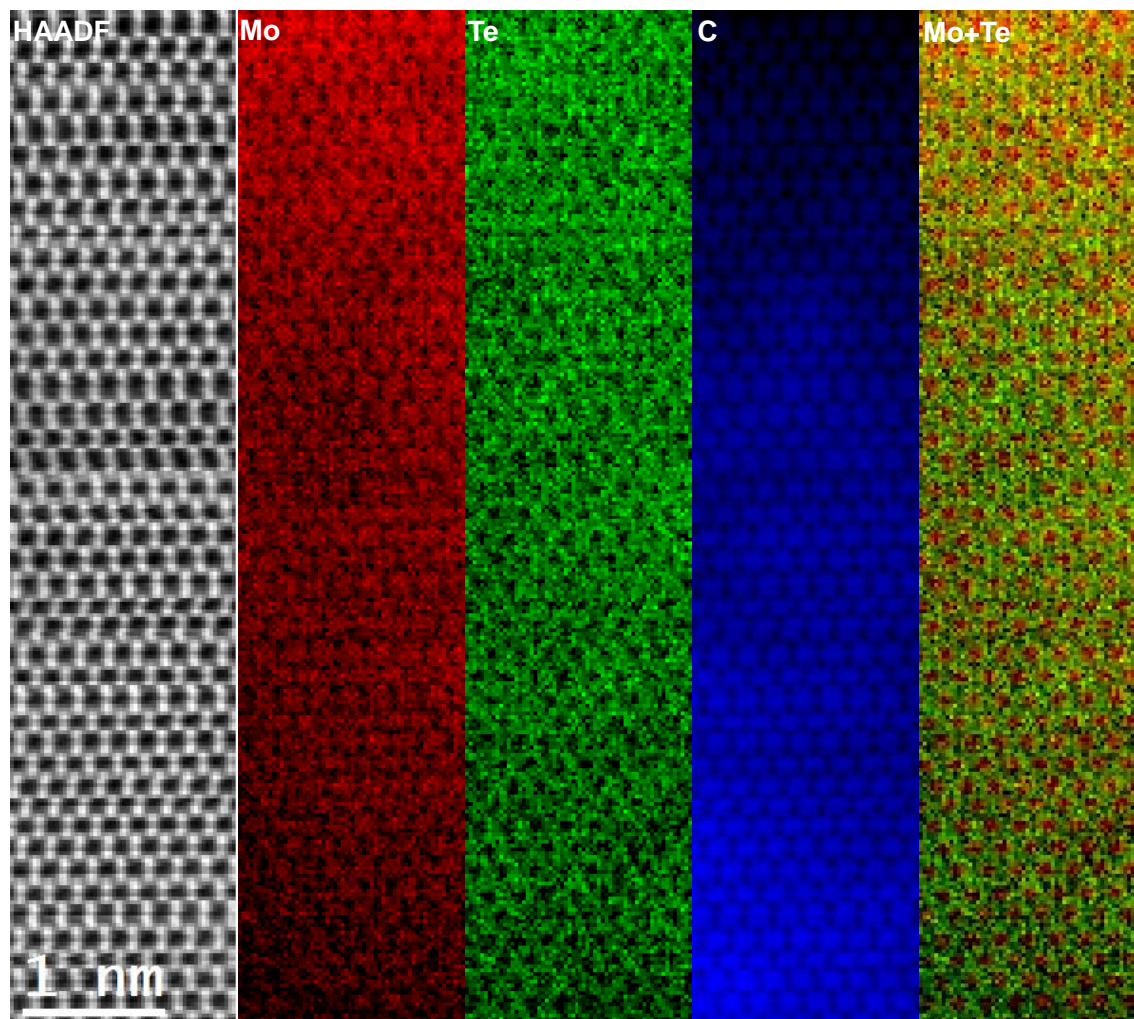


Figure 2.7 Atomic resolution EELS chemical composition maps of MoTe₂ supported onto the Lacey carbon-Cu grid. From left to right: atomic resolution HAADF STEM micrograph, individual Mo (red), Te (green), C (blue) maps and Mo-Te composite map.

It is well known that EELS elemental mapping can be used for the identification of different elements, as displayed in **Figure 2.7**. If the energy resolution is high enough, plenty of useful information can be obtained from the fine shape of the edges. State-of-art microscopes that benefit from the application of monochromators and aberration correctors can also enable the determination of oxidation states, chemical

bonds as well as coordination geometry. [12-15] In addition, plasmonic, bandgap and even phononic analyses, which are based on the low-loss region of the EELS spectra, have drawn plenty of attention in materials science field recently. [16-18]

2.1.6 Atomic Modelling and TEM/STEM Image Simulations via Rhodius, Eje-Z and STEM Cell

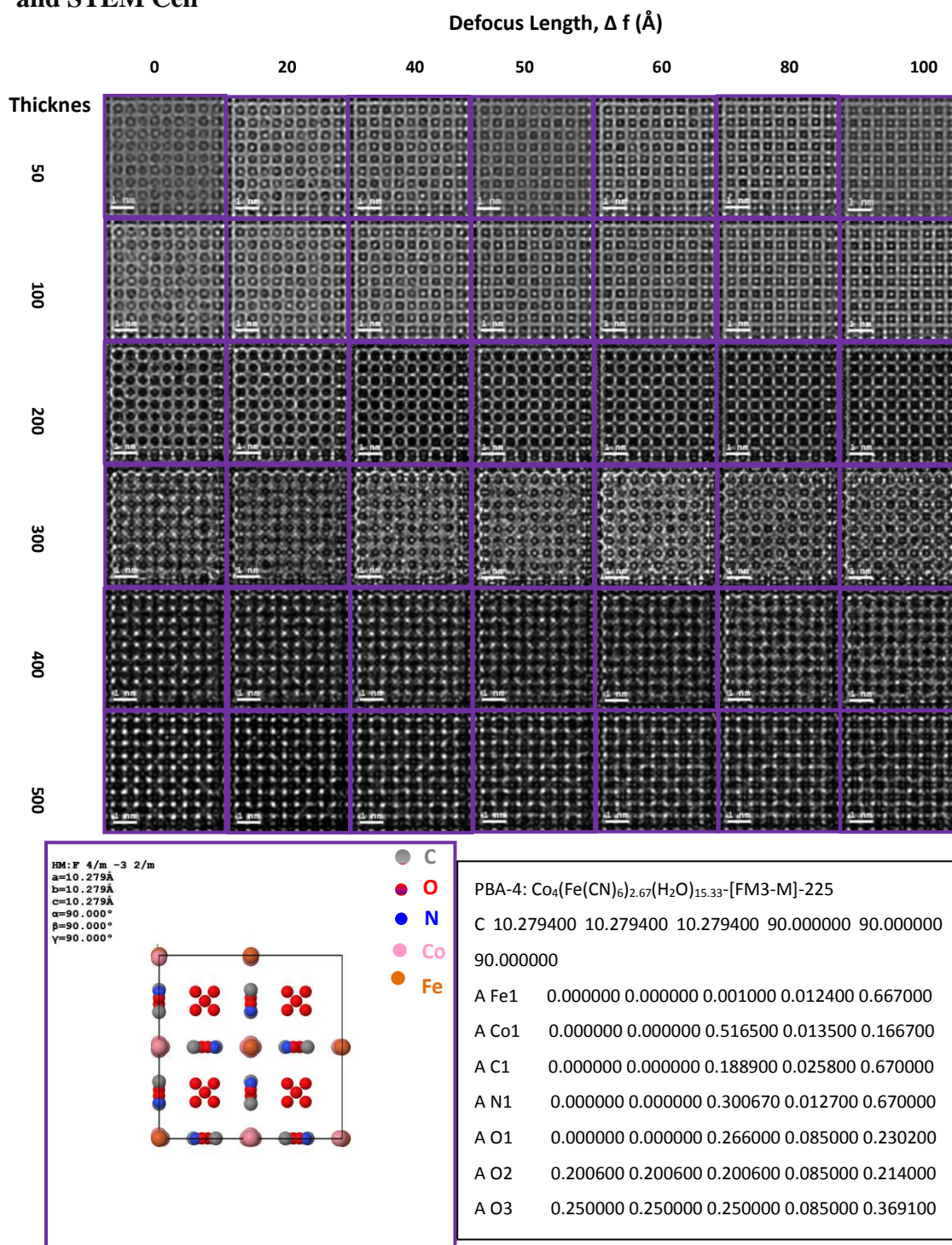


Figure 2.8 Simulated HREM images of PBA-4 along the [100] projection as function of the specimen

thickness (t) from 50 Å to 500 Å and the defocus length of the objective lenses (Δf) from 0 to 100 Å. At each t and Δf , recognizable variation in the HRTEM images can be found in the PBA-4 ordered structures. Bottom: we show the corresponding crystal cell and crystal parameters. [23]

The first step for TEM or HAADF STEM image simulation is to build the corresponding crystal model. Herein, the atomic models were created by using Eje-Z and Rhodius, [19] which were provided by Universidad de Cadiz. They are free on-line software, which enables the creation of heterojunction nanostructures with detailed facets. The methods of image simulation can be classified into Bloch wave formalism and multislice routines. The Bloch wave formalism takes the individual probe interaction with each atomic column into consideration. The multislice routines, instead, first slice the sample and accumulate the electron beam's interactions with the different slices. Therefore, the projected potential from different slices can be illustrated by different approximations, such as the absorptive potential and the frozen lattice. In order to obtain realistic atomic resolution HAADF STEM simulated images with the TDS contribution, the thermal vibration of the lattice can be frozen by averaging random atomic displacement: in another words, different frozen lattice configurations can be averaged.

The image simulations in this dissertation were calculated by using the STEM CELL software package, [20-21] which is a free software based on frozen phonon routines developed by V. Grillo. [22] By convolving the squared probe with the atomic potential, this software can be used to calculate simple image simulations, which qualitatively predict the experimental intensity, without accounting for the channelling effects. The software can also be used to count source size effects ($S(r)$), which are supposed to blur the image and are derived from the incoherent contribution during the formation of the probe. The source size effects are illustrated by a Gaussian function and the corresponding mathematical expression for the intensity is

$$I(r) = P_{(r)}^2 \otimes O(r) \otimes S_{(r)} \quad (12)$$

Based on this equation, the software develops a Wiener filter, which can be used to

filter the experimental images to eliminate environmental noise and thus improve the acquired image quality.

As aforementioned, it is very difficult to identify the real position of atoms based on the HRTEM image because HRTEM derives from the interference of the elastically scattered electrons, which makes HRTEM simulation necessary, as displayed in **Figure 2.8**. Although identification of the position of atoms is usually easy with HAADF STEM, image simulation is still necessary when dealing with more complicated samples.

2.2 The Fundamental Concepts in Electrochemistry

2.2.1. Cyclic Voltammetry

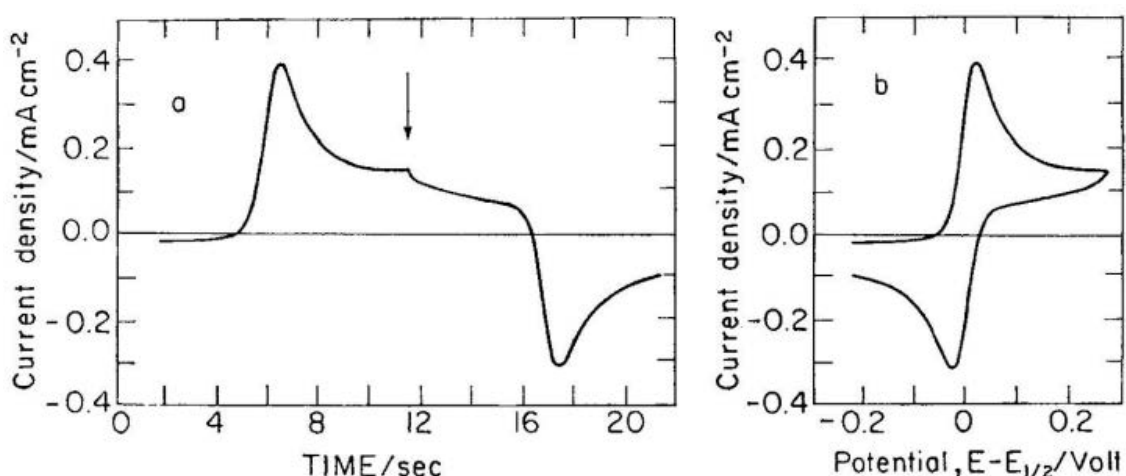


Figure 2.9 Plots of current versus time and versus potential for the same data obtained in cyclic voltammetry, recorded (a) on a strip chart recorder and (b) on an X-Y recorder. Adapted from ref. [24]

Linear potential sweep is a potentiostatic technique, in which potential is the only externally controlled parameter. The potential is changed at a constant rate: [24]

$$v = \frac{dE}{dt} \quad (13)$$

where the resulting current response is followed as a function of time. Typically, the current is plotted as a function of potential on an X-Y plotter. Cyclic voltammetry refers to the condition when the potential is swept forward and backward in a

potential window. In this case, the current measured at a particular potential in the anodic sweep can readily be compared with the current measured at the same potential in the cathodic sweep. **Figure 2.9** presents the same data in the form of an i/t plot and an i/E plot, for comparison. Most of the literature data is presented in the later form.

In cyclic voltammetry, the potential is set to change linearly with time in the specified potential window. Normally, the current response in the first cycle is slightly different from that in the second cycle, but the system settles down after 5-10 cycles, and the current response is independent of the cycle number. It is usually named "steady-state voltammogram", which is based on the current changing periodically with potential and time. The term used here, means that the voltammogram is independent of time, which makes the experiment highly reproducible. Furthermore, the voltammograms are stable over long periods of time, sometimes in the range of hours.

In this dissertation, the cyclic voltammetry was used for the calculation of the specific capacitance for supercapacitor applications, including the specific capacitance contribution from double-layer capacitance and faraday capacitance. For photochemical water splitting, the resulting steady state photocurrent response can be interpreted as

$$j = qLG - qL(k_s(f - f_0)N_{ss} + k_{cb}(n - n_0)) \quad (14)$$

in which, f is the steady occupation probability of surface states:

$$f = \frac{\beta_n n + k_s f_0}{\omega_t} \quad (15)$$

$$\omega_t = \beta_n n + \epsilon_n + k_s \quad (16)$$

where q is the elementary charge, j is a faradic/resistive current response and includes the charge transfer from surface states. [25] It is worth noting that indirect electron transfer from surface states (second term in the right-hand side of Equation 14) is very similar to the direct electron transfer from the conduction band (third term in the right-hand side of Equation 14). Therefore, there is no way to distinguish between direct and indirect charge transfer from a single cyclic voltammetry measurement.

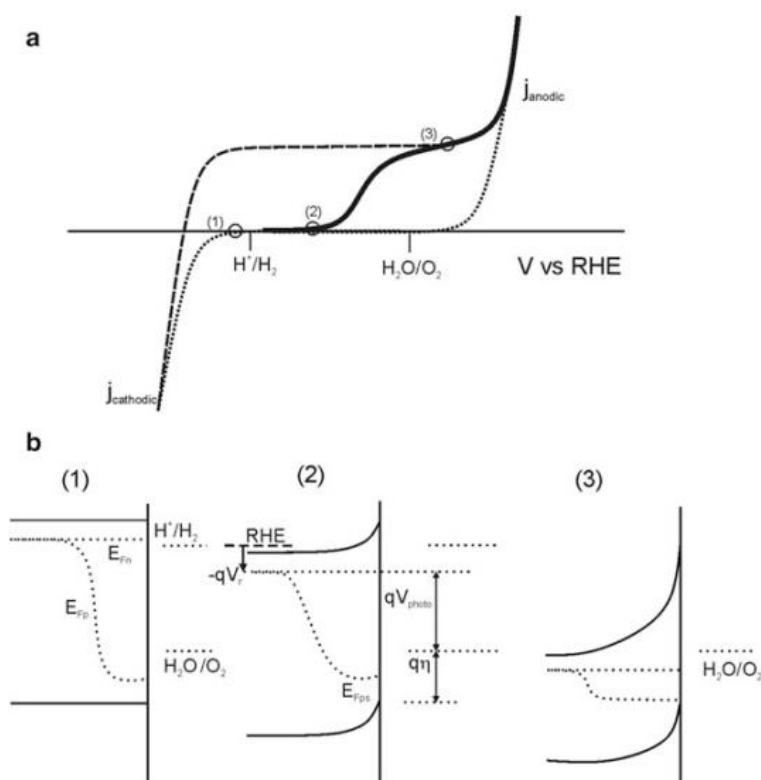


Figure 2.10. (a) Current density-voltage curves resulting from the PEC operation of a semiconductor photoanode. Dotted line is dark current density-voltage curve for the oxygen evolution reaction. Dashed line is the idealized curve under illumination. The solid line curve is a realistic curve including normal features of semiconductor/electrolyte junction as recombination of electrons and holes. (b) Representation of the energy diagram of a semiconductor/water interface at different voltages vs. RHE. The points 1, 2, 3 correspond to the different electrode potentials indicated in (a). Adapted from ref. [26]

The operation of photoelectrodes under variation of voltage and light illumination is described in **Figure 2.10**. For a n-type photoelectrode, the concentration of minority carriers (holes) is rather small in the dark; hence, an anodic current only occurs at strong positive bias by hole injection from the substrate, **Figure 2.10 a** (point 1). The electron-hole pairs induced by light illumination lead to the separation of Fermi levels, **Figure 2.10 b**, and cause an anodic photocurrent as indicated in **Figure 2.10 a**. Ideally, the photocurrent is added to the dark current that consists of a separate oxidation reaction, as in the dashed line of **Figure 2.10 a** (point 3). However, strong recombination and slow charge transfer may delay the onset of photocurrent to more

anodic voltage than the flat band potential, as displayed by the dark line in **Figure 2.10 a** (point 2).

2.2.2 Electrochemical Impedance Spectroscopy

As mentioned in the first chapter, the surface state plays a vital role in the interpretation of PEC performance and mechanism investigation of photoelectrodes. It is relatively easy to characterize the photocurrent response via cyclic voltammetry. To understand the effect of the competition between the surface state-mediated recombination and the indirect charge transfer processes on water oxidation, a simple kinetic model that neglects any electrostatic influence such as the presence of an electric field has been developed by J. Bisquert et al., as displayed in **Figure 2.11a**. [27-32]

At low potential, direct holes that transfer from the valence band can be neglected and the three processes that occur at the semiconductor/electrolyte interface are trapping/detrapping of electrons, trapping/detrapping of holes and charge transfer of holes. It is worth noting that the detrapping kinetic constant is indeed proportional to the trapping constant based on the detailed balance principle. [27] Hence, it is equivalent to refer to either trapping or detrapping kinetics indistinctly.

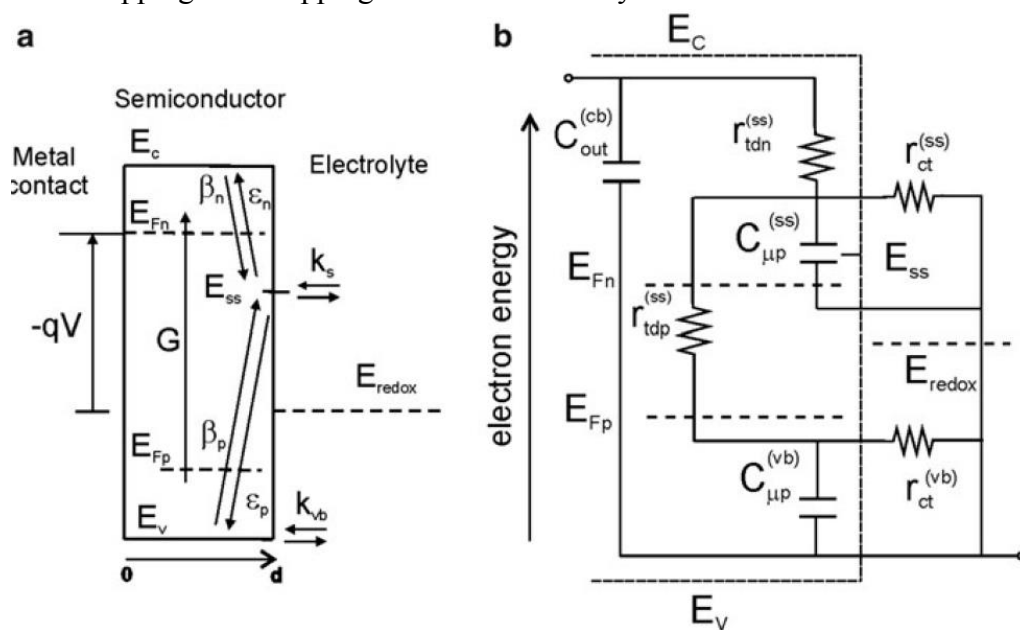


Figure 2.11 (a) Scheme of the kinetics of the processes occurring at the semiconductor/electrolyte interface: generation of electrons and holes at a rate G , trapping of electrons from the conduction band

(kinetic constant β_n) and detrapping (ϵ_n). Trapping of holes from the valence band (β_p) and detrapping (ϵ_p). Charge transfer of holes from the surface states (k_s) and from the valence band (k_{vb}). (b) Equivalent circuit obtained from a small ac perturbation. C_{out}^{cb} represents the semiconductor capacitance, $C_{\mu p}^{ss}$ represents the traps chemical capacitance, $C_{\mu p}^{vb}$ represents the valence band chemical capacitance, r_{tdn}^{ss} represents the trapping/detrapping resistance of electrons from the conduction band, r_{tdp}^{ss} represents the trapping/detrapping resistance of holes from the valence band, r_{ct}^{ss} represents the charge transfer resistance from the traps and r_{ct}^{vb} represents holes transfer resistance from the valence band. Adopted from reference [26].

The model in **Figure 2.11a** has been employed for the quantitative calculation of impedance spectroscopy and equivalent circuit involving the direct and indirect charge transfer pathways. [27] The corresponding full equivalent circuit of this model is presented in **Figure 2.11b**, which illustrates the kinetics of electrons/holes surface state-assisted recombination as well as the charge transfer at the semiconductor /electrolyte interface in dynamic regime. This circuit is showing three chemical capacitances that are associated to the separate modes of carrier storage in the system: the conduction band, the valence band, and the surface states, as displayed in **Figure 2.12**.

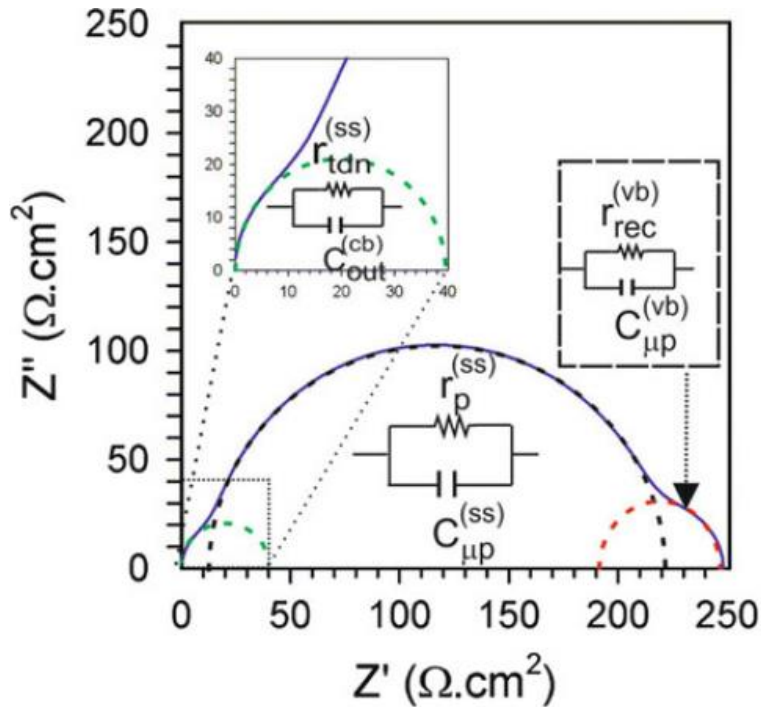


Figure 2.12 Illustration of the impedance in the complex plane presenting three semicircles. The first semicircle at low frequency represents the valence band charge transfer, the second one represents the

surface states charge transfer, and the last one at higher frequencies represents the electrons trapping/detrapping. Adopted from reference [28].

The wide band gap semiconductors used for water splitting usually allow for the observation of a maximum of two semicircles rather than three in the complex plane. Thus, no more than two resistance and capacitance values can be extracted from the electrochemical impedance spectrum. The extraction of these components and their accurate physical interpretation relies on the suitable choice of an equivalent circuit. In the following section, the typical approaches useful for the analysis of the electrochemical impedance spectrum are presented.

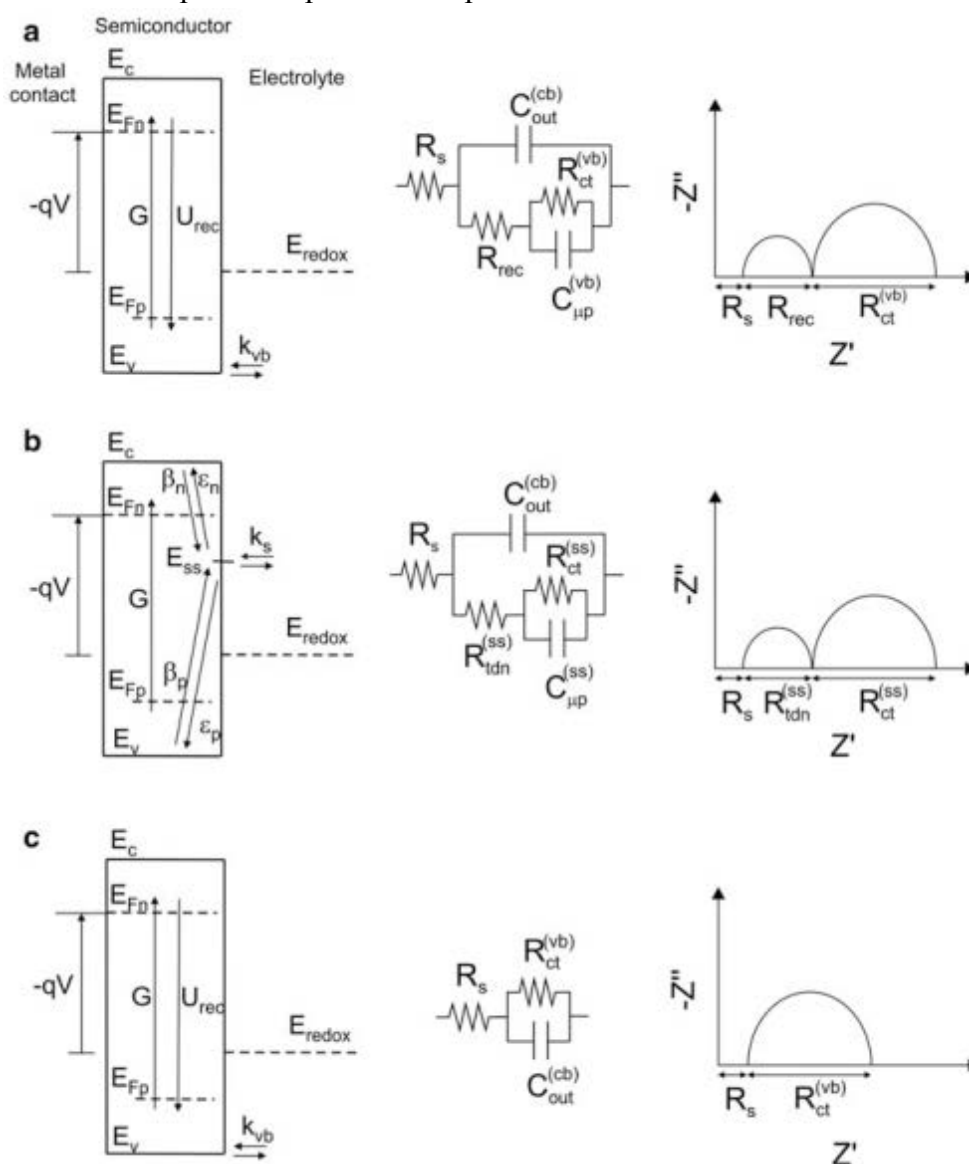


Figure 2.13 Main simplifications of the kinetic model of **Figure 2.11** available in the literature for the interpretation of experimental data, the associated equivalent circuit obtained from a small *ac*

perturbation, and the corresponding complex plane electrochemical impedance spectra for (a) the direct hole transfer model, (b) the indirect hole transfer model, and (c) the reduced direct charge transfer model. In these circuits, C_{out}^{cb} is the semiconductor capacitance, $C_{\mu p}^{ss}$ is the surface state chemical capacitance, R_{rec} is the band to band recombination resistance, R_{ct}^{vb} is the hole transfer resistance from the valence band, R_{tdn}^{ss} is the trapping/detrapping resistance of electrons from the conduction band, and R_{ct}^{ss} is the hole transfer resistance from the surface states. Adopted from reference [26].

Figure 2.13 shows different simplifications of the kinetic model and electrochemical impedance spectra of **Figure 2.11** as well as the relevant resistances which can be extracted from the electrochemical impedance spectra. **Figure 2.13a** shows the kinetic model and electrochemical impedance spectra for the direct charge transfer mechanism without surface states. With this equivalent circuit, two capacitances and resistances can be extracted, which are assigned to the conduction and valence band carriers. Specifically, the capacitance located in the low frequency region is along with the hole storage in the valence band. **Figure 2.13b** shows the classical equivalent circuit for the trapping/detrapping as well as the charge transfer of the majority carriers, [33] which allows the extraction of these two resistances and two capacitances associated with the conduction band and surface states. In this equivalent circuit, the low frequency capacitance is assigned to the hole storage in surface states.

J. Bisquert et al. employed the equivalent circuit in **Figure 2.13b** to model the indirect hole transfer for water oxidation with hematite. [34-36] It is worth noticing that the ratio between the electron trapping/detrapping resistance R_{tdn}^{ss} and the charge transfer resistance from the surface states R_{ct}^{ss} can be directly related to the ratio ε_n/k_s :

$$\frac{R_{ct}^{ss}}{R_{tdn}^{ss}} = \frac{\varepsilon_n + \beta_n \eta}{k_s} \quad (17)$$

Finally, the simple Randles circuit in **Figure 2.13c** has been utilized to model the carrier dynamics of hematite photoanodes in the dark because only one arc was present in the measured Nyquist plots and there was no evidence of the presence of the surface states affecting the carrier dynamics of the system. [34-36] The detail illustration of the fundamental concept of EIS please refer to references. [37-38]

References

- [1] D. B. Williams, C. B. Carter. Transmission electron microscopy. *Springer*, **1996**, New York.
- [2] M. Haider, H. Rose, S. Uhlemann, E. Schwan, B. Kabius, K. Urban. A spherical-aberration-corrected 200 kV transmission electron microscope, *Ultramicroscopy*, **1998**, 75, 53-60.
- [3] L. M. Brown, P. E. Batson, N. Dellby, O. L. Krivanek, Brief history of the Cambridge STEM aberration correction project and its progeny, *Ultramicroscopy*, **2015**, 157, 88-90.
- [4] M. Weyland, and D. A. Muller, Tuning the convergence angle for optimum STEM performance, *FEI Nanosolutions*, **2005**, 1, 24-35.
- [5] Z.W. Wang, Z.Y. Li, S.J. Park, A. Abdela, D. Tang, R.E. Palmer. Quantitative Z-contrast imaging in the scanning transmission electron microscope with size-selected clusters. *Phys. Rev. B*, **2011**, 84, 073408.
- [6] R. Ishikawa, E. Okunishi, H. Sawada, Y. Kondo, F. Hosokawa, E. Abe, Direct imaging of hydrogen-atom columns in a crystal by annular bright-field electron microscopy, *Nat. Mater.*, **2011**, 10, 278-281.
- [7] S. D. Findlay, N. Shibata, H. Sawada, E. Okunishi, Y. Kondo, Y. Ikuhara. Dynamics of annular bright field imaging in scanning transmission electron microscopy. *Ultramicroscopy*, **2010**, 110, 903-923.
- [8] E. Okunishi, I. Ishikawa, H. Sawada, F. Hosokawa, M. Hori, Y. Kondo, Visualization of light elements at ultrahigh resolution by STEM annular bright field microscopy. *Microsc. Microanal.*, **2009**, 15, 164.
- [9] S. D. Findlay, N. Shibata, H. Sawada, E. Okunishi, Y. Kondo, T. Yamamoto, Y. Ikuhara. Robust atomic resolution imaging of light elements using scanning transmission electron microscopy, *Appl. Phys. Lett.*, **2009**, 95, 191913.
- [10] T. J. Pennycook, A. R. Lupini, H. Yang, M. F. Murfitt, L. Jones, P. D. Nellist, Efficient phase contrast imaging in STEM using a pixelated detector. Part I: Experimental demonstration at atomic resolution, *Ultramicroscopy*, **2015**, 151, 160-167.
- [11] H. Yang, T. J. Pennycook, P. D. Nellist, Efficient phase contrast imaging in STEM using a pixelated detector. Part II: optimisation of imaging conditions, *Ultramicroscopy*, **2015**, 151, 232-239.
- [12] H. Tan, S. Turner, E. Yucelen, J. Verbeeck, G. V. Tendeloo. 2D atomic mapping of oxidation states in transition metal oxides by scanning transmission electron microscopy and electron energy loss spectroscopy. *Phys. Rev. Lett.*, **2011**, 107, 10760.
- [13] D. A. Muller, L. F. Kourkoutis, M. Murfitt, J. H. Song, H. Y. Hwang, J. Silcox, N. Dellby, O. L. Krivanek, Atomic-scale chemical imaging of composition and bonding by aberration-corrected microscopy. *Science*, **2008**, 319, 1073-1076.
- [14] M. Bosman, M. Watanabe, D. T. L. Alexander, V. J. Keast. Mapping chemical and bonding information using multivariate analysis of electron energy-loss spectrum images. *Ultramicroscopy*, **2006**, 106, 1024-1032.

- [15] S. Turner, J. Verbeeck, F. Ramezanipour, J. E. Greedan, G. V. Tendeloo, G. A. Botton. Atomic resolution coordination mapping in $\text{Ca}_2\text{FeCoO}_5$ brownmillerite by spatially resolved electron energy loss spectroscopy. *Chem. Mat.*, **2012**, 24, 1904-1909.
- [16] J. Nelayah, M. Kociak, O. Stephan, F. J. Garcıade-Abajo, M. Tence, L. Henrard, D. Taverna, I. Pastoriza-Santos, L. M. Liz-Marzan, C. Colliex. Mapping surface plasmons on a single metallic nanoparticle, *Nat. Phys.*, **2007**, 3, 348-353.
- [17] M. Bosman, V. J. Keast, M. Watanabe, A. I. Maaroof, M. B. Cortie. Mapping surface plasmons at the nanometre scale with an electron beam, *Nanotechnology*, **2007**, 18, 165505.
- [18] A. Genç, J. Patarroyo, J. Sancho-Parramon, R. Arenal, M. Duchamp, E. E. González, L. Henrard, N. G. Bastús, R. E. Dunin-Borkowski, V. F. Puentes, J. Arbiol, Tuning the plasmonic response up: hollow cuboid metal nanostructures, *ACS Photonics*, **2016**, 3, 770-779.
- [19] S. Bernal, F. J. Botana, J. J. Calvino, C. Lo, J. A. Pe, The interpretation of HREM images of supported metal catalysts using image simulation: profile view images. *Ultramicroscopy*, **1998**, 72:135-164.
- [20] V. Grillo, E. Rotunno. STEM CELL: a software tool for electron microscopy: part 1-simulations, *Ultramicroscopy*, **2013**, 125, 97-111.
- [21] V. Grillo, F. Rossi, STEM_CELL: A software tool for electron microscopy. Part 2-analysis of crystalline materials, *Ultramicroscopy*, **2013**, 125, 112-129.
- [22] E J Kirkland. *Advanced Computing in Electron Microscopy*, **1998**, Springer New York.
- [23] L.J. Han, P.Y. Tang, A. Reyes-Carmona, B. Rodriguez-Garcia, M. Torrens, J. R. Morante, J. Arbiol, J. R. Galan-Mascaros, Enhanced activity and acid pH stability of Prussian blue-type oxygen evolution electrocatalysts processed by chemical etching, *J. Am. Chem. Soc.*, **2016**, 138, 16037-16045.
- [24] E. Gileadi, *Electrode kinetics for chemists, chemical engineers, and materials scientists*, **1993**, Capstone.
- [25] L. Bertoluzzi, J. B. Mascarell, S. G. Julia, Surface state assisted charge transfer and recombination processes at the semiconductor/electrolyte interface, **2016**, Jaume I University.
- [26] S. Giménez, J. Bisquert, J. Photoelectrochemical Solar Fuel Production. **2016**, Springer Berlin.
- [27] J. Bisquert, Theory of the impedance of charge transfer via surface states in dye-sensitized solar cells. *J. Electroanal Chem.*, **2010**, 646, 43-51.
- [28] L. Bertoluzzi, J. Bisquert, Equivalent circuit of electrons and holes in thin semiconductor films for photoelectrochemical water splitting applications. *J. Phys. Chem. Lett.*, **2012**, 3, 2517-2522.
- [29] L. Bertoluzzi, P. Lopez-Varo, J.A. Jimenez-Tejada JA, J. Bisquert, Charge transfer processes at the semiconductor/electrolyte interface for solar fuel production: insight from impedance spectroscopy. *J. Mater. Chem. A*, **2016**, 4, 2873-2879.
- [30] J. Bisquert, Theory of the impedance of electron diffusion and recombination in a thin layer. *J. Phys. Chem. B*, **2002**, 106, 325-333.
- [31] J. Bisquert, Beyond the quasi-static approximation: impedance and capacitance of an exponential distribution of traps, *Phys. Rev. B*, **2008**, 77, 235203.

- [32] J. Bisquert, Nanostructured energy devices: equilibrium concepts and kinetics, *CRC Press*, **2014**, Boca Raton.
- [33] Z. Hens, the electrochemical impedance on one-equivalent electrode processes at dark semiconductor redox electrodes involving charge transfer through surface states. *J. Phys. Chem. B*, **1999**, 103, 122-129.
- [34] B. Klahr, S. Gimenez, F. Fabregat-Santiago, T. Hamann, J. Bisquert, Water oxidation at hematite photoelectrodes: The role of surface states, *J. Am. Chem. Soc.* **2012**, 134, 4294-4302.
- [35] B. Klahr, S. Gimenez, F. Fabregat-Santiago, J. Bisquert, T. W. Hamann, Photoelectrochemical and impedance spectroscopic investigation of water oxidation with “Co-Pi” coated hematite electrodes, *J. Am. Chem. Soc.* **2012**, 134, 16693-16700.
- [36] B. Klahr, S. Gimenez, F. Fabregat-Santiago, J. Bisquert, T. W. Hamann, Electrochemical and photoelectrochemical investigation of water oxidation with hematite electrodes, *Energy Environ. Sci.*, **2012**, 5, 7626-7636.
- [37] 曹楚南, 张鉴清. 电化学阻抗谱导论. 科学出版社, **2002**.
- [38] A. J. Bard, L.R. Faulkner, *Electrochemical methods: Fundamentals and applications*, 2nd Edition, ISBN: 978-0-471-04372-0, **2000**.

Chapter 3

Hematite-Polypyrrole Based Nanoflakes as Negative Electrodes for Asymmetric Supercapacitors

3.1 Introduction

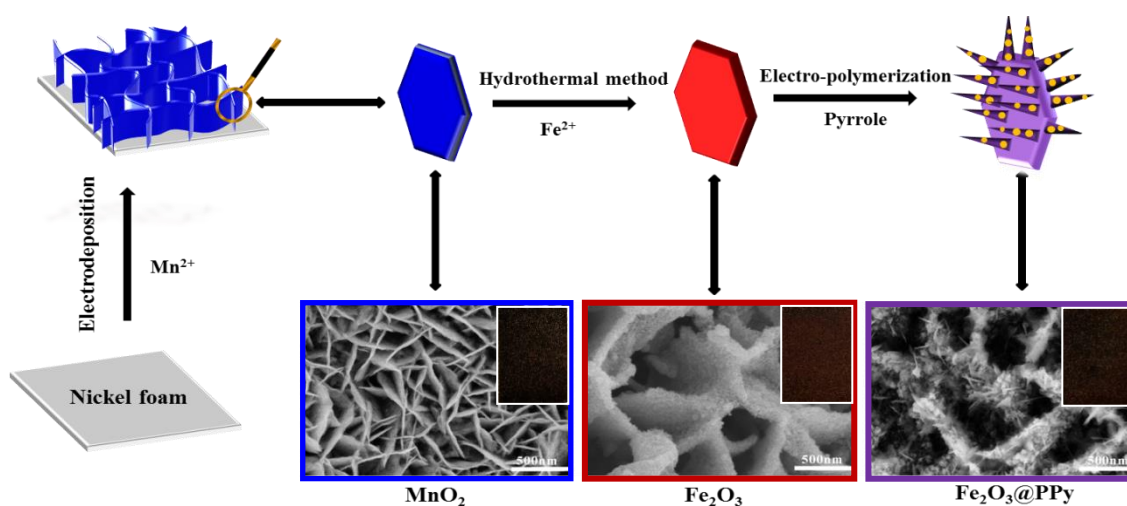
Supercapacitors, which bridge the gap between high energy batteries and high power dielectric capacitors, are regarded as important energy storage devices for high power supplies, electric and hybrid vehicles, and portable electronics. [1] Typically, the energy density (E , Wh kg^{-1}) of supercapacitors depends on the cell potential (V) and specific capacitance (C_{sp} , F g^{-1}), $E=0.5 C_{\text{sp}}V^2$. [2-6]. Due to their limited cell potential (e.g. the value of commercial MAWELL capacitors is ca. 0.7 V), [4] the energy density of conventional symmetrical supercapacitors is much lower than that of batteries. For this reason, asymmetrical supercapacitors (ASCs) with wider cell potential came into being. ASCs are basically composed of a battery-type faradaic positive electrode and a double-layer-type negative electrode. [5-7] To date, various metal oxides and conductive polymers have been extensively investigated as positive electrodes, [8-9] coupling with negative electrodes, such as carbon sheets, [10] activated carbon (AC) [11], carbon nanotubes (CNTs), [12] and graphene [13-14] for high-performance ASCs. Advances in this type of prototypes have yielded ASCs with good power density, whereas the low specific capacitance of carbon materials (maximum ca. 300 F g^{-1}) still limits their energy density. [15-18] In order to improve the energy-density limit of ASCs, the exploration of alternative, state-of-the-art negative electrodes with higher specific capacitance than carbon materials is highly valuable and significant.

Recently, some emerging transition metal oxides or sulphides, such as V_2O_5 , [19] V_3S_4 , [20] In_2O_3 , [21] MoO_3 , [22] and Co_9S_8 [23] as negative electrodes for ASC applications have attracted the attention of numerous researcher groups worldwide. Among these materials, hematite ($\alpha\text{-Fe}_2\text{O}_3$) is one of the most promising candidates because of its large theoretical specific capacitance (3265 F g^{-1}), suitable working window, low cost, abundance, and environmentally-friendly characteristics. [9, 24] However, the practical implementation of negative electrodes based on Fe_2O_3 has been prevented due to its poor electrical conductivity ($\sim 10^{-14}$ S/cm). [25] To tackle this obstacle and improve its electrochemical performance, much effort has have been made to construct nanostructured Fe_2O_3 , such as oxygen-deficient nanorods, [9] nanoflowers, [25]

nanowires, [26] and nanoneedles, [27] etc. Other researchers have alternatively combined Fe_2O_3 with highly conductive materials including CNTs, [28] graphene [29-31] and poly (3, 4-ethylenedioxythiophene) (PEDOT) [6] taking advantage of the excellent conductivity of carbon or conductive polymer species. For example, X. H. Lu et al. fabricated a $\text{Ti-Fe}_2\text{O}_3@\text{PEDOT}$ core-shell electrodes, which showed a high specific capacitance of 311.6 F g^{-1} at 1 mA cm^{-2} with superior cycling durability and more than 96% capacitance retention after 30,000 cycles.[6] Nonetheless, the obtained specific capacitance ($\sim 9.5\%$) was still much lower than the theoretical specific capacitance expected for hematite. Additionally, an enhanced life cycle was obtained by sacrificing the energy density, [6] which was supposed to be improved by incorporating three-dimensional (3D) branched nanoarchitectures self-aligned on the substrate. [32]

Compared with 0D nanoparticles, 1D nanowires and 2D nanosheets, 3D branched nanoarchitectures possess extraordinary advantages, including structural hierarchy, higher surface areas and direct electron and ion transport pathways. These nanomaterials therefore hold great promise as regards their functionality for application fields such as solar cells, water splitting, lithium-ion batteries, supercapacitors etc. [32-35] In spite of these merits, for supercapacitors application, controlling the size, dimension, and composition of the building blocks and maintaining their structure stability and good electrical conductivity during repeated cycles are still great challenges. [32] Recently, B. A. Lu et al. reported that nanoengineered honeycomb-like CoMoO_4 (96.3% capacitance retention) was more stable than CoMoO_4 with nanowire-like morphology (74.14% capacitance retention) or as nanosheet shape (84.69% capacitance retention) during continuous life cycling of 1000 times at 15.71 A g^{-1} . [36] With this in mind, honeycomb-like matrices combining branched nanoarchitectures to form core-branch nanostructures may further boost their life cycle. In this regard, PPy species serving as a protective shell of metal oxides, such as layered double hydroxide, [16] MnO_2 , [37] and MoS_2 , [38] to form core-shell nanostructures have been evidenced to be a powerful tool for effectively improving the

electrochemical behaviour of positive electrodes. Furthermore, C. Debiemme-Chouvy et al.'s report on the fabrication of well-defined PPy nanowires on Au film through simple electropolymerization by controlling the weak-acidic and non-acidic anions content in the deposition electrolyte, sheds light on the construction of a highly conductive ordered branch structure on a backbone matrix. [39-40] However, research combining the merits of the stability of the honeycomb-like matrix (metal oxides) on ion transportation and the superiority of branch structure (conductive polymers) on electron transferring are still scarce. In the same way, there are also scarce reports elucidating the mechanisms underlying the formation and morphogenetic evolution of core-branch nanostructures to extract design principles that may enable conductive polymer formations on other metal oxides with similar capabilities.



Schematic 3.1 Fabrication process of core-branch Fe₂O₃@PPy heterostructures (the insets show the digital photographs of MnO₂, Fe₂O₃ and Fe₂O₃@PPy electrodes).

In this chapter, we synthesized core-branch honeycomb-like Fe₂O₃ nanoflakes@PPy nanoleave arrays grown on a three-dimensional nickel foam (NF) scaffold, composed of one-dimensional (1-D) leaf-like PPy, 2-D mesoporous Fe₂O₃ nanoflakes, and 3-D macroporous NF, as displayed in **Schematic 3.1**. We then thoroughly investigated the formation mechanism of branched PPy nanoleaves. The as-prepared core-branch Fe₂O₃@PPy electrode showed a remarkably large specific capacitance of 1167.8 F g⁻¹ at 1 A g⁻¹ with a good rate capability.

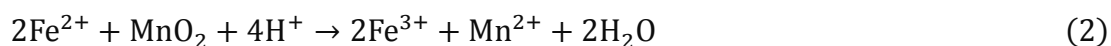
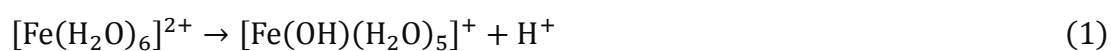
3.2 Experimental Section

3.2.1 Synthesis of MnO₂ Nanosheets on Nickel Foam

The MnO₂ nanosheets were synthesized by a cathode electrodeposition in a three-electrode system. [41-42] In this setup, NF (active area: 1.5 cm× 2 cm; thickness: 1.8 mm, pore density: 110 ppi, Changsha Liyuan New Material) served as the working electrode, which was first cleaned by acetone and then deionized water. Platinum (Pt) plate and saturated calomel electrode (SCE) served as the counter and reference electrodes, respectively; and 0.02 M manganese acetate and 0.02 M sodium sulphate aqueous solution worked as the electrolyte. The electrodeposition of MnO₂ nanoflakes on a NF substrate was carried out at a constant potential of -1.6 V for 150 s. The obtained sample was then rinsed in deionized water for several times and then dried at 200 °C for 2 h.

3.2.2 Synthesis of Honeycomb-like Fe₂O₃ Nanoflakes on NF

The obtained MnO₂ nanosheet sample was employed as a sacrificed template to synthesize the honeycomb-like Fe₂O₃ nanoflakes according to a reported method with slight modifications. [43] Details of the process are as follows: 21 mg of FeSO₄·7H₂O (Aladdin, 99.9 %) was dissolved in 30 mL of mixed ethylene glycol and deionized water (v/v = 1/7). After stirring for about 10 min, this translucent solution and the as-prepared MnO₂ nanoflakes on NF were both transferred to a 50 mL Teflon-lined stainless steel autoclave, followed by heating at 120 °C for 0.5 h in an electric oven. After heating, the autoclave was cooled naturally to room temperature. The nickel foam with iron hydroxides were obtained from the following reaction during the hydrothermal process (equation 1 and 2),



The samples were then removed and rinsed thoroughly with absolute ethanol and dried

at room temperature (equation 3). The honeycomb-like α -Fe₂O₃ nanoflakes were obtained by annealing the prepared iron hydroxide product at 400 °C in air for 2 h with a heating rate of 2 °C min⁻¹.

3.2.3 Synthesis of PPy Nanoleaves Decorated Honeycomb-like Hematite Nanoflakes on NF

The aforementioned honeycomb-like Fe₂O₃ nanoflakes on NF were then used as the working electrode for the deposition of PPy nanoleaves. The PPy species were deposited at a constant potential of 1.0 V vs. SCE in an aqueous medium consisting of 80 mM pyrrole, 100 mM LiClO₄, and 140 mM sodium dodecyl sulphate. [44] Finally, the obtained sample was washed with deionized water several times, and then dried at 60 °C. The mass of PPy shell and core Fe₂O₃ species was determined by a high-precision microbalance with a sensitivity of 0.1 mg.

3.2.4 Assembly of the ASC

For the construction of the asymmetric supercapacitor device, MnO₂ nanosheets and core-branch Fe₂O₃@PPy and pieces of commercial supercapacitor separator membrane (DR2012, thickness: 0.12 ± 0.01mm, Suzhou Beige New Materials & Technology Co. Ltd.) were used as the positive and negative electrodes and separator. The electrodes, 0.5 M Na₂SO₄ and separator were enveloped in aluminium plastic bags.

3.2.5 Characterization of Microstructural Properties

The as-synthesized samples were characterized using an X-ray powder diffraction (XRD; Rigaku RU-300 diffractometer; monochromated Cu K α 1 radiation, λ = 1.540 598 Å; 60.0 kV, 30.0 mA), field emission scanning electron microscopy (SEM, 5.0 kV, SU-8010, Hitai), transmission electron microscopy (TEM, 200kV, Tecnai F20, FEI), scanning transmission electron microscopy-electron energy loss spectroscopy (STEM-EELS, 200 kV under a high angle annular dark field (HAADF), Tecnai F20, FEI). Energy dispersive X-ray spectrometer (EDS), X-ray photoelectron spectroscopy (XPS, Escalab 250Xi) and Raman Spectrum (incident wavelength: 514 nm, InVia-RENISHAW).

3.2.6 Measurement of Electrochemical Properties

The electrochemical performance of MnO₂ nanosheets and core-branch Fe₂O₃@PPy electrodes and the corresponding asymmetric supercapacitor was characterized by cyclic voltammetry (CV), galvanostatic charge-discharge (GCD), and electrochemical impedance spectroscopy (EIS, recorded at open circuit potential with amplitude of 5 mV in the frequency range of 10⁻²-10⁵ Hz) techniques on a CHI 760E electrochemical workstation at ambient temperature. All the measurements were carried out in a 0.5 M Na₂SO₄ aqueous solution. In the three-electrode system, a Pt plate of 2.0 cm × 2.0 cm and a SCE were applied as the counter and reference electrodes, respectively. The specific capacitance measured by chronopotentiometry was calculated according to the following equation:

$$C_p = I \times \frac{\Delta t}{\Delta V \times m} \quad (4)$$

where C_{sp} (F g⁻¹) is the specific capacitance of the electrode (C_{sp-e}) or ASC (C_{sp-a}), I (A) is the constant discharging current, Δt (s) is the discharging time, ΔV (V) is the voltage change excluding IR drop at a constant discharge current, and m (g) is the active material mass of a single electrode or the total active material mass of positive and negative electrodes.

For the two-electrode configuration, energy (E , Wh kg⁻¹) and power densities (P , kW kg⁻¹) were calculated using the following equations:

$$E = \frac{C_{sp-d}\Delta V^2}{2}, P = \frac{\Delta VI}{2m} \quad (5)$$

where C_{sp-d} (F g⁻¹), is the specific capacitance of the asymmetric supercapacitor, ΔV (V) is the voltage change excluding IR drop at a constant discharge current, I (A) is the discharging current and m (g) is the total active material mass of positive and negative electrodes.

3.3 Results and Discussion

3.3.1 Optimization of the Hydrothermal Reaction Time of Fe₂O₃ Samples

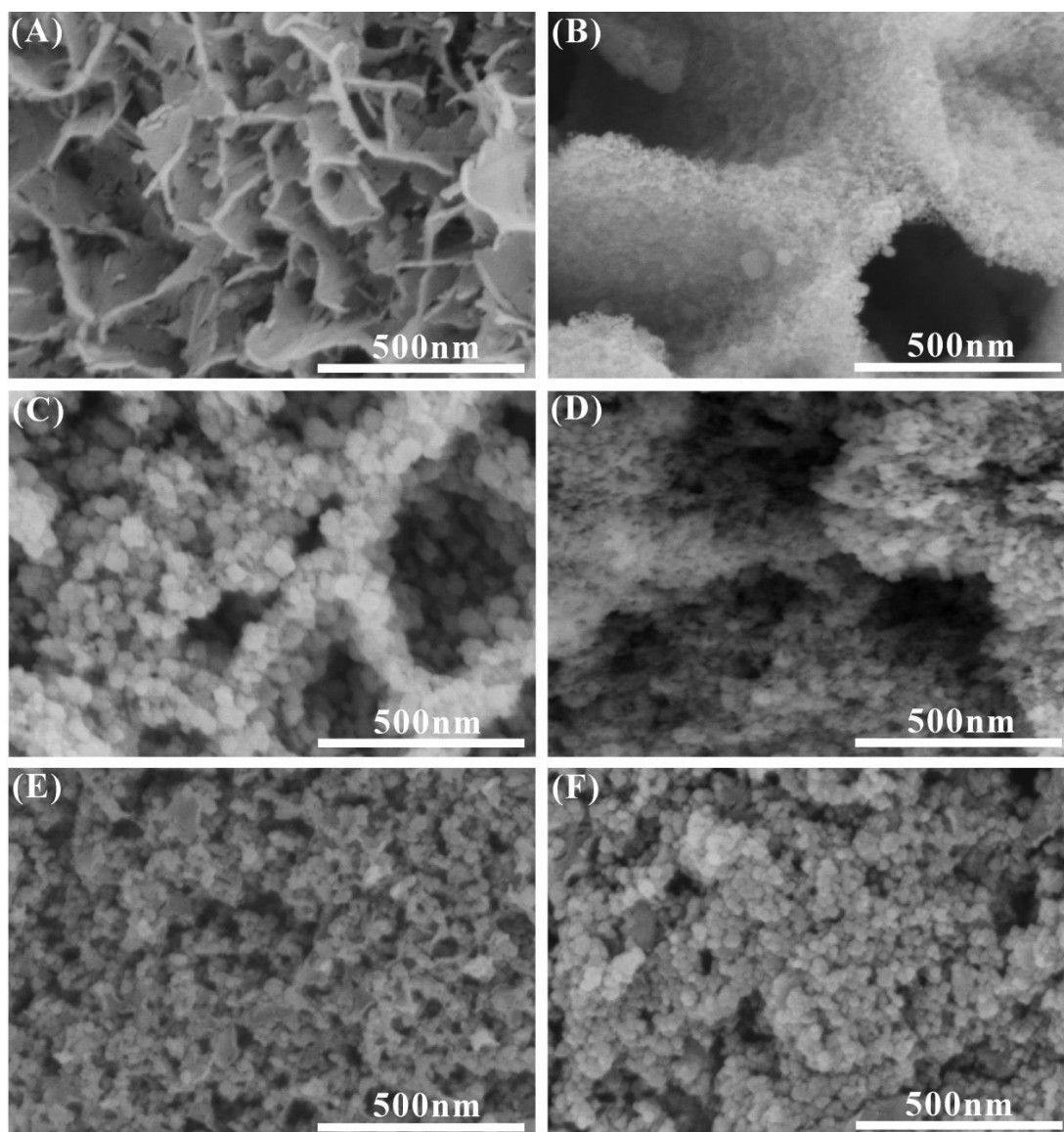


Figure 3.1 SEM images of Fe₂O₃ samples with different hydrothermal times: 15 min (A), 30 min (B), 45min (C), 1 h (D), 75 min (E) and 2 h (F).

Aliquots were drawn at different times to produce six additional Fe₂O₃ samples with different degrees of substitution reaction. SEM images showing the time evolution of the Fe₂O₃-nanoflakes are shown in **Figure 3.1**. At the very early stage of the reaction, quasi-flake structures were formed (**Figure 3.1A**) and during the first 30min, a progressive change of morphology and composition was observed. The MnO₂ species completely transformed into Fe₂O₃ nanoflakes (**Figure 3.1B**). At this point, the element Mn was not observed in the sample, as proved by EDS in **Figure 3.2**. In the next 15

minutes of the reaction, the nanoflakes decomposed into nanoparticles (**Figure 3.1C**). At this stage of the reaction, nanoflake profiles could still be found but their content was minimal. As the hydrothermal reaction proceeded further, the nanoflakes evolved into dispersible nanoparticles (**Figure 3.1D-F**). Therefore, the 30 min reaction time was selected as the optimized hydrothermal time since it transformed the MnO_2 nanoflakes into Fe_2O_3 nanoflakes without damaging their honeycomb-like structure. [45]

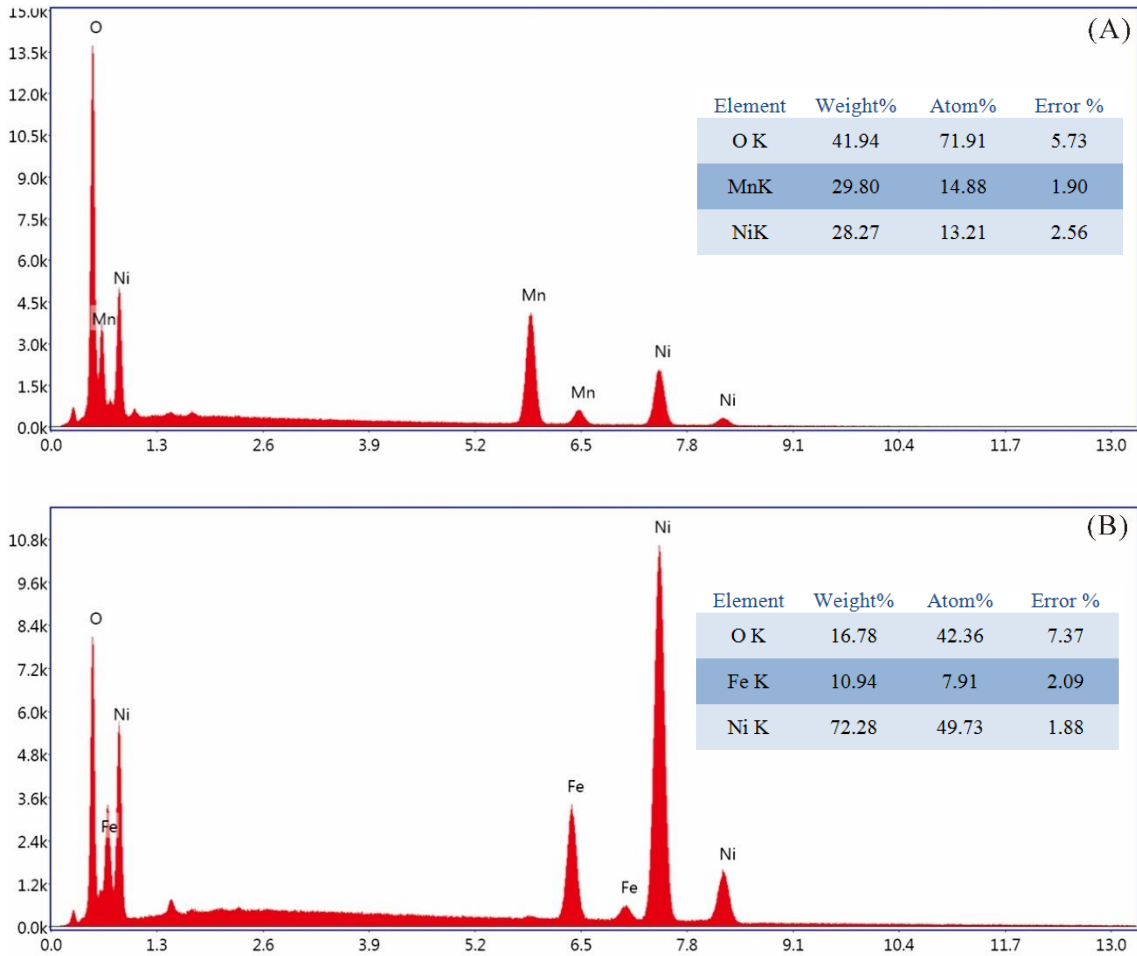


Figure 3.2 The EDS spectrum of MnO_2 nanosheets and honeycomb-like Fe_2O_3 -30 min nanoflakes.

3.3.2 Optimization of PPy Deposition Charges in Core-Shell Fe_2O_3 @PPy Samples

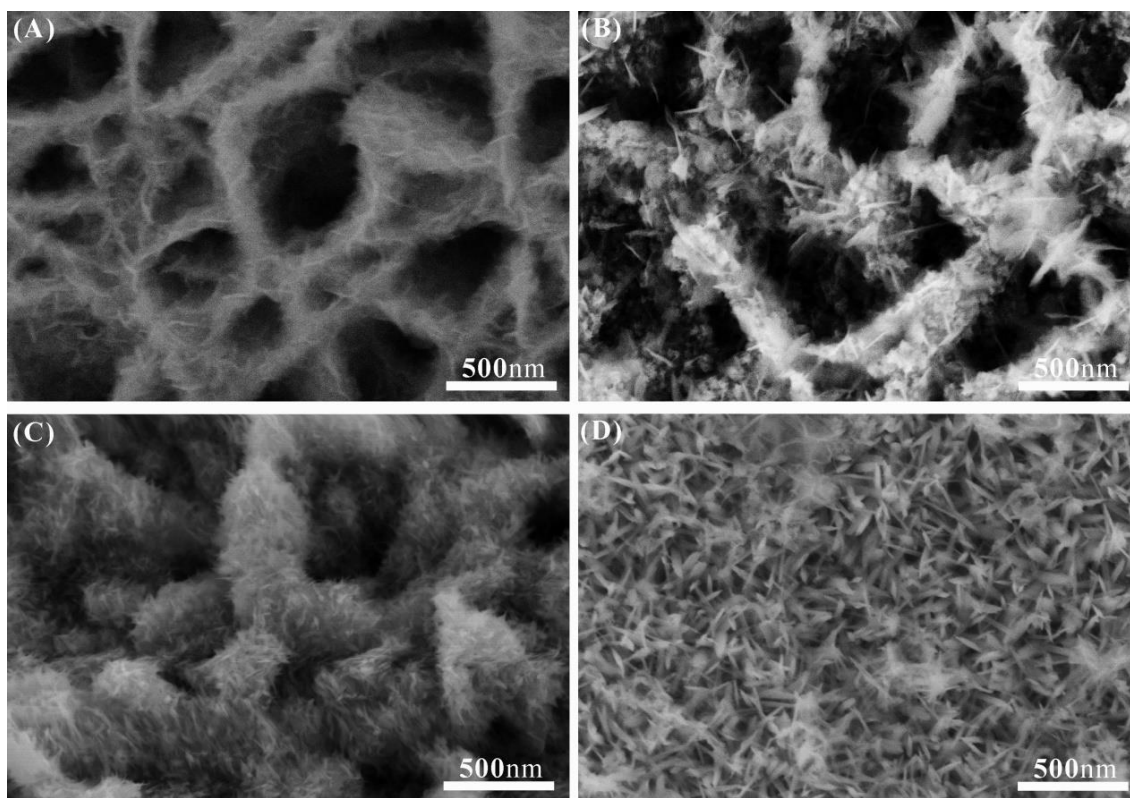


Figure 3.3 SEM images of core-branch Fe_2O_3 nanoflakes@PPy nanoleaves with different PPy deposition charges: 0.1 C (A), 0.3 C (B), 0.5 C (C) and 1.0 C (D).

To optimize the structure of Fe_2O_3 @PPy, a parallel experiment in terms of controlling the deposition of PPy was also conducted (**Figure 3.3**). As the electrochemical polymerization proceeded, the PPy nanoleaves grew into locally jammed structures, which not only blocked the electrolyte ion accessibility but also could deteriorate their electrochemical performance. As a proof-of-concept of the advantages of core-branch Fe_2O_3 @PPy, CV and GCD rate capabilities and EIS were performed in a three-electrode electrochemical cell, as displayed in **Figure 3.4**. As can be observed, the CV curve of $\alpha\text{-Fe}_2\text{O}_3$ has one pair of redox peaks, involving the $\text{Fe}^{2+}/\text{Fe}^{3+}$ redox couple and probably mediated by the Na^+ ions in the neutral electrolyte. Previous studies show that when scanned to the negative potential direction, Fe^{3+} is reduced to Fe^{2+} with a peak at about -1.05 V vs. (Hg/HgO). [31] To avoid the appreciable H_2 evolution, in this work, the CV curves of all Fe_2O_3 based electrodes were cycled from -1.0 V to -0.2 V vs. SCE. Typically, Fe^{2+} is oxidized to Fe^{3+} when scanned in the positive direction, consistent with the oxidation peak observed at ca. -0.6 V vs.

SCE. in CV of the Fe_2O_3 nanoflakes electrode, as shown in **Figure 3.4A**. [31] With the increasing of PPy deposition, the CVs of $\text{Fe}_2\text{O}_3@\text{PPy}$ electrodes exhibited a quasi-rectangular shape, indicating their reversible performance.

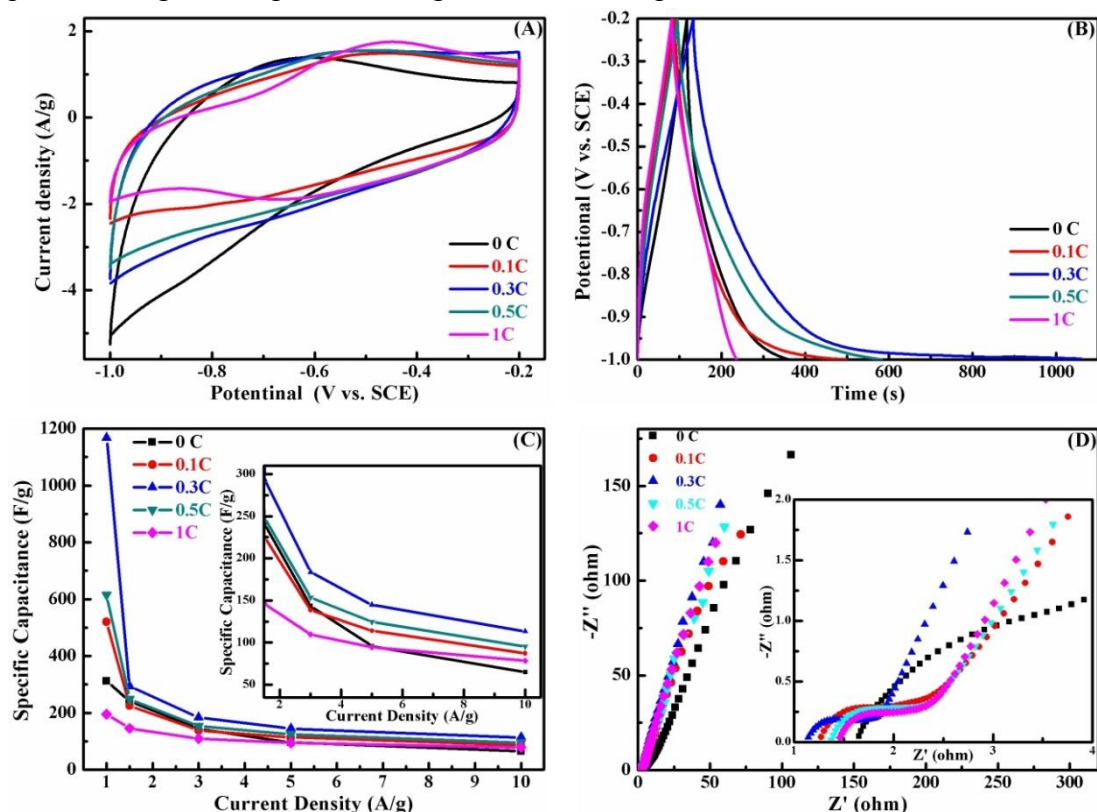


Figure 3.4 The electrochemical properties of Fe_2O_3 and core-branch $\text{Fe}_2\text{O}_3@\text{PPy}$ with different PPy deposition charges: (A) CV curves at 10 mV s^{-1} , (B) GCD at 1 A g^{-1} , (C) the relationship between specific capacitance and current density and (D) the Nyquist diagrams.

When the PPy deposition reached 1.0 C , another pair of peaks appeared which can be assigned to doping/unhopping processes between PPy and Na^+ for charge storage. And the redox peaks of Fe_2O_3 almost disappeared probably because of the shielding effectiveness of the over-deposited PPy species (**Figure 3.3D**). Among these core-branch electrodes, the $\text{Fe}_2\text{O}_3@\text{PPy}$ electrode with 0.3C PPy deposition (donated as $\text{Fe}_2\text{O}_3@\text{PPy}-0.3\text{C}$ electrode) possessed the largest integral area as well as the maximum current response per unit. Moreover, even at a scan rate of 500 mV s^{-1} (**Figure 3.5**), the CV profile still maintained a quasi-rectangular shape, revealing its good rate characteristics. **Figure 3.4B** reveals that the $\text{Fe}_2\text{O}_3@\text{PPy}-0.3\text{C}$ electrode possessed the longest discharge time at a current density of 1 A g^{-1} , which is

consistent with the aforementioned CV results. [46] According to **Figure 3.4C**, with the increment of PPy deposition charges, the specific capacitance of Fe₂O₃@PPy core-branch nanoflakes increased at the beginning to a maximum (1167.8 F g⁻¹ at 1 A g⁻¹) at 0.3 C PPy deposition, which is much higher than that of the pristine Fe₂O₃ nanoflakes electrode (312.5 F g⁻¹ at 1 A g⁻¹). These results further demonstrate the great advantages of the Fe₂O₃@PPy core-branch structure. Afterwards it decreased upon further increment of PPy deposition because the overloaded PPy (see the SEM in **Figure 3.3 C and D** of 0.5 C and 1.0 C PPy deposition) hindered the electrolyte ions from penetrating into the Fe₂O₃ nanoflakes' pores.

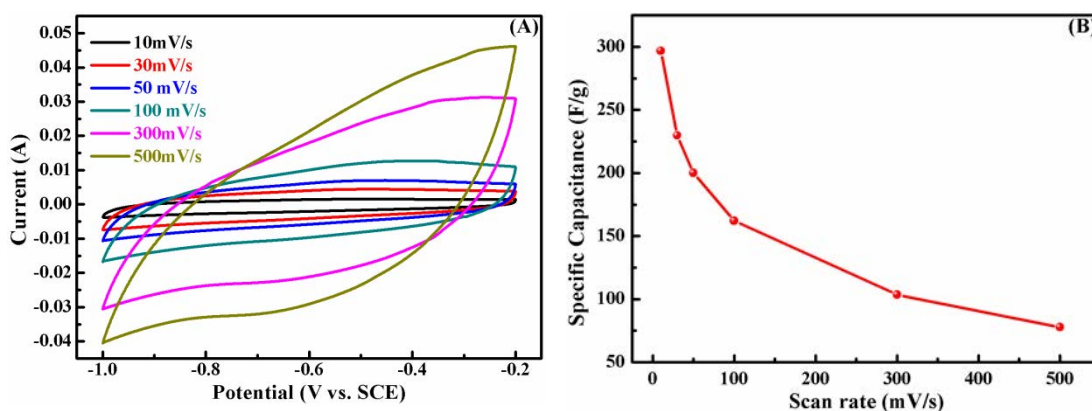


Figure 3.5 Electrochemical properties of the Fe₂O₃@PPy-0.3C at different scan rates (A) and relationship between specific capacitance and scan rates (B).

Rate capability is also one of the most important factors in evaluating the power application of supercapacitors. Consequently, in this study, the GCD profiles of the pristine Fe₂O₃ and Fe₂O₃@PPy electrodes at different current densities were measured. From the inset of **Figure 3.4C**, the pristine Fe₂O₃ electrode shows a specific capacitance of 65.0 F g⁻¹ at 10 A g⁻¹. The Fe₂O₃@PPy-0.3C electrode, by contrast, still maintains a specific capacitance as high as 113.4 F g⁻¹. [47] The enhanced capacitance and rate capability of the Fe₂O₃@PPy-0.3C electrode can be attributed to the improvement of the electrode's electrical conductivity after coating with the optimized PPy nanoleaves. The fast ion diffusion kinetics and effective electron transfer rate in the Fe₂O₃@PPy nanoflakes electrodes are further confirmed by the EIS in **Figure 3.4D**. It is well established that the impedance at high frequency (100 kHz) reflects the equivalent series resistance (ESR) in the electrode/electrolyte system,

which is related to the electrical conductivity of the electrode. [48-49] The ESR of pristine Fe_2O_3 and core-shell $\text{Fe}_2\text{O}_3@\text{PPy}$ electrodes with 0.1, 0.3, 0.5 and 1.0 C PPy deposition charges is 1.65, 1.27, 1.14, 1.37 and 1.46 Ω , concurring the best conductivity of the core-shell $\text{Fe}_2\text{O}_3@\text{PPy-0.3C}$ electrode. In addition, the semicircle of the Nyquist diagram corresponds to the faradaic reactions; its diameter represents the interfacial charge-transfer resistance (R_{ct}), and the linear part corresponds to the Warburg impedance, which is described as a diffusive resistance of the electrolyte into the electrode pores. [50] The R_{ct} of the $\text{Fe}_2\text{O}_3@\text{PPy-0.3C}$ electrode is the lowest one among these electrodes and the highest slope at low frequency partly demonstrates its superior ion diffusion ability compared to the other electrodes. These results demonstrate that the combination of the high electrical conductivity pathways for charge transfer derived from the coating of PPy nanoleaves as well as the fast ion diffusion kinetics result from the honeycomb-like Fe_2O_3 , is responsible for the excellent electrochemical performance of the $\text{Fe}_2\text{O}_3@\text{PPy-0.3C}$ electrodes.

3.3.3 Investigation of PPy Growth Mechanism in Core-shell $\text{Fe}_2\text{O}_3@\text{PPy}$ Samples

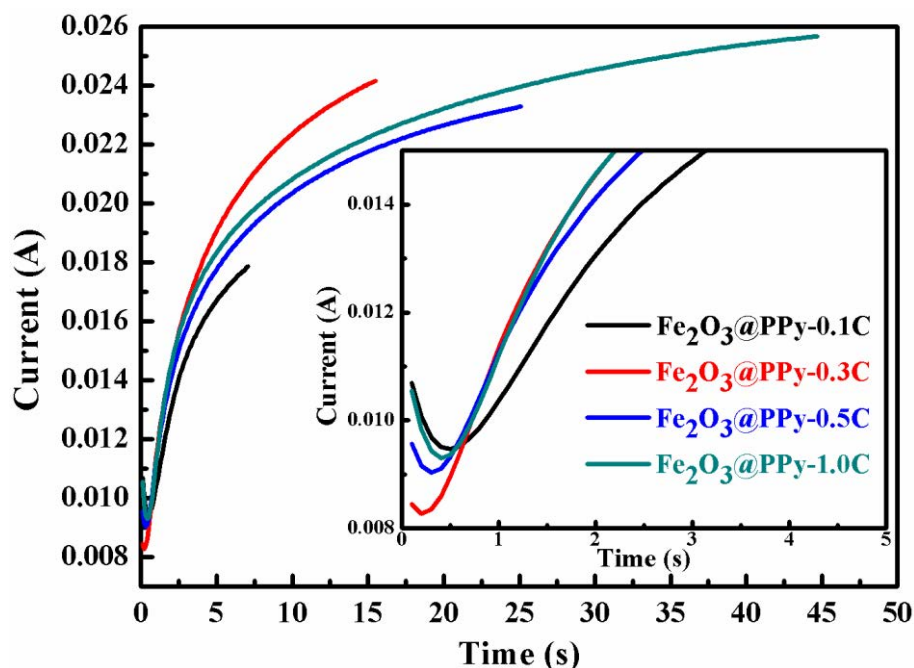
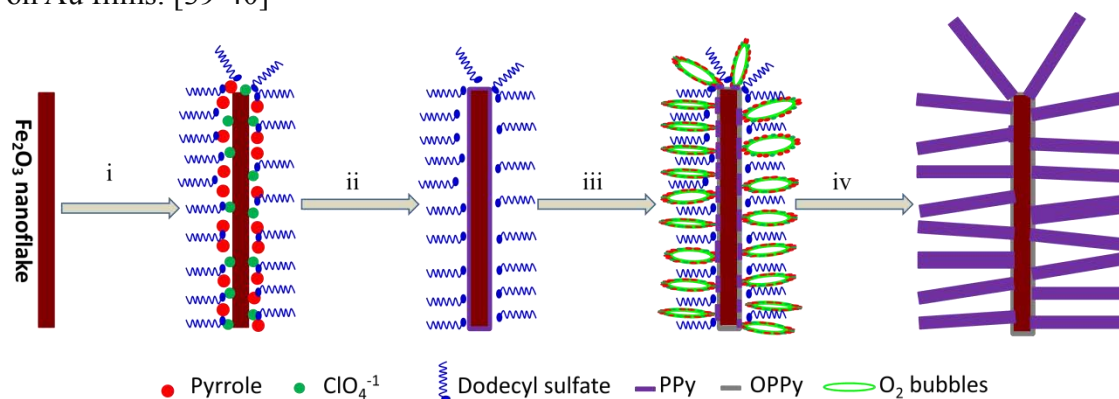


Figure 3.6 Current versus time, $I(t)$, of polarization pyrrole at 1.0 V vs. SCE in the aqueous medium of 80 mM pyrrole, 100 mM LiClO_4 , and 140 mM sodium dodecyl sulphate.

The $I(t)$ curves shown in **Figure 3.6** were obtained in the presence of ClO_4^- and

dodecyl sulphate anions. As can be observed, with these two anions, first the anodic current is high and then it decreases rapidly up to a very low value (as shown in the inset of **Figure 3.6**). However, after that, the current slightly increases with prolonging the deposition time. The $I(t)$ response curves of PPy electropolymerization in this case are similar to previously reported pyrrole (Py) deposited in weak-acidic and non-acidic anions, which results in the formation of well-defined PPy nanowires on Au films. [39-40]



Schematic 3.2 Possible mechanism of the PPy nanoleaves formation on the Fe_2O_3 nanoflakes according to C. D. Chouvy's report. [44]

Thus, the deposition of branched PPy on Fe_2O_3 nanoflakes may follow a possible mechanism, as shown in **Schematic 3.2**: [44]

The first stages (i and ii), represent the classical electrodeposition of a thin PPy film (leading to proton release and therefore to a decrease of ClO_4^{-1} anion concentration at the Fe_2O_3 nanoflakes/electrolyte interface).

The second stage (iii), is very short and involves the oxidation of water leading in some places to the overoxidation of the polymer due to hydroxyl radicals, and in other places to the formation of O_2 nanobubbles that protect the already synthesized polymer against the overoxidation of OH^{-1} . Then, at the Fe_2O_3 nanoflakes/solution interface, the anion (ClO_4^{-1}) concentration begins to increase due to the anion diffusion from the electrolyte bulk and polymer dedopage.

The last step (iv), concerns the quick growth of the PPy nanowires at places where O_2 has evolved with the assistance of dodecyl sulfate anions. Finally, the growth process

results in PPy nanowires with cylindrical shaped Fe_2O_3 decorated nanoflakes.

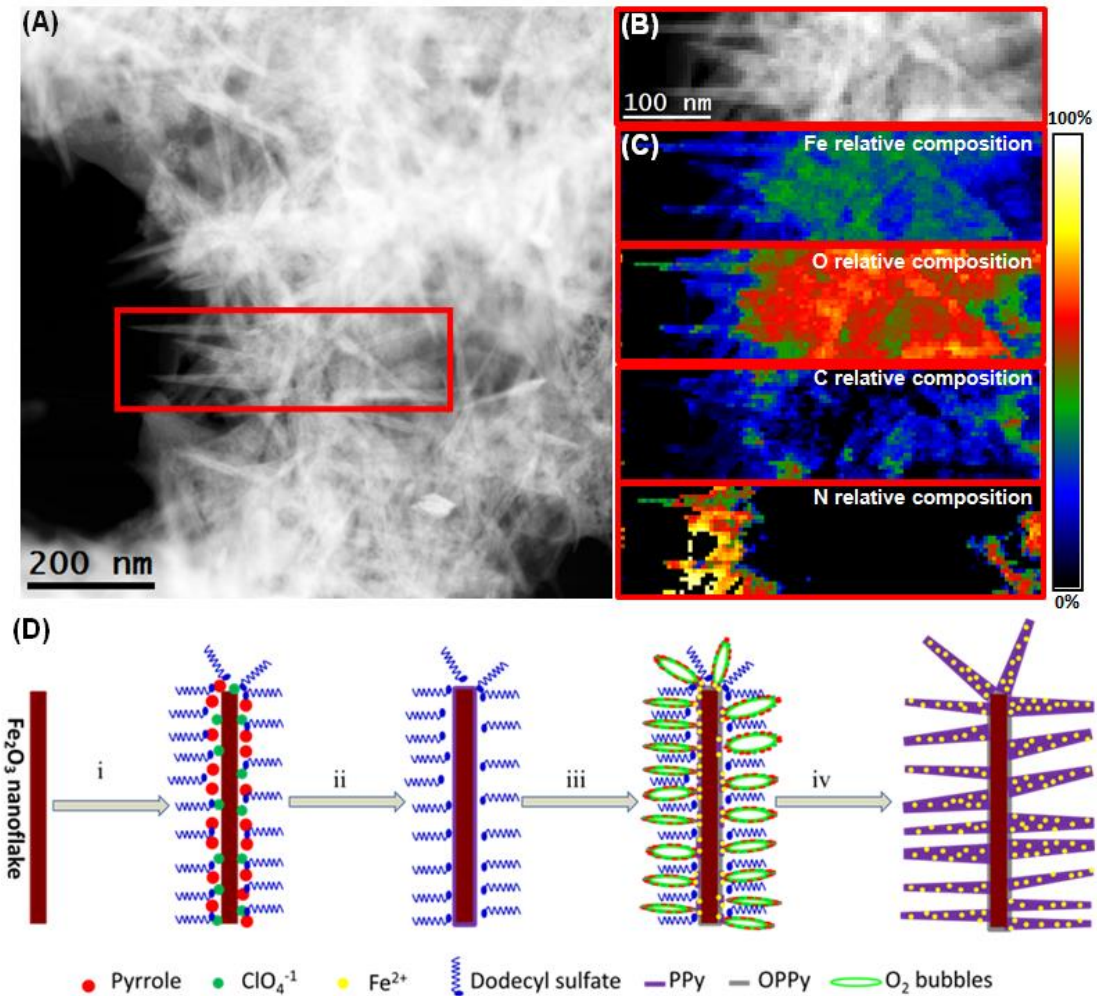


Figure 3.7 STEM-EELS chemical composition maps of core-branch $\text{Fe}_2\text{O}_3@$ PPy obtained from the red-rectangle area shown in the STEM micrograph (A), simultaneously obtained HAADF STEM micrograph (B) and relative compositions (C) of Fe, O, C and N (The scale bar is the same for all composition maps, as in (B)). (D) The Schematic illustrates the formation mechanism of the PPy nanoleaves on Fe_2O_3 nanoflakes, Step (i): immersing Fe_2O_3 nanoflakes in the aqueous solution of 80 mM pyrrole, 100 mM LiClO_4 , and 140 mM sodium dodecyl sulfate, Step (ii): Electrodeposition of an ultrathin PPy film on Fe_2O_3 nanoflakes when applied a high potential of 1.0V vs. SCE, Step (iii): Generation of OH^- which overoxidizes PPy, Step (iv): Further electropolymerization growth of the PPy species.

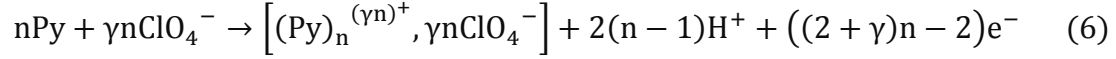
To precisely figure out the composition in the nanoleaves and nanoflakes of the core-branch $\text{Fe}_2\text{O}_3@$ PPy-0.3C electrode and understanding the growth mechanism of PPy leaves, STEM-HAADF and STEM-EELS were employed, as displayed in **Figure**

3.7. Figures 3.7A and B are the HAADF STEM images of the core-branch $\text{Fe}_2\text{O}_3@\text{PPy}$, showing a general view and a magnified detail, respectively. The relative compositions of Fe, O, C and N elements in the nanoflake and nanoleave regions (**Figure 3.7C**) were mapped by means of EELS analysis using the Hartree-Slater model for signal quantification and power law for background removal. The elemental relative composition maps suggest a fairly homogeneous distribution of Fe and O throughout the nanoflakes. Specifically, the Fe and O elements in the nanoflake region have a relative composition of $\sim 35 \pm 4$ at% and 60 ± 5 at %, which is almost equal to the nominal compositions of the Fe_2O_3 phase (Fe: 40 %, O: 60 %); whilst these values in nanoleave regions are $\sim 20 \pm 4$ at % and 25 ± 5 at %, which is nearly equal to the nominal compositions of the FeO phase (Fe: O=1:1). These results reveal that the Fe_2O_3 content dominates the nanoflake region, while the FeO phase is mainly located in the nanoleave region. Meanwhile, the signals of C and N elements are relatively weak at the centre of the nanoflakes, indicating there is an extremely thin PPy film on the surface plane of the Fe_2O_3 nanoflakes. In addition, the elemental relative compositions of C and N in the nanoleave regimes are 25 ± 5 at%, and 45 ± 5 at%, respectively, indicating that the PPy species dominate the nanoleave region. The EELS map and relative composition analyses of the $\text{Fe}_2\text{O}_3@\text{PPy}-0.3\text{C}$ electrode evidence that the Fe element penetrates in the form of FeO into the region where the PPy nanoleaves exist, as displayed in **Figure 3.7**.

Based on these results, the formation process of the PPy nanoleaves on Fe_2O_3 nanoflakes is proposed in **Schematic 3.7D**:

Step (i): the obtained Fe_2O_3 nanoflakes are immersed in an aqueous solution of 80 mM pyrrole, 100 mM LiClO_4 , and 140 mM sodium dodecyl sulfate (SDS). Due to the inducing covalent bonding between the Fe^{3+} and the partial negative charge of the N atom in the Py structure, dodecyl sulphate and ClO_4^{-1} ions, these anions are absorbed on the wall of the nanoflakes. Specifically, ClO_4^{-1} ions were close to the Fe_2O_3 nanoflakes, whereas the dodecyl sulfate of SDS was relatively far away from the Fe_2O_3 nanoflakes because of its long alkyl chain structure.

Step (ii): Electrodeposition of an ultrathin PPy film on the Fe₂O₃ nanoflakes when a high potential of 1.0 V vs. SCE is applied. The oxidation of pyrrole (Py) leads to the formation of a thin polypyrrole film under its oxidized form on the surface of the Fe₂O₃ nanoflakes doped with anions (ClO₄⁻), according to the following reaction [39]:



where γ stands for the doping level of the polymer, generally ranging from 0.25 to 0.33.



Step (iii): Generation of OH \cdot which overoxidizes PPy (OPPy) based on equations (7) and (8). Since hydroxyl radical can also react with itself, leading to H₂O₂ that is further oxidized to O₂, the produced O₂ nanobubbles will protect partial PPy species against the action of OH \cdot , according to equations (9) and (10). Furthermore, the H⁺ byproduct around the interface of Fe₂O₃ and O₂ bubbles makes the Fe₂O₃ on the surface of the nanoflake region into Fe³⁺ ion due to the localized low pH value, which can be up to 1 (equation 11). [40]



Step (iv): Further electropolymerization (equation 12) growth of the PPy species based on the template composed of O₂ nanobubbles and dodecyl sulfate, finally leading to the formation of PPy nanowires. At the same time, the induced Fe³⁺ ions diffuse into the electrolyte and favorably bind with the nitrogen-containing groups on PPy nanoleaves via complexation and electrostatic interactions.[29] During the subsequent electrochemical growth stage of PPy nanowires, Fe³⁺ elements interact

with Py species inside the nanowire region, simultaneously forming a microcell for chemical polymerization (equations 12), which results in leaf-like PPy nanowires with conical shapes because of the Fe^{3+} gradient in the growth direction of the PPy nanowires. Then, the subsequent heat treatment in air enables the transformation of the doped Fe^{2+} in the PPy nanoleaves into FeO species. Indeed, the doping of the Fe element into the PPy regime through electrostatic interaction is analogous to the carbonization of iron ions adsorbed onto polyaniline nanosheet/graphene oxide hybrid material reported by Z.J. Fan et al. [29]

3.3.4 The Structural and Electrochemical Characterization of Representative MnO_2 , Fe_2O_3 and $\text{Fe}_2\text{O}_3@PPy$ Nanoflake Samples

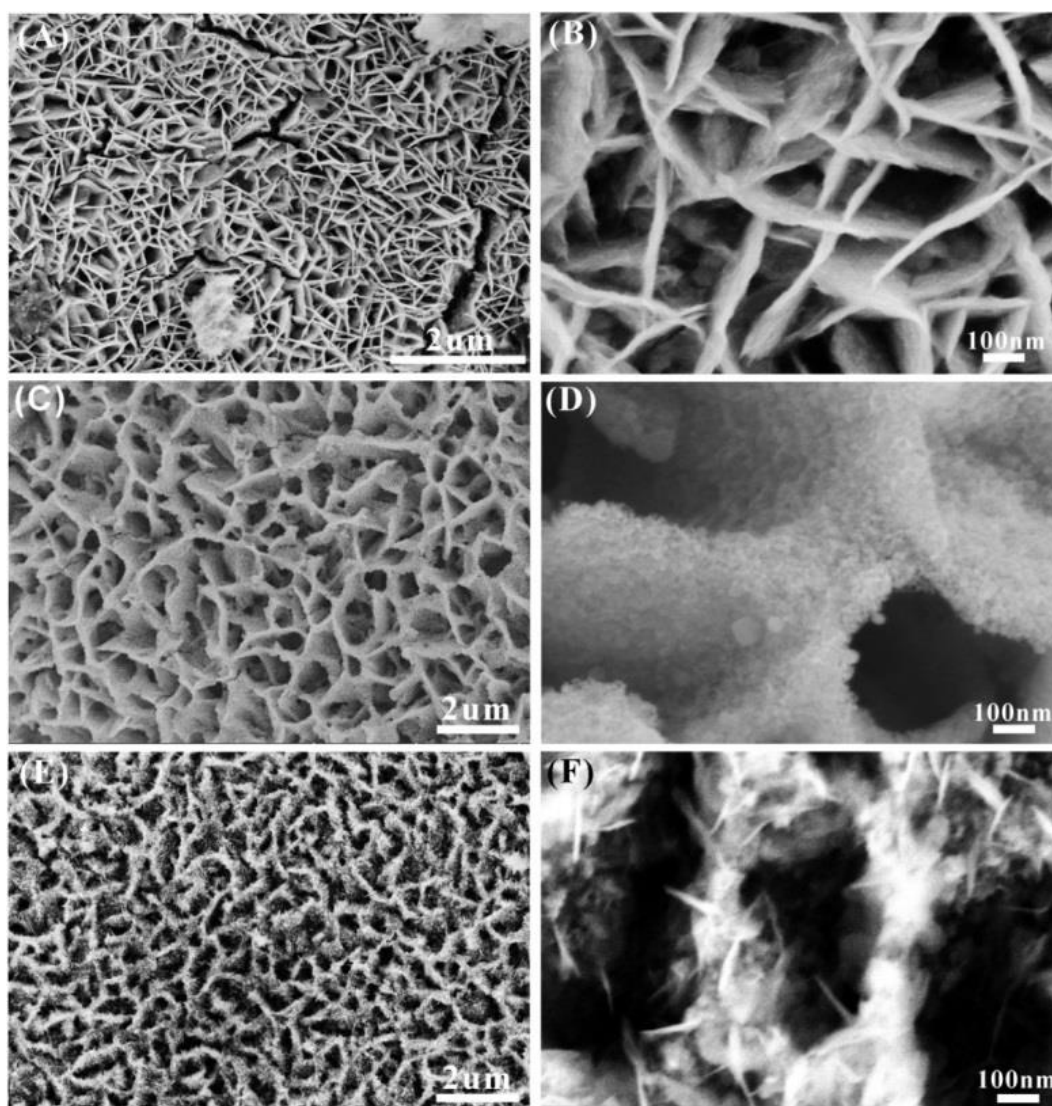


Figure 3.8 SEM images of MnO_2 nanosheets (A-B), honeycomb-like Fe_2O_3 nanoflakes (C-D) and $\text{Fe}_2\text{O}_3@PPy$ nanoflakes (E-F).

optimized honeycomb-like Fe₂O₃ nanoflakes@PPy nanoleaves (E-F).

As shown in **Figure 3.8A** and **B**, quasi-vertical MnO₂ nanosheets were first grown on NF through a hydrogen bubble dynamic template induced by an externally applied voltage of -1.6 V. [41-42] The obtained MnO₂ nanosheets worked as the sacrificed template for the subsequent growth of Fe₂O₃ species through hydrothermal methods. In **Figure 3.8C**, it is clear that the honeycomb-like Fe₂O₃ in the form of a seamless interconnected network comprised of ordered oriented nanoflakes almost replicated the morphology of MnO₂ nanosheets without collapsing and cracking. High magnification SEM in **Figure 3.8D** reveals that the Fe₂O₃ nanoflakes are composed of numerous nanoparticles. The EDS in **Figure 3.2** confirms that all MnO₂ species in the nanosheets have been converted to Fe₂O₃ species. Additionally, the honeycomb-like Fe₂O₃ nanoflakes at various reaction stages were presented in the **Figure 3.1** by setting the reaction time, demonstrating the importance of controlling the reaction time of the hydrothermal process. PPy species were successfully deposited onto the wall of the Fe₂O₃ nanoflakes by further electrochemical polymerization, as displayed in **Figure 3.8E**. The high magnification SEM image in **Figure 3.8F** confirms that the Fe₂O₃ nanoflakes were fully wrapped by PPy nanoleaves with a length of ca. 100 nm to form Fe₂O₃@PPy-0.3C core-branch arrays, which provides a large interfacial area for reaction, and numerous channels for a rapid diffusion of the electrolyte ions.

The nanosheet structure of the MnO₂ sample was further confirmed by TEM inspection as shown in **Figure 3.9A**. **Figure 3.9B** reveals that the interplanar spacing is ca. 0.235 nm, which is indexed to ε-MnO₂ (JCPDS NO.12-0141). [41-42] The resultant Fe₂O₃ nanoflakes (**Figure 3.9C**) is made of a large variety of small nanoparticles with diameter from 2 nm to 6 nm, and thus presents a mesoporous structure in the plane of α-Fe₂O₃ (JCPDS NO. 33-0664). [6, 44-45] Moreover, PPy nanoleaves strongly coupled with mesoporous Fe₂O₃ nanoflakes forming a homogenous structure, as proved by **Figure 3.9E**. Additionally, there are no exposed Fe₂O₃ nanoparticles, further demonstrating that the mesoporous Fe₂O₃ nanoflakes were well wrapped by the PPy nanoleaves (**Figure 3.9F**).

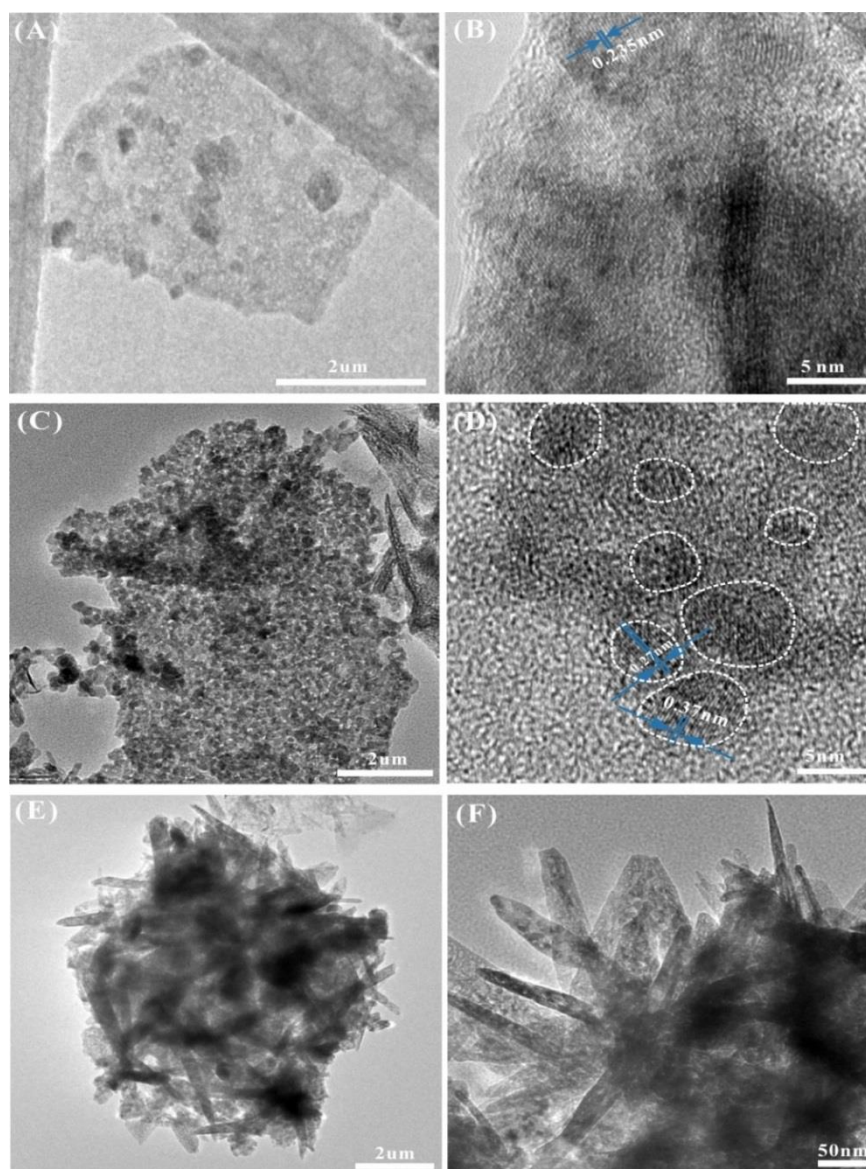


Figure 3.9 TEM images of MnO₂ nanosheets (A-B), honeycomb-like Fe₂O₃ nanoflakes (C-D) and optimized honeycomb-like Fe₂O₃ nanoflakes@PPy nanoleaves (E-F).

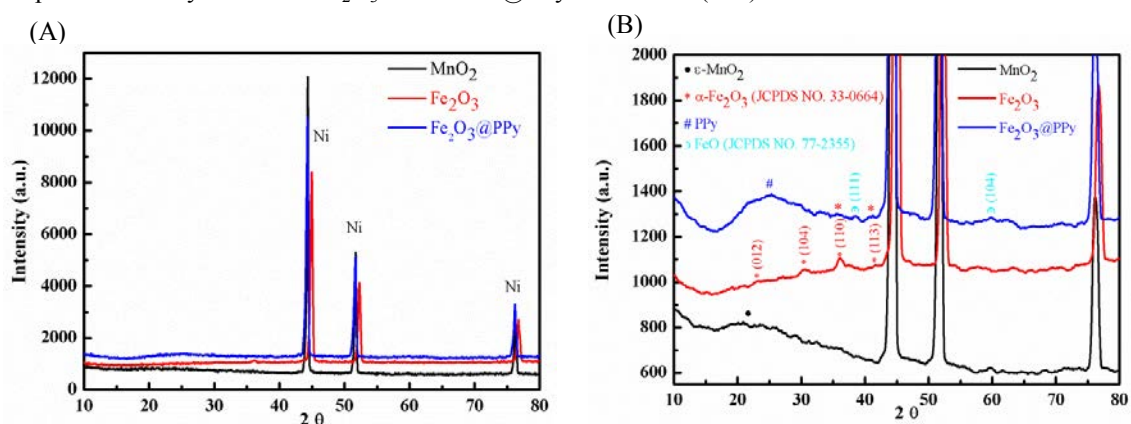


Figure 3.10 XRD patterns obtained on the MnO₂ nanosheets, Fe₂O₃ honeycomb-like and optimized core-branch Fe₂O₃@PPy-0.3C: (A) general view, (B) enlarged view of the smoothed XRD pattern.

The crystal structure of MnO₂, Fe₂O₃ and core-shell Fe₂O₃@PPy nanocomposite were monitored by XRD, as shown in **Figure 3.10**. Unfortunately, in **Figure 3.10A**, the structural information from the initial XRD pattern could not be obtained clearly because of the extremely tiny active material mass (mg scale) compared to the nickel foam substrate (g scale), in addition to the small particle size of Fe₂O₃ species, which led to a broadening effect on the diffraction peaks. Nevertheless, signals from the active materials could be observed in the enlarged view of the smoothed XRD pattern, but with much smaller peak intensities, as displayed in **Figure 3.10B**. There is a broad and weak peak around 23 degrees in the XRD pattern of MnO₂ sample, which is assigned to ε-MnO₂ (JCPDS NO.12-0141). Excluding the intense peaks of the substrate (Ni), the small diffraction peaks at 24.1°, 33.2°, 35.6°, 40.8° of Fe₂O₃ and Fe₂O₃@PPy-0.3C samples can be indexed to (012), (104), (110) and (113) planes of hematite (JCPDS NO. 33-0664). Compared to the Fe₂O₃ sample, a broad peak at 25° is observed for the Fe₂O₃@PPy sample, suggesting that the PPy was successfully incorporated into the Fe₂O₃ species; and the new emergent peaks confirm the presence of tiny FeO (JCPDS NO. 77-2355) species in the Fe₂O₃@PPy sample.

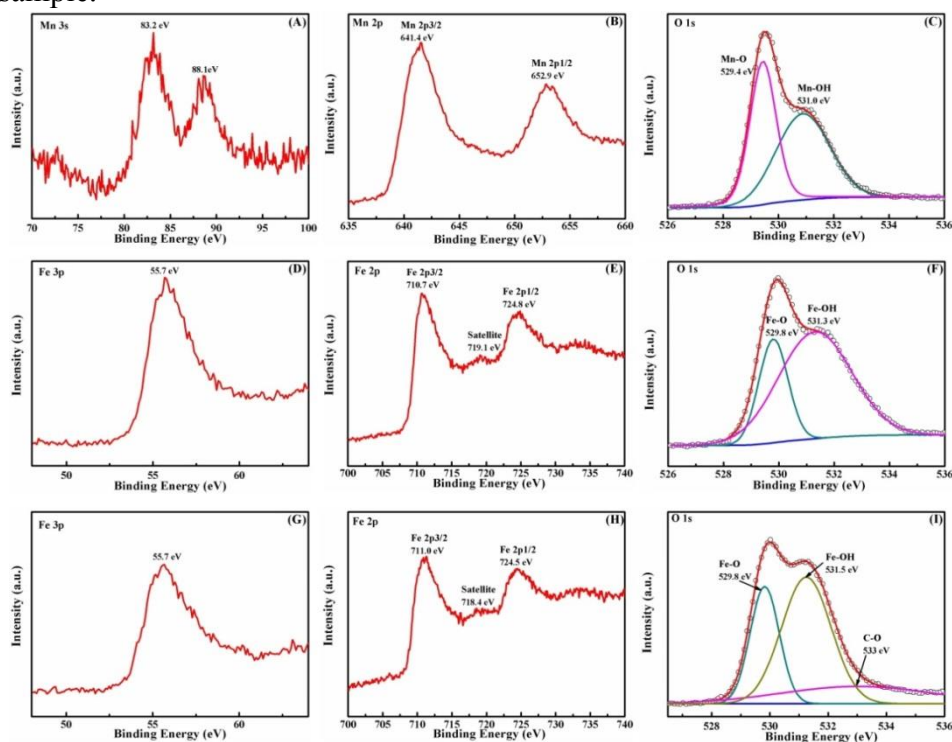


Figure 3.11 Core level Mn 3s, Mn 2p, and O 1s XPS spectra collected for the MnO₂ sample (A-C); Fe

3p, Fe 2p, and O 1s XPS spectra collected for Fe₂O₃ sample (D-F) and optimized Fe₂O₃@PPy sample (G-I).

The Mn oxidation state can be determined from the binding energy width (ΔE) between the separated Mn 3s peaks caused by multiplet splitting. By reference to the ΔE data of 5.79 eV, 5.50 eV, 5.41 eV and 4.78 eV obtained from pristine samples of MnO, Mn₃O₄, Mn₂O₃ and MnO₂, respectively, the binding energy ($\Delta E=4.9$ eV) shown in **Figure 3.11A** suggests that valence of Mn in our sample is +4. Mn 2p_{3/2} and Mn 2p_{1/2} peaks are located at 641.4 eV and 652.9 eV (**Figure 3.11B**), which are consistent with the reported values for MnO₂. The band at 529.4 eV and 531.0 eV in **Figure 3.11C** can be assigned to the oxygen bond of Mn-O and Mn-OH, respectively. In addition, for Fe₂O₃ and optimized Fe₂O₃@PPy samples, the Fe 3p peak position for Fe³⁺ was found to be 55.7 eV in **Figure 3.11D** and **G**. The Fe 2p_{3/2} and 2p_{1/2} peaks of both samples (**Figure 3.11E** and **F**) are centred at the binding energies of ~711.0 and ~724.5 eV, which are the typical peaks for Fe₂O₃ species. T. Yamashita et al. reported that the Fe oxidation state can be determined from the binding energy width (ΔE) between the Fe 2p_{3/2} peak and the corresponding satellite peak, and the ΔE data of genuine samples of Fe₃O₄, Fe₂O₃, FeSiO₄ and Fe_{0.94}O are N.A., 8.8 eV, 5.9eV and 6.0 eV, respectively. The satellite peaks for Fe 2p_{3/2} of Fe₂O₃ and Fe₂O₃@PPy samples were observed at 719.1 eV and 718.4 eV in **Figure 3.11E** and **H**; and the binding energy difference between the Fe 2p_{3/2} peak and the satellite peak are 8.4 eV and 7.4 eV, revealing that the deposition of PPy nanoleaves reduced part of Fe³⁺ of Fe₂O₃ species into Fe²⁺. Furthermore, the O 1s spectrum in **Figure 3.11F** and **I** can be disassembled into two peaks centred at 529.8 eV (Fe-O) and 531.3 eV (Fe-OH). Compared to the Fe₂O₃ sample, the small peak at 533 eV of the Fe₂O₃@PPy sample (**Figure 3.11I**) represents the C-O bonds from the PPy component.

In **Figure 3.12**, the MnO₂ nanosheets exhibit a typical peak at 638 cm⁻¹ while pristine Fe₂O₃ nanoflakes show characteristic Raman peaks at ~218, ~286, ~400, ~478, ~596, ~670 and ~1300 cm⁻¹. After PPy coating, these peaks decrease substantially in

intensity probably because of the shielding effect from the branch PPy species and some other new peaks appear at $\sim 1585\text{ cm}^{-1}$, $\sim 1414\text{ cm}^{-1}$, $\sim 1048\text{ cm}^{-1}$, $\sim 986\text{ cm}^{-1}$ observed for $\nu(\text{C}=\text{C})$, $\nu(\text{C}-\text{N})$, $\beta(\text{C}-\text{H})$ and $\nu(\text{ring})$ of PPy species, indicating the successful coating of PPy on the Fe_2O_3 nanoflakes. But the main peak of the FeO species located at 652 cm^{-1} is not observed in the Raman spectrum, which is probably ascribed to the intrinsic tiny content as well as the shielding effect from the branch PPy species. In concordance with analysis of elemental relative composition of the well-retained $\text{Fe}_2\text{O}_3@PPy$ core-branch region, the XRD (**Figure 3.10**), XPS (**Figure 3.11**) and Raman Spectra (**Figure 3.12**) of flaking debris unambiguously conclude the formation of a core-branch structure.

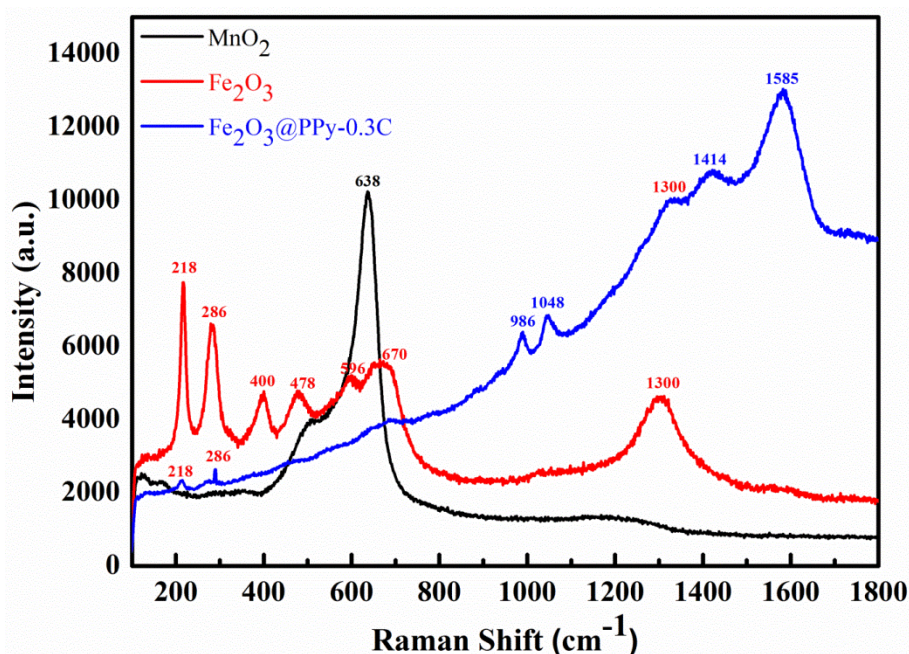


Figure 3.12 Raman spectra obtained on the MnO_2 nanosheets, Fe_2O_3 and optimized core-branch $\text{Fe}_2\text{O}_3@PPy-0.3C$ nanoflakes.

Since the electrochemical properties of optimized core-branch $\text{Fe}_2\text{O}_3@PPy$ samples as a negative electrode were investigated and displayed in **Figure 3.4**, the electrochemical properties of the MnO_2 positive electrodes 0.5 M Na_2SO_4 aqueous solution were further investigated by CV, GCD and EIS, as displayed in **Figure 3.13A-D**. The mass ratio of negative electrode to positive electrode was calculated based on charge balance theory according to the electrochemical data shown in **Figure 3.13E**.

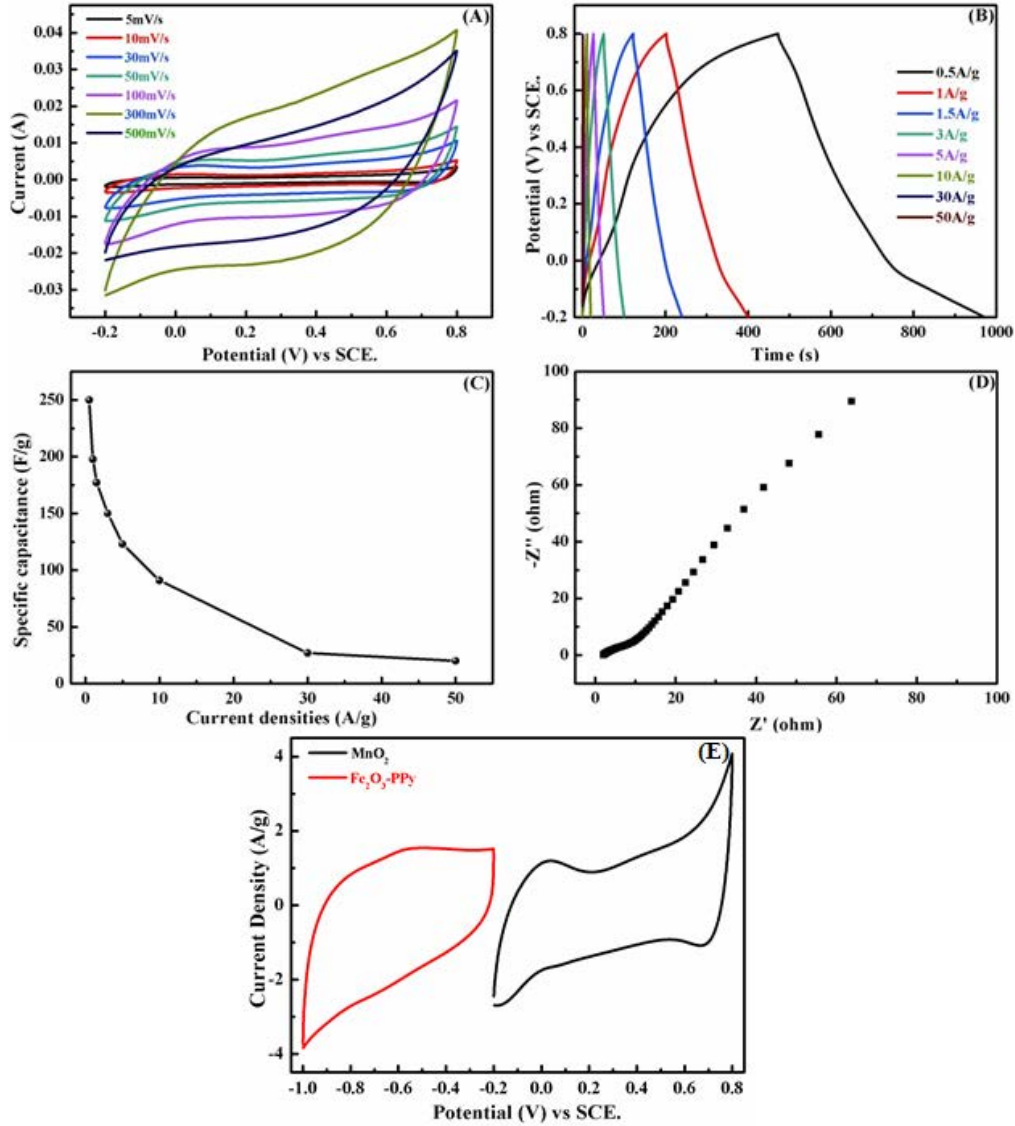


Figure 3.13 The electrochemical properties of MnO₂ nanosheets: (A) CV curves at different scan rates, (B) galvanostatic charge-discharge at different current densities, (C) the relationship between specific capacitance and current density and (D) the Nyquist diagrams. (E) The CV curves at 10 mV s⁻¹ of MnO₂ nanosheets and core-branch Fe₂O₃@PPy.

According to **Figure 3.13E** and the equation:

$$C_{\text{sp}} = \frac{Q}{\Delta V \times m} \quad (13)$$

where C_{sp} (F g⁻¹) is the specific capacitance, Q (C) is the average charge during the charging and discharging process, ΔV (V) is the potential window, and m (g) is mass of active materials, the specific capacitance of MnO₂ nanosheets and core-branch

$\text{Fe}_2\text{O}_3@\text{PPy}$ at 10mV s^{-1} can be calculated as 256.7 F g^{-1} and 296.7 F g^{-1} , respectively.

For an ASC, the charge balance should follow the relationship $q^+=q^-$, where q^+ means that the charges were stored at the positive electrode while q^- means that the charges were stored at the negative electrode. The stored charges are related to the specific capacitance (C_{sp}), the potential window of the charge/discharge process (ΔV), and the mass of the electrode (m) as reported by

$$q = C_{\text{sp}} \times \Delta V \times m \quad (14)$$

In order to get $q^+=q^-$, the mass balancing follows the equation:

$$\frac{m_-}{m_+} = \frac{C_{\text{sp}+} \times \Delta V_+}{C_{\text{sp}-} \times \Delta V_-} \quad (15)$$

On the basis of the specific capacitance values and potential windows of these positive and negative electrodes, in this ASC system, the theoretical mass ratio between negative/positive electrodes should be $m_-/m_+=1.08$.

3.3.5 The Electrochemical Properties of Fabricated ASCs

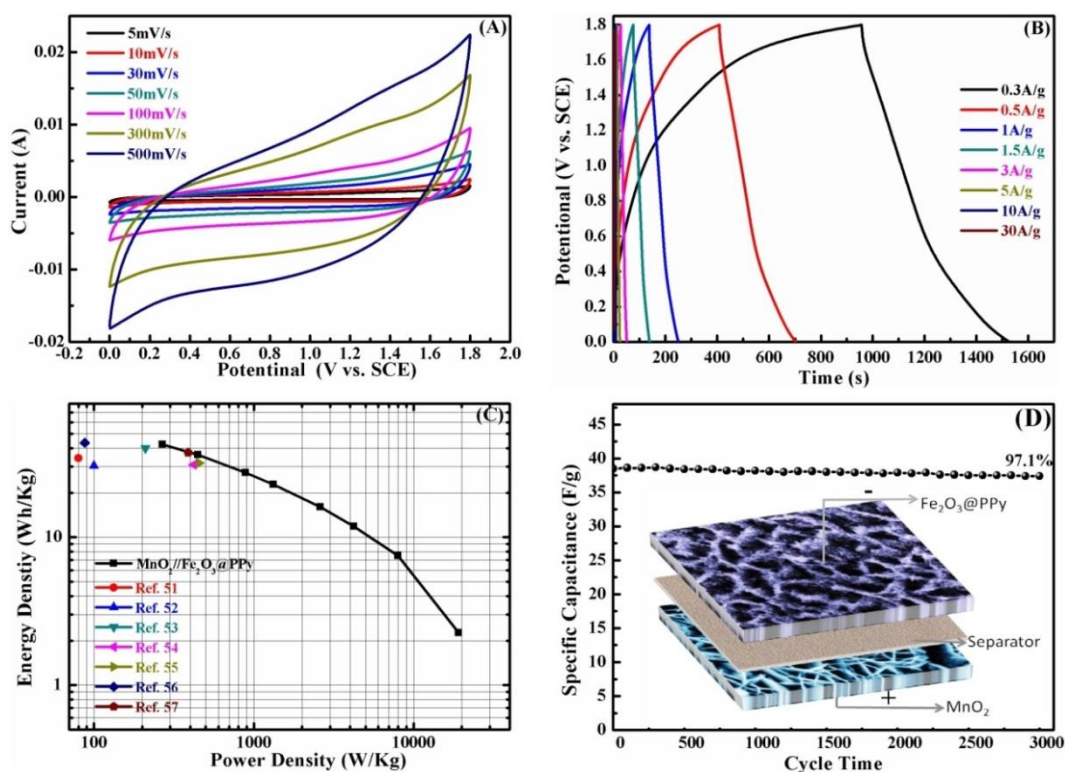


Figure 3.14 Electrochemical properties of bi-metal oxide ASC: (A) CV curves at different scan rates,

(B) the GCD curves at different current densities, (C) the Ragone plot, (D) the life cycle stability at a current density of 3 A g^{-1} (the schematic of the ASC device shown in the inset).

To further testify the potential applications for energy storage devices, a bi-metal oxide ASC device was assembled (as shown in the inset of **Figure 3.14D**) based on the electrochemical results of **Figure 3.13** with MnO_2 nanosheets and the core-branch $\text{Fe}_2\text{O}_3@\text{PPy}-0.3\text{C}$ electrodes as the positive electrode and negative electrode, respectively. The as-prepared bi-metal oxide ASC exhibits an ideal capacitive behaviour with approximately rectangular CV curves from 5 to 500 mV s^{-1} (**Figure 3.14A**) within a potential window of 1.8 V, indicating its excellent power characteristics. [46] Furthermore, the GCD curves of the supercapacitor device at various current densities illustrated in **Figure 3.14B** maintain good symmetry even at a high current density of 30 A g^{-1} , demonstrating its good rate capability.

The corresponding calculated Ragone plot in **Figure 3.14C** reveals that the bi-metal oxide ASC delivers an energy density as high as 42.4 Wh kg^{-1} at a power density of 268.8 W kg^{-1} and maintains 2.3 Wh kg^{-1} at an extremely high power density of 19140 W kg^{-1} , which exhibits superior performance over the $\text{Co}_3\text{O}_4/\text{PPy}/\text{MnO}_2//\text{AC}$ (34.3 Wh kg^{-1} at 80.0 W kg^{-1}) [51] and the MnO_2 nanowire/ graphene//graphene (30.4 Wh kg^{-1} at 100 W kg^{-1}), [52] reported elsewhere. The performance is also superior to graphitic hollow carbon spheres/ MnO_2 //graphitic hollow carbon spheres (40.0 Wh kg^{-1} at 210 W kg^{-1}), [53] $\text{Ni}(\text{OH})_2$ /graphene//reduced Hummers' graphene oxide (31 Wh kg^{-1} at 420 W kg^{-1}), [54] MnO_2 -graphene foam// CNT-graphene (31.8 Wh kg^{-1} at 453.6 W kg^{-1}) [55] and $\text{CoO}/\text{PPy}/\text{AC}$ (43.5 Wh kg^{-1} at 87.5 W kg^{-1}) [56] with graphene or AC as negative electrodes and is even higher than $\text{MnO}_2//\gamma\text{-FeOOH}$ bi-metal oxides ASC (37.4 Wh kg^{-1} at 388.5 W kg^{-1}). [57] Furthermore, the supercapacitor possesses long-term stability over 3000 cycles at a current density of 3 A g^{-1} as shown in **Figure 3.14D**. The specific capacitance of the device retains 37.4 F g^{-1} after 3000 cycles, corresponding to 97.1% of its initial specific capacitance (38.1 F g^{-1}), higher than MnO_2 nanowire/graphene// graphene (79% after 1000 cycles), [52] and iron/graphene sheets// $\text{Ni}(\text{OH})_2$ /CNTs (78% after 2000 cycles). [29]

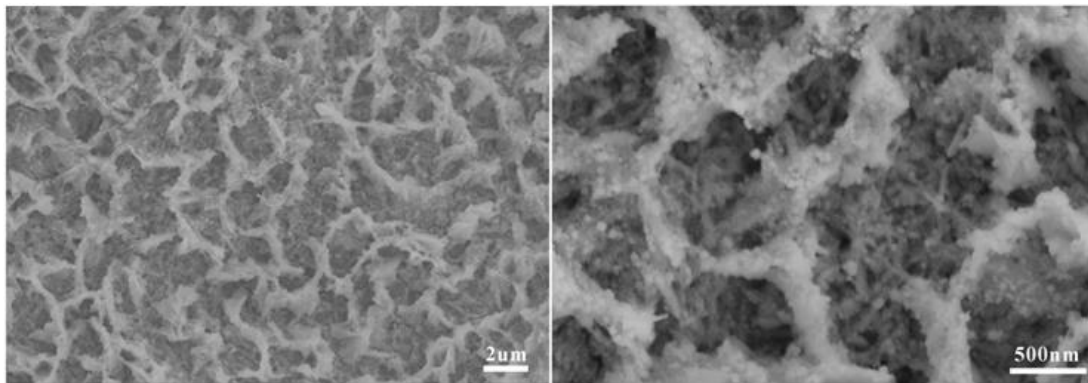
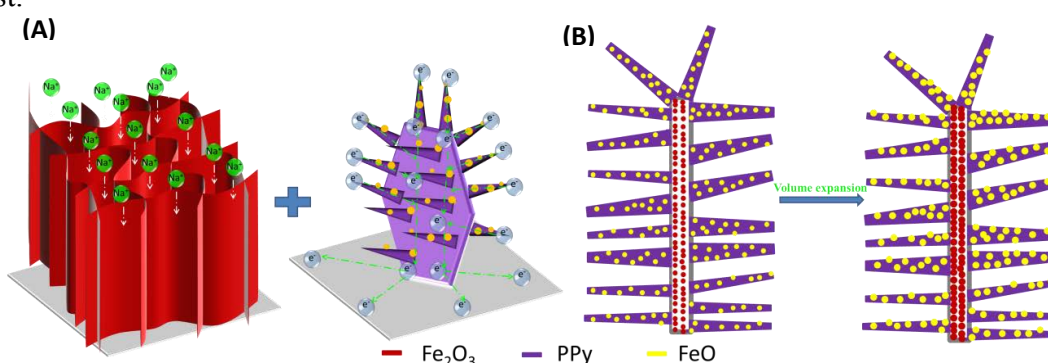


Figure 3.15 SEM images of optimized core-branch honeycomb-like Fe_2O_3 nanoflake@PPy nanoleaves electrode after 3000 times charge and discharge.

In order to validate this result, we further performed SEM analysis of the core-branch Fe_2O_3 @PPy-0.3C after 3000 cycles (**Figure 3.15**). It is clear that core-branch Fe_2O_3 @PPy-0.3C still retains a honeycomb-like structure with randomly distributed PPy nanoleaves on the wall, revealing that the protective PPy shell could tolerate the volume expansion and contraction of the Fe_2O_3 backbone during the cycle test.



Schematic 3.3 Schematic representation of the electrolyte ion and electron transportation path (A) and volume change (B) during cycle.

The overall performances of the assembled supercapacitor using 3D core-branch Fe_2O_3 @PPy-0.3C as a negative electrode is superior to those with 0D (nanoparticles), 1D (nanotubes or nanorods), 2D (nanosheets), nanocomposites or core-shell structures as shown in **Table 3.1**. The better performance could be attributed to the following structure merits: (i) the formation of honeycomb-like Fe_2O_3 backbone provides a large contact area between the active material and the electrolyte (as shown on the left part of **Schematic 3.3A**), resulting in a more efficient transportation of the electrolyte ions

and a great increase in material utilization efficiency; (ii) the wrapped PPy branch has superior electrical conductivity compared to Fe₂O₃ species, which could work as “superhighways”, as illustrated in the right part of **the Schematic 3.3A**. This core-branch structure leads to the fact that electrons can transport more efficiently during charge-discharge processes, resulting in a large improvement in specific capacitance; (iii) the excellent cycling stability of the obtained supercapacitor device using core-branch Fe₂O₃@PPy as a negative electrode material could be due to the strong synergistic effect of honeycomb-like mesoporous Fe₂O₃ nanoflakes and PPy nanoleaves. Specifically, the mesoporous feature of honeycomb-like Fe₂O₃ nanoflakes [36] and the protective function of branched PPy nanoleaves prevent drastic volume variation of Fe₂O₃ and FeO nanoparticles during the electrolyte ions insertion/extraction process, [16, 37-38] which together improve the life cycle, as displayed in **Schematic 3.3B**.

Table 3.1 the electrochemical performance comparison of iron oxides/hydroxides based electrodes.

Reference no.	Current density or scan rate	Specific capacitance	Material structure	Cycle Life
[6]	100 mV/s	163.6 mF/cm ²	Ti-Doped Fe ₂ O ₃ @PEDOT nanorods	96.1% (30 000 cycles)
[58]	1.4 A/g	257.8 F/g	amorphous Fe ₂ O ₃ nanotubes	84% (5000 cycles)
[57]	0.13 A/g	310.3 F/g	γ-FeOOH nanosheet	-
[59]	0.5 A/g	116 F/g	nanosized β-FeOOH	85% (2000 cycles)
[60]	0.4 A/g	207.7 F/g	Fe ₃ O ₄ nanoparticles	100% (2000 cycles)
[61]	1A/g	368 F/g	Fe ₃ O ₄ nanoparticles/graphene	109% (1000 cycles)
[62]	0.5A/g	235 F/g	mesoporous carbon/iron oxide	95 % (380 cycles)
[63]	1A/g	226 F/g	Fe ₂ O ₃ /graphene	-
[64]	0.5A/g	618 F/g	Fe ₂ O ₃ /N-rGO hydrogel	56.7% (5000 cycles)
[9]	10 mV/s	64.5 F/g	oxygen-deficient hematite nanorods	95% (10 000 cycles)
[29]	2 mV/s	717F/g	graphene-supported iron nanosheets	78% (2000 cycles)
[28]	5 mA/cm ²	659.5 mF/cm ²	graphite foam/carbon nanotube/Fe ₂ O ₃	95.4 (5000 cycles)
[65]	1 mV/s	638 F/g	graphene/Fe ₂ O ₃ /polyaniline	92% (5000 cycles)
[66]	2 mA/cm ²	504 F/g	Fe ₂ O ₃ nanorods/graphene	-
[31]	0.5A/g	235F/g	mesoporous Carbon/Fe ₂ O ₃ nanoparticle	95% (380 cycles)
This work [67]	1A/g	1167.8 F/g	core-branch Fe₂O₃@PPy	97.1% (3000 cycles)

3.4 Summary

The rational assembly of unique branched heterostructures is one of the facile nanoengineering techniques to improve the electrochemical figure of merit of materials. By taking advantage of hydrogen bubble dynamic templates, hydrothermal methods and electrochemical polymerization, branched polypyrrole (PPy) nanoleaves decorated honeycomb-like hematite nanoflakes (core-branch $\text{Fe}_2\text{O}_3@\text{PPy}$) were fabricated. XRD, XPS, SEM, TEM and STEM in high angle annular dark field mode together with EELS were combined to elucidate the mechanisms underlying the formation and the morphogenetic evolution of core-branch $\text{Fe}_2\text{O}_3@\text{PPy}$ heterostructures. Benefiting from the stability of honeycomb-like hematite nanoflakes and the high conductivity of PPy nanoleaves, the resultant core-branch $\text{Fe}_2\text{O}_3@\text{PPy}$ exhibited an ultrahigh capacitance of 1159 F g^{-1} at 1 A g^{-1} in $0.5 \text{ M Na}_2\text{SO}_4$ aqueous solution. Moreover, the assembled bi-metal oxide asymmetric supercapacitor ($\text{Fe}_2\text{O}_3@\text{PPy}//\text{MnO}_2$) gave rise to a maximum energy density of 42.8 Wh kg^{-1} and a maximum power density of 27 kW kg^{-1} with an excellent cycling performance of 97.1% retention after 3000 cycles at 3 A g^{-1} . These performance features are superior to the previously reported iron oxide/hydroxide-based supercapacitors, offering an important guideline for the future design of advanced next-generation supercapacitors.

References

- [1] P. Simon, Y. Gogotsi, Materials for electrochemical capacitors, *Nat. Mater.* **2008**, 7, 845-854.
- [2] G. P. Wang, L. Zhang, J.J. Zhang, A review of electrode materials for electrochemical supercapacitors, *Chem. Soc. Rev.* **2012**, 41, 797-828.
- [3] Y.W. Zhu, S. Murali, M.D. Stoller, K.J. Ganesh, W.W. Cai, P.J. Ferreira, A. Pirkle, R.M. Wallace, K.A. Cychosz, M. Thommes, D. Su, E.A. Stach, R.S. Ruoff, Carbon-based supercapacitors produced by activation of graphene, *Science*, **2011**, 332, 1537-1541.
- [4] A. Chu, P. Braatz, Comparison of commercial supercapacitors and high-power lithium-ion batteries for power-assist applications in hybrid electric vehicles: I. Initial characterization, *J. Power Sources*, **2002**, 112, 236-246.
- [5] J. Jiang, Y. Y. Li, J. P. Liu, X. T. Huang, C.Z. Yuan, X. W. D. Lou, Recent advances in metal oxide-based electrode architecture design for electrochemical energy storage, *Adv. Mater.*, **2012**, 24, 5166-5180.
- [6] Y. X. Zeng, Y. Han, Y. T. Zhao, Y. Zeng, M. H. Yu, Y.J. Liu, H.L. Tang, Y. X. Tong, X. H. Lu, Advanced Ti-doped Fe₂O₃@PEDOT core/shell anode for high-energy asymmetric supercapacitor, *Adv. Energy Mater.*, **2015**, 5, 1402176.
- [7] L.Y. Yuan, X.H. Lu, X. Xiao, T. Zhai, J.J. Dai, F.C. Zhang, B. Hu, X. Wang, L. Gong, J. Chen, C.G. Hu, Y.X. Tong, J. Zhou, Z.L. Wang, Flexible solid-state supercapacitors based on carbon nanoparticles/MnO₂ nanorods hybrid structure, *ACS Nano*, **2011**, 6, 656-661.
- [8] K. Jost, D.P. Durkin, L.M. Haverhals, E.K. Brown, M. Langenstein, H.C.D. Long, P. C. Trulove, Y. Gogotsi, G. Dion, Natural fiber welded electrode yarns for knittable textile supercapacitors, *Adv. Energy Mater.* **2015**, 5, 1401286.
- [9] X. H. Lu, Y. X. Zeng, M. H. Yu, T. Zhai, C. L. Liang, S. L. Xie, M. S. Balogun, Y. X. Tong, Oxygen-deficient hematite nanorods as high-performance and novel negative electrodes for flexible asymmetric supercapacitors, *Adv. Mater.*, **2014**, 26, 3148-3155.
- [10] Z. Y. Jin, A. H. Lu, Y. Y. Xu, J. T. Zhang, W. C. Li, Ionic liquid-assisted synthesis of microporous carbon nanosheets for use in high rate and long cycle life supercapacitors, *Adv. Mater.*, **2014**, 26, 2700-3705.
- [11] J. Gamby, P. Taberna, P. Simon, J. Fauvarque, M. Chesneau, Studies and characterisations of various activated carbons used for carbon/carbon supercapacitors, *J. Power Sources*, **2001**, 101, 109-116.
- [12] S. Park, M. Vosguerichian, Z.N. Bao, A review of fabrication and applications of carbon nanotube film-based flexible electronics, *Nanoscale*, **2013**, 5, 1727-1752.
- [13] M.F. El-Kady, V. Strong, S. Dubin, R.B. Kaner, Laser scribing of high-performance and flexible graphene-based electrochemical capacitors, *Science*, **2012**, 335, 1326-1330.
- [14] F. Bonaccorso, L. Colombo, G.H. Yu, M. Stoller, V. Tozzini, A.C. Ferrari, R.S. Ruoff, V. Pellegrini, Graphene, related two-dimensional crystals, and hybrid systems for energy conversion and storage, *Science*, **2015**, 347, 6217.

- [15] Z. Tang, C.H. Tang, H. Gong, A High energy density asymmetric supercapacitor from nano-architected Ni (OH)₂/carbon nanotube electrodes, *Adv. Funct. Mater.*, **2012**, 22, 1272-1278.
- [16] M.F. Shao, Z.H. Li, R.K. Zhang, F.Y. Ning, M. Wei, D.G. Evans, X. Duan, Hierarchical conducting polymer@clay core-shell arrays for flexible all-solid-state supercapacitor devices, *Small*, **2015**, 11, 3530-3538.
- [17] X.H. Lu, M.H. Yu, G.M. Wang, Y.X. Tong, Y. Li, Flexible solid-state supercapacitors: design, fabrication and applications, *Energy Environ. Sci.*, **2014**, 7, 2160-2181.
- [18] Z. Chen, Y.C. Qin, D. Weng, Q.F. Xiao, Y.T. Peng, X.L. Wang, H.X. Li, F. Wei, Y.F. Lu, Design and synthesis of hierarchical nanowire composites for electrochemical energy storage, *Adv. Funct. Mater.*, **2009**, 19, 3420-3426.
- [19] T. Zhai, X.H. Lu, H.Y. Wang, G.M. Wang, T. Mathis, T.Y. Liu, C. Li, Y.X. Tong, Y. Li, An electrochemical capacitor with applicable energy density of 7.4 Wh/kg at average power density of 3000 W/kg, *Nano Lett.*, **2015**, 15, 3189-3194.
- [20] P.C. Chen, G.Z. Shen, Y. Shi, H.T. Chen, C.W. Zhou, Preparation and characterization of flexible asymmetric supercapacitors based on transition-metal-oxide nanowire/single-walled carbon nanotube hybrid thin-film electrodes, *ACS Nano*, **2010**, 4, 4403-4411.
- [21] J. Chang, M.H. Jin, F. Yao, T.H. Kim, V.T. Le, H.Y. Yue, F. Gunes, B. Li, A. Ghosh, S.S. Xie, Y.H. Lee, Asymmetric supercapacitors based on graphene/MnO₂ nanospheres and graphene/MoO₃ nanosheets with high energy density, *Adv. Funct. Mater.*, **2013**, 23, 5074-5083.
- [22] J. Xu, Q.F. Wang, X.W. Wang, Q.Y. Xiang, B. Liang, D. Chen, G.Z. Shen, Flexible asymmetric supercapacitors based upon Co₉S₈ nanorod//Co₃O₄@RuO₂ nanosheet arrays on carbon cloth, *ACS Nano*, **2013**, 7, 5453-5462.
- [23] Q.T. Qu, S.B. Yang, X.L. Feng, 2D sandwich-like sheets of iron oxide grown on graphene as high energy anode material for supercapacitors, *Adv. Mater.*, **2011**, 23, 5574-5580.
- [24] X. Chen, K.F. Chen, H. Wang, D.F. Xue, Composition design upon iron element toward supercapacitor electrode materials, *Mater. Focus*, **2015**, 4, 78-80.
- [25] S. Shivakumara, T.R. Penki, N. Munichandraiah, Synthesis and characterization of porous flowerlike α -Fe₂O₃ nanostructures for supercapacitor application, *ECS Electrochem. Lett.*, **2013**, 2, 60-62.
- [26] F. Meng, S.A. Morin, J. Song, Rational solution growth of α -FeOOH nanowires driven by screw dislocations and their conversion to α -Fe₂O₃ nanowires, *J. Am. Chem. Soc.*, **2011**, 133, 8408-8411.
- [27] L.F. Chen, Z.Y. Yu, X. Ma, Z.Y. Li, S.H. Yu, In situ hydrothermal growth of ferric oxides on carbon cloth for low-cost and scalable high-energy-density supercapacitors, *Nano Energy*, **2014**, 9, 345-354.
- [28] C. Guan, J.L. Liu, Y.D. Wang, L. Mao, Z.X. Fan, Z.X. Shen, H. Zhang, J. Wang, Iron oxide-decorated carbon for supercapacitor anodes with ultrahigh energy density and outstanding cycling stability, *ACS Nano*, **2015**, 9, 5198-5207.
- [29] C.L. Long, T. Wei, J. Yan, L.L. Jiang, Z.J. Fan, Supercapacitors based on graphene-supported

iron nanosheets as negative electrode materials, *ACS Nano*, **2013**, 7, 11325-11332.

[30] H.T. Sharifi, E. Gracia-Espino, H.R. Barzegar, X.E. Jia, F. Nitze, G.Z. Hu, P. Nordblad, C.W. Tai, T. Wagberg, Formation of nitrogen-doped graphene nanoscrolls by adsorption of magnetic γ -Fe₂O₃ nanoparticles, *Nat. Commun.*, **2013**, 4, 2319.

[31] H.W. Wang, Z.J. Xu, H. Yi, H.G. Wei, Z.H. Guo, X.F. Wang, One-step preparation of single-crystalline Fe₂O₃ particles/graphene composite hydrogels as high performance anode materials for supercapacitors, *Nano Energy*, **2014**, 7, 86-96.

[32] C.W. Cheng, H.J. Fan, Branched nanowires: synthesis and energy applications, *Nano Today*, **2012**, 327-343.

[33] W.W. Zhou, C.W. Cheng, J.P. Liu, Y.Y. Tay, J. Jiang, X.T. Jia, J.X. Zhang, H. Gong, H.H. Hng, T. Yu, H.J. Fan, Epitaxial growth of branched α -Fe₂O₃/SnO₂ nano-heterostructures with improved lithium-ion battery performance, *Adv. Funct. Mater.*, **2011**, 21, 2439-2445.

[34] R.R. Zamani, M. Ibáñez, M. Luysberg, N.G. Castelló, L. Houben, J.D. Prades, V. Grillo, R. E. Dunin-Borkowski, J.R. Morante, A. Cabot, J. Arbiol, Polarity-driven polytypic branching in Cu-based quaternary chalcogenide nanostructures, *ACS Nano*, **2014**, 8, 2290-2301.

[35] H.B. Li, A.G. Kanras, L. Manna, Colloidal branched semiconductor nanocrystals: state of the art and perspectives, *Acc. Chem. Res.*, **2013**, 46, 1387-1396.

[36] X.Z. Yu, B.A. Lu, Z. Xu, Super long-life supercapacitors based on the construction of nanohoneycomb-like strongly coupled CoMoO₄-3D graphene hybrid electrodes, *Adv. Mater.*, **2014**, 26, 1044-1051.

[37] K. Liang, T.L. Gu, Z.Y. Cao, X.Z. Tang, W. C. Hu, B.Q. Wei, In situ synthesis of SWNTs@MnO₂/polypyrrole hybrid film as binder-free supercapacitor electrode, *Nano Energy*, **2014**, 9, 245-251.

[38] H.J. Tang, J.Y. Wang, H.J. Yin, H.J. Zhao, D. Wang, Z.Y. Tang, Growth of polypyrrole ultrathin films on MoS₂ monolayers as high-performance supercapacitor electrodes, *Adv. Mater.*, **2015**, 27, 1117-1123.

[39] A. Fakhry, F. Pillier, C. Debiecme-Chouvy, Templateless electrogeneration of polypyrrole nanostructures: impact of the anionic composition and pH of the monomer solution, *J. Mater. Chem. A*, **2014**, 2, 9859-9865.

[40] A. Fakhry, H. Cachet, C. Debiecme-Chouvy, Mechanism of formation of templateless electro-generated polypyrrole nanostructures, *Electrochimica Acta*, **2015**, 179, 297-303.

[41] D.W. Liu, Q.F. Zhang, P. Xiao, B.B. Garcia, Q. Guo, R. Champion, G.Z. Cao, Hydrrous manganese dioxide nanowall arrays growth and their Li⁺ ions intercalation electrochemical properties, *Chem. Mater.*, **2008**, 20, 1376-1380.

[42] D. W. Liu, B.B. Garcia, Q.F. Zhang, Q. Guo, Y.H. Zhang, S. Sepehri, G.Z. Cao, Mesoporous hydrrous manganese dioxide nanowall arrays with large lithium ion energy storage capacities, *Adv. Funct. Mater.*, **2009**, 19, 1015-1023.

[43] G.X. Gao, L. Yu, H.B. Wu, X.W. Lou, Hierarchical tubular structures constructed by carbon-coated α -Fe₂O₃ nanorods for highly reversible lithium storage, *Small*, **2014**, 10, 1741-1745.

- [44] C. D. Chouvy, Template-free one-step electrochemical formation of polypyrrole nanowire array, *Electrochem. Commun.*, **2009**, 11, 298-301.
- [45] M.V. Reddy, T. Yu, C.H. Sow, Z.X. Shen, C.T. Lim, G.V.S. Rao, B.V. R. Chowdari, α -Fe₂O₃ nanoflakes as an anode material for Li-ion batteries, *Adv. Funct. Mater.*, **2007**, 17, 2792-2799.
- [46] X.H. Xia, D.L. Chao, X.Y. Qi, Q.Q. Xiong, Y.Q. Zhang, J.P. Tu, H. Zhang, H.J. Fan, Controllable growth of conducting polymers shell for constructing high-quality organic/inorganic core/shell nanostructures and their optical-electrochemical properties, *Nano Lett.*, **2013**, 13, 4562-4568.
- [47] Q. Li, Z.L. Wang, G.R. Li, R. Guo, L.X. Ding, Y.X. Tong, Design and synthesis of MnO₂/Mn/MnO₂ sandwich-structured nanotube arrays with high supercapacitive performance for electrochemical energy storage, *Nano Lett.*, **2012**, 12, 3803-3807.
- [48] X. Yang, J. Zhu, L. Qiu, D. Li, Bioinspired effective prevention of restacking in multilayered graphene films: towards the next generation of high-performance supercapacitors, *Adv. Mater.*, **2011**, 23, 2833-2838.
- [49] X. Zhang, W. Shi, J. Zhu, D.J. Kharistal, W. Zhao, B.S. Lalia, H.H. Hng, Q. Yan, High-power and high-energy-density flexible pseudocapacitor electrodes made from porous CuO nanobelts and single-walled carbon nanotubes, *ACS Nano*, **2011**, 5, 2013-2019.
- [50] J.B. Han, Y.B. Dou, J.W. Zhao, M. Wei, D.G. Evans, X. Duan, Flexible CoAl LDH@ PEDOT core/shell nanoplatelet array for high-performance energy storage, *Small*, **2012**, 9, 98-106.
- [51] L.J. Han, P.Y. Tang, L. Zhang, Hierarchical Co₃O₄@ PPy@MnO₂ core-shell-shell nanowire arrays for enhanced electrochemical energy storage, *Nano Energy*, **2014**, 7, 42-51.
- [52] Z.S. Wu, W. Ren, D.W. Wang, F. Li, B. Liu, H.M. Cheng, High-energy MnO₂ nanowire/graphene and graphene asymmetric electrochemical capacitors, *ACS Nano*, **2010**, 4, 5835-5842.
- [53] Z. Chen, V. Augustyn, J. Wen, Y.W. Zhang, M.Q. Shen, B. Dunn, Y.F. Lu, High-performance supercapacitors based on intertwined CNT/V₂O₅ nanowire nanocomposites, *Adv. Mater.*, **2011**, 23, 791-795.
- [54] H. L. Wang, Y. Y. Liang, T. Mirfakhrai, Z. Chen, H. S. Casalongue, H. J. Dai, Advanced asymmetrical supercapacitors based on graphene hybrid materials, *Nano Res.*, **2011**, 4, 729-736.
- [55] Z.Y. Zhang, F. Xiao, L.H. Qian, J.W. Xiao, S. Wang, Y.Q. Liu, Facile Synthesis of 3D MnO₂-graphene and carbon nanotube-graphene composite networks for high-performance, flexible, all-solid-state asymmetric supercapacitors, *Adv. Energy Mater.*, **2014**, 4, 1400064.
- [56] C. Zhou, Y.W. Zhang, Y.Y. Li, J.P. Liu, Construction of high-capacitance 3D CoO@ polypyrrole nanowire array electrode for aqueous asymmetric supercapacitor, *Nano Lett.*, **2013**, 13, 2078-2085.
- [57] Y.C. Chen, Y.G. Lin, Y.K. Hsu, S.C.K. Yen, H. Chen, L.C. Chen, Novel iron oxyhydroxide lepidocrocite nanosheet as ultrahigh power density anode material for asymmetric supercapacitors, *Small*, **2014**, 10, 3803-3810.
- [58] P. H. Yang, Y. Ding, Z.Y. Lin, Z.W. Chen, Y. Z. Li, P.F. Qiang, M. Ebrahimi, W.J. Mai, C.P. Wong, Z.L. Wang, Low-cost high-performance solid-state asymmetric supercapacitors based on MnO₂ nanowires and Fe₂O₃ nanotubes, *Nano Lett.*, **2014**, 14, 731-736.

- [59] W.H. Jin, G.T. Cao, J.Y. Sun, Hybrid supercapacitor based on MnO₂ and columned FeOOH using Li₂SO₄ electrolyte solution, *J. Power Sources*, **2008**, 175, 686-691.
- [60] L. Wang, H.M. Ji, S.S. Wang, L.J. Kong, X.F. Jiang, G. Yang, Preparation of Fe₃O₄ with high specific surface area and improved capacitance as a supercapacitor, *Nanoscale*, **2013**, 5, 3793-3799.
- [61] M.M. Liu, J. Sun, In situ growth of monodisperse Fe₃O₄ nanoparticles on graphene as flexible paper for supercapacitor, *J. Mater. Chem. A*, **2014**, 2, 12068-12074.
- [62] Y. Lin, X. Y. Wang, G. Qian, J. J. Watkins, Additive-driven self-assembly of well-ordered mesoporous carbon/iron oxide nanoparticle composites for supercapacitors, *Chem. Mater.*, **2014**, 26, 2128-2137.
- [63] Z. Wang, C.Y. Ma, H.L. Wang, Z.H. Liu, Z.P. Hao, Facilely synthesized Fe₂O₃-graphene nanocomposite as novel electrode materials for supercapacitors with high performance, *J. Alloy. Compd.*, **2013**, 552, 486-491.
- [64] Z.L. Ma, X.B. Huang, S. Dou, J.H. Wu, S.Y. Wang, One-pot synthesis of Fe₂O₃ nanoparticles on nitrogen-doped graphene as advanced supercapacitor electrode materials, *J. Phys. Chem. C*, **2014**, 118, 17231-17239.
- [65] X.F. Xia, Q.L. Hao, W. Lei, W.J. Wang, D.P. Sun, X. Wang, Nanostructured ternary composites of graphene/Fe₂O₃/polyaniline for high-performance supercapacitors, *J. Mater. Chem.*, **2012**, 22, 16844-16850.
- [66] Q.X. Low, G.W. Ho, Facile structural tuning and compositing of iron oxide-graphene anode towards enhanced supercapacitive performance, *Nano Energy*, **2014**, 5, 28-35.
- [67] P.Y. Tang, L.J. Han, A. Genç, Y. M. He, X. Zhang, L. Zhang, J. R. Galán-Mascarós, J. R. Morante, J. Arbiol, Synergistic effects in 3D honeycomb-like hematite nanoflakes/branched polypyrrole nanoleaves heterostructures as high-performance negative electrodes for asymmetric supercapacitors. *Nano Energy*, **2016**, 22, 189-201.

Chapter 4

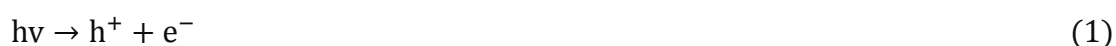
**ITO/Hematite/Fe₂TiO₅/FeNiOOH Composite Nanowires as
Photoanodes for Water Splitting in Alkaline Electrolyte**

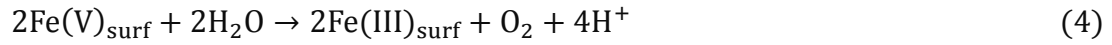
4.1 Introduction

Hematite based photoanodes have been intensively investigated on account of several promising properties, such as low cost, environmentally-friendly and high natural abundancy, which makes it as a potential candidate for water splitting photoanodes. Moreover, in terms of its applications in PEC, hematite possesses high photo-chemical stability, a narrow bandgap (1.9-2.2 eV), and a theoretical maximum solar-to-hydrogen (STH) efficiency of 15.4 %, corresponding to 12.5 mA cm^{-2} at Air-Mass 1.5 Global solar illumination, which exceeds the STH benchmark efficiency of 10% required for practical applications. [1-2] However, its relatively low absorption coefficient, short excited-state lifetime (10^{-6} s), [3-4] poor oxygen evolution reaction kinetics, short hole diffusion length, and poor electrical conductivity leads to multiple electron-hole recombination pathways occurring in the bulk, interfaces, and surfaces, as well as significantly limits the photoelectrochemical (PEC) activity of hematite. [2] As a rapid charge transport and transfer between the back substrate, photoactive semiconductor, the catalyst and electrolyte is necessary for efficient STH performance, the electronic and structural properties of back substrate/semiconductor/catalyst/electrolyte interfaces play a vital role in PEC performance. [5-10] The electron-hole recombination at the interface of the back substrate and hematite is critical for the electron transport from bulk hematite to the current collector and thus affects the overall PEC performance. [2, 9, 11-14] For instance, Zheng et al. reported an integrated hematite, TiO_x and FeOOH photoanode and obtained a photocurrent around 1.5 mA cm^{-2} , which is still much lower than the theoretical value (12.5 mA cm^{-2}) for hematite. [12] Even though this design simultaneously reduces charge recombination in the bulk and surface of hematite, the obtained photocurrent response suffers from intensive back electron-hole recombination between hematite nanowires and FTO substrate. This phenomenon is likely derived from the Sn loss in FTO substrate during the high temperature ($1000 \text{ }^\circ\text{C}$) sintering treatment which leads to poor electron conductivity in the back contact. [13-14] Therefore, it is essential to optimize the back interface of the FTO substrate

and hematite. This may be accomplished by introducing a conductive buffer layer, such as an ITO underlayer between hematite matrix and the FTO substrate. Moreover, the energetic and electronic structure of hematite can be tuned by forming an advantageous heterojunction interface, which can reduce the charge recombination at the semiconductor junction interface and thus facilitates hole transport to the electrolyte for oxygen evolution reaction (OER). [10, 12] Recently, we prepared mesoporous hematite-Fe₂TiO₅ heterojunction film, with an optimized 10% TiO₂ doping, which possessed a 15-fold photocurrent increment (up to 1.3 mA cm⁻² at 1.23 V vs RHE). [10] Furthermore, iron-nickel oxide hydroxides (FeNiOOH) have attracted widespread attention as oxygen evolution catalysts (OEC) due to their unique structure and good OER activity in alkaline medium, whose OER activity can be adjusted according to film thickness. [15-17] Coupling FeNiOOH OEC on hematite photoanodes is supposed to effectively suppress the electron-hole pair recombination and accelerate reaction kinetics at the photoactive semiconductor/electrolyte interface (SEI). [18-19] In light of this, it is thereby of high interest to design an integrated quaternary multilayer photoanode with a high electrical conductive underlayer (ITO layer, to protect against Sn loss from the FTO substrate), an advantageous heterojunction (Fe₂O₃/Fe₂TiO₅), [10] and an efficient OEC layer (FeNiOOH) to simultaneously reduce the interfacial, bulk and surface charge recombination as well as to enhance its PEC performance.

On the other hand, the kinetic process of water oxidation at SEI [10, 20-22] and the identification of the active sites [23-25] for water splitting have drawn the attention of many researchers. L. M. Peter et al. proposed that OER in hematite involves high-valent iron states formed at the surface and employed photoelectrochemical impedance spectroscopy (PEIS) for the kinetic analysis of the multistep water oxidation reaction. [20] The water oxidation on hematite surface is a 4-electron process, which occurs following the equations (1-4), with the holes being ‘stored’ in the Fe(IV) and Fe(V) intermediate states. [20]





T. Hamann et al. illustrated a general physical model and systematically discussed the suitable equivalent circuit for illustrating the electrochemical impedance spectroscopy (EIS) data for the hematite electrode, including surface states (SS) at the SEI where holes accumulate. [21] Most recently, T. Hamann et al. investigated the water-oxidation reaction on hematite via in-situ infrared spectroscopy; directly observing the existence of $\text{Fe}^{\text{IV}}=\text{O}$ group (an intermediate in the PEC water oxidation reaction), which is the origin of the presence of hematite surface states. [26] Moreover, our previous investigation has proposed a charge transfer mechanism through hole trapping at surface state and its isoenergetic transfer to water for the hematite/ Fe_2TiO_5 composite system and demonstrated that the surface state density of hematite can be tuned by controlling the amount of TiO_2 . [10] In addition, it is well established that SS exist due to the lattice periodicity termination at the species' surface, and the unpaired electrons in the dangling bonds of surface atoms interact with each other forming an electronic state with a narrow energy band (mid band) at the semiconductor band gap. [27-28] In this regard, we propose that, by integrating the hematite nanowires with an ITO underlayer, Fe_2TiO_5 and FeNiOOH coating layers step by step, the SS would be finely regulated because the chemical environment of $\text{Fe}^{\text{IV}}=\text{O}$ present at SEI will vary slightly during the water oxidation process. [29-32]

4.2 Experimental Section

4.2.1 Chemicals and Materials

All commercially available reagents and solvents were used as received without further purification unless otherwise indicated. All chemical reagents were purchased from Sigma-Aldrich. If not specified, all solutions were prepared with Milli-Q water (ca. $18.2 \text{ M}\Omega\cdot\text{cm}$ resistivity). Fluorine-tin-oxide (FTO) coated glass substrate (735167-1EA, $7 \Omega/\text{sq}$) was purchased from Sigma-Aldrich.

4.2.2 Electrode Preparation

FTO substrates were cut into small pieces with 1 cm × 3 cm area and washed by sonicating in a (1: 1: 1) mixture of acetone (Sigma-Aldrich, 99.9 %), isopropanol (Sigma-Aldrich, 99.9 %) and water. After rinsing the FTO substrates thoroughly with distilled water, the substrates were washed in ethanol (Fluka, 99.8%) and then dried in air at 300 °C for 1 h (heating rate: 8.5 °C min⁻¹). A part of the substrates (ca. 1 cm × 2 cm) was covered using a polymer tape (Kaptons® Foil, VWR International) prior to the following process. The uncoated part of the FTO was later employed as electric contact for the electrodes in the photo-electrochemical cell.

Fe₂O₃ electrodes. A 200 ml Teflon-lined stainless-steel autoclave was filled with 60 ml aqueous solution containing 0.15 M ferric chloride (FeCl₃, 97%) and 1 M sodium nitrate (NaNO₃, 99%) and 316 μL hydrochloric (HCl, wt 37%). Six pieces of washed FTO substrates were put into the autoclave and heated at 95 °C for 4 hours. A uniform layer of iron oxyhydroxides (FeOOH) nanowires was formed on the FTO substrate. The FeOOH-coated substrate was then washed with deionized water to remove any residual salt, and subsequently sintered in air at 550 °C (heating rate: 8.5 °C min⁻¹) for 2 hours. To further reduce the surface defective sites, the hematite nanowires were treated at 750 °C for additional 30 min and subsequently quenched in air within 1 min (post-quenched process).

ITO/Fe₂O₃ electrodes. Different thickness (49 nm, 105 nm, 149 nm, 196 nm and 245 nm) of indium doped tin dioxide (ITO, In₂O₃: SnO₂= 90/10 wt %) were deposited onto the FTO substrate by DC-pulsed sputtering. After that, the ITO coated FTO substrates were subjected to the same hydrothermal and pre-sintering process for Fe₂O₃ electrode as described above to grow hematite nanowires on the surface of ITO/FTO substrates. For the post-quenched process of ITO/Fe₂O₃, a quenched condition at 750 °C for 30 min has been employed.

ITO/Fe₂O₃/Fe₂TiO₅ electrodes. The obtained ITO/Fe₂O₃ samples after pre-sintering process were further subjected to TiO₂ atomic layer deposition (ALD) process. The

ALD was performed in R200 Picosun Atomic Layer Deposition system at 150 °C with TiCl₄ (Sigma-Aldrich, 99 %) and water as the precursors in an 8 mbar N₂ flow atmosphere, reaching a growth rate of 0.27 Å cycle⁻¹. The typical pulse time for the TiCl₄ and water was 0.1 s and the purge time was 10 s. The TiO₂ thickness of ITO/Fe₂O₃/Fe₂TiO₅ electrode was controlled by changing the deposition cycle, i.e., 15 cycles, 30 cycles, 50 cycles, 100 cycles and 150 cycles. After that, a varying quenched time slot (10 min, 30 min, 40 min and 80 min) at 750 °C has been tuned to optimize the sintering condition and transform the ALD TiO₂ into Fe₂TiO₅.

ITO/Fe₂O₃/Fe₂TiO₅/FeNiOOH electrodes. The optimized ITO/Fe₂O₃/Fe₂TiO₅ electrodes were further coated with FeNiOOH via photo-electrodeposition. Photo-electrodeposition of FeNiOOH on the ITO/Fe₂O₃/Fe₂TiO₅ electrodes were carried out in a mixture solution containing 0.01 M FeSO₄·7H₂O (≥ 99 %) and 0.1 M NiSO₄·6H₂O (99 %). Prior to the photo-electrodeposition of FeNiOOH, the solution was purged with nitrogen gas for 30 min. A three-electrode cell was used, composed of an ITO/Fe₂O₃/Fe₂TiO₅ electrode (work electrode), a Pt wire (counter electrode), and a Ag/AgCl (3 M KCl, reference electrode). A 150 W AM 1.5 G solar simulator (Solar Light Co., 16S-300-002 v 4.0) with an incident light intensity set at 1 Sun (100 mWcm⁻²) was used as the light source, and the light density was calibrated using a thermopile (Gentec-EO, XLPF12-3S-H2-DO) coupled with an optical power meter (Gentec-EO UNO). The light was illuminated through the glass side (back-side illumination) and the light intensity was 100 mW cm⁻². For clarification, the FeOOH grown on the back side of the FTO glass during the hydrothermal process has been carefully removed for all samples by lens wiping paper before the sintering treatment. To facilitate the photoelectrodeposition, an external bias of ca. 0.25 V vs Ag/AgCl (3M KCl) was applied. During illumination, the holes generated in the valence band of Fe₂O₃ were used to oxidize Fe²⁺/Ni²⁺ ions to Fe³⁺/Ni³⁺ ions, which precipitate as FeNiOOH on the surface of the ITO/Fe₂O₃/Fe₂TiO₅ electrode (Fe²⁺/Ni²⁺(aq) + h⁺ + 3OH⁻ → FeNiOOH(s) + H₂O). Various deposition charges (i.e., 5 mC, 10 mC, 15 mC and 20 mC) were deposited onto the surface of the ITO/Fe₂O₃/Fe₂TiO₅ nanowires by

controlling the deposition time.

4.2.3 Optical, Structural and Morphological Characterization

The grazing incidence X-ray diffraction (XRD) analyses were performed on a Bruker D4 X-ray powder diffractometer using the Cu K α radiation (1.54184 Å) and a 1D Lynkeye detector, which is equipped with a Gobel mirror in the incident beam and equatorial Soller slits in the diffracted beam (51 incidence angle, 2° step⁻¹). Optical properties of all electrodes were characterized by using a UV-vis spectrophotometer (Lambda 950, Perkin Elmer) equipped with an integrating sphere (150 mm diameter sphere covered with Spectralon as the reflecting material, Perkin Elmer). Absorbance (A) measurements were obtained from measured reflectance (R, %) and transmission (T, %), using a wavelength range of 350 to 800 nm and a step of 5 nm, respectively. The morphology of the films was characterized using a field emission gun scanning electron microscope (FE-SEM, Zeiss Series Auriga microscopy) equipped with an electron dispersive X-ray spectroscopy (EDX) detector. X-ray photoelectron spectroscopy (XPS) was performed with a Phoibos 150 analyser (SPECS GmbH, Berlin, Germany) in ultra-high vacuum conditions (base pressure 4×10⁻¹⁰ mbar) with a monochromatic aluminium K α X-ray source (1486.74 eV). The energy resolution as measured by the FWHM of the Ag 3d_{5/2} peak for a sputtered silver foil was 0.8 eV. All the samples for (S)TEM analyses were prepared by using a mechanical process. HRTEM and HAADF STEM images have been obtained by using a FEI Tecnai F20 field emission gun microscope with a 0.19 nm point-to-point resolution at 200 kV equipped with an embedded Quantum Gatan Image Filter for EELS analyses. Images have been analysed by means of Gatan Digital Micrograph software. Atomic supercell modelling was performed by the Eje-Z, Rhodius and JMOL software packages with the corresponding crystal phase parameters for each species obtained from the Inorganic Crystal Structure Database (ICSD), [33] which were verified by HRTEM and STEM-EELS spectrum imaging (SI).

4.2.4 Photo-electrochemical Measurements

Photocurrent (j , mA cm⁻²) vs. potential (E , V) curves were taken using an undivided three-electrode cell. The working, counter and reference electrodes were the composite hematite nanowires (1 cm² geometric area), a Pt wire and a Ag/AgCl (3 M KCl) electrode (Metrohm, $E=0.203$ vs. NHE), respectively. The electrolyte was a 1 M NaOH solution (pH=13.6). The electrolyte was purged with N₂ during the experiments. CV was taken using a computer-controlled potentiostat (VMP3, BioLogic Science Instruments). Potential was scanned from -0.45 V vs. Ag/AgCl to 0.85 V vs. Ag/AgCl, with a scan rate of 20 mV s⁻¹. The photocurrent density is referred to the geometric area. All potentials were corrected at 80% for the ohmic drop, which was determined using the automatic current interrupt (CI) method implemented by the potentiostat, [15] and are converted and reported with respect to the reversible hydrogen electrode (RHE): E (V vs. RHE) = E (V vs. Ag/AgCl) + 0.0592×pH + 0.203. Light illumination was performed using a 150 W AM 1.5G solar simulator (Solar Light Co., 16S-300-002 v 4.0) with an incident light intensity set at 1 Sun (100 mW cm⁻²), as measured using a thermopile (Gentec-EO, XLPF12-3S-H2-DO) coupled with an optical power meter (Gentec-EO UNO). In the PEC characterization, the light came from the front side (electrode-electrolyte interface, front side illumination). PEIS data were acquired with an alternate current (AC) perturbation of 5 mV in amplitude and a 100 mHz to 1 MHz frequency range, both in the dark and under illumination, and under selected direct current (DC) potentiostatic conditions (-0.45 to 0.85 V vs. Ag/AgCl). Nyquist plots (imaginary vs. real components of impedance, Z_{Im} vs. Z_{Re}) were fitted to the corresponding equivalent circuits using the Z-fit software package (BioLogic Associates). Fitted capacitances and resistances are referred to the electrode geometric area (1 cm × 1cm). Error bars stem from the goodness of the EIS data fittings.

4.2.5 Incident Photon to Current Efficiency (IPCE)

IPCE were characterized using a xenon light source (Abet 150 W Xenon Lamp) coupled with a monochromator (Oriel Cornerstone 260 1/4 m monochromator).

The wavelength was scanned from 350 to 800 nm (step: 10 nm step⁻¹) keeping the voltage fixed at 1.23 V vs. RHE. To calculate IPCE, the following relation was used:

$$\text{IPCE (\%)} = (1240/\lambda) \times (I/J_{\text{light}}) \times 100 \quad (5)$$

Where I is the photocurrent density (mA cm⁻²) obtained using a potentiostat (mentioned earlier) recording the i-t curve at 1.23 V vs. RHE, λ is the incident light wavelength (nm) from monochromatic, and J_{light} (mW cm⁻²) is the power density of monochromatic light at a specific wavelength. A source meter (Keithley Instruments Inc., model no. 2400) coupled with the standard Silicon Photodiode (Thorlabs, S120VC) was used to measure the power density of monochromatic light.

4.3 Result and Discussion

4.3.1 Structure of the Pristine Hematite Electrode

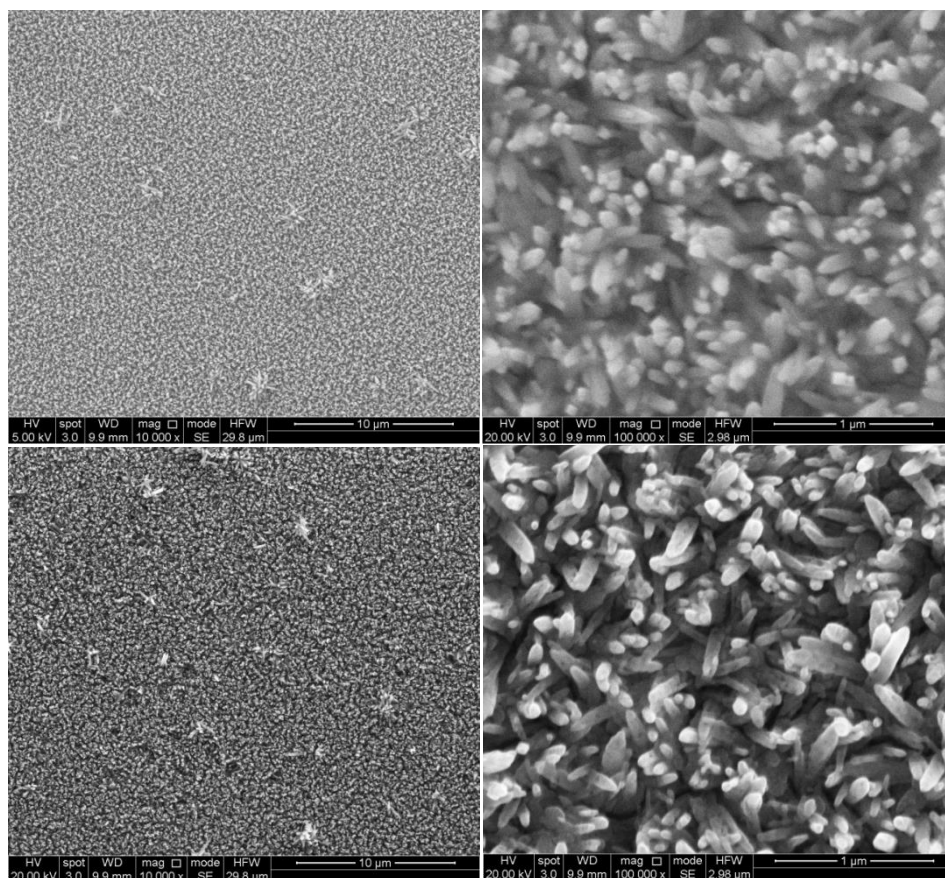


Figure 4.1 **Top row:** SEM images of FeOOH nanowires on FTO substrate. **Bottom row:** SEM images of FeOOH nanowires on FTO substrate after sintering at 550 °C for 2h.

As shown in **Figure 4.1**, a uniform layer of iron oxyhydroxide (FeOOH) nanowires was formed on the FTO substrate. The FeOOH-coated substrate was then washed with deionized water to remove any residual salt, and subsequently sintered in air at 550 °C (heating rate: 8.5 °C min⁻¹) for 2 hours. During this pre-sintering process, the FeOOH nanowires were converted into hematite nanowires without deterioration of the nanowire structure, as shown in the bottom of **Figure 4.1**. Further modifications or treatments, such as post-sintering and ALD TiO₂ deposition, are based on this sample.

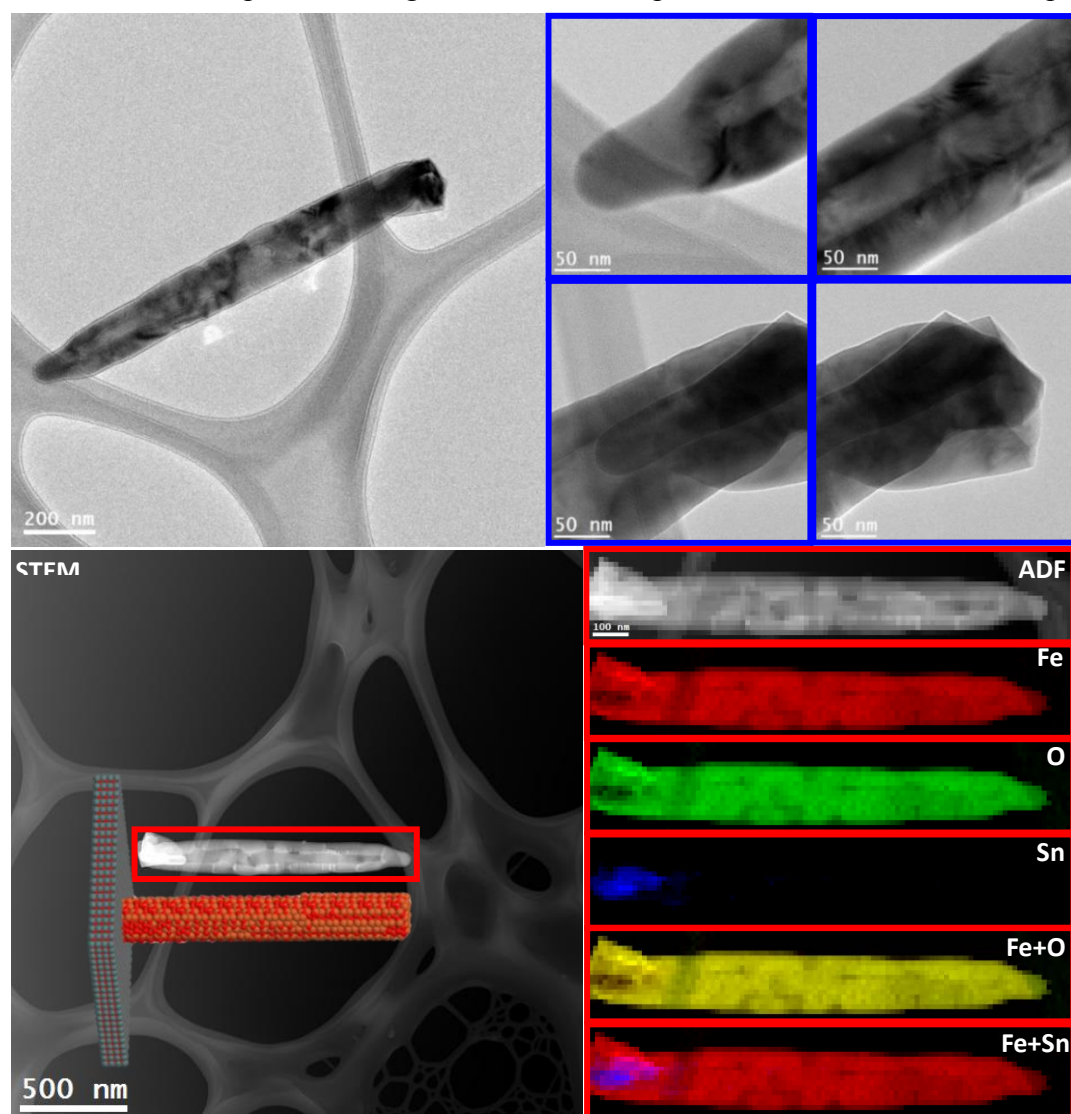


Figure 4.2 **Top row:** Low magnification TEM images of a nanowire from the Fe₂O₃ electrode. Left: low magnification TEM micrograph showing the nanowire morphology of the Fe₂O₃ electrode; Right:

several TEM images showing the detailed structure of the Fe_2O_3 nanowire. **Bottom rows:** EELS chemical composition maps obtained from the red rectangled area of the ADF-STEM micrograph of a nanowire extracted from the Fe_2O_3 electrode. Individual Fe (red), O (green), Sn (blue) maps and their composites. (The inset of the ADF-STEM micrograph shows the 3D atomic model for a Fe_2O_3 electrode nanowire).

As displayed in top rows of **Figure 4.2**, the low magnification TEM images from the Fe_2O_3 electrode indicate that the nanowires structure is prevalent in the Fe_2O_3 electrode. Moreover, the STEM-EELS mapping of Fe_2O_3 electrode in the bottom rows of **Figure 4.2** reveals that Sn diffuses from the FTO substrate into the hematite nanowires matrix.

4.3.2 Optimization of the ITO Thickness in the ITO/ Fe_2O_3 Electrodes

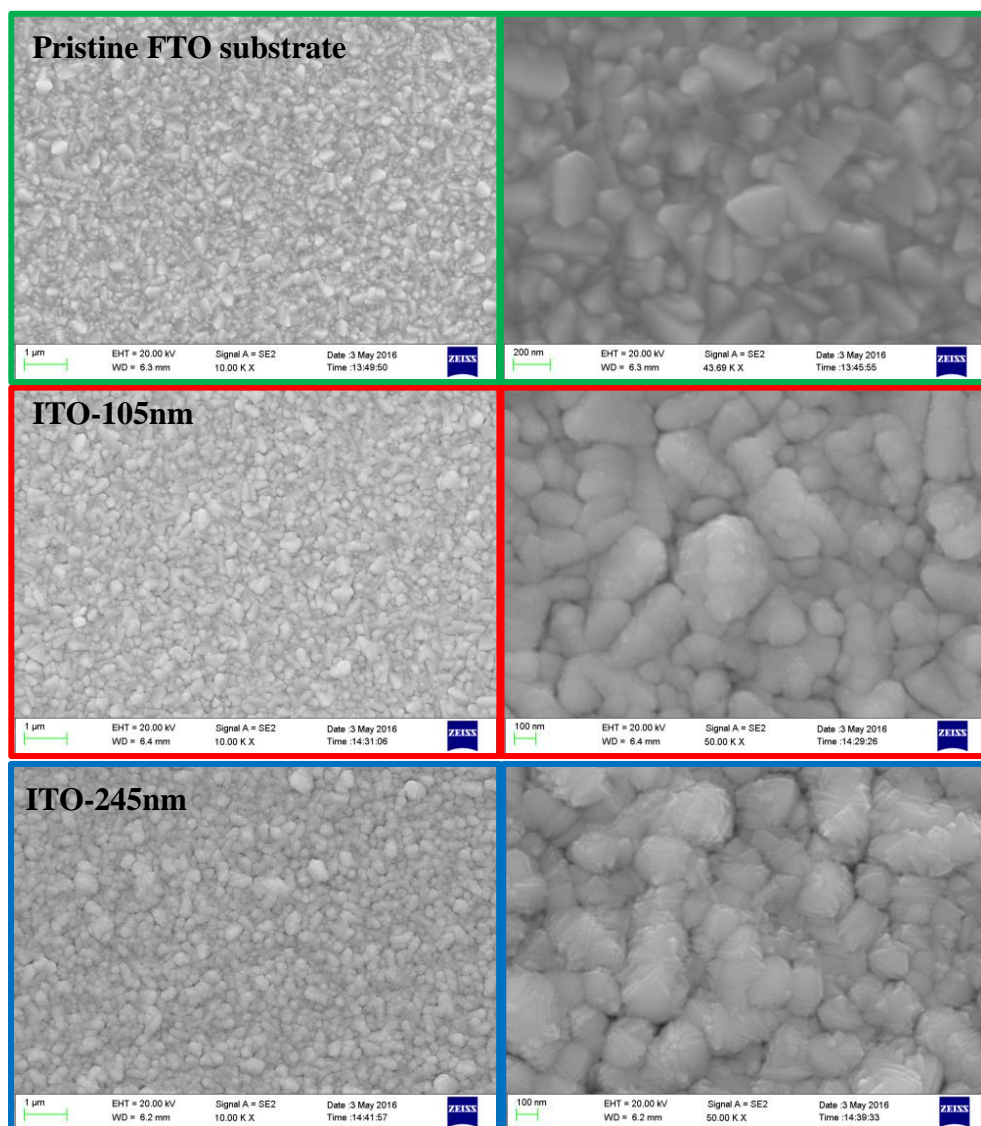


Figure 4.3 SEM images of the pristine FTO substrate, ITO-105 nm, ITO-245 nm electrodes.

With the ITO sputtering time increase, the ITO layer presents the formation of an increasing density of tiny crystalline nanoparticles supported onto the big nano-grains of the FTO substrate, as shown in **Figure 4.3**.

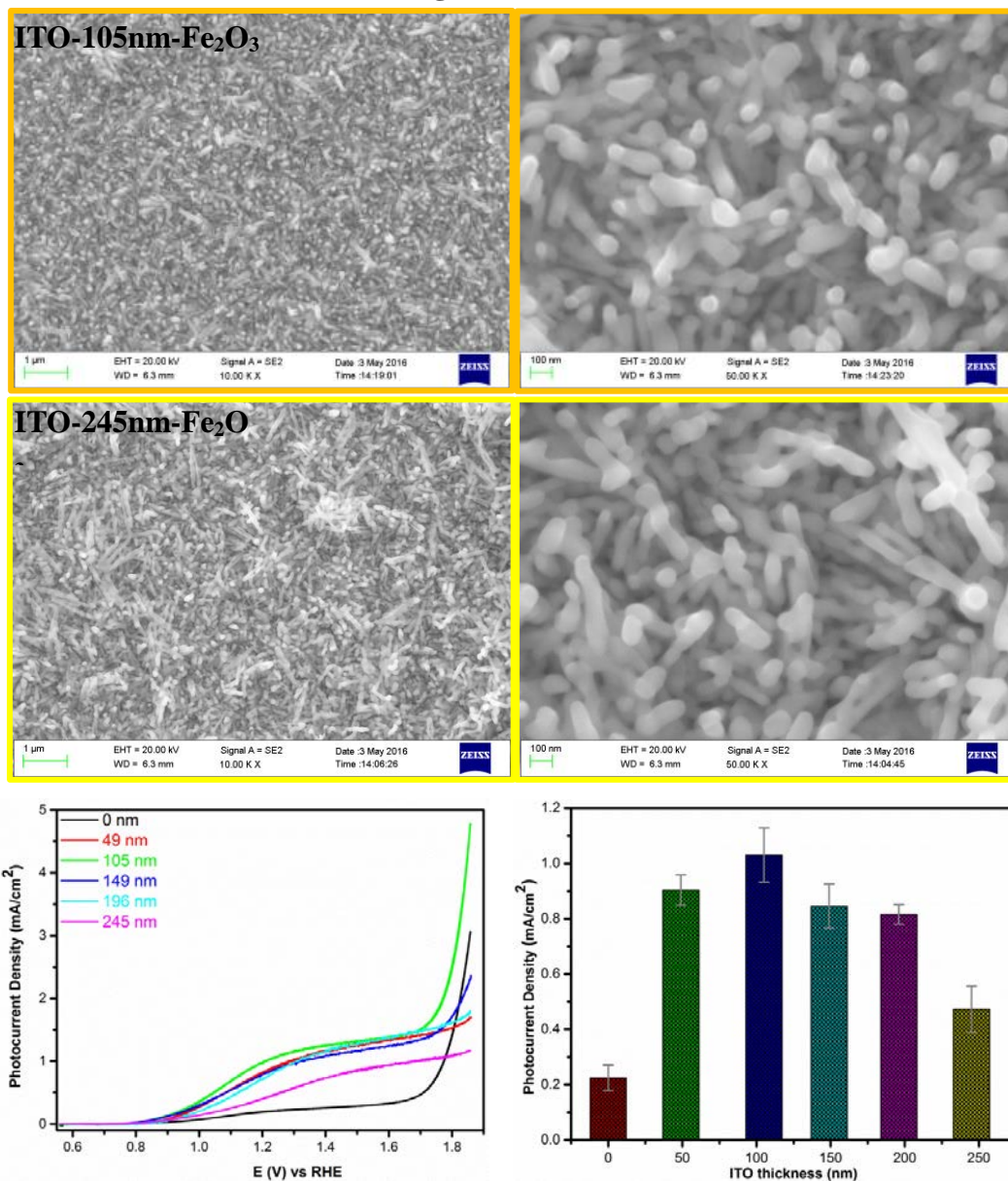


Figure 4.4 Top rows: SEM images of the pristine ITO-105 nm-Fe₂O₃ and ITO-245 nm-Fe₂O₃ electrodes. Bottom rows: Left: CV curves of the ITO/Fe₂O₃ electrodes with different ITO thickness sintering on 750 °C for 30min under illumination; Right: the photocurrent density at 1.23 V vs. RHE related to the ITO thickness (the error bar stemmed from the standard deviation of statistic data collected at least on three repeated electrodes).

As displayed in **Figure 4.4**, with the increment of ITO deposition thickness from 0

nm to 105 nm, the photocurrent at 1.23 V vs. RHE gradually increases to 1.05 mA cm⁻². In stark contrast, the corresponding photocurrent at 1.23 V vs. RHE decreases intensively upon further extending ITO deposition thickness to 245 nm. This intensive reduction of photocurrent might be attributed to the deteriorated nanowire structure of hematite because of the exorbitantly doped Sn from the thick ITO matrix, which is evidenced by the randomly inclined hematite nanowires of ITO-245nm-Fe₂O₃ electrode as shown in the top rows of **Figure 4.4**.

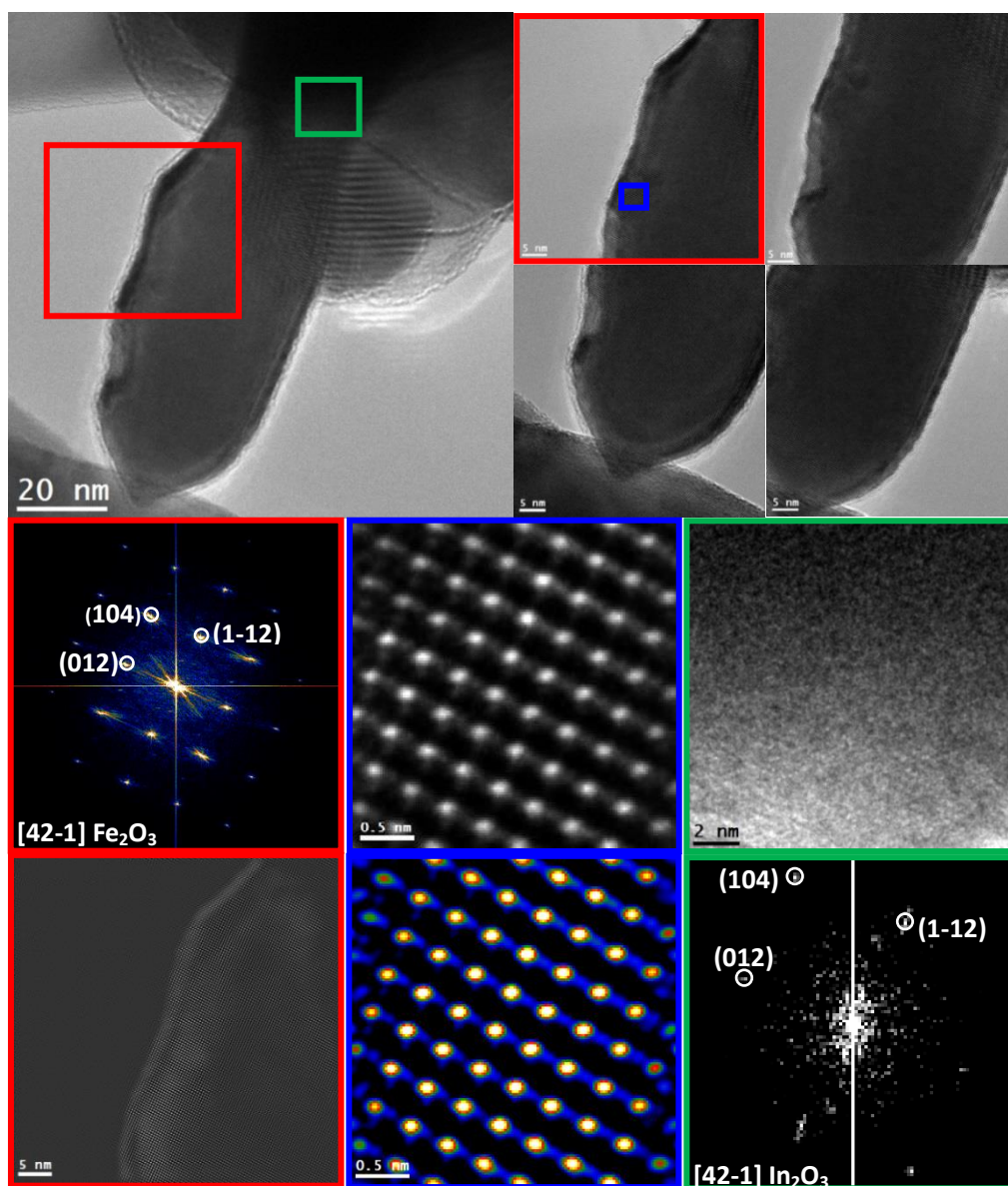


Figure 4.5 HRTEM, power spectrum (FFT) and frequency filtered HRTEM images obtained on a nanowire extracted from the optimized ITO/Fe₂O₃ electrode. **Top rows:** left: low magnification TEM micrograph showing the morphology of a small Fe₂O₃ nanowire directly grown onto the ITO matrix;

Right: detailed crystal structure of different regions on the small nanowire. **Bottom rows:** left column: power spectrum of the red squared area indicating its single crystal structure corresponding to trigonal Fe_2O_3 , [R3-CH]-Space group 167, also known as hematite, with lattice parameters of $a = b = 0.50342$ nm, $c = 1.37483$ nm, and $\alpha = \beta = 90^\circ$ and $\gamma = 120^\circ$ as visualized along the [42-1] direction; and the frequency filtered HRTEM image of the red squared area. Middle column: HRTEM and temperature colored HRTEM of the blue squared area showing the ordered structure of hematite. Right column: HRTEM of the green squared area and the corresponding power spectrum indicating that the species can be assigned to Trigonal In_2O_3 , [R3-CH]-space group 167, with lattice parameters of $a = b = 0.5438$ nm, $c = 1.4474$ nm, and $\alpha = \beta = 90^\circ$ and $\gamma = 120^\circ$ as visualized along [42-1] direction.

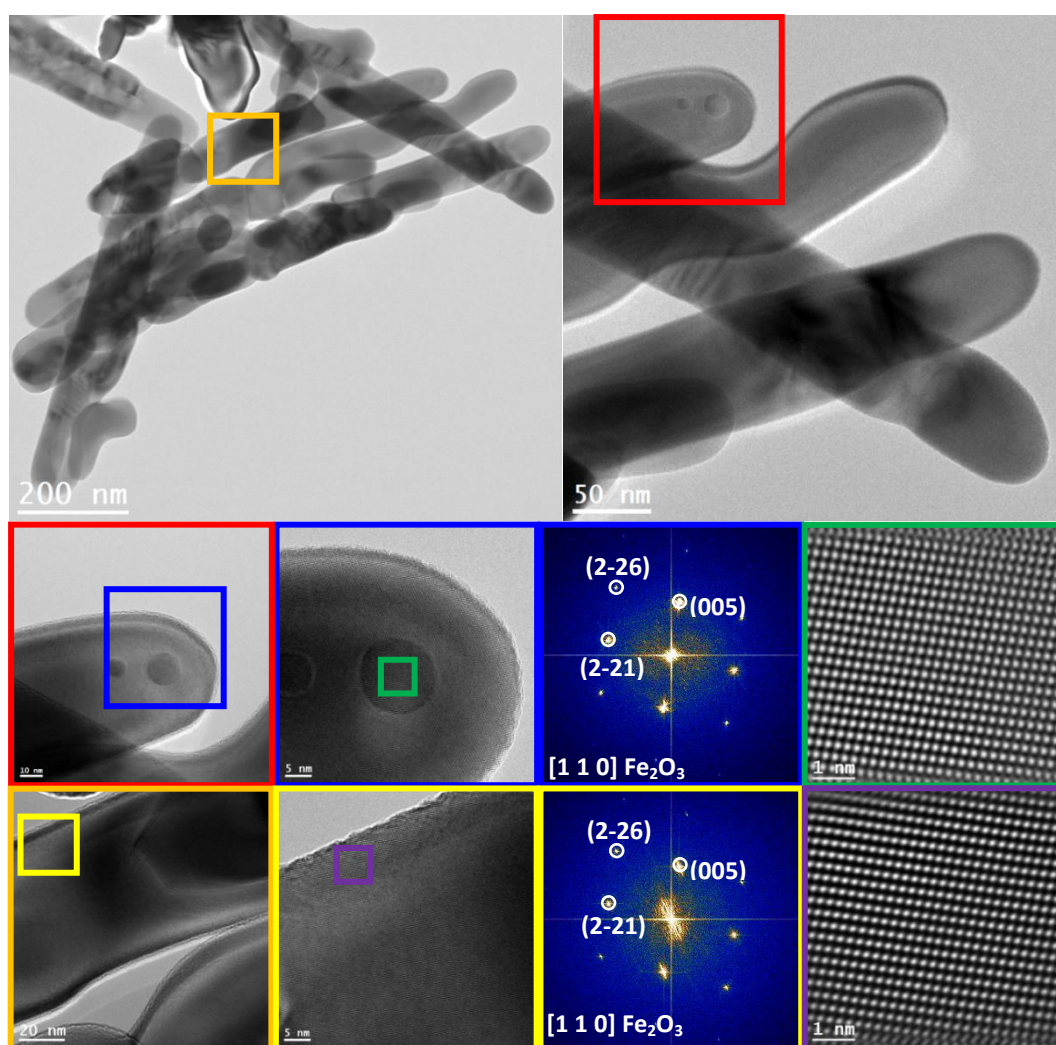


Figure 4.6 HRTEM, power spectrum and frequency filtered HRTEM images corresponding to the nanowire-like structures extracted from the optimized ITO/ Fe_2O_3 electrode. Top rows: left: low magnification TEM micrograph showing the distribution of several nanowires; Right: the magnified TEM images of these nanowires. Middle rows: left: HRTEM obtained on the red squared area; Middle:

detailed structure obtained on the blue squared area and its corresponding power spectrum indicating its hematite single crystal structure as visualized along the [110] direction; Right: frequency filtered HRTEM image of the green squared area. Bottom rows: left: HRTEM micrograph corresponding to the orange squared area; Middle: detail of the structure in the yellow squared area and the corresponding power spectrum indicating its hematite single crystal structure as visualized along the [110] direction; Right: atomic frequency filtered HRTEM image of the purple squared area.

From **Figures 4.5** and **4.6**, we observe that the bulk matrix crystallizes in the trigonal In_2O_3 phase, while the small Fe_2O_3 nanowires are directly grown on top of it. It is noteworthy that the Fe_2O_3 nanowires grown with an ITO underlayer present a single crystal hematite phase, as confirmed by the power spectra obtained on the HRTEM images displayed in **Figures 4.5** and **4.6**. The improved crystal quality of the Fe_2O_3 nanowires may be derived from the epitaxial relationship between the Fe_2O_3 and In_2O_3 phases since they belong to the same Space group-167 [R3-CH] and crystal constants with mismatches of about 7.4 % and 5.0% for a and c lattice parameters, respectively. Besides, **Figure 4.6** indicates that even the nanowire structure shows a slightly curved-shape, the nanowires crystal orientation does not vary at different regions. Furthermore, the STEM-EELS SI (**Figure 4.7**) was employed to identify the spatial distribution of ITO and Fe_2O_3 species in the ITO/ Fe_2O_3 electrode, which is consistent with the results obtained via HRTEM.

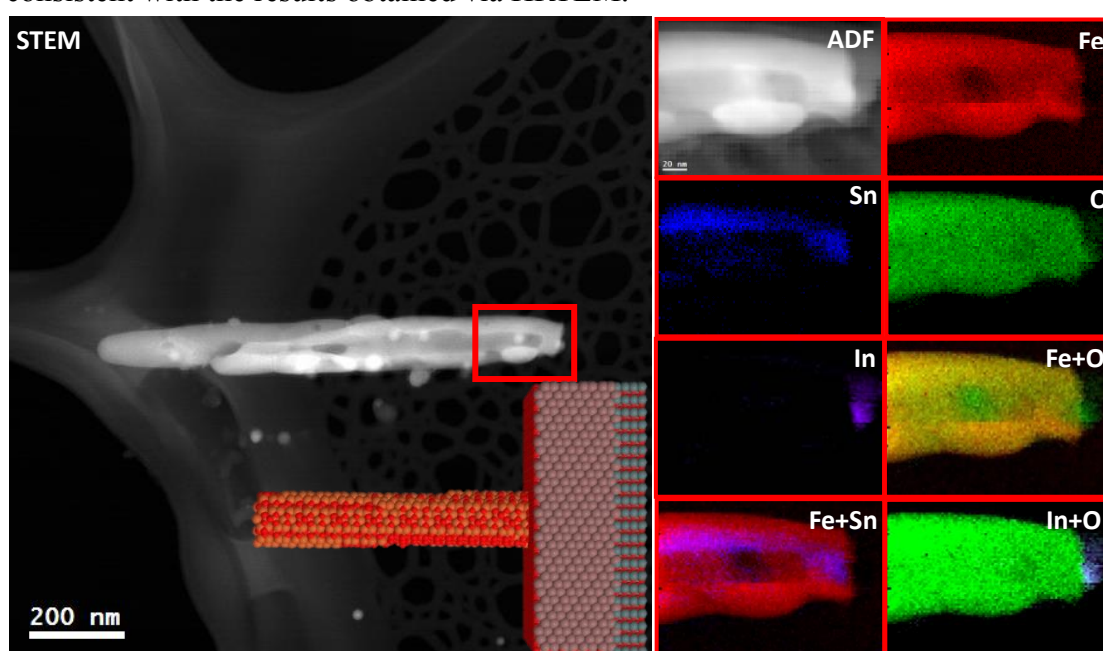


Figure 4.7 EELS chemical composition maps obtained from the red rectangled area on the ADF-STEM micrograph in the nanowire-like structure extracted from the optimized ITO/Fe₂O₃ electrode. Individual Fe (red), O (green), Sn (blue) and In (purple) maps and their composites. (The inset of the ADF-STEM micrograph shows the 3D atomic model for the ITO/Fe₂O₃ electrode nanowire-like structure).

4.3.3 The Optimization of the Sintering Conditions and ALD TiO₂ Thickness of ITO/Fe₂O₃/Fe₂TiO₅ Electrodes

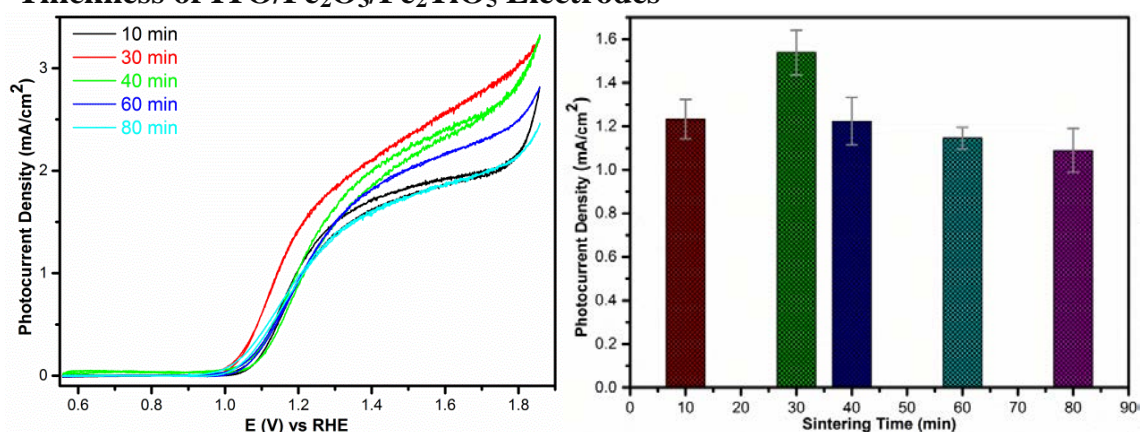


Figure 4.8 Left: CV curves of the ITO/Fe₂O₃/Fe₂TiO₅-30 cycles electrodes with different sintering time on 750 °C under illumination; Right: the photocurrent density at 1.23 V vs. RHE related to the sintering time (the error bar stemmed from the standard deviation of statistic data collected at least on three repeated electrodes).

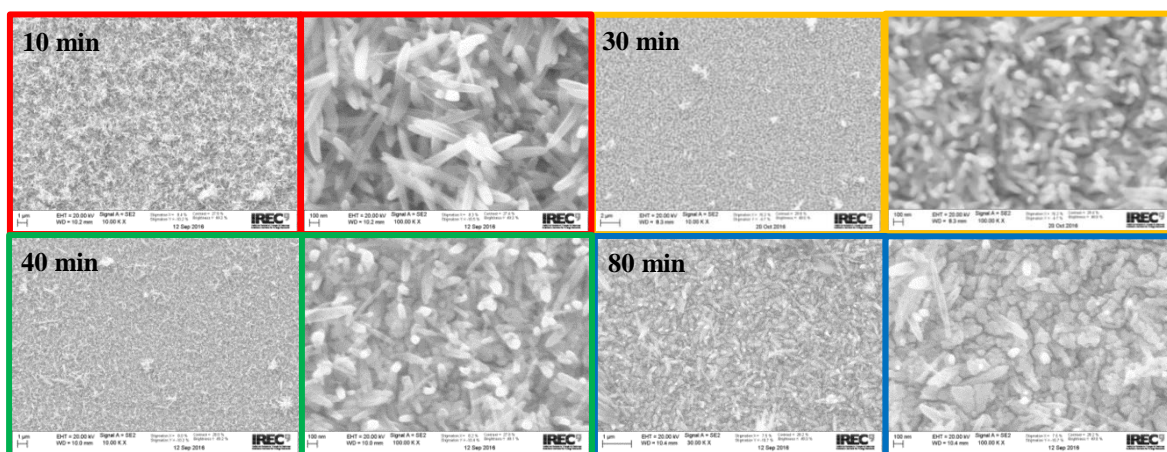


Figure 4.9 SEM images of the ITO/Fe₂O₃/Fe₂TiO₅-30 cycles electrodes with different sintering time at 750 °C, e.g. 10 min, 30 min, 40 min and 80 min.

To reduce the surface defects, enhance the Sn doping and retain the nanostructure texturing of hematite nanowires at the same time, an optimization of the sintering time

for the ITO/Fe₂O₃/Fe₂TiO₅-30 cycles electrode has been performed, as shown in **Figures 4.8** and **4.9**. **Figure 4.9** reveals how the sintering time substantially affects the morphology of the Fe₂O₃/Fe₂TiO₅ nanowires. When the sintering time exceeds 30 min at 750 °C, the Fe₂O₃/Fe₂TiO₅ nanowires initiate the deformation and finally evolve into a film-like structure, which somehow reduce the surface area exposure to the electrolyte. The monitoring of the PEC performance in **Figure 4.8** indicates that the highest photocurrent response of the ITO/Fe₂O₃/Fe₂TiO₅-30 cycles electrode can be obtained with a 30 min sintering process at 750 °C.

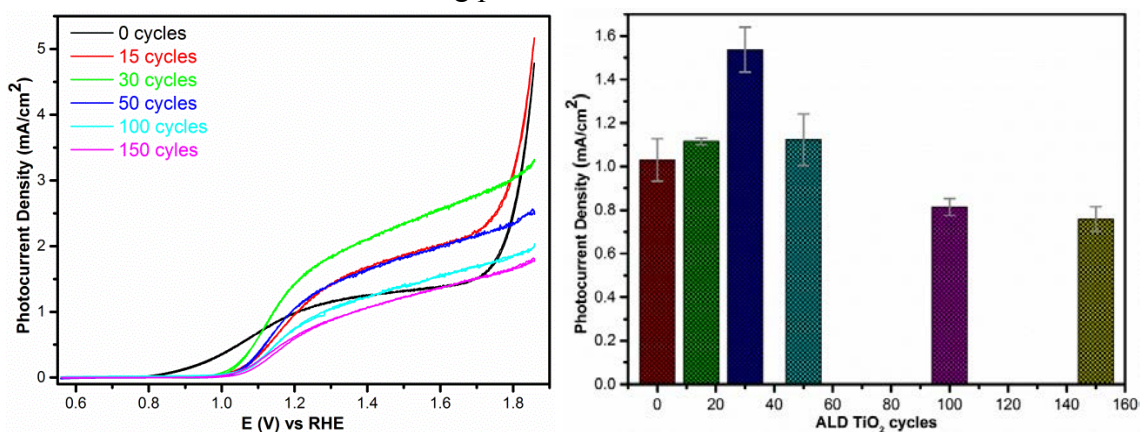


Figure 4.10 Left: CV curves of the ITO/Fe₂O₃/Fe₂TiO₅ electrodes with different ALD TiO₂ cycles (thickness) sintering at 750 °C for 30 min under illumination; Right: the photocurrent density at 1.23 V vs. RHE related to the ALD TiO₂ cycles (the error bar stemmed from the standard deviation of statistic data collected at least on three repeated electrodes).

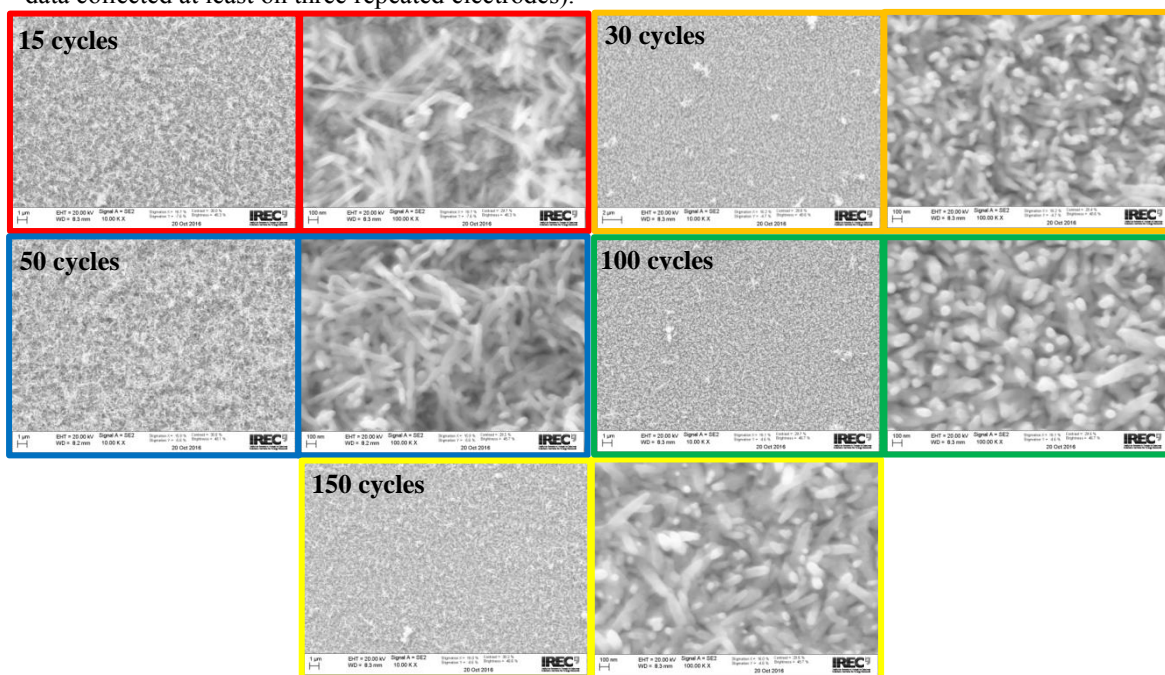


Figure 4.11 SEM images of the ITO/Fe₂O₃/Fe₂TiO₅ electrodes with different ALD cycles (TiO₂)

thickness), e.g. 15 cycles, 30 cycles, 50 cycles, 100 cycles and 150 cycles.

Figure 4.10 and 4.11 correlate the photocurrent response of the ITO/Fe₂O₃/Fe₂TiO₅ electrodes with the ALD TiO₂ deposition cycles. **Figure 4.10** shows that the photocurrent of the ITO/Fe₂O₃/Fe₂TiO₅ electrodes varies with the increment of the ALD TiO₂ deposition cycles. At 30 ALD TiO₂ deposition cycles, the ITO/Fe₂O₃/Fe₂TiO₅ electrode possesses the highest photocurrent, with a value of 1.56 mA cm⁻², indicating a suitable coating of the Fe₂TiO₅ onto the ITO/Fe₂O₃ electrode, without residual TiO₂ on the surface of the ITO/Fe₂O₃/Fe₂TiO₅ electrode and the formation of a deleterious heterojunction like the Fe₂O₃/Fe₂TiO₅/TiO₂, as confirmed by the HRTEM and STEM-EELS SI results in **Figures 4.12 and 4.13**.

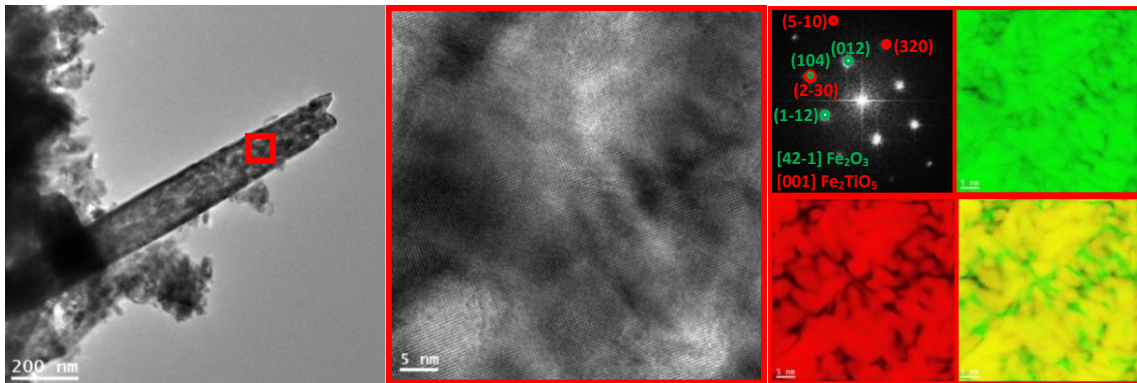


Figure 4.12 HRTEM and RGB colored frequency filtered HRTEM images (structural mapping) of the optimized ITO/Fe₂O₃/Fe₂TiO₅ electrode. left: low magnification TEM image showing a Fe₂O₃/Fe₂TiO₅ composite nanowire directly grown on the ITO matrix; Middle: detail of the structure at the red squared area; Right: corresponding power spectrum indicating that it is composed of hematite and pseudobrookite visualized along [42-1] and [001] directions, respectively; RGB colored structural maps of hematite, pseudobrookite and their composites, indicating the homogenous coating of pseudobrookite on the surface of the hematite nanowires.

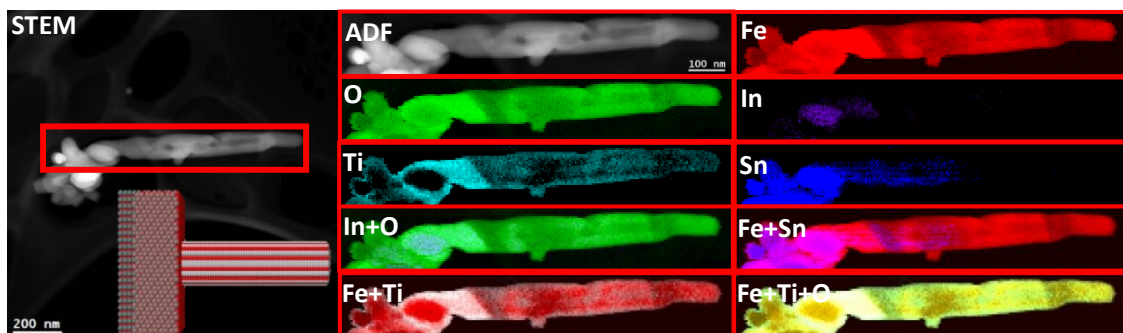


Figure 4.13 EELS chemical composition maps obtained from the red rectangled area in the

ADF-STEM micrograph in the nanowire-like structure extracted from the optimized ITO/Fe₂O₃/Fe₂TiO₅ electrode. Individual Fe (red), O (green), Sn (blue), In (purple) and Ti (indigo) maps and their composites. (The inset in the ADF-STEM micrograph shows the 3D atomic model for ITO/Fe₂O₃/Fe₂TiO₅ electrode nanowire-like structure).

4.3.4 Optimization of the FeNiOOH Deposition Charge in the ITO/Fe₂O₃/Fe₂TiO₅/FeNiOOH Electrodes

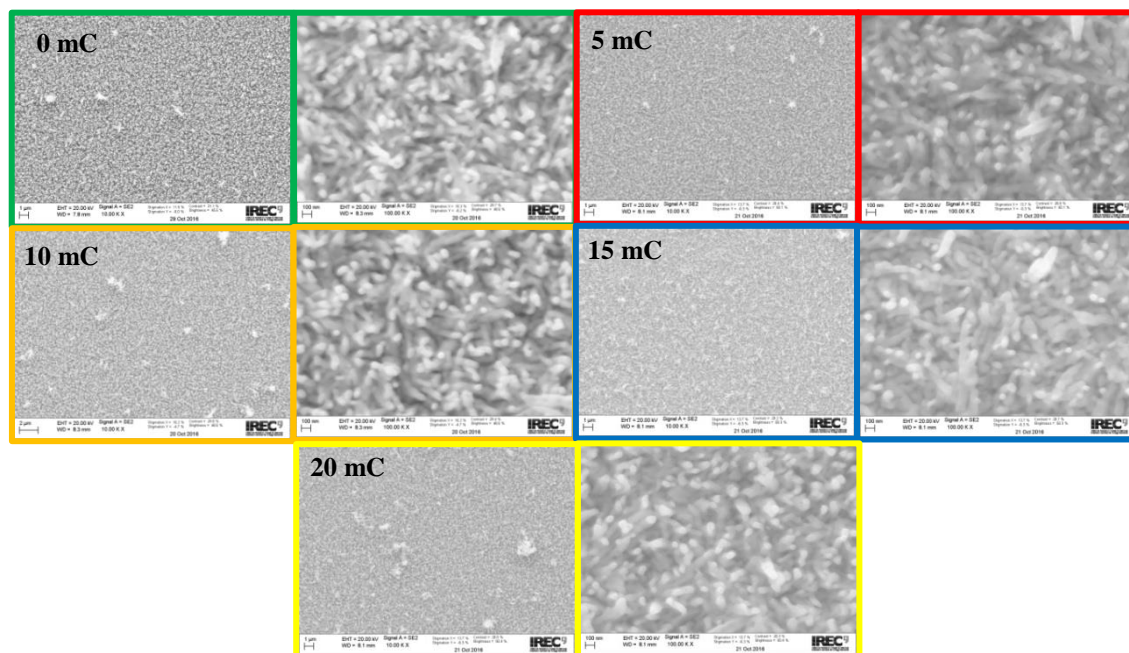


Figure 4.14 SEM images of the ITO/Fe₂O₃/Fe₂TiO₅/FeNiOOH electrodes with different FeNiOOH deposition charge, e.g. 0 mC, 5mC, 10 mC, 15 mC and 20 mC.

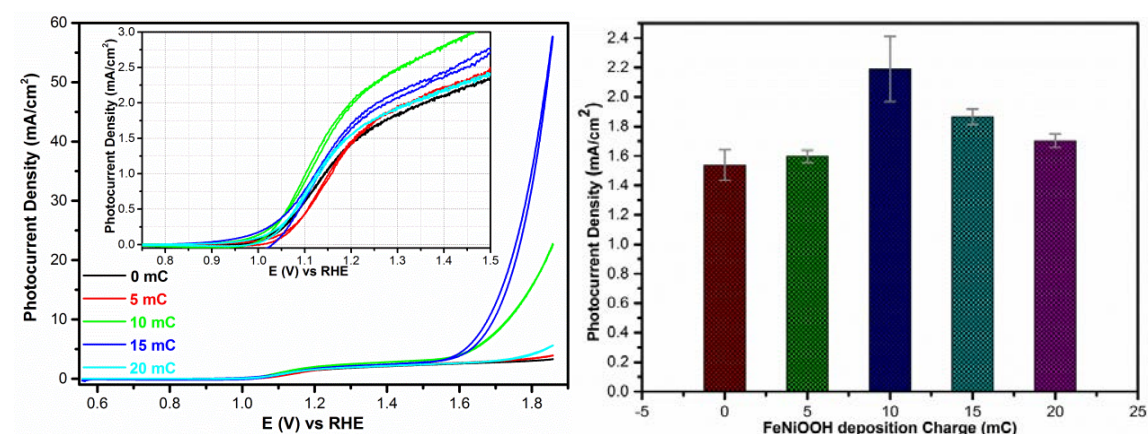


Figure 4.15 Left: CV curves of the ITO/Fe₂O₃/Fe₂TiO₅/FeNiOOH electrodes with different FeNiOOH deposition charge under illumination; Right: the photocurrent density at 1.23 V vs. RHE related to the FeNiOOH deposition charge (the error bar stemmed from the standard deviation of statistic data collected at least on three repeated electrodes).

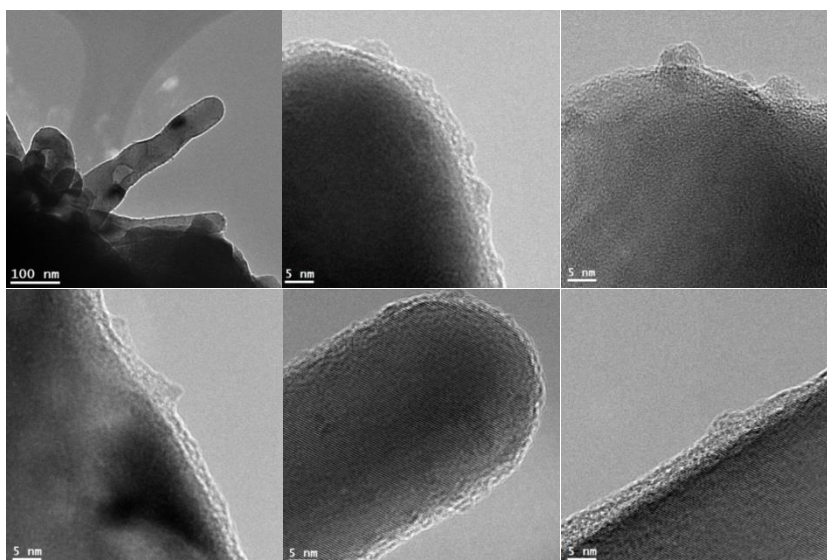


Figure 4.16 Several TEM images showing the distribution of the FeNiOOH nanodots on the surface of the Fe₂O₃/Fe₂TiO₅ composite nanowires in the optimized ITO/Fe₂O₃/Fe₂TiO₅/FeNiOOH electrode.

It is well established that the OER activity of the FeNiOOH can be adjusted according to the OEC film thickness. In our case, the electrodeposition charges of FeNiOOH onto the ITO/Fe₂O₃/Fe₂TiO₅ electrodes have been optimized, as displayed in **Figures 4.14** and **4.15**. With 10 mC decorations of FeNiOOH nanodots, the photocurrent of the ITO/Fe₂O₃/Fe₂TiO₅ electrode can be further enhanced to 2.2 mA cm⁻². It reveals that coupling the FeNiOOH on the ITO/Fe₂O₃/Fe₂TiO₅ electrode effectively suppresses the electron-hole pair recombination and accelerates the reaction kinetics at the SEI. The HRTEM and STEM-EELS SI maps in **Figures 4.16** and **4.17** further demonstrated that the FeNiOOH species are successfully deposited onto the nanowires surface, presenting a nanodot-like structure.

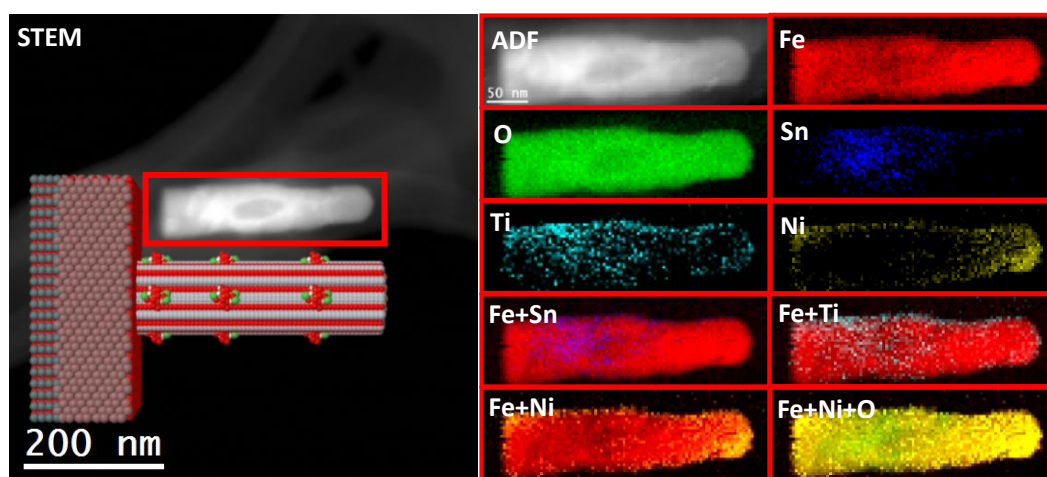


Figure 4.17 EELS chemical composition maps obtained from the red rectangled area in the ADF-STEM micrograph in the nanowire-like structure extracted from the optimized ITO/Fe₂O₃/Fe₂TiO₅/FeNiOOH electrode. Individual Fe (red), O (green), Sn (blue), Ti (indigo) and Ni (yellow) maps and their composites. (The inset of the ADF-STEM micrograph shows the 3D atomic model for the ITO/Fe₂O₃/Fe₂TiO₅/FeNiOOH electrode composite nanowire-like structure).

4.3.5 Optimization of the Sintering Conditions in the Fe₂O₃/Fe₂TiO₅ Electrodes

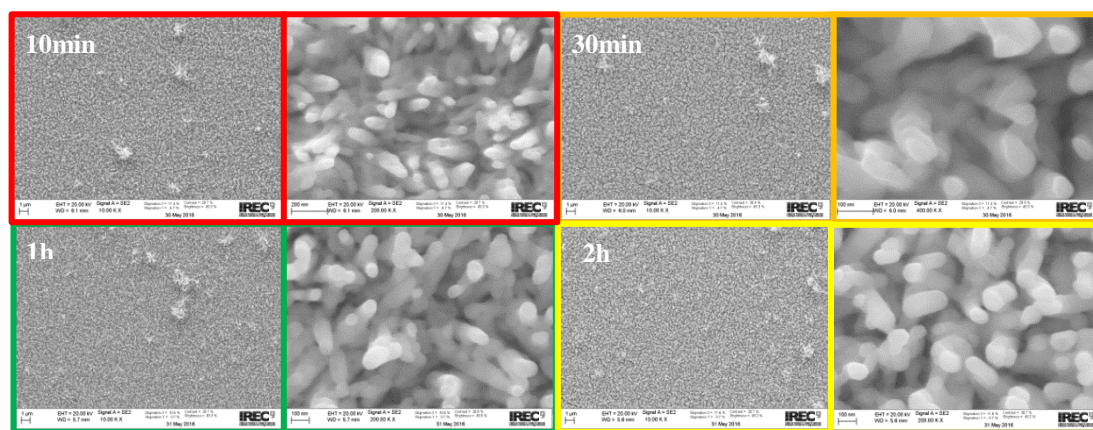


Figure 4.18 SEM images of the Fe₂O₃/Fe₂TiO₅-30 cycles electrodes with different sintering time at 750 °C, e.g. 10 min, 30min, 1 h and 2 h.

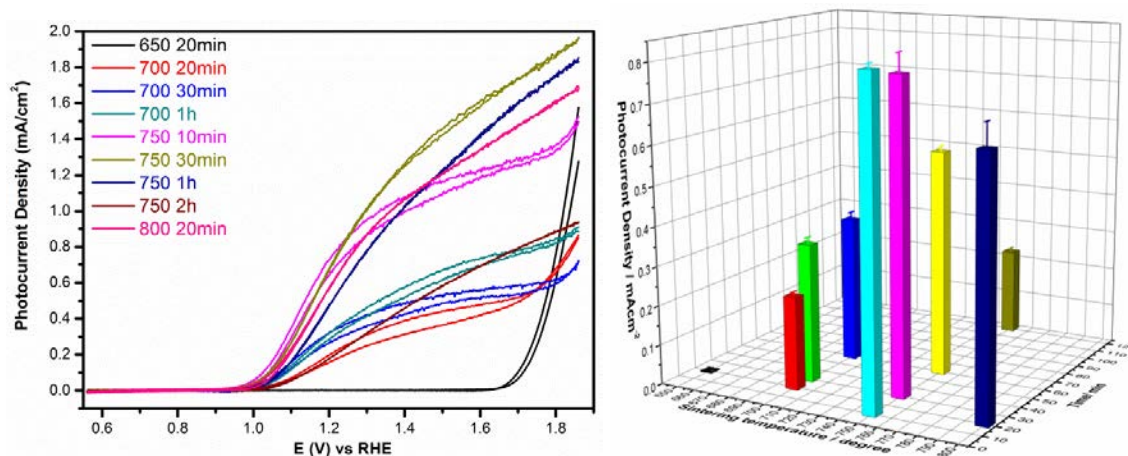


Figure 4.19 Left: CV curves of the Fe₂O₃/Fe₂TiO₅-30 cycles electrodes with different sintering conditions under illumination; Right: photocurrent density at 1.23 V vs. RHE related to the sintering conditions (the error bar stemmed from the standard deviation of statistic data collected at least on three repeated electrodes).

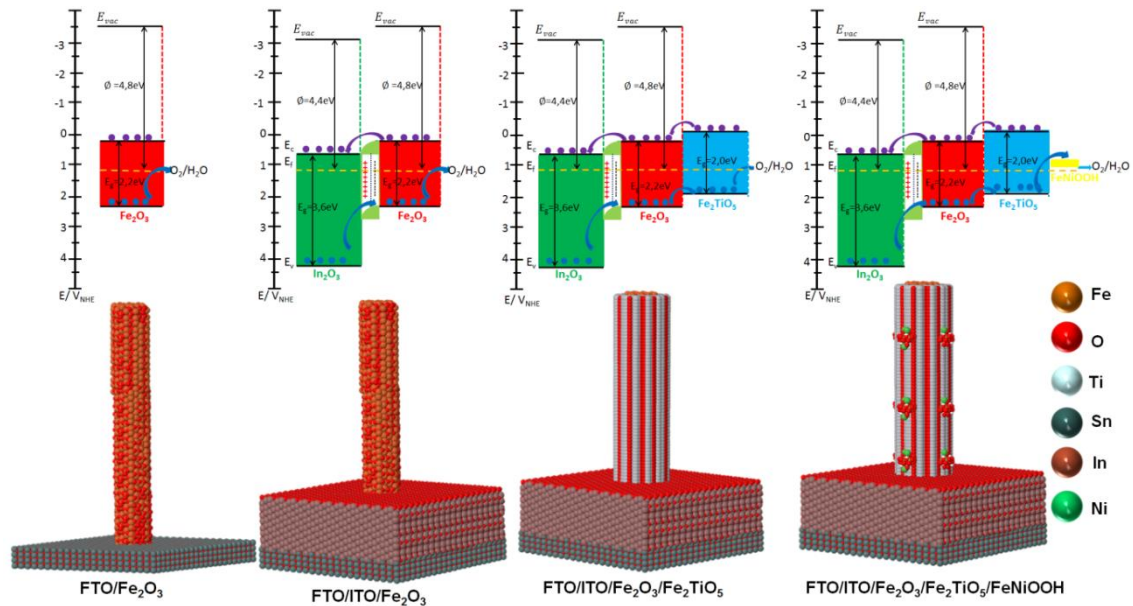
As a proof of the necessity of an ITO underlayer between FTO substrate and Fe₂O₃/

Fe₂TiO₅ nanowires, a Fe₂O₃/Fe₂TiO₅-30 cycles electrode was also fabricated and the sintering condition optimized, as presented in **Figures 4.18** and **4.19**. According to **Figure 4.19**, the optimization sintering condition for the Fe₂O₃/Fe₂TiO₅-30 cycles electrode is 750 °C for 30 min, while the corresponding photocurrent is 0.81 mA cm⁻², which is much lower than the 1.56 mA cm⁻² obtained for the ITO/Fe₂O₃/Fe₂TiO₅-30 cycles electrode. This latest result further confirms the beneficial function of the ITO underlayer.

4.3.6 Systematically Structural, PEC Performance Comparison of Optimized Fe₂O₃, ITO/Fe₂O₃, ITO/Fe₂O₃/Fe₂TiO₅ and ITO/Fe₂O₃/Fe₂TiO₅/FeNiOOH Electrodes

Based on the wealth of reported band gap information for In₂O₃, hematite, Fe₂TiO₅ and FeNiOOH, [10, 34] a type II band alignment composed of multiple ITO/Fe₂O₃/Fe₂TiO₅/FeNiOOH interfaces can be constructed via gradual incorporation of ITO, Fe₂TiO₅ and FeNiOOH layers in hematite nanowires. [27, 35] As illustrated in **Schematic 4.1**, upon light illumination, the pristine Fe₂O₃ electrode suffers from a large recombination rate that yields a low photo-current, as holes are sluggishly transferred to water. For ITO/Fe₂O₃ electrode, since both In₂O₃ and hematite are n-type semiconductors with different work functions, a heterojunction with a potential barrier will form at their interface. In₂O₃ (main ingredient of ITO) has a lower work function compared to hematite, thus the electrons in the Fermi level (E_f) of In₂O₃ will migrate to E_f of Fe₂O₃ until their E_f equalized. [34] At the equilibrium state, an electron depletion layer (marked as double layer charge between hematite and In₂O₃) will be generated at the heterojunction interface and thus a built-in electron field will be formed, which will accelerate the separation of photo-generated charge carriers and reduce the recombination rate and thus result in enhanced photocurrent. [27, 36] Since Fe₂TiO₅ and hematite's relative conduction band (CB) and valence band (VB) edge positions enable a cascade of charge migration, holes are transferred from Fe₂O₃ to Fe₂TiO₅ and conversely electrons are transferred from Fe₂TiO₅ to Fe₂O₃ in a conveyor belt fashion. [10]

Upon coating of ultrathin Fe_2TiO_5 onto $\text{ITO}/\text{Fe}_2\text{O}_3$ nanowires, the hematite nanowires can accommodate the ultrathin pseudobrookite phase shell at the surface, forming the advantageous $\text{Fe}_2\text{O}_3/\text{Fe}_2\text{TiO}_5$ heterojunction. The heterojunctions in the $\text{ITO}/\text{Fe}_2\text{O}_3/\text{Fe}_2\text{TiO}_5$ electrode reduce the grain boundary recombination by preventing charge accumulation in the nanowires and at the interfaces, thus it is expected to further enhance the photocurrent response. Finally, there is consensus that, coupling FeNiOOH on photoanodes effectively suppresses the charge recombination and accelerates reaction kinetics at the SEI. [37-43] The deposition of FeNiOOH onto the $\text{ITO}/\text{Fe}_2\text{O}_3/\text{Fe}_2\text{TiO}_5$ nanowires should further increase the surface work function, resulting in a remarkable enhancement of the barrier height and built-in electric field for the migration of photogenerated holes to the electrode surface. [37-39] With this in mind, an $\text{ITO}/\text{Fe}_2\text{O}_3/\text{Fe}_2\text{TiO}_5/\text{FeNiOOH}$ heterojunction nanowire was designed and fabricated via a combination of sputtering, hydrothermal, ALD and photo-electrochemical deposition techniques, as displayed in **Schematic 4.2**.



Schematic 4.1 Top: Thermodynamic scheme for the charge transfer processes at 1.23 V vs. RHE of SEI under illumination for Fe_2O_3 , $\text{ITO}/\text{Fe}_2\text{O}_3$, $\text{ITO}/\text{Fe}_2\text{O}_3/\text{Fe}_2\text{TiO}_5$, and $\text{ITO}/\text{Fe}_2\text{O}_3/\text{Fe}_2\text{TiO}_5/\text{FeNiOOH}$ electrodes. The black arrows indicate the bandgap of In_2O_3 (ITO matrix), hematite and Fe_2TiO_5 . The dark blue arrow refers to the hole transfer process at the heterojunction interfaces. The purple arrow refers to the electron transfer process present at the heterojunction interfaces. For simplicity, interfacial

charge transfer is considered to occur through the E_V and/or E_C states directly, without the intervention of interfacial SS. In all photoanodes, 4 electron-hole couples per visible active semiconductor are depicted. In_2O_3 (main ingredient of ITO matrix): green; Fe_2O_3 : red; Fe_2TiO_5 : indigo; FeNiOOH : yellow. Bottom: the atomic supercell models illustrate the interfaces existing at In_2O_3 (ITO matrix), hematite, Fe_2TiO_5 and FeNiOOH species in the integrated electrodes.

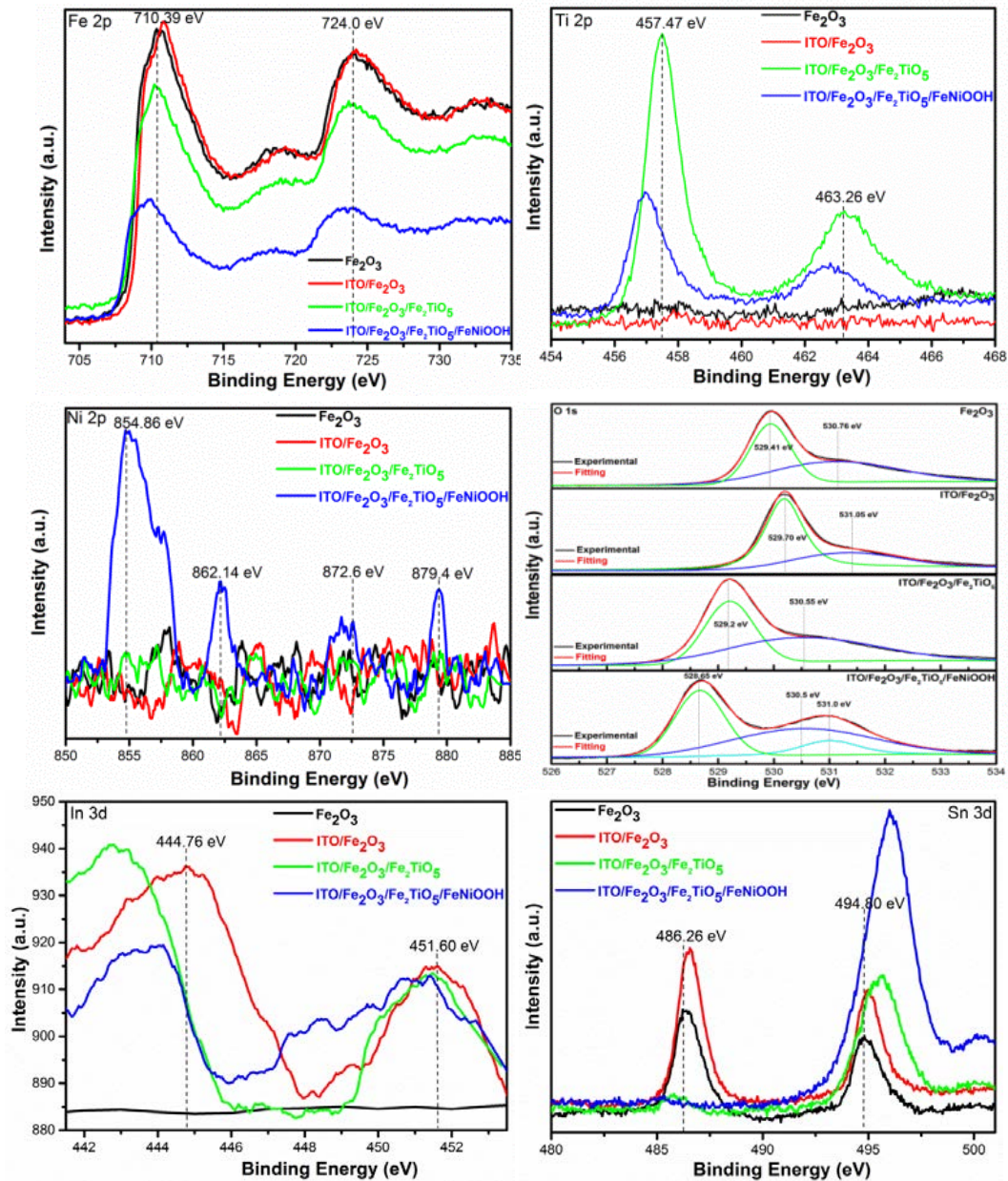


Figure 4.20 High resolution XPS spectra of Fe 2p, Ti 2p, Ni 2p, O 1s, In 3d and Sn 3d from the Fe_2O_3 , ITO/ Fe_2O_3 , ITO/ $\text{Fe}_2\text{O}_3/\text{Fe}_2\text{TiO}_5$, and ITO/ $\text{Fe}_2\text{O}_3/\text{Fe}_2\text{TiO}_5/\text{FeNiOOH}$ electrodes.

The surface electronic states and composition of each electrode were analysed by XPS and all binding energies were corrected for samples charging effect regarding the C 1s

line at 284.6 eV. **Figure 4.20** presents the Sn 3d, O 1s, Fe 2p, In 3d, Ti 2p and Ni 2p core level XPS scans at higher resolution over smaller energy windows. The Fe 2p_{1/2} and 2p_{3/2} peaks at the binding energies of 710.39 eV and 724.00 eV confirm the presence of Fe in these four electrodes. Additionally, two satellite peaks of the Fe 2p main line are at approximately 8.1-8.5 eV lower energy than the main line, indicating the presence of Fe³⁺ species. [10, 44] A positive shift of the Fe peaks after the sputtering of ITO under layer reflects a decrease in the electron density of the Fe₂O₃ due to electron transfer from Fe₂O₃ to ITO layer. Conversely, a negative shift of the Fe peak is detected after the deposition of Fe₂TiO₅ and FeNiOOH layers. These shifts can be ascribed to the surface binding interaction between ITO, Fe₂O₃, Fe₂TiO₅ and FeNiOOH, which induces an electron transfer in the integrated photoanode following the order: FeNiOOH → Fe₂TiO₅ → Fe₂O₃ → ITO as depicted in **Schematic 4.1**. [45] The Sn 3d_{3/2} and Sn 3d_{5/2} peaks at 494.80 eV and 486.26 eV with splitting energy of 8.54 eV are consistent with reported values of Sn⁴⁺. [34, 46] Furthermore, the In 2p_{1/2} and 2p_{3/2} core level XPS spectrum has two weak, broad peaks around 451.60 and 444.76 eV, in good agreement with In₂O₃. [34] Comparing with the strong intensity of Sn 3d peaks, the relative weak intensity of In 2p peaks means that the formation of In³⁺ ions is closer to the substrate, indicating that Sn doping dominates the Fe₂O₃ nanowires rather than In doping. The Ti 2p_{1/2} and 2p_{3/2} peaks at 463.26 and 457.27 eV reveal the successful coating of Fe₂TiO₅ for ITO/Fe₂O₃/Fe₂TiO₅ and ITO/Fe₂O₃/Fe₂TiO₅/FeNiOOH electrodes. [10] Coinciding with the observed shift of the Fe 2p peaks, after the FeNiOOH deposition, the Ti peaks shift to a negative binding energy direction, again imply electron transfers from the FeNiOOH to the Fe₂TiO₅ layer. Moreover, the presence of Ni in FeNiOOH was also investigated. The weak Ni 2p_{1/2} and 2p_{3/2} core level XPS peaks located at 872.60 eV and 854.86 eV and their associated satellite peaks at 862.14 eV and 879.40 eV are observed in the ITO/Fe₂O₃/Fe₂TiO₅/FeNiOOH electrode, confirming the presence of FeNiOOH. [45] The O 1s XPS spectrum of ITO/Fe₂O₃/Fe₂TiO₅/FeNiOOH electrode is composed by three peaks. The low binding energy at 529.41 eV and the higher binding energy

component at 531.05 eV are attributed to the coordination of oxygen bounded to iron atoms from the Fe_2O_3 moiety and surface absorbed OH groups, respectively. [47] The shift behaviour of these two O 1s peaks of Fe_2O_3 is in accordance with shifts observed for the Fe 2p and Ti 2p peaks. Whereas, the 531.00 eV O1s peak can be assigned to the OOH bonding likely to the FeNiOOH species. [45] The consistent shifts in the binding energy observed in the XPS data for these electrodes indicate charge transfer processes that benefit electron-hole separation, further supporting the well-constructed multiple ITO/hematite/ Fe_2TiO_5 / FeNiOOH heterojunction with type II band alignment.

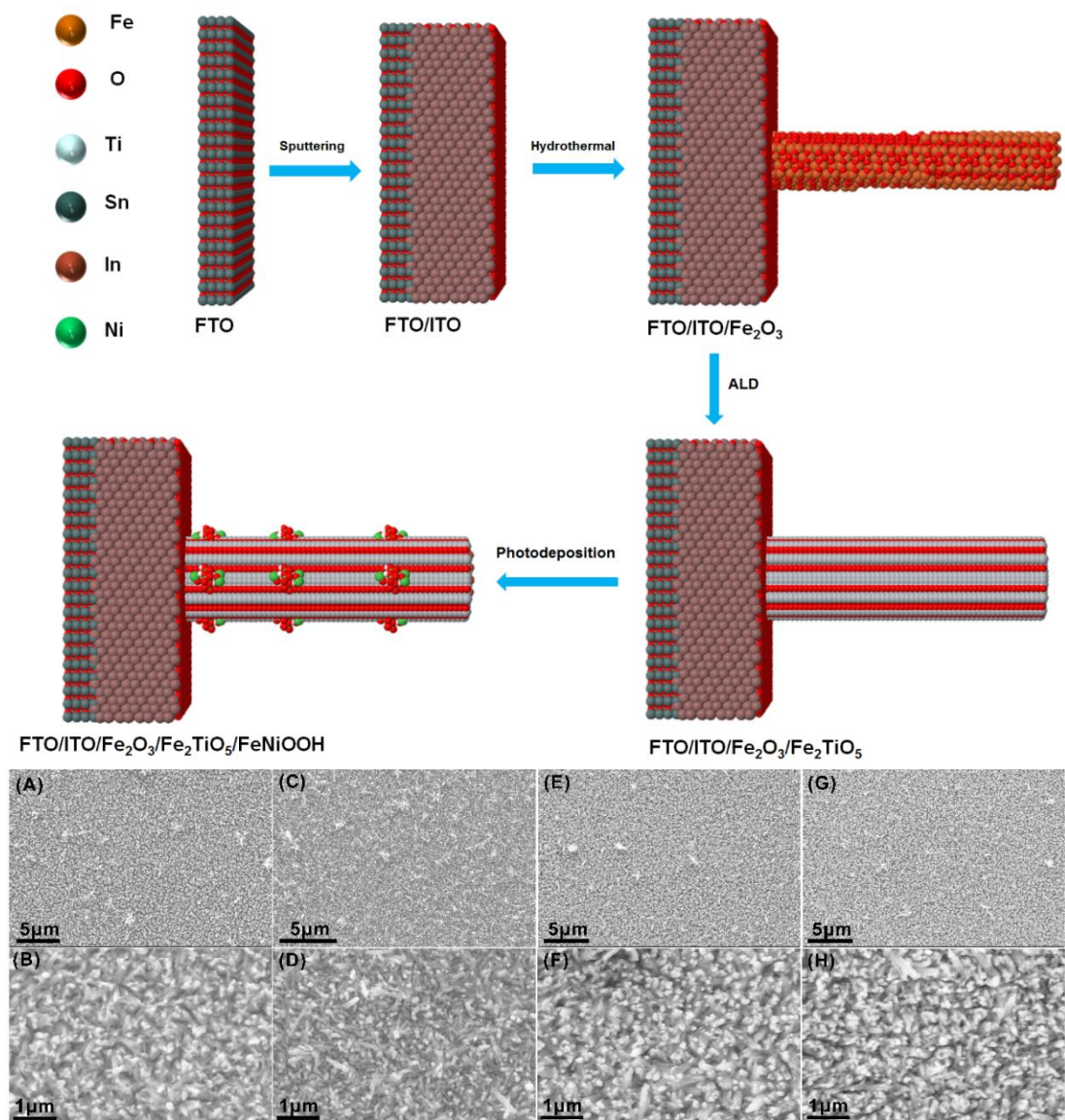


Figure 4.21 Top: **Schematic 4.2.** Atomic supercell model illustration of the synthetic procedure for

ITO/Fe₂O₃/Fe₂TiO₅/FeNiOOH integrated photoanodes. Bottom: SEM images (top view) of Fe₂O₃ (A, B), ITO/Fe₂O₃ (C, D), ITO/Fe₂O₃/Fe₂TiO₅ (E, F), and ITO/Fe₂O₃/Fe₂TiO₅/FeNiOOH (G, H) electrodes.

The morphology and crystal phase evolution of these electrodes were monitored by SEM, EDS, XRD, TEM and STEM-EELS maps. Vertically aligned Fe₂O₃ nanowires were grown on a FTO or 105 nm ITO coated FTO substrate via a previously reported hydrothermal method. [48] The Fe₂O₃ nanowires have a diameter range from 50 to 100 nm (**Figures 4.21A-D**). Subsequently, an ultrathin TiO₂ layer was coated onto the ITO/Fe₂O₃ nanowires by ALD (30 cycles). The surface TiO₂ was subsequently transformed into Fe₂TiO₅ through a post-quenching process in atmosphere at 750 °C for 30 min. As displayed in **Figures 4.21E and F**, the Fe₂TiO₅ coating onto ITO/Fe₂O₃ is homogeneous with no change in the nanowires configuration. Interestingly, the ITO/Fe₂O₃/Fe₂TiO₅ nanowires appear to be straighter than the ITO/Fe₂O₃ nanowires, this is likely due to the confinement effect from the ultrathin Fe₂TiO₅ layer (This phenomenon is similar to the function of SiO₂ in the fabrication of mesoporous Fe₂O₃ reported by K. Sivula et al). [49] When 10 mC FeNiOOH were further photoelectrodeposited onto the ITO/Fe₂O₃/Fe₂TiO₅ nanowires, no visible nanostructure could be observed on the nanowires surface (**Figures 4.21G and H**), indicating its ultrathin configuration. The crystal phase and elemental information were characterized by EDS (**Figure 4.22**) and XRD (**Figure 4.23**), confirming the presence of In₂O₃, hematite, pseudobrookite and FeNiOOH in the corresponding electrodes.

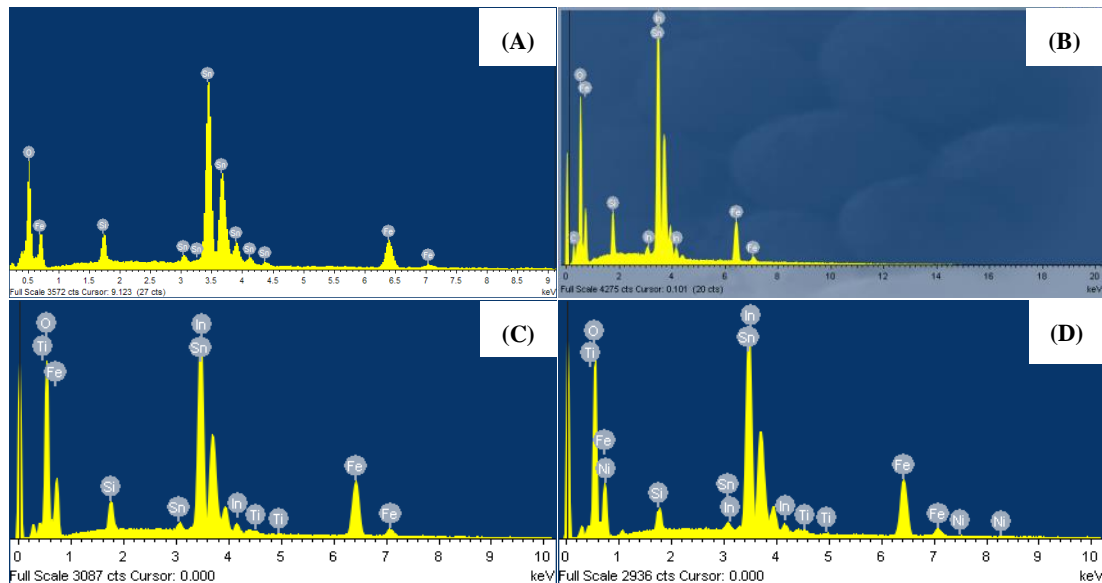


Figure 4.22 EDS obtained on the Fe₂O₃ (A), ITO/Fe₂O₃ (B), ITO/Fe₂O₃/Fe₂TiO₅ (C), and ITO/Fe₂O₃/Fe₂TiO₅/FeNiOOH (D) electrodes.

Characteristic XRD peaks of Fe₂O₃ (JCPDS no. 33-0664) and SnO₂ (JCPDS no. 41-1445, mainly derived from FTO substrate) can be observed in the four electrodes shown in **Figure 4.23A**. The XRD pattern of the ITO/Fe₂O₃, ITO/Fe₂O₃/Fe₂TiO₅, and ITO/Fe₂O₃/Fe₂TiO₅/FeNiOOH electrodes exhibit the diffraction peaks assigned to In₂O₃ (JCPDS no. 22-0336) from the initial sputtered ITO underlayer. The diffraction peaks related to the pseudobrookite (Fe₂TiO₅, JCPDS no. 41-1432) phase of ITO/Fe₂O₃/Fe₂TiO₅, and ITO/Fe₂O₃/Fe₂TiO₅/FeNiOOH electrodes are very weak, which is attributed to the Fe₂TiO₅ ultrathin coating shell (30 ALD cycles, estimated ca. 0.81 nm). Besides, there is a weak broad peak located at 11°, which can be assigned to the FeNiOOH, indicating its poor crystalline structure.

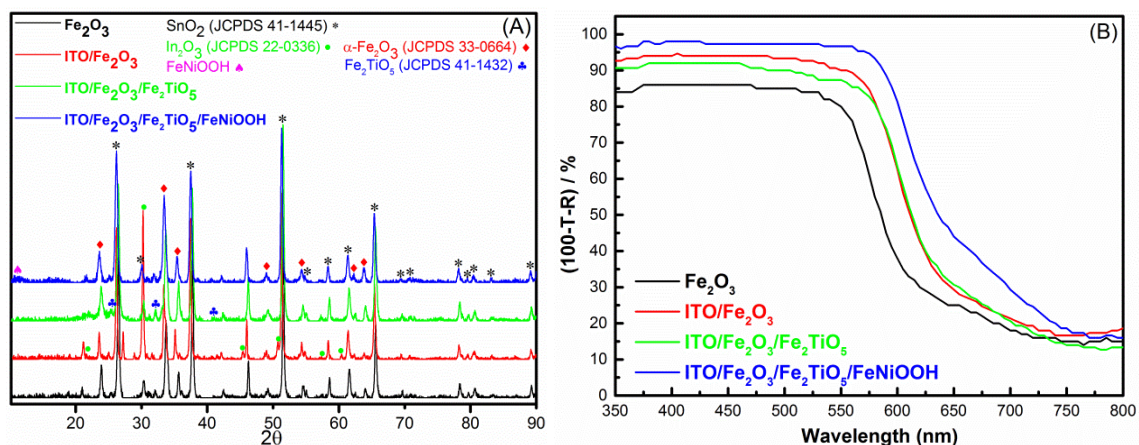


Figure 4.23 (A): Grazing incidence XRD patterns of the Fe₂O₃, ITO/Fe₂O₃, ITO/Fe₂O₃/Fe₂TiO₅, and ITO/Fe₂O₃/Fe₂TiO₅/FeNiOOH electrodes. (B): Absorbance of the Fe₂O₃, ITO/Fe₂O₃, ITO/Fe₂O₃/Fe₂TiO₅, and ITO/Fe₂O₃/Fe₂TiO₅/FeNiOOH electrodes; this plot was obtained from transmittance (T, %) and total reflectance (R, %) measurements on these electrodes by UV-Vis spectrum.

UV-vis absorbance spectra are obtained to account for the photo-activity of the Fe₂O₃, ITO/Fe₂O₃, ITO/Fe₂O₃/Fe₂TiO₅, and ITO/Fe₂O₃/Fe₂TiO₅/FeNiOOH electrodes, as shown in **Figure 4.23B**. All photoanodes exhibit an overall high absorption in the visible region (wavelength < 580 nm) with a relative steep absorption edge at approximately 580 nm.

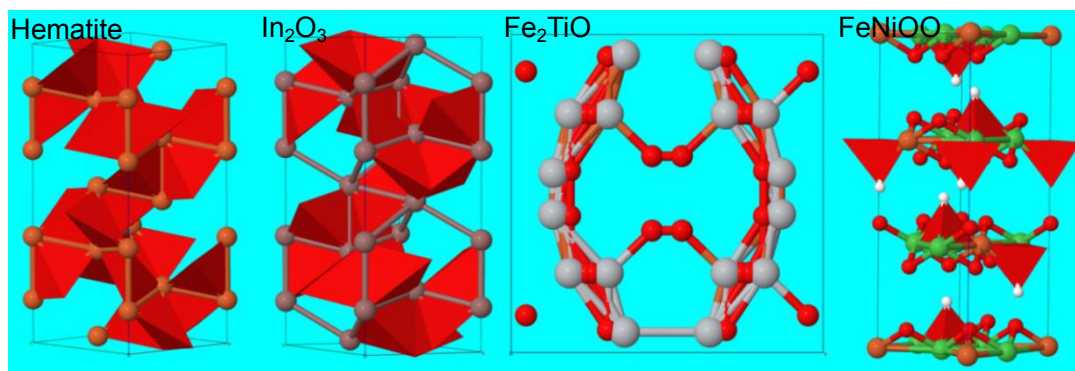


Figure 4.24. 1*1*1 unit crystal model of hematite, In_2O_3 , Fe_2TiO_5 and FeNiOOH based on the crystal data in ICSD for the identification of the crystal phase.

To identify each crystal phases via HRTEM and probe the spatial distribution of these components in the integrated electrodes, we created crystal models based on the single crystal data in the Inorganic Crystal Structure Database (ICSD), as displayed in **Figure 4.24**. With these crystal models, the diffraction patterns visualized from different zone axis of each phase can be simulated. The simulated diffraction pattern is compared with the power spectrum (FFT) obtained on the atomic resolution HRTEM experimental images for the identification of the crystal phases in the composite electrodes.

Figure 4.2 shows low magnification TEM images of the Fe_2O_3 electrode with nanowire-like morphology, while its HRTEM and detailed atomic structure are displayed in **Figure 4.25 A**. The corresponding temperature coloured power spectrum (**Figure 4.25 A** right) indicates that the structure corresponds to the trigonal Fe_2O_3 , [R3-CH]-Space group 167, also known as hematite, with lattice parameters of $a = b = 0.50342 \text{ nm}$, $c = 1.37483 \text{ nm}$, and $\alpha = \beta = 90^\circ$ and $\gamma = 120^\circ$ as visualized along the [21-2] direction. The HRTEM and atomic structure detail of the ITO/ Fe_2O_3 electrode in **Figure 4. 25B** demonstrate that the modification of FTO substrate with 105 nm ITO underlayer does not alter the crystal phase of the Fe_2O_3 nanowires. The temperature coloured power spectrum (right of **Figure 4.25 B**) obtained on the ITO/ Fe_2O_3 electrodes indicates that the nanowires retain their single crystal hematite nature as visualized along the [110] direction. This is further supported by **Figures 4.5** and **4.6**.

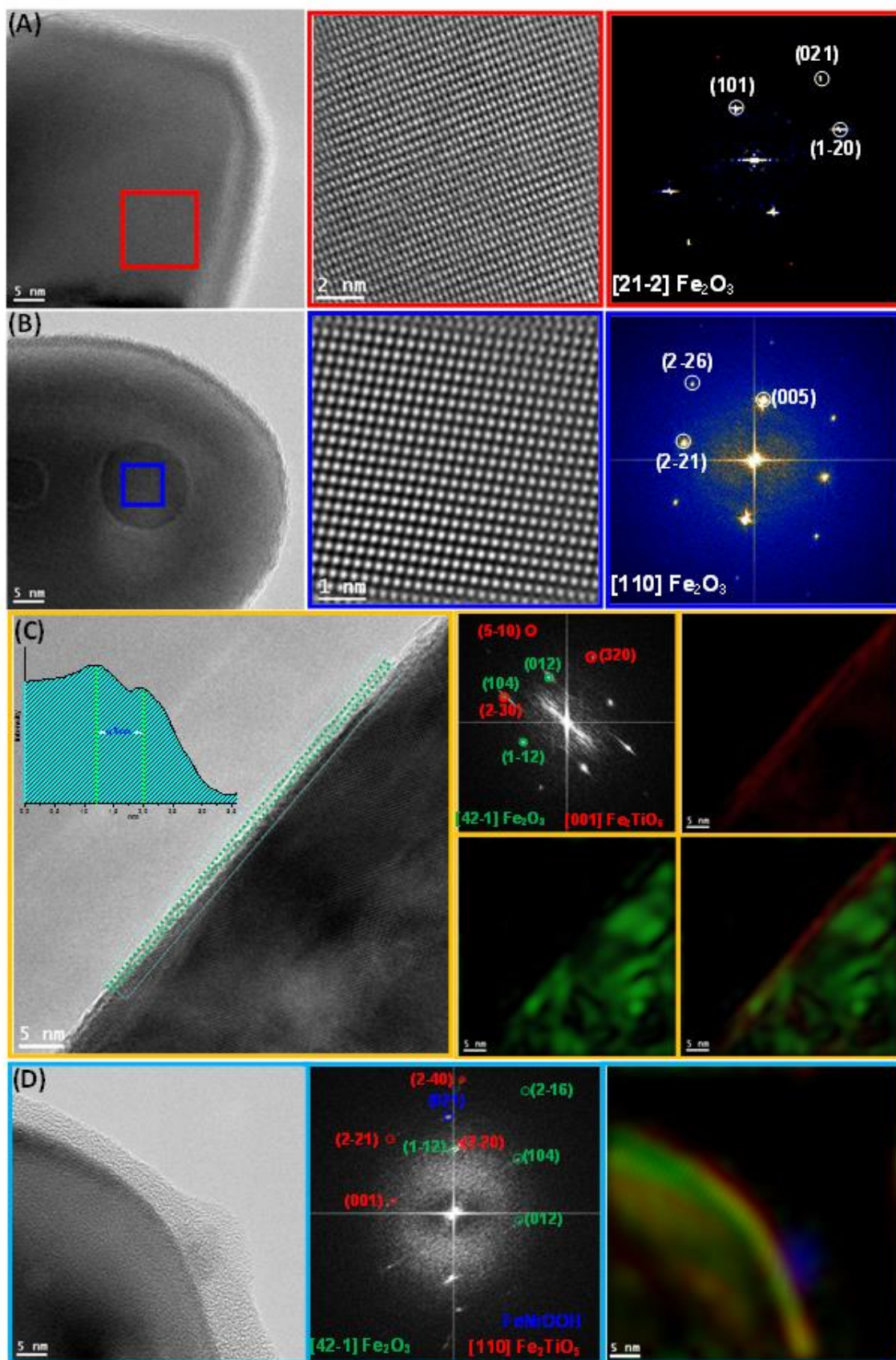


Figure 4.25. HRTEM, power spectrum and RGB coloured phase (frequency) filtered structural images of the Fe_2O_3 (A), $\text{ITO}/\text{Fe}_2\text{O}_3$ (B), $\text{ITO}/\text{Fe}_2\text{O}_3/\text{Fe}_2\text{TiO}_5$ (C) and $\text{ITO}/\text{Fe}_2\text{O}_3/\text{Fe}_2\text{TiO}_5/\text{FeNiOOH}$ (D)

electrodes.

Figure 4.25 C (left) shows a HRTEM image of the edge region of a single ITO/Fe₂O₃/Fe₂TiO₅ nanowire extracted from the ITO/Fe₂O₃/Fe₂TiO₅ electrode nanowire array. The corresponding power spectrum (**Figure 4.25 C** right) shows that the nanowire is composed of a hematite core (Fe₂O₃) and a Fe₂TiO₅ shell ([BBMM]-Space group 63, with lattice parameters of a= 0.9793 nm, b= 0.9979 nm, c= 0.3732 nm, and $\alpha = \beta = \gamma = 90^\circ$), as visualized along the [42-1] and [001] directions, respectively. RGB coloured phase filtered images corresponding to the selected area of ITO/Fe₂O₃/Fe₂TiO₅ electrode in **Figure 4.25 C** are exhibited on the right. **Figures 4.12 and 4.13** clearly confirm the homogenous coating of the Fe₂TiO₅ layer on the surface of the Fe₂O₃ nanowires. Moreover, the atomic density profile in the inset of the left HRTEM image in **Figure 4.25 C**, reveals that the thickness of the Fe₂TiO₅ shell is 0.78 ± 0.02 nm thick, in agreement with the estimated 0.81 nm from the ALD process. **Figure 4.25 D** displays a HRTEM image (left) of the electrode after the deposition of FeNiOOH to form the quaternary ITO/Fe₂O₃/Fe₂TiO₅/FeNiOOH structure. The presence of hematite and pseudobrookite phases was identified by their power spectrum (**Figure 4.25 D** middle). It is noteworthy that the crystal diffraction spots of FeNiOOH, while visible, are weak showing few crystallites (low magnification TEM images are displayed in **Figure 4.16**), consistent with the XRD results indicating that it is primarily amorphous.[45, 50-53] Moreover, the corresponding RGB phase filtered image (**Figure 4.25 D** right) illustrates the localized presence of hematite (nanowire core), pseudobrookite (shell) and FeNiOOH nanodot (surface crystallite in blue, showing a 0.256 nm plane distance corresponding to its (021) plane). [53-56]

The chemical composition of the interfaces in the ITO/Fe₂O₃/Fe₂TiO₅/FeNiOOH electrodes, were investigated by EELS SI using the K edge for O, M edges for In and Sn, and the L edges for Fe, Ti and Ni. The STEM-EELS composition maps of Fe₂O₃ (**Figure 4.2**), ITO/Fe₂O₃ (**Figure 4.7**) and ITO/Fe₂O₃/Fe₂TiO₅ (**Figure 4.13**) electrodes are included in the aforementioned composite electrode optimization part.

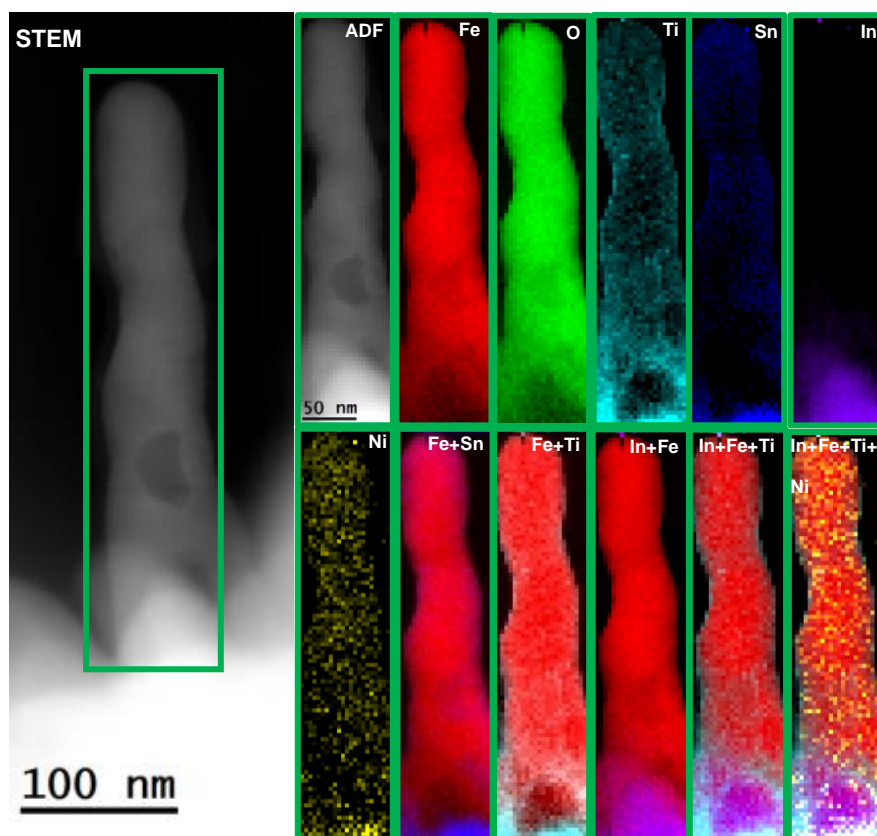


Figure 4.26 EELS chemical composition maps obtained from the green rectangular area on the ADF-STEM micrograph selected on one of the nanowires extracted from the ITO/Fe₂O₃/Fe₂TiO₅/FeNiOOH electrode sample. Individual Fe (red), O (green), Sn (blue), In (purple), Ti (indigo) and Ni (yellow) maps and their RGB composite.

As displayed in the STEM image of **Figure 4.26**, the Fe₂O₃/Fe₂TiO₅/FeNiOOH composite nanowire (green squared region) is grown directly onto the ITO matrix (brighter bottom region). The individual Fe, Sn and Fe+Sn RGB composite EELS maps in **Figure 4.26** show that the Sn from ITO matrix diffuses into the hematite nanowires, revealing an intensive Sn doping throughout the ITO/Fe₂O₃/Fe₂TiO₅/FeNiOOH electrode as compared to weak Sn signal detected in the nanowires corresponding to the Fe₂O₃ electrode (**Figure 4.2**). By contrast, In, in the form of In₂O₃, is only present in the bottom region of the electrode corresponding to the ITO under layer, as supported by the individual In and O EELS mappings shown in **Figure 4.26** and the HRTEM results in **Figure 4.5**. Together with the STEM-EELS maps obtained in the ITO/Fe₂O₃ electrode (**Figure 4.7**) and the ITO/ Fe₂O₃/Fe₂TiO₅

electrode (**Figure 4.13**), these data demonstrate that there is almost no In doping into the Fe_2O_3 nanowires upon the sputtering of the ITO underlayer, which is consistent with the XPS result. The Fe, Ti and Fe+Ti RGB composite EELS elemental maps obtained on the ITO/ Fe_2O_3 / Fe_2TiO_5 / FeNiOOH electrode (**Figure 4.26**) show a complete coverage of the ultrathin Fe_2TiO_5 shell over the Fe_2O_3 nanowires. The individual Fe, Ni and O EELS elemental maps illustrate the presence of discontinuously distributed FeNiOOH species decorating the nanowires surface, in good agreement with the nanodot-like FeNiOOH structure observed in **Figures 4.25 D, 4.16** and **4.17**. RGB composite EELS elemental maps of In+Fe, In+Fe+Ti and In+Fe+Ti+Ni together illustrate the successful construction of the quaternary ITO/ Fe_2O_3 / Fe_2TiO_5 / FeNiOOH heterojunction nanowires via the step-wise nanoengineered incorporation of ITO, Fe_2O_3 , Fe_2TiO_5 and FeNiOOH .

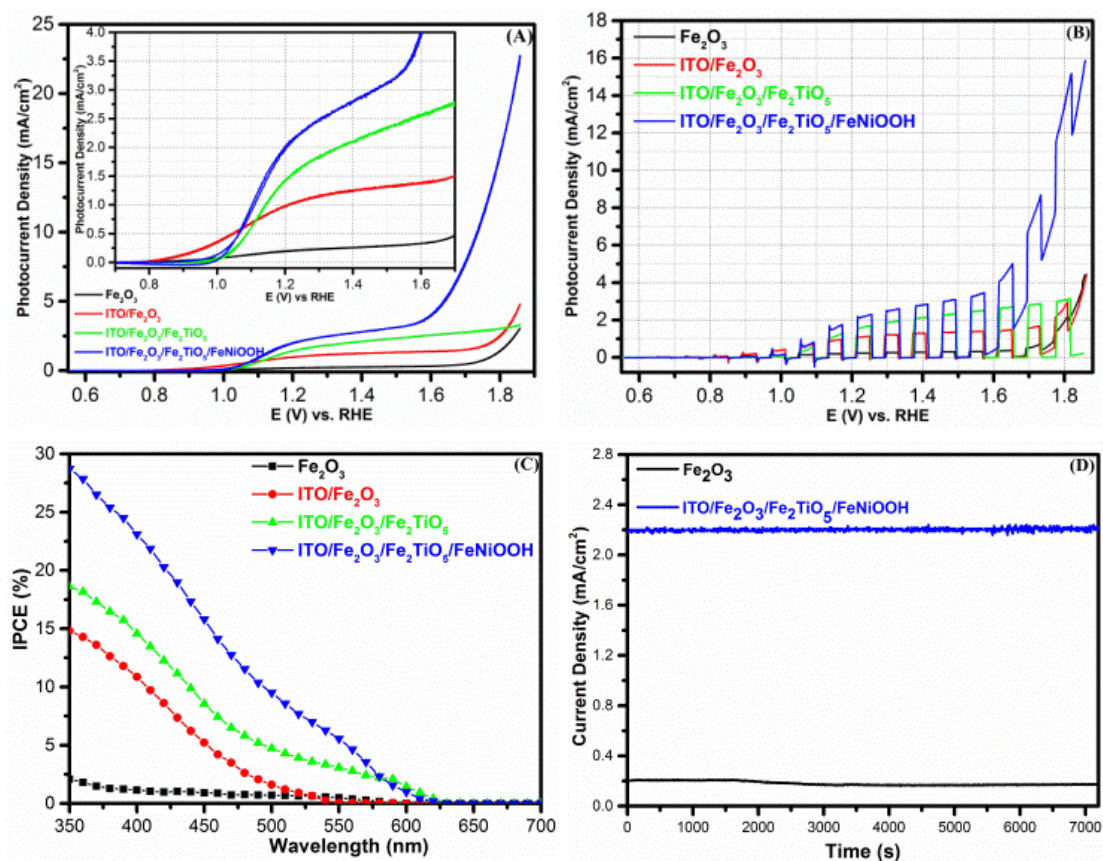


Figure 4.27 (A) Cyclic voltammetry (the inset shows its magnified plot), (B) chopped light photocurrent-potential curves, (C) IPCE and (D) photoelectrochemical stability test operated at 1.23 V vs RHE for the Fe_2O_3 , ITO/ Fe_2O_3 , ITO/ Fe_2O_3 / Fe_2TiO_5 , and ITO/ Fe_2O_3 / Fe_2TiO_5 / FeNiOOH electrodes.

All polarization potentials reported here are relative to the reversible hydrogen electrode (RHE), and current densities are per geometric area.

The optimum conditions for the integration of ITO/Fe₂O₃/Fe₂TiO₅/FeNiOOH electrodes and the different synthesis parameters (including ITO thickness, TiO₂ cycles, post-quench sintering conditions and FeNiOOH deposition charge) were examined in **sections 4.3.1-4.3.4**. For comparison, the PEC performance measured for the optimized four representative photoanodes is displayed in **Figure 4.27**. CVs of pristine Fe₂O₃ nanowires (**Figure 4.27 A**) show a relatively low photo-response over the whole potential window with a photocurrent density of 0.205 mA cm⁻² at 1.23 V vs RHE, thermodynamic potential for OER. Upon introduction of the ITO underlayer, the photocurrent density increases to 1.05 mA cm⁻² at 1.23V vs RHE. The onset potential of ITO/Fe₂O₃ still remains at 0.85 V, which is the same as that of the pristine Fe₂O₃ electrode. Besides, the CV curve of Fe₂O₃ and ITO/Fe₂O₃ electrodes at high potential region (over 1.7 V) exhibits the same trend, indicating the presence of similar Fe₂O₃|electrolyte interface. [15] In contrast, the ITO/Fe₂O₃/Fe₂TiO₅ electrode exhibits an anodic shift in the onset potential to 1.0 V vs RHE, along with an increase in the photocurrent density to 1.56 mA cm⁻² at 1.23 V vs RHE. The positive shift in the onset potential upon coating Fe₂TiO₅ onto the hematite nanowires is consistent with the results reported by J. Zhong et al. [54] While, the CV curve of ITO/Fe₂O₃/Fe₂TiO₅ electrodes at high potential region (over 1.7 V) is somehow suppressed compared with that of Fe₂O₃ and ITO/Fe₂O₃ electrodes, illustrating its SEI variation. Despite some improvement, the PEC performance for the ITO/Fe₂O₃/Fe₂TiO₅ nanowires remains unsatisfactory, likely caused by the slow water oxidation kinetics. [55] Thus, an optimized OEC, 10 mC FeNiOOH was deposited on the surface of the ITO/Fe₂O₃/Fe₂TiO₅ nanowires. In the case of ITO/Fe₂O₃/Fe₂TiO₅/FeNiOOH electrode, a cathodic shift in onset potential for OER to 0.95 V is observed relative to the ITO/Fe₂O₃/Fe₂TiO₅ electrode. Its photocurrent density of 2.2 mA cm⁻² at 1.23 V vs. RHE represents the highest value among these four photoanodes. The tremendous increment of the photocurrent at high potential region (over 1.6 V,

dominated by the dark current response from OEC) implies the successfully combination of the merits of the photocatalytic activity of ITO/Fe₂O₃/Fe₂TiO₅ and the electrocatalytic activity of FeNiOOH. [15] Besides, there is a photocurrent plateau for all electrodes, which is derived from the transition of hole acceptor from OH⁻ to water in the electrolyte according to the report of J.C. Zhao et al. [22] Furthermore, transient photocurrent measurements, based on the CVs under chopped light illumination, were performed for each photoanode. As shown in **Figure 4.27 B**, all electrodes exhibit a prompt and reproducible photocurrent response with respect to the irradiation signal ON-OFF cycles. The current density of these electrodes under illumination follows an ascending order as: Fe₂O₃ < ITO/Fe₂O₃ < ITO/Fe₂O₃/Fe₂TiO₅ < ITO/ Fe₂O₃/Fe₂TiO₅/FeNiOOH photoanodes. This is in high accordance with the CV results and further demonstrates the enhancement in PEC performance provided by the addition of ITO, Fe₂TiO₅ and FeNiOOH to the hematite nanowires.

The incident photon-to-current conversion efficiency (IPCE) was measured to understand the relationship between the photocatalytic activity and light absorption. All samples exhibit photocatalytic activity in the visible light region (**Figure 4.27 C**). Maximum IPCEs obtained at 350 nm, for Fe₂O₃, ITO/Fe₂O₃, ITO/Fe₂O₃/Fe₂TiO₅, and ITO/Fe₂O₃/Fe₂TiO₅/FeNiOOH photoanodes are 2.1%, 14.8%, 18.6%, and 28.7%, respectively. The large enhancement of IPCE for the ITO/Fe₂O₃/Fe₂TiO₅/FeNiOOH nanowires further supports the integrated coupling effect of ITO, Fe₂TiO₅ and FeNiOOH to the PEC performance. Additionally, the IPCE curves for all of these electrodes correlate with the UV-Vis absorption spectrum of Fe₂O₃ presented in **Figure 4.23 B**, indicating that the Fe₂O₃ indeed acts as the sole visible light responsive semiconductor material. Thus, the enhanced PEC performance is preliminary attributed to a synergistic effect between ITO, Fe₂O₃, Fe₂TiO₅ and FeNiOOH rather than the primitively tandem function of each semiconductor material. The photoelectrochemical stability is operated by chronopotentiometric response at a constant applied working potential of 1.23 V vs RHE, as shown in **Figure 4.27 D**. The photocurrent of Fe₂O₃ slightly decreases from 0.205 mA cm⁻² to 0.17 mA cm⁻² over

the course of the 2h experiment. In contrast, no photocurrent degradation was observed for the ITO/Fe₂O₃/ Fe₂TiO₅/FeNiOOH electrode during the stability test and maintained a photocurrent of 2.2 mA cm⁻² throughout, indicating its excellent stability.

4.3.7 Mechanism Investigation of Optimized Fe₂O₃, ITO/Fe₂O₃, ITO/Fe₂O₃/Fe₂TiO₅ and ITO/Fe₂O₃/Fe₂TiO₅/FeNiOOH Electrodes via PEIS

All the above results illustrate that the incorporation of ITO, Fe₂TiO₅ and FeNiOOH largely improve the PEC performance of the hematite nanowires photoanode. Given that a physical model of the illuminated SEI for SS-mediated, indirect hole transfer has been well established and occurs in two consecutive steps: (i) hole trapping by SS, and (ii) hole transfer from SS to water molecules at the SEI. [10, 23-24]

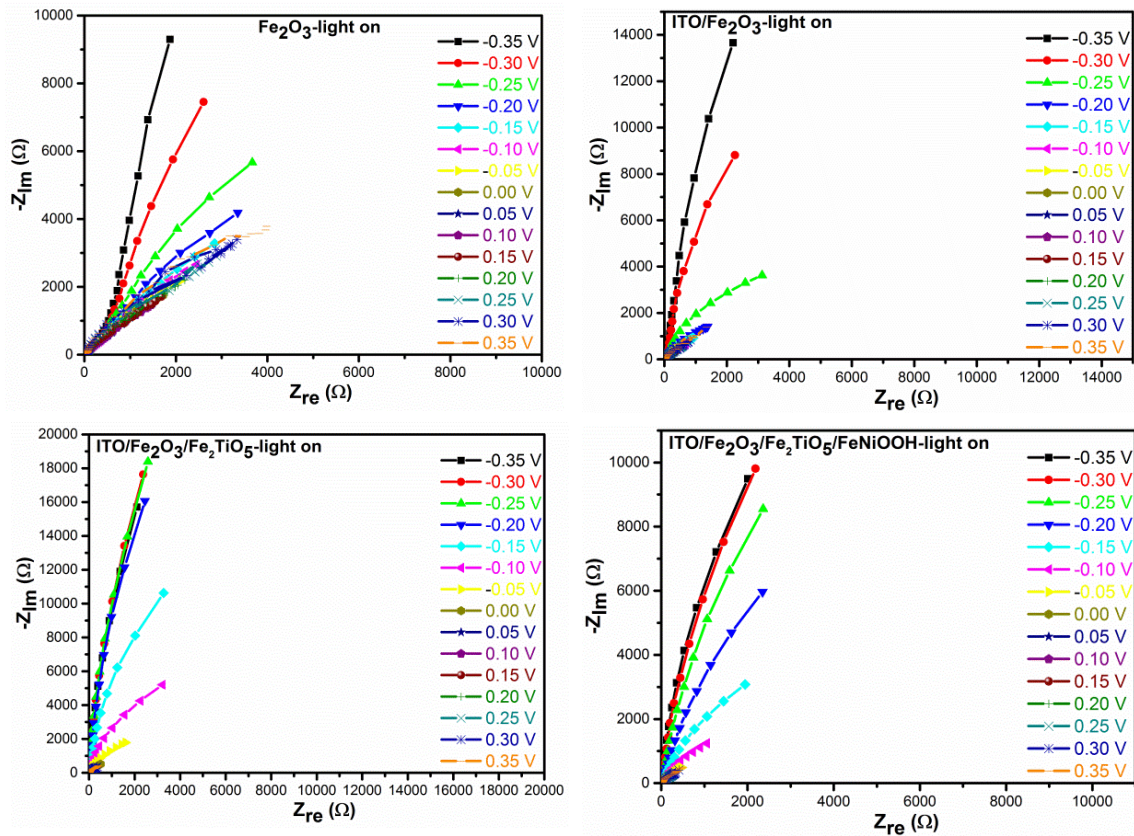


Figure 4.28 Nyquist (Imaginary vs. Real component of impedance) plots under light illumination of the Fe₂O₃, ITO/Fe₂O₃, ITO/Fe₂O₃/Fe₂TiO₅, and ITO/Fe₂O₃/Fe₂TiO₅/FeNiOOH electrodes at -0.35, -0.3, -0.25, -0.2, -0.15, -0.10, -0.05, 0.00, 0.05, 0.10, 0.15, 0.20, 0.25, 0.30 and 0.35 V vs. Ag/AgCl reference electrode. (Electrolyte: 1 M NaOH. AC amplitude: 5 mV. Frequency range: 100 mHz - 1MHz.)

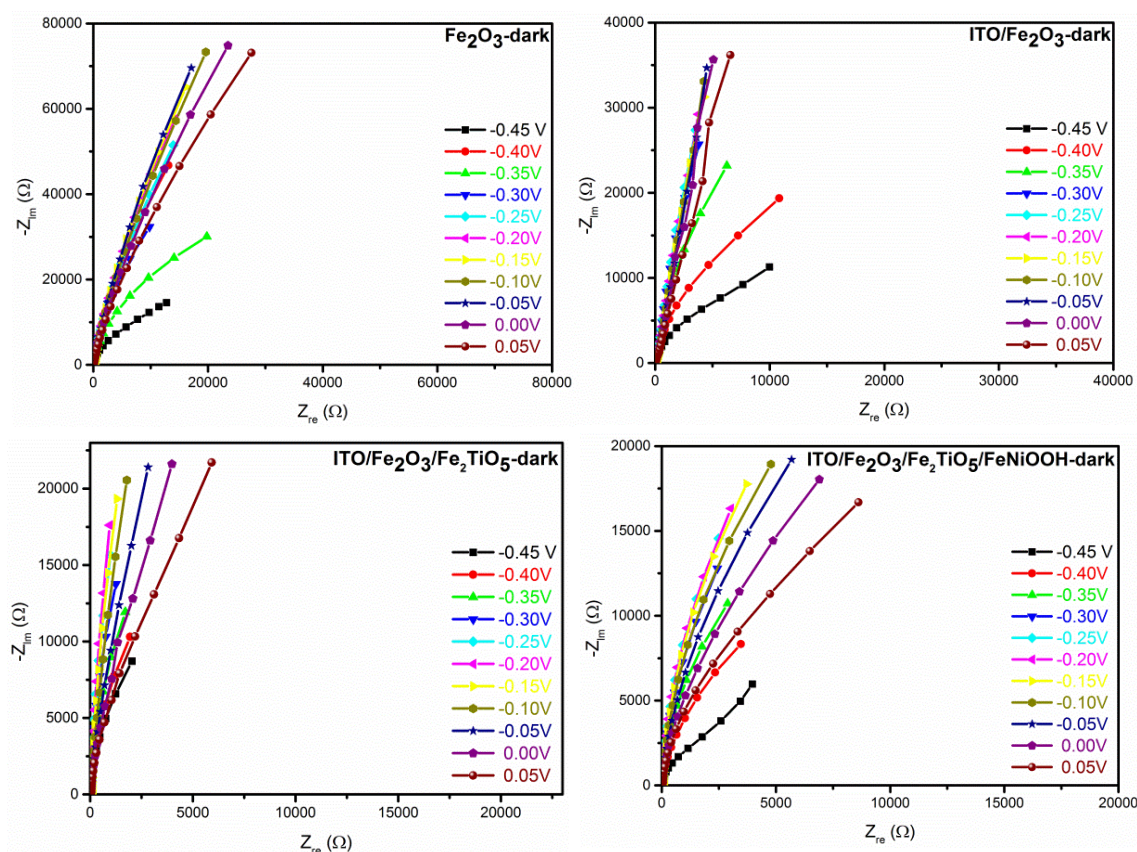
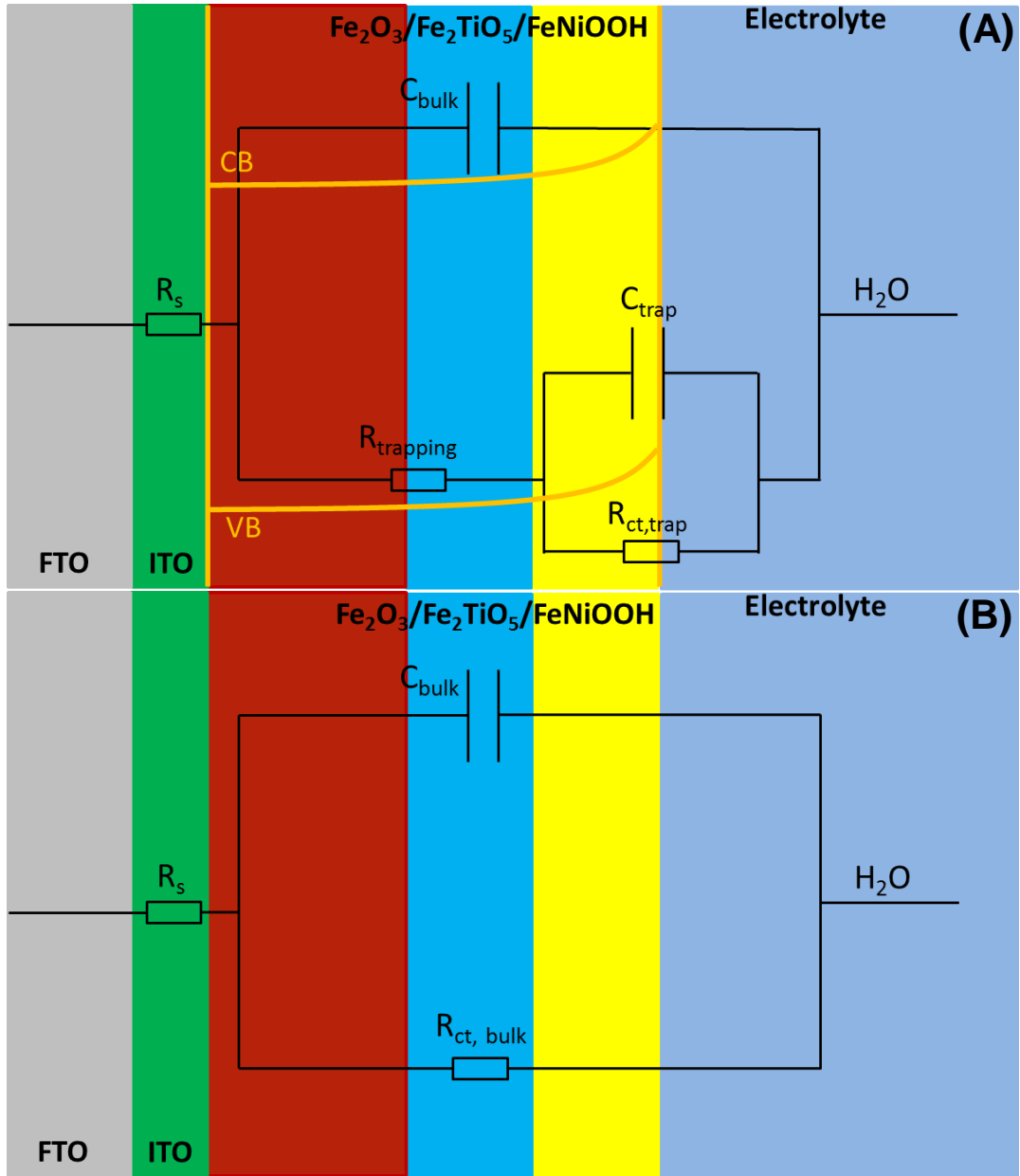


Figure 4.29 Nyquist (Imaginary vs. Real component of impedance) plots in the dark of the Fe_2O_3 , $\text{ITO}/\text{Fe}_2\text{O}_3$, $\text{ITO}/\text{Fe}_2\text{O}_3/\text{Fe}_2\text{TiO}_5$, and $\text{ITO}/\text{Fe}_2\text{O}_3/\text{Fe}_2\text{TiO}_5/\text{FeNiOOH}$ electrodes at -0.45, -0.4, -0.35, -0.3, -0.25, -0.2, -0.15, -0.10, -0.05, 0.00 and 0.05 V vs Ag/AgCl reference electrode. (Electrolyte: 1 M NaOH. AC amplitude: 5 mV. Frequency range: 100 mHz - 1MHz.)

To gain further insight into the mechanism of this interfacial coupling effect, primary PEIS (**Figures 4.28-4.29**) has been employed to identify the functions of the ITO, Fe_2O_3 , Fe_2TiO_5 and FeNiOOH in the integrated $\text{ITO}/\text{Fe}_2\text{O}_3/\text{Fe}_2\text{TiO}_5/\text{FeNiOOH}$ electrodes. PEIS measurements were performed at potentials, ranging from 0.65 V vs. RHE (before the onset of photocurrent) to 1.36 V vs RHE (before the light-flux limited photocurrent region) because the effect of SS is more prevalent when unaffected by the light-flux limited and dark oxygen evolution factors. [10] The obtained PEIS data was fitted based on the equivalent circuit displayed in the **Schematic 4.3A**.



Schematic 4.3 A: Equivalent circuit (EC) for the charge transfer process of hematite composite under illumination, the hematite composite/electrolyte interface is mediated by surface states. R_s , resistance associated with the electric contacts of the electrode, electrolyte, etc. $R_{trapping}$, resistance associated with charge trapping at surface states. C_{bulk} , capacitance associated with charge accumulation in the bulk. $R_{ct, trap}$, resistance associated with the charge transfer process from surface states. C_{trap} , capacitance associated with charge accumulation on the surface states. B: simple Randles circuit for the charge transfer process of hematite composite under dark. R_s , resistance associated with the electric contacts of the electrode, electrolyte, etc. In this case, the $C_{ct,trap}$ and R_{ct} are eliminated because there is no surface states mediated process under dark.

Typically, the R_s , series resistance includes the resistance at the interface between the FTO substrate, or ITO underlayer, and Fe_2O_3 nanowires. [9, 20] A substantial reduction in R_s is observed from ca. $70 \Omega \text{ cm}^{-2}$ for the pristine Fe_2O_3 electrode to ca. $35 \Omega \text{ cm}^{-2}$ for composite Fe_2O_3 electrodes modified with the ITO underlayer, as displayed in **Figure 4.30 A**. These results mean that the ITO underlayer is able to efficiently improve the back electrical contact and facilitate the electron transport from Fe_2O_3 to the FTO substrate. This improvement is attributed to the enhanced Sn doping in hematite nanowires [13-14] and the epitaxial relationship between the Fe_2O_3 and In_2O_3 phases, as demonstrated by the HRTEM and STEM-EELS maps results.

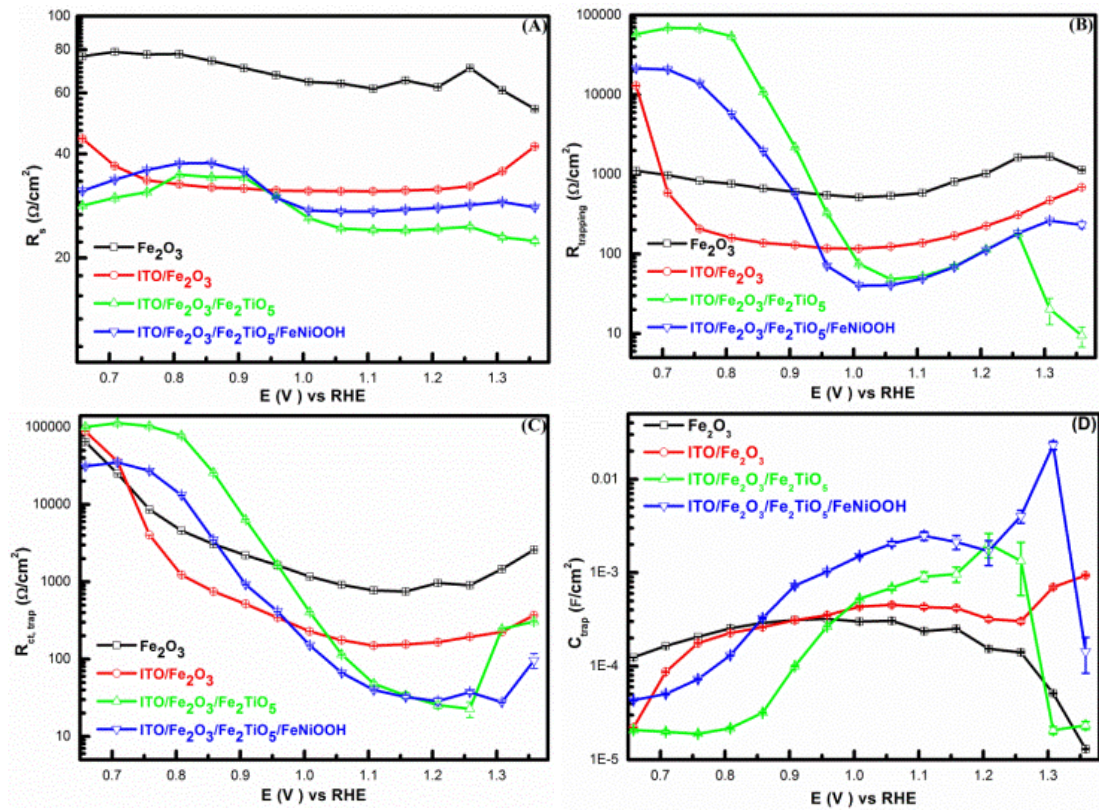


Figure 4.30 Equivalent circuit parameters obtained from fitting IS data for the optimized Fe_2O_3 , $\text{ITO}/\text{Fe}_2\text{O}_3$, $\text{ITO}/\text{Fe}_2\text{O}_3/\text{Fe}_2\text{TiO}_5$, and $\text{ITO}/\text{Fe}_2\text{O}_3/\text{Fe}_2\text{TiO}_5/\text{FeNiOOH}$ electrodes in contact with 1M NaOH electrolytes under 1 sun illumination. R_s (A), R_{trapping} (B), $R_{\text{ct,trap}}$ (C) and C_{trap} (D) as a function of the applied potential. R_s , resistance associated with the electric contacts of the electrode, electrolyte, etc. R_{trapping} , resistance associated with charge trapping at surface states. $R_{\text{ct,trap}}$, resistance associated with the charge transfer process from surface states. C_{trap} , capacitance associated with charge accumulation on the surface states.

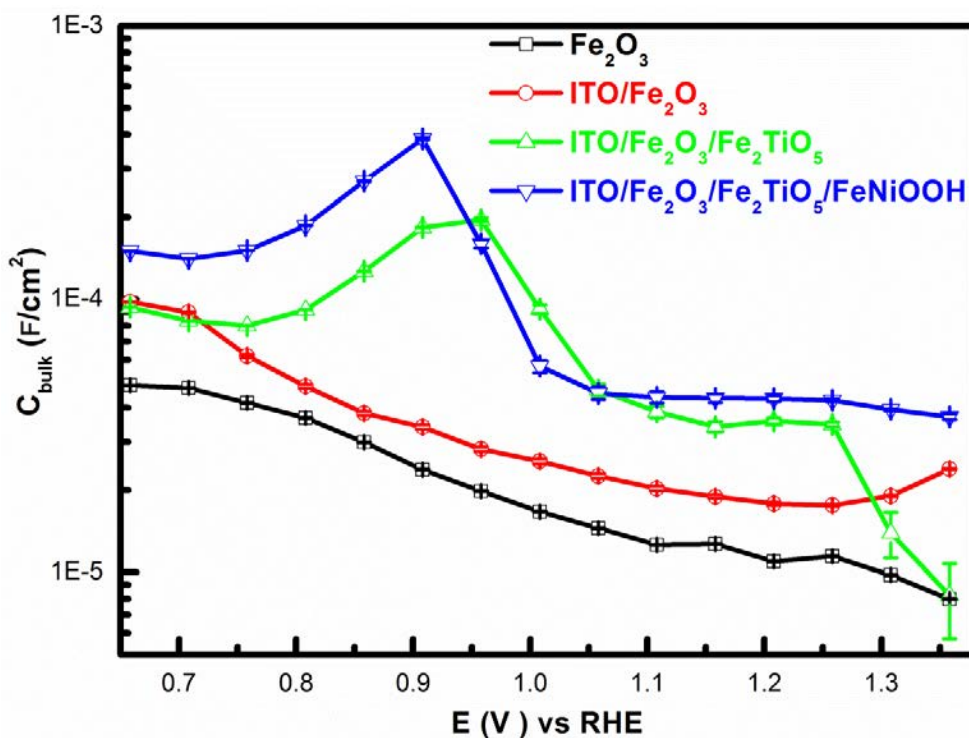


Figure 4.31 C_{bulk} of the optimized Fe_2O_3 , $\text{ITO}/\text{Fe}_2\text{O}_3$, $\text{ITO}/\text{Fe}_2\text{O}_3/\text{Fe}_2\text{TiO}_5$, and $\text{ITO}/\text{Fe}_2\text{O}_3/\text{Fe}_2\text{TiO}_5/\text{FeNiOOH}$ electrodes as a function of the applied potential obtained from fitting EIS data in contact with 1M NaOH electrolytes under 1 sun illumination. Error bars stem from the goodness of the EIS data fittings.

However, the capacitance associated with charge accumulation in the bulk (C_{bulk} , **Figure 4.31**) was measured to be on the same order of magnitude for these electrodes with the exception of an abrupt peak at ca. 0.9 V for $\text{ITO}/\text{Fe}_2\text{O}_3/\text{Fe}_2\text{TiO}_5$, and $\text{ITO}/\text{Fe}_2\text{O}_3/\text{Fe}_2\text{TiO}_5/\text{FeNiOOH}$ electrodes. It may be due to the addition of the ultrathin Fe_2TiO_5 shell, which slightly changes the electronic state of the electrodes.[36] **Figure 4.30 B** shows the lowest value of the R_{trapping} for the $\text{ITO}/\text{Fe}_2\text{O}_3/\text{Fe}_2\text{TiO}_5/\text{FeNiOOH}$ electrode as compared to the Fe_2O_3 , $\text{ITO}/\text{Fe}_2\text{O}_3$ and $\text{ITO}/\text{Fe}_2\text{O}_3/\text{Fe}_2\text{TiO}_5$ electrodes at the potential window (0.9 V to 1.36 V).[10] This is consistent with the correlation of a dip in the $R_{\text{ct,trap}}$ and a peak in the C_{trap} profile resulting in more efficient charge transfer kinetics during PEC.[56] Previous works by Hamann and coworkers,[21, 57-58] suggest that a large C_{trap} and a low $R_{\text{ct,trap}}$ would eventually render larger photocurrents, provided that the charge is transferred from SS to electrolyte. As shown in **Figure 4.30 C**, for each of these four electrodes, a gradual

decrease in $R_{ct,trap}$ is observed as the applied potential increases implying an increment of the associated photocurrent response. Notably, the ITO/Fe₂O₃/Fe₂TiO₅/FeNiOOH photoanode possess a relative minimum $R_{ct,trap}$ from 0.9 V to 1.25 V, in line with the larger photocurrent variation at this region dominated by SS (**Figure 4.27 A**). The $R_{ct,trap}$ at 1.25 V for ITO/Fe₂O₃/Fe₂TiO₅/FeNiOOH photoanode is ca. 34 times lower than that of the pristine Fe₂O₃ nanowires, further evidencing its best photocurrent response. While, the C_{bulk} (**Figure 4.31**) and C_{trap} (**Figure 4.30 D**) show opposite tendencies. With the potential increase, the C_{bulk} decreases, whereas the C_{trap} increases, implying a larger percentage of charge located on SS; similarly, a relative optimum value (C_{trap}/C_{bulk} at 1.23 V vs RHE) is observed in the ITO/Fe₂O₃/Fe₂TiO₅/FeNiOOH electrode.

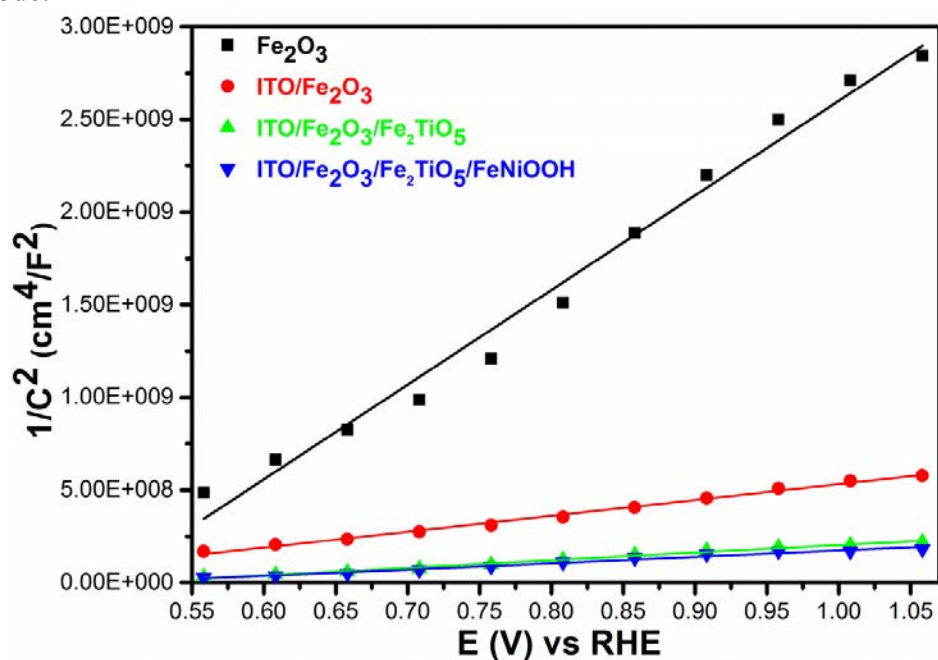


Figure 4.32 Mott-Schottky plots (C^{-2} vs. E) of the Fe₂O₃, ITO/Fe₂O₃, ITO/Fe₂O₃/Fe₂TiO₅, and ITO/Fe₂O₃/Fe₂TiO₅/FeNiOOH electrodes. Each point was obtained upon fitting the corresponding Nyquist plot at each potential in the dark to a classic Randles circuit (i.e. resistance and capacitance in parallel). Linear fittings (obtained in the 0.55-1.05 V vs. RHE potential range) are also depicted on each case. Electrolyte: 1 M NaOH. AC amplitude: 5 mV. Frequency range: 100 mHz - 1 MHz.

In order to gain further information on the bulk of composite hematite nanowires, impedance measurements were performed in the dark to derive the corresponding Mott-Schottky plots. Upon fitting the Nyquist plots to a Randles circuit (**Schematic**

4.3B), the potential-dependent capacitances were plotted following the Mott-Schottky model (C^{-2} vs. E). When this model holds, equation (6) is used to fit the plots:

$$\frac{1}{C^2} = \frac{2}{e\epsilon\epsilon_r N_D} \left(E - E_{fb} - \frac{kT}{e} \right) \quad (6)$$

where N_D is the charge donor density (cm^{-3}), E_{fb} is the flat band potential (V), ϵ is the vacuum permittivity ($8.85 \times 10^{-12} \text{ F m}^{-1}$), ϵ_r is the relative dielectric constant of hematite ($\epsilon_r = 32$), k is the Boltzmann constant ($1.38 \times 10^{-23} \text{ J K}^{-1}$) and T is the absolute temperature (K).

Table 4.1 Flat band potential values (E_{fb}), bulk donor densities (N_d) and total surface state density (N_{ss}) of the Fe_2O_3 , ITO/ Fe_2O_3 , ITO/ $\text{Fe}_2\text{O}_3/\text{Fe}_2\text{TiO}_5$, and ITO/ $\text{Fe}_2\text{O}_3/\text{Fe}_2\text{TiO}_5/\text{FeNiOOH}$ electrodes. E_{fb} and N_D values were respectively estimated from the x-intercepts (at $C^{-2} = 0$) and slopes of the Mott-Schottky plots.

Samples	N_d/cm^{-3}	$E_{fb}/\text{V vs. RHE}$	N_{ss}/cm^{-2}
Fe_2O_3	4.60E+18	0.465	9.53E+14
ITO/ Fe_2O_3	2.75E+19	0.353	1.54E+15
ITO/ $\text{Fe}_2\text{O}_3/\text{Fe}_2\text{TiO}_5$	5.80E+19	0.475	2.17E+15
ITO/ $\text{Fe}_2\text{O}_3/\text{Fe}_2\text{TiO}_5/\text{FeNiOOH}$	6.89E+19	0.468	1.23E+16

Figure 4.32 and **Table 4.1** reveal that the bulk donor density for the ITO/ Fe_2O_3 electrode ($2.75\text{E}+19 \text{ cm}^{-3}$) is 6 times higher than that for the pristine Fe_2O_3 electrode ($4.60\text{E}+18 \text{ cm}^{-3}$). This effect is derived from the enhanced Sn doping in the hematite nanowires that results from the addition of the ITO underlayer and is in good agreement with the significantly improved photocurrent response of the ITO/ Fe_2O_3 electrode.[13-14] With the coating of the Fe_2TiO_5 onto the ITO/ Fe_2O_3 electrode, the bulk donor density is further improved to $5.80\text{E}+19 \text{ cm}^{-3}$, indicating that there may be a small amount of Ti doping in the Fe_2O_3 nanowires and thus additional photocurrent enhancement (1.56 mA cm^{-2}) observed for the ITO/ $\text{Fe}_2\text{O}_3/\text{Fe}_2\text{TiO}_5$ electrode.[10]

The general behaviour of the integrated multi-layer nanowires has been interpreted

and phenomenologically correlated with the SS; a deeper investigation of the photo-induced processes (i.e. charge generation and the subsequent transport to and transfer from the interfaces) is required to elucidate the interfacial charge transfer mechanism. In order to highlight the role of SS in the interfacial charge transfer process, we calculated the values for the density of surface states (DOSS) from the C_{trap} using equation (7): [10, 21]

$$N_{\text{SS}}(E) = C_{\text{trap}}(E)/q \quad (7)$$

Where $N_{\text{SS}}(E)$ is the DOSS ($\text{cm}^{-2} \text{eV}^{-1}$) as a function of the applied potential and q is the electron charge ($1.602 \times 10^{-19} \text{ C}$). As shown in **Figure 4.33**, it is possible to observe the SS energy distribution located below the photocurrent onset with its Fermi level pinned at SS. [21]

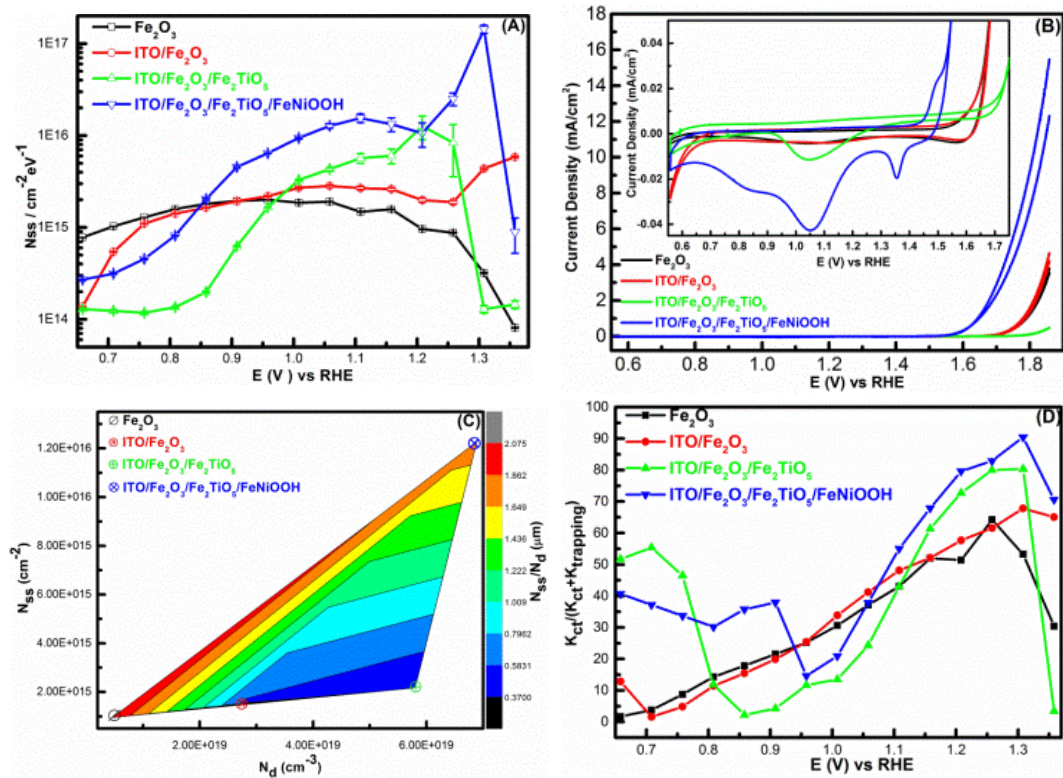


Figure 4.33 (A): Density of surface states (DOSS) as a function of the applied potential on the Fe_2O_3 , $\text{ITO}/\text{Fe}_2\text{O}_3$, $\text{ITO}/\text{Fe}_2\text{O}_3/\text{Fe}_2\text{TiO}_5$, and $\text{ITO}/\text{Fe}_2\text{O}_3/\text{Fe}_2\text{TiO}_5/\text{FeNiOOH}$ electrodes. Error bars stem from the goodness of the EIS data fittings. (B): CV curves scanned in dark at 20 mV s^{-1} immediately after holding the electrode potential at 1.85V vs. RHE. for 1 min under illumination of Fe_2O_3 , $\text{ITO}/\text{Fe}_2\text{O}_3$, $\text{ITO}/\text{Fe}_2\text{O}_3/\text{Fe}_2\text{TiO}_5$, and $\text{ITO}/\text{Fe}_2\text{O}_3/\text{Fe}_2\text{TiO}_5/\text{FeNiOOH}$ electrodes. (The inset shows its magnified plot).

(C): Total surface state density (N_{SS}), donor density (N_d), and their ratio (N_{SS}/N_d) for Fe_2O_3 , ITO/ Fe_2O_3 , ITO/ Fe_2O_3/Fe_2TiO_5 , and ITO/ $Fe_2O_3/Fe_2TiO_5/FeNiOOH$ electrodes. N_d was estimated from the slopes of the Mott-Schottky plots in the dark, whereas N_{SS} was obtained from integration of DOSS profiles (**Figure 4.33 A**). A colour bar with a unit of μm is plotted at right Y axis for N_{SS}/N_d . (D): Ratio of the charge transfer rate constant (k_{ct}) and the sum of k_{ct} and trapping rate constant ($k_{trapping}$) at different potential.

Our previous report [10] has demonstrated that there is a direct correlation between the percentage of available filled surface states (larger DOSS) near the thermodynamic potential for OER, and the observed photocurrent response at 1.23 V vs. RHE due to the required isoenergetic hole transfer process at the SEI. [21, 59] As displayed in **Figure 4.33 A**, the N_{SS} of the four photoanodes follows the order: $Fe_2O_3 < ITO/Fe_2O_3 < ITO/Fe_2O_3/Fe_2TiO_5 < ITO/Fe_2O_3/Fe_2TiO_5/FeNiOOH$ across the entire SS dominated region (0.9 V to 1.36 V). The extended SS distribution from 0.65 V to 1.36 V in Fe_2O_3 and ITO/ Fe_2O_3 electrodes probably spans inside the CB and triggers a deleterious Fermi level pinning at SS, which could be responsible for their relatively low photocurrent response. Moreover, the potential of the DOSS peak for the photoanodes shifts to more positive values, e.g., 0.9 V, 0.95 V, 1.25 V for the Fe_2O_3 , ITO/ Fe_2O_3 , ITO/ Fe_2O_3/Fe_2TiO_5 electrodes, respectively. Interestingly, the DOSS curve for the ITO/ $Fe_2O_3/Fe_2TiO_5/FeNiOOH$ electrode displays two peaks located at ca. 1.1 V and 1.3 V. This peak splitting phenomenon displayed by the ITO/ $Fe_2O_3/Fe_2TiO_5/FeNiOOH$ photoanode was further investigated by obtaining the CV curves scanned in the cathodic direction in dark at 20 mV s^{-1} of these electrodes immediately after holding the electrode potential at 1.85 V vs. RHE. for 1 min under illumination to photoelectrochemically oxidize the surface states. [26, 29, 60] As displayed in **Figure 4.33 B**, for the ITO/ $Fe_2O_3/Fe_2TiO_5/FeNiOOH$ electrode, two cathodic peaks appear at around 1.05 V and 1.35 V, which is relatively consistent with the DOSS peaks position for the ITO/ $Fe_2O_3/Fe_2TiO_5/FeNiOOH$ electrode. Besides, T. Hamann et al. has quantitatively correlated the C_{trap} measured by both cyclic voltammetry and impedance spectroscopy with the absorption peak at 572 nm via operando UV-vis

experiments, corresponding to the formation of Fe (IV) intermediate. [29] The splitting of one C_{trap} peak into two C_{trap} peaks were also observed upon ultra-thin ALD aluminium layer onto the hematite film, which is derived from the insufficient covering of aluminium overlayer and partial exposure of the hematite film.[29] Moreover, H. Irie et al. conducted preliminary in-situ UV-Vis absorption spectra of FeNiOOH; and the incorporation of Fe into the NiOOH was found to induce an increase in absorption peak similar to that observed for hematite electrode, demonstrating the formation of an Fe(IV) intermediate in the FeNiOOH during the electrochemical test. [30] In our case, the DOSS peak splitting performance of the ITO/Fe₂O₃/Fe₂TiO₅/FeNiOOH electrode can be attributed to the incomplete coverage of FeNiOOH nanodots on the nanowire surface in a manner consistent with the aluminium coated hematite reported by T. Hamann et al. [29] The peak located at 1.1 V vs RHE likely arises from Fe^{IV}=O surface intermediates on partially exposed Fe₂TiO₅ coating, [31] as the same DOSS peak is observed for the ITO/Fe₂O₃/Fe₂TiO₅ electrode. The DOSS peak located at 1.3 V can then be assigned to the Fe^{IV}=O intermediates localized on the discontinuously distributed FeNiOOH nanodots. [30] In brief, the atomic level of Fe₂TiO₅ and FeNiOOH nanodots coatings can regulate the surface state density and energy level of hematite nanowires, which is probably attributed to the chemical environment variation of Fe^{IV}=O intermediates. After all, the identification of OER active sites in the integrated hematite photoanode and further insights about the evolution of Fe^{IV}=O intermediates in these electrodes will need in-situ TEM experiments, [61-62] which is beyond the scope of this work.

A combined comparison of the N_{ss} , N_{d} and $N_{\text{SS}}/N_{\text{d}}$ ratio is presented in **Figure 4.33 C** and **Table 4.1**. A large $N_{\text{SS}}/N_{\text{d}}$ ratio does not ensure a good photoactivity because the number of donors in the hematite nanowires may not be high enough to endue the nanowires with good conductivity. This is demonstrated by the pristine Fe₂O₃ electrode which displays a high $N_{\text{SS}}/N_{\text{d}}$ ratio but poor PEC performance. In stark contrast, ITO/Fe₂O₃ and ITO/Fe₂O₃/Fe₂TiO₅ electrodes display a relatively low $N_{\text{SS}}/N_{\text{d}}$ ratio which possess enough donors in the nanowires to provide good

conductivity, but a lack of surface reactive sites still limit the PEC performance of these electrodes. In the case of the ITO/Fe₂O₃/Fe₂TiO₅/FeNiOOH electrode, a relatively high N_{SS}/N_d ratio corresponds to an scenario in which N_{SS} and N_d are both numerous enough to give a larger photocurrent response. In addition, the charge transfer efficiency at the SEI is estimated through (equation (8)): [10, 20]

$$\text{Transfer efficiency(\%)} = \frac{k_{ct}}{k_{ct}+k_{trapping}} = \frac{R_{trapping}}{R_{ct,trap}+R_{trapping}} \quad (8)$$

Where k_{ct} and $k_{trapping}$ are the charge transfer and trapping rate constants, respectively. The charge transfer efficiency obtained from the PEIS data is shown in **Figure 4.33 D**. The abnormally high transfer efficiency (TE) in the low applied potential region (before the onset potential) might be due to deviations of the charge transfer kinetic models at the region, where the effect of SS is less prevalent.[10, 63] In essence, although the application of ITO underlayer provides an additional Sn doping amount, it does not affect the rate of surface electron-hole recombination at Fe₂O₃|electrolyte interface, evidenced by the same trend of TE values in the Fe₂O₃ and ITO/Fe₂O₃ electrodes. In both cases, significant surface electron-hole recombination is expected. The surface electron-hole recombination in the ITO/Fe₂O₃/Fe₂TiO₅ and ITO/Fe₂O₃/Fe₂TiO₅/FeNiOOH electrodes has been suppressed; and in the case of the ITO/Fe₂O₃/Fe₂TiO₅/FeNiOOH electrode, over 80 % of the holes are being transferred into the electrolyte at 1.23V vs RHE. The calculated TE values of these electrodes also agree well with the steady-state current-voltage relationship (**Figure 4.27 A**). Our result here highlights the effectiveness of the atomic level Fe₂TiO₅ and FeNiOOH nanodots coating on regulating the surface state density and energy level of hematite nanowires as well as reducing the surface electron-hole recombination rate to speed up its water oxidation rate.

Table 4.2 Photoelectrochemical performance comparison of hematite-based electrodes.

Reference no.	Materials	Fabrication methods	Photocurrent at 1.23 V vs RHE

			(mA/cm ²)
[10]	Fe ₂ O ₃ /Fe ₂ TiO ₅	Sol-gel	1.35
[64]	Fe ₂ O ₃ /molecular Ir catalyst	Hydrothermal, soaking reaction	0.66
[65]	Fe ₂ O ₃ /NiO _x	Hydrothermal, photoelectrodeposition	0.6
[66]	Fe ₂ O ₃ /Fe-Pi	Hydrothermal, furnace heating	0.8
[67]	Fe ₂ O ₃ /TiO ₂	Hydrothermal, CBD	1.3
[68]	Fe ₂ O ₃ /graphene	Hydrothermal, CBD	0.5
[69]	Fe ₂ O ₃	Hydrothermal	0.8
[70]	C/Co ₃ O ₄ -Fe ₂ O ₃	Hydrothermal, electrodeposition	1.48
[8]	Fe ₂ O ₃ /TiO ₂	Thermal oxidation, lithography	0.45
[71]	Mesoporous Fe ₂ O ₃	Chemical etching	0.61
[72]	Fe ₂ O ₃ film	Spray pyrolysis	0.65
[73]	Fe ₂ O ₃ /FeOOH	PLD, photodeposition	0.85
[74]	TiO ₂ /Fe ₂ O ₃ /Ni(OH) ₂	ALD, hydrothermal, dipping	0.3
[12]	Fe ₂ O ₃ /TiO _x /FeOOH	Hydrothermal, electrodeposition	1.5
[75]	Co-N _x P doped carbon/graphene/Fe ₂ O ₃	Hydrothermal, chemical bath	2.15
[76]	Acid etched Fe ₂ O ₃	Chemical etching	1.0
[77]	Fe ₂ O ₃ /FeOOH	Hydrothermal, chemical bath	1.21
[78]	Fe ₂ O ₃ /TiO ₂	PE-CVD, ALD	1.8
[79]	Fe ₂ O ₃ /ZrO ₂ /Co-Pi	Hydrothermal, ALD, photo-electrodeposition	1.87
[80]	Fe ₂ O ₃ /IrO _x	Hydrothermal, Soaking	0.7
[81]	Fe ₂ O ₃	Electrodeposition	1.0
[56]	Fe ₂ O ₃ /Fe ₂ TiO ₅	Hydrothermal	1.4
[82]	Fe ₂ O ₃ /cobalt phosphate	Reactive ballistic and photo depositions	2.0
[83]	Fe ₂ O ₃ /NiO _x	Hydrothermal, photodeposition	0.6
[84]	Fe ₂ O ₃ /SiO ₂ /Sn doping	Hydrothermal, Chemical bath	2.0
Our work	ITO/Fe ₂ O ₃ /Fe ₂ TiO ₅ /FeNiOOH	Sputtering, Hydrothermal, ALD, photoelectrodeposition	2.20
[85]			

4.4 Summary

In summary, an electrode composed of ITO/Fe₂O₃/Fe₂TiO₅/FeNiOOH nanowires with a quaternary multilayer heterostructure has been successfully integrated by a stepwise deposition of ITO underlayer, ultrathin Fe₂TiO₅ and FeNiOOH nanodots onto Fe₂O₃ nanowires. The resulting quaternary multilayer nanowires exhibit significantly enhanced PEC performance, such as a large photocurrent (2.2 mA cm⁻²), which is even higher than the photocurrent response of recently reported state-of-the-art Fe₂O₃ composite photoanodes (**Table 4.2**). A deep and careful investigation into the mechanism responsible for the enhanced PEC performance has been conducted. These studies show that: (i) the ITO underlayer is used as a high quality electrical back contact to reduce the back-contact interface charge recombination and as a Sn doping source for tuning the donor density, (ii) the atomic level Fe₂TiO₅ coating, serves as the surface state density and energy level modulation layer and effectively suppresses the charge recombination at the semiconductor junction interface, (iii) the FeNiOOH nanodots, increase the surface active sites, and thus accelerate the OER kinetics at the SEI. The interfacial coupling effect between the ITO underlayer, the ultrathin Fe₂TiO₅ and the FeNiOOH nanodots in the ITO/Fe₂O₃/Fe₂TiO₅/FeNiOOH photoanodes simultaneously enhances the charge separation and water oxidation efficiency, and suggests a path forward to design improved integrated photoanodes.

References

- [1] K. Sivula, R. V. D. Krol. Semiconducting materials for photoelectrochemical energy conversion, *Nature Rev. Mater.*, **2016**, 1, 15010.
- [2] S. H. Shen, S. A. Lindley, X. Y. Chen, J. Z. Zhang, Hematite heterostructures for photoelectrochemical water splitting: rational materials design and charge carrier dynamics, *Energy Environ. Sci.*, **2016**, 9, 2744 -2775.
- [3] Z. Q. Huang, Y.J. Lin, X. Xiang, W. Rodríguez-Córdoba, K. J. McDonald, K. S. Hagen, K. S. Choi, B. S. Brunschwig, D. G. Musaev, C. L. Hill, D.W. Wang, T.Q. Lian, In situ probe of photocarrier dynamics in water-splitting hematite (α -Fe₂O₃) electrodes, *Energy Environ. Sci.*, **2012**, 5, 8923-8926.
- [4] S. R. Pendlebury, A. J. Cowan, M. Barroso, K. Sivula, J. H. Ye, M. Grätzel, D. R. Klug, J. W. Tang, J. R. Durrant, Correlating long-lived photogenerated hole populations with photocurrent densities in hematite water oxidation photoanodes, *Energy Environ. Sci.*, **2012**, 5, 6304-6312.
- [5] T. A. Pham, Y. Ping, G. Galli, Modelling heterogeneous interfaces for solar water splitting, *Nature Mater.*, **2017**, 16, 401-408.
- [6] J. T. Li, S. K. Cushing, P. Zheng, F.K. Meng, D. Chu, N.Q. Wu, Plasmon-induced photonic and energy-transfer enhancement of solar water splitting by a hematite nanorod array, *Nature Commun.*, **2013**, 4, 2651.
- [7] M. E. McBriarty, G. F. V. Rudorff, J. E. Stubbs, P. J. Eng, J. Blumberger, K. M. Rosso, Dynamic stabilization of metal oxide-water interfaces, *J. Am. Chem. Soc.*, **2017**, 139, 2581-2584.
- [8] B. Iandolo, B. Wickman, E. Svensson, D. Paulsson, A. Hellman, Tailoring charge recombination in photoelectrodes using oxide nanostructures, efficient photoelectrochemical water splitting with ultrathin films of hematite on three-dimensional nanophotonic structures, *Nano Lett.* **2016**, 16, 2381-2386.
- [9] Y. C. Qiu, S. F. Leung, Q. P. Zhang, B. Hua, Q. F. Lin, Z. H. Wei, K. H. Tsui, G. Zhang, S. H. Yang, Z. Y. Fan, Efficient photoelectrochemical water splitting with ultrathin films of hematite on three-dimensional nanophotonic structures, *Nano Lett.* **2014**, 14, 2123-2129.
- [10] D. M. Satoca, M. Bartsch, C. Fabrega, A. Genç, S. Reinhard, T. Andreu, J. Arbiol, M. Niederberger, J.R. Morante, What do you do, titanium? Insight into the role of titanium oxide as a water oxidation promoter in hematite-based photoanodes, *Energy Environ. Sci.*, **2015**, 8, 3242-3254.
- [11] Y.J. Lin, S. Zhou, S. W. Sheehan, D.W. Wang, Nanonet-based hematite heteronanostructures for efficient solar water splitting, *J. Am. Chem. Soc.* **2011**, 133, 2398-2401.
- [12] I. S. Cho, H. S. Han, M. Logar, J. Park, X. L. Zheng, Enhancing low-bias performance of hematite photoanodes for solar water splitting by simultaneous reduction of bulk, interface, and surface recombination pathways, *Adv. Energy Mater.* **2015**, 1501840.
- [13] A. Annamalai, A. Subramanian, U. Kang, H. Park, S. H. Choi, J. S. Jang, Activation of hematite photoanodes for solar water splitting: Effect of FTO deformation, *J. Phys. Chem. C*, **2015**, 119, 3810-3817.
- [14] P. S. Shinde, A. Annamalai, J. H. Kim, S. H. Choi, J. S. Lee, J. S. Jang, Exploiting the dynamic Sn

diffusion from deformation of FTO to boost the photocurrent performance of hematite photoanodes, *Sol. Energy Mater. Sol. Cells*, **2015**, 141, 71-79.

[15] L.J. Han, P.Y. Tang, A. Reyes-Carmona, B. Rodriguez-Garcia, M. Torrens, J. R. Morante, J. Arbiol, J. R. Galan-Mascaros, Enhanced activity and acid pH stability of Prussian blue-type oxygen evolution electrocatalysts processed by chemical etching, *J. Am. Chem. Soc.*, **2016**, 138, 16037-16045.

[16] F. Song, X. Hu, Exfoliation of layered double hydroxides for enhanced oxygen evolution catalysis, *Nat. Commun.* **2014**, 5, 4477.

[17] Y. Zhao, X. Jia, G. Chen, L. Shang, G. I. Waterhouse, L. Z. Wu, C. H. Tung, D. O'Hare, T. Zhang, Ultrafine NiO nanosheets stabilized by TiO₂ from monolayer NiTi-LDH precursors: An active water oxidation electrocatalyst, *J. Am. Chem. Soc.* **2016**, 138, 6517-6524.

[18] T. W. Kim, K. S. Choi, Nanoporous BiVO₄ photoanodes with dual-layer oxygen evolution catalysts for solar water splitting, *Science*, **2014**, 343, 990-994.

[19] L. Wang, F. Dionigi, N. T. Nguyen, R. Kirchgeorg, M. Gliech, S. Grigorescu, P. Strasser, P. Schmuki, Tantalum nitride nanorod arrays: Introducing Ni-Fe layered double hydroxides as a cocatalyst strongly stabilizing photoanodes in water splitting, *Chem. Mater.* **2015**, 27, 2360-2366.

[20] K. G. U. Wijayantha, S. Saremi-Yarahmadi, L. M. Peter, Kinetics of oxygen evolution at α -Fe₂O₃ photoanodes: a study by photoelectrochemical impedance spectroscopy, *Phys. Chem. Chem. Phys.*, **2011**, 13, 5264-5270.

[21] B. Klahr, S. Gimenez, F. Fabregat-Santiago, T. W. Hamann, J. Bisquert, Water oxidation at hematite photoelectrodes: The role of surface states, *J. Am. Chem. Soc.*, **2012**, 134, 4294-4302.

[22] Y. C. Zhang, H. N. Zhang, H. W. Ji, W. H. Ma, C. C. Chen, J. C. Zhao, Pivotal role and regulation of proton transfer in water oxidation on hematite photoanodes, *J. Am. Chem. Soc.*, **2016**, 138, 2705-2711.

[23] Y. D. Su, C. L. Liu¹, S. Brittman, J. Y. Tang, A. Fu, N. Kornienko, Q. Kong, P. D. Yang, Single-nanowire photoelectrochemistry, *Nature Nano.*, **2016**, 11, 609-612.

[24] J. B. Sambur, T.Y. Chen, E. Choudhary, G.Q. Chen, E. J. Nissen, E. M. Thomas, N. M. Zou, P. Chen, Sub-particle reaction and photocurrent mapping to optimize catalyst-modified photoanodes, *Nature*, **2016**, 530, 77-80.

[25] S. C. Warren¹, K. Voitchovsky, H. Dotan, C. M. Leroy, M. Cornuz, F. Stellacci, C. Hébert, A. Rothschild, M. Grätzel, Identifying champion nanostructures for solar water-splitting, *Nature Mater.*, **2013**, 12, 842-849.

[26] O. Zandi, T. W. Hamann, Determination of photoelectrochemical water oxidation intermediates on hematite electrode surfaces using operando infrared spectroscopy, *Nature Chem.*, **2016**, 8, 778-783.

[27] Z. Zhang, J. T. Yates Jr, Band bending in semiconductors: chemical and physical consequences at surfaces and interfaces, *Chem. Rev.* **2012**, 112, 5520-5551.

[28] B. Iandolo, A. Hellman, The Role of surface states in the oxygen evolution reaction on hematite, *Angew. Chem.* **2014**, 53, 13404-13408.

[29] B. Klahr, T. Hamann, Water oxidation on hematite photoelectrodes: Insight into the nature of

- surface states through in situ spectroelectrochemistry, *J. Phys. Chem. C*, **2014**, 118, 10393-10399.
- [30] T. Takashima, K. Ishikawa, H. Irie, Detection of intermediate species in oxygen evolution on hematite electrodes using spectroelectrochemical measurements, *J. Phys. Chem. C*, **2016**, 120, 24827-24834.
- [31] Q. H. Liu, J. F. He, T. Yao, Z. H. Sun, W. R. Cheng, S. He, Y. Xie, Y. H. Peng, H. Cheng, Y. F. Sun, Y. Jiang, F. C. Hu, Z. Xie, W. S. Yan, Z. Y. Pan, Z. Y. Wu, S. Q. Wei, Aligned Fe₂TiO₅-containing nanotube arrays with low onset potential for visible-light water oxidation, *Nat. Commun.*, **2014**, 5, 5122.
- [32] M. R. Nellist, F. A. L. Laskowski, F. D. Lin, T. J. Mills, S. W. Boettcher, Semiconductor-electrocatalyst interfaces: Theory, experiment, and applications in photoelectrochemical water splitting, *Acc. Chem. Res.* **2016**, 49, 733-740.
- [33] <http://icsd.iqfr.csic.es/icsd/>.
- [34] Z. M. Zhang, C. T. Gao, Y. X. Li, W. H. Han, W. B. Fu, Y. M. He, E. Q. Xie, Enhanced charge separation and transfer through Fe₂O₃/ITO nanowire arrays wrapped with reduced graphene oxide for water-splitting, *Nano Energy*, **2016**, 30, 892-899.
- [35] J. Resasco, H. Zhang, N. Kornienko, N. Becknell, H. Lee, J. H. Guo, A. L. Briseno, P. D. Yang, TiO₂/BiVO₄ nanowire heterostructure photoanodes based on type II band alignment, *ACS Cent. Sci.* **2016**, 2, 80-88.
- [36] T. T. Yao, R. T. Chen, J. J. Li, J. F. Han, W. Qin, H. Wang, J. Y. Shi, F. T. Fan, C. Li, Manipulating the interfacial energetics of n-type silicon photoanode for efficient water oxidation, *J. Am. Chem. Soc.* **2016**, 138, 13664-13672.
- [37] I. Roger, M. A. Shipman, M. D. Symes, Earth-abundant catalysts for electrochemical and photoelectrochemical water splitting, *Nat. Rev. Chem.*, **2017**, 1, 3.
- [38] J.C. Hill, A.T. Landers, J.A. Switzer, An electrodeposited inhomogeneous metal-insulator-semiconductor junction for efficient photoelectrochemical water oxidation, *Nat. Mater.*, **2015**, 14, 1150-1155.
- [39] F. D. Lin and S. W. Boettcher, Adaptive semiconductor/electrocatalyst junctions in water-splitting photoanodes, *Nat. Mater.*, **2014**, 13, 81-86.
- [40] M. W. Louie, A. T. Bell, An investigation of thin-film Ni-Fe Oxide catalysts for the electrochemical evolution of oxygen, *J. Am. Chem. Soc.* **2013**, 135, 12329-12337.
- [41] D. Friebel, M. W. Louie, M. Bajdich, K. E. Sanwald, Y. Cai, A. M. Wise, M.J. Cheng, D. Sokaras, T. C. Weng, R. Alonso-Mori, R. C. Davis, J. R. Bargar, J. K. Nørskov, A. Nilsson, A. T. Bell, Identification of highly active Fe sites in (Ni,Fe)OOH for electrocatalytic water Splitting, *J. Am. Chem. Soc.* **2015**, 137, 1305-1313.
- [42] L. Trotochaud, S. L. Young, J. K. Ranney, S. W. Boettcher, Nickel-iron oxyhydroxide oxygen-evolution electrocatalysts: The role of intentional and incidental iron incorporation, *J. Am. Chem. Soc.* **2014**, 136, 6744-6753.
- [43] H. S. Ahn, A. J. Bard, Surface interrogation scanning electrochemical microscopy of Ni_{1-x}Fe_xOOH (0 < x < 0.27) oxygen evolving catalyst: Kinetics of the “fast” Iron Sites, *J. Am. Chem. Soc.* **2016**, 138,

313-318.

[44] P.Y. Tang, L. J. Han, A. Genç, Y. M. He, X. Zhang, L. Zhang, J. R. Galán-Mascarós, J. R. Morante, J. Arbiol, Synergistic effects in 3D honeycomb-like hematite nanoflakes/branched polypyrrole nanoleaves heterostructures as high-performance negative electrodes for asymmetric supercapacitors, *Nano Energy*, **2016**, *22*, 189-201.

[45] F. Y. Ning, M. F. Shao, S. M. Xu, Y. Fu, R. K. Zhang, M. Wei, D. G. Evans, X. Duan, TiO₂/graphene/NiFe-layered double hydroxide nanorod array photoanodes for efficient photoelectrochemical water splitting, *Energy Environ. Sci.*, **2016**, *9*, 2633-2643.

[46] Z. M. Zhang, C. T. Gao, Z. M. Wu, W. H. Han, Y. L. Wang, W. B. Fu, X. D. Li and E. Q. Xie, toward efficient photoelectrochemical water-splitting by using screw-like SnO₂ nanostructures as photoanode after being decorated with CdS quantum dots, *Nano Energy*, **2016**, *19*, 318-327.

[47] A. Brauna, Y. L. Hu, F. Boudoiea, D. K. Boraa, D. D. Sarmad, M. Grätzel, C. M. Eggleston, The electronic, chemical and electrocatalytic processes and intermediates on iron oxide surfaces during photoelectrochemical water splitting, *Catal. Today*, **2016**, *260*, 72-81.

[48] Y. C. Ling, G. M. Wang, D. A. Wheeler, J. Z. Zhang, Y. Li, Sn-doped hematite nanostructures for photoelectrochemical water splitting, *Nano Lett.*, **2011**, *11*, 2119-2125.

[49] J. Brillet, M. Gratzel, K. Sivula, Decoupling feature size and functionality in solution-processed, porous hematite electrodes for solar water splitting, *Nano Lett.* **2010**, *10*, 4155-4160.

[50] J. Y. C. Chen, L. N. Dang, H. F. Liang, W. L. Bi, J. B. Gerken, S. Jin, E. E. Alp, S. S. Stahl, Operando analysis of NiFe and Fe oxyhydroxide electrocatalysts for water oxidation: Detection of Fe⁴⁺ by mössbauer spectroscopy, *J. Am. Chem. Soc.* **2015**, *137*, 15090-15093.

[51] M. Görlin, P. Chernev, J. F. d. Araújo, T. Reier, S. Dresch, B. Paul, R. Krämer, H. Dau, P. Strasser, Oxygen evolution reaction dynamics, faradaic charge efficiency, and the active metal redox states of Ni-Fe oxide water splitting electrocatalysts, *J. Am. Chem. Soc.* **2016**, *138*, 5603-5614.

[52] X. W. Yu, M. Zhang, W. J. Yuan, G. Q. Shi, A high-performance three-dimensional Ni-Fe layered double hydroxide/graphene electrode for water oxidation, *J. Mater. Chem. A*, **2015**, *3*, 6921-6928.

[53] J. J. Deng, X. X. Lv, H. Zhang, B. H. Zhao, X. H. Sun, J. Zhong, Loading the FeNiOOH cocatalyst on Pt-modified hematite nanostructures for efficient solar water oxidation, *Phys. Chem. Chem. Phys.*, **2016**, *18*, 10453-10458.

[54] J. J. Deng, X. X. Lv, K. Q. Nie, X. L. Lv, X. H. Sun, J. Zhong, Lowering the onset potential of Fe₂TiO₅/Fe₂O₃ photoanodes by interface structures: F- and Rh-based treatments, *ACS Catal.*, **2017**, *7*, 4062-4069.

[55] K. J. McDonald, K. S. Choi, A new electrochemical synthesis route for a BiOI electrode and its conversion to a highly efficient porous BiVO₄ photoanode for solar water oxidation, *Energy Environ. Sci.*, **2012**, *5*, 8553-8557.

[56] P. S. Bassi, R. P. Antony, P. P. Boix, Y.N. Fang, J. Barber, L. H. Wong, Crystalline Fe₂O₃/Fe₂TiO₅ heterojunction nanorods with efficient charge separation and hole injection as photoanode for solar water oxidation, *Nano Energy*, **2016**, *22*, 310-318.

[57] B. Klahr, S. Gimenez, F. Fabregat-Santiago, J. Bisquert, T.W. Hamann, Photoelectrochemical and

impedance spectroscopic investigation of water oxidation with “Co-Pi” coated hematite electrodes, *J. Am. Chem. Soc.* **2012**, 134, 16693-16700.

[58] B. Klahr, S. Gimenez, F. Fabregat-Santiago, J. Bisquert, T. W. Hamann, Electrochemical and photoelectrochemical investigation of water oxidation with hematite electrodes, *Energy Environ. Sci.*, **2012**, 5, 7626-7636.

[59] T. L. Villarreal, R. Gomez, M. Neumann-Spallart, N. Alonso-Vante and P. Salvador, Semiconductor photooxidation of pollutants dissolved in water: A kinetic model for distinguishing between direct and indirect interfacial hole transfer. I. Photoelectrochemical experiments with polycrystalline anatase electrodes under current doubling and absence of recombination, *J. Phys. Chem. B*, **2004**, 108, 15172-15181.

[60] O. Zandi, T. W. Hamann, Enhanced water splitting efficiency through selective surface state removal, *J. Phys. Chem. Lett.*, **2014**, 5, 1522-1526.

[61] Z. X. Su, J. S. Baskin, W. Z. Zhou, J. M. Thomas, A. H. Zewail, Ultrafast elemental and oxidation-state mapping of hematite by 4D electron microscopy, *J. Am. Chem. Soc.* **2017**, 139, 4916-4922.

[62] B. H. Han, K. A. Stoerzinger, V. Tileli, A. D. Gamalski, E. A. Stach, S. H. Yang, Nanoscale structural oscillations in perovskite oxides induced by oxygen evolution, *Nature Mater.*, **2017**, 16, 121-126.

[63] W. Li, D. He, S. W. Sheehan, Y. M. He, J. E. Thorne, X. H. Yao, G. W. Brudvig, D. W. Wang, Comparison of heterogenized molecular and heterogeneous oxide catalysts for photoelectrochemical water oxidation, *Energy Environ. Sci.*, **2016**, 9, 1794-1802.

[64] W. Li, S.W. Sheehan, D., Y. He, X. Yao, R. L. Grimm, G. W. Brudvig, D. W. Wang, Hematite-based solar water splitting in acidic solutions: Functionalization by mono- and multilayers of Iridium oxygen-evolution catalysts, *Angew. Chem. Int. Ed.* **2015**, 54, 11428-11432.

[65] F. Malara, F. Fabbri, M. Marelli, A. Naldoni, Controlling the surface energetics and kinetics of hematite photoanodes through few atomic layers of NiO_x, *ACS Catal.* **2016**, 6, 3619-3628.

[66] Z. F. Hu, Z. R. Shen, J. C. Yu, Covalent fixation of surface oxygen atoms on hematite photoanode for enhanced water oxidation, *Chem. Mater.* **2016**, 28, 564-572.

[67] Y. G. Li, X. L. Wei, B. W. Zhu, H. Wang, Y. X. Tang, T. C. Sum, X. D. Chen, Hierarchically branched Fe₂O₃@TiO₂ nanorod arrays for photoelectrochemical water splitting: facile synthesis and enhanced photoelectrochemical performance, *Nanoscale*, **2016**, 8, 11284-11290.

[68] S. X. Liu, L. X. Zheng, P. P. Yu, S. C. Han, X. S. Fang, Novel composites of α -Fe₂O₃ tetrakaidecahedron and graphene oxide as an effective photoelectrode with enhanced photocurrent performances, *Adv. Funct. Mater.* **2016**, 26, 3331-3339.

[69] Y. C. Zhang, H. N. Zhang, H. W. Ji, W. H. Ma, C. C. Chen, J. C. Zhao, Pivotal role and regulation of proton transfer in water oxidation on hematite photoanodes, *J. Am. Chem. Soc.*, **2016**, 138, 2705-2711.

[70] P. Zhang, T. Wang, X.X. Chang, L. Zhang, J. L. Gong, Synergistic cocatalytic effect of carbon nanodots and Co₃O₄ nanoclusters for the photoelectrochemical water oxidation on hematite, *Angew.*

Chem. Int. Ed. **2016**, 55, 5851-5855.

- [71] C. W. Wang, S. Yang, W. Q. Fang, P. Liu, H. J. Zhao, H. G. Yang, Engineered hematite mesoporous single crystals drive drastic enhancement in solar water splitting, *Nano Lett.*, **2016**, 16, 427-433.
- [72] P. Dias, A. Vilanova, T. Lopes, L. Andrade, A. Mendes, Extremely stable bare hematite photoanode for solar water splitting, *Nano Energy*, **2016**, 23, 70-79.
- [73] Q. Yu, X. G. Meng, T. Wang, P. Li, J. H. Ye, Hematite films decorated with nanostructured ferric oxyhydroxide as photoanodes for efficient and stable photoelectrochemical water splitting, *Adv. Funct. Mater.*, **2015**, 25, 2686-2692.
- [74] L. Steier, J.S. Luo, M. Schreier, M. T. Mayer, T. Sajavaara, M. Grätzel, Low-temperature atomic layer deposition of crystalline and photoactive ultrathin hematite films for solar water splitting, *ACS Nano*, **2015**, 9, 11775-11783.
- [75] Y. Hou, M. Qiu, T. Zhang, J. Ma, S. H. Liu, X. D. Zhuang, C. Yuan, X. L. Feng, Efficient electrochemical and photoelectrochemical water splitting by a 3D nanostructured carbon supported on flexible exfoliated graphene foil, *Adv. Mater.*, **2017**, 29, 1604480.
- [76] Y. Yang, M. Forster, Y.C. Ling, G.M. Wang, T. Zhai, Y.X. Tong, A. J. Cowan, Y. Li, Acid treatment enables suppression of electron-hole recombination in hematite for photoelectrochemical water splitting, *Angew. Chem. Int. Ed.*, **2016**, 55, 3403-3407.
- [77] J. Y. Kim, D. H. Youn, K. Kang, J. S. Lee, Highly conformal deposition of an ultrathin FeOOH layer on a hematite nanostructure for efficient solar water splitting, *Angew. Chem. Int. Ed.*, **2016**, 55, 10854-10858.
- [78] A. Mettenbörgera, Y. Gönüllüa, T. Fischera, T. Heisiga, A. Sasinskaa, C. Macatob, G. Carrarob, C. Sadac, D. Barrecad, L. Mayrhofere, M. Moselere, A. Helde, S. Mathur, Interfacial insight in multi-junction metal oxide photoanodes for water-splitting applications, *Nano Energy*, **2016**, 19, 415-427.
- [79] C. C. Li, A. Li, Z. B. Luo, J. J. Zhang, X. X. Chang, Z. Q. Huang, T. Wang, J. L. Gong, Surviving high-temperature calcination: ZrO₂-induced hematite nanotubes for photoelectrochemical water oxidation, *Angew. Chem. Int. Ed.*, **2017**, 56, 4214-4219.
- [80] O. Zandi, A. R. Schon, H. Hajibabaei, T.W. Hamann, Enhanced charge separation and collection in high-performance electrodeposited hematite films, *Chem. Mater.*, **2016**, 28, 765.
- [82] Z.B. Luo, C.C. Li, S. S. Liu, T. Wang, J. L. Gong, Gradient doping of phosphorus in Fe₂O₃ nanoarray photoanodes for enhanced charge separation, *Chem. Sci.*, **2017**, 8, 91-100.
- [83] F. Malara, F. Fabbri, M. Marelli, A. Naldoni, Controlling the surface energetics and kinetics of hematite photoanodes through few atomic layers of NiOx, *ACS Catal.* **2016**, 6, 3619-3628.
- [84] M. Y. Li, Y. Yang, Y. C. Ling, W. T. Qiu, F. X. Wang, T. Y. Liu, Y. Song, X. X. Liu, P. P. Fang, Y. X. Tong, Y. Li, Morphology and doping engineering of Sn-doped hematite nanowire photoanodes, *Nano Lett.*, **2017**, 17, 2490-2495.
- [85] P.Y. Tang, H.B. Xie, C. Ros, L.J. Han, M. Biset-Peiró, Y.M. He, W. Kramer, A. Perez-Rodriguez, E. Saucedo, J. Galan-Mascaros, T. Andreu, J. R. Morante, J. Arbiol, Enhanced photoelectrochemical water

splitting of hematite multilayer nanowires photoanode with tuning surface state via bottom-up interfacial engineering, *Energy Environ. Sci.*, **2017**, 10, 2124-2136.

Chapter 5

**Hematite/Fe₂TiO₅/CoFe Prussian Blue Analogues Composite
Nanowires as Photoanodes for Water Splitting in Acidic
Electrolyte**

5.1 Introduction

PEC water splitting devices, using earth abundant semiconductor electrodes, long considered to be the “Holy Grail” of the solar energy conversion and storage revolution, have offered the promise of solar-to-fuel conversion through artificial photosynthesis. [1-4] However, carrying out the constituent oxidation (photoanodes) and reduction (photocathodes) half-reactions of PEC water splitting efficiently at a reasonable cost has not been substantially addressed. [5] Given that the proton exchange membranes enabling efficiently separation of the photoanodes and photocathodes and the water reduction are much easier to be carried out in acidic electrolytes, the development of efficient OECs functionalized photoanodes in acidic electrolytes deserves special attention. [6-8] There is, indeed, a dearth of low-cost alternative OECs that are active and stable in acidic conditions rather than the state-of-the-art ruthenium and iridium based OECs. [9] Accordingly, plenty of researchers have hitherto devoted their efforts to the development of affordable effective OECs, which could survive in acid electrolytes, including cobalt-containing polyoxometalates (Co-POMs), [9] Ti-stabilized MnO_2 , [10] $\text{W}_{1-x}\text{Ir}_x\text{O}_{3-\delta}$, [11] $\text{Ni}_x\text{Mn}_{1-x}\text{Sb}_{1.6-1.8}\text{O}_y$, [12] and CoFe PBA. [13-14] Recently, we have reported a highly active phase of hetero-bimetallic cyanide-bridged CoFe Prussian Blue Analogues (CoFe PBA) electrocatalysts based on chemical etching process, which is able to promote water oxidation under neutral, basic ($\text{pH} < 13$) and acidic conditions ($\text{pH} > 1$). [13]

On the other hand, OECs functionalized photoanodes are composed of two complementary parts: the light absorber semiconductors and the OECs. Since the inappropriate combination of OECs with semiconductor light absorbers limits the development of efficient photoanodes in acidic electrolytes, it is necessary to consider the light absorption of the semiconductors and the OECs' catalytic function, simultaneously. [6] Up to date, there are few reports about the smart integration of the hematite matrix with Ir based OECs as photoanodes for PEC water splitting. [6, 15-17] For instance, D.W. Wang et al. utilized monolayer molecular Ir OECs onto hematite

for solar water splitting, showing a 0.66 mA cm^{-2} photocurrent response at 1.23 V vs. RHE in a pH = 1.01 electrolyte. [6] Further investigation about the charge transfer kinetics of molecular and heterogeneous oxide Ir-based OECs functionalized hematite photoanodes unravels that the catalyst mechanisms by which the molecular Ir and IrO_x OECs enhance the PEC performance of hematite electrodes are fundamentally distinct. [16] Recently, C.H. Cui et al. combined atomically dispersed hybrid Ir-Ni sites with hematite photoanodes, only obtaining ca. 0.7 mA cm^{-2} at 1.23 V vs. RHE in 1M NaOH electrolyte. [17] Nevertheless, even coupling with noble Ir-based OECs, the photocurrent response of the hematite composite photoanodes is still much lower than the theoretical value (12.5 mA cm^{-2}) of hematite. [18] In addition, the mechanisms of charge transfer across the semiconductor/electrolyte interfaces (SEI) in acidic electrolytes are still ambiguous. [19] Herein, we show the fabrication of type II $\text{Fe}_2\text{O}_3/\text{Fe}_2\text{TiO}_5$ heterostructured nanowires decorated with CoFe PBA OECs for PEC water splitting in acidic electrolyte via hydrothermal, atomic layer deposition (ALD) and chemical bath, as displayed in **Figure 5.5A**. Moreover, an unambiguous correlation between surface states, charge transfer kinetics and PEC performance has been established via PEIS.

5.2 Experimental Section

5.2.1 Chemicals and Materials

All commercially available reagents and solvents were used as received without further purification unless otherwise indicated. All chemical reagents were purchased from Sigma-Aldrich. If not specified, all solutions were prepared with Milli-Q water (ca. $18.2 \text{ M}\Omega\cdot\text{cm}$ resistivity). Fluorine-tin-oxide (FTO) coated glass substrate (735167-1EA, $7 \text{ }\Omega/\text{sq}$) was purchased from Sigma-Aldrich.

5.2.2 Electrode Preparation

FTO substrates were cut into small pieces with $1 \text{ cm} \times 3 \text{ cm}$ area and washed by sonicating in a (1: 1: 1) mixture of acetone (Sigma-Aldrich, 99.9%), isopropanol (Sigma-Aldrich, 99.9%) and water. After rinsing the FTO substrates thoroughly with

distilled water, the FTO substrates were washed in ethanol (Fluka, 99.8%) and then dried in air at 300 °C for 1 h (heating rate: 8.5 °C min⁻¹). Part of the FTO substrates (ca. 1 cm × 2 cm) was covered using a polymer tape (Kaptons® Foil, VWR International) prior to the following process. The uncoated part of the FTO was later employed as electric contact for the electrodes in the photoelectrochemical cell.

Fe₂O₃ electrodes: Hematite nanowires were prepared according to our previous procedure. [20] Typically, a 200 ml Teflon-lined stainless-steel autoclave was filled with 60 ml aqueous mixture solution of 0.15 M ferric chloride (FeCl₃, 97%), 1 M sodium nitrate (NaNO₃, 99%) and 316 μL hydrochloric (HCl, wt 37%). 6 pieces of FTO substrates were put into the autoclave and heated at 95 °C for 4 hours. A uniform layer of iron oxyhydroxide (FeOOH) nanowires was grown onto the FTO substrate. After that, the FeOOH-coated substrate was washed with deionized water to remove any residual salt, and subsequently pre-sintered in air at 550 °C (heating rate: 8.5 °C min⁻¹) for 2 hours to transfer FeOOH nanowires into hematite nanowires. To further reduce the surface defective sites, the obtained hematite nanowires were treated at 750 °C in air for additional 30 min and subsequently quenched in air within 1 min.

Fe₂O₃/Fe₂TiO₅ electrodes: The obtained hematite samples after pre-sintering process (550 °C for 2h) were further subjected to TiO₂ atomic layer deposition (ALD) process. [21] The TiO₂ ALD was performed in R200 Picosun Atomic Layer Deposition system at 150°C with TiCl₄ (Sigma-Aldrich, 99%) and water as the precursors in an 8 mbar N₂ flow atmosphere, reaching a growth rate of 0.27Å cycle⁻¹. The pulse time for the TiCl₄ and water was 0.1 s and the purge time was 10 s. The TiO₂ thickness onto the Fe₂O₃ nanowires was controlled by changing the ALD deposition cycle. In this case, the optimized TiO₂ was 30 cycles according to our previous report. [20, see also Chapter 4] After that, a quenched process at 750 °C for 30 min was performed to transform the surface ALD TiO₂ into Fe₂TiO₅.

Fe₂O₃/Fe₂TiO₅/CoFe PBA electrodes: The obtained Fe₂O₃/Fe₂TiO₅ electrodes were further coated with CoFe PBA via chemical bath. [13] Chemical bath deposition of CoFe PBA on the Fe₂O₃/Fe₂TiO₅ electrodes were carried out according to the

following procedure: First, $\text{Co}(\text{NO}_3)_2 \cdot 6\text{H}_2\text{O}$ (700 mg) and $\text{K}_3\text{Fe}(\text{CN})_6$ (350 mg) powder were dissolved in 40 mL of Milli-Q water under vigorous stirring. After that, one piece of the $\text{Fe}_2\text{O}_3/\text{Fe}_2\text{TiO}_5$ electrodes was immersed in a 5 mL glass vial with 4 mL freshly prepared mixture solution containing $\text{Co}(\text{NO}_3)_2 \cdot 6\text{H}_2\text{O} + \text{K}_3\text{Fe}(\text{CN})_6$. The glass vial was sealed and then heated at 60 °C for different reaction times in the oven. Finally, the obtained samples were rinsed with Milli-Q water to remove any impurities and were dried in the oven at 60 °C overnight.

5.2.3 Structural and Morphological Characterization

The grazing incidence X-ray diffraction (XRD) analyses were performed on a Bruker D4 X-ray powder diffractometer using the Cu $K\alpha$ radiation (1.54184 Å) and a 1D Lynkeye detector, which is equipped with a Gobel mirror in the incident beam and equatorial Soller slits in the diffracted beam (51 incidence angle, 2° step⁻¹). The morphology of the films was characterized using a field emission gun scanning electron microscope (FE-SEM, Zeiss Series Auriga microscopy) equipped with an electron dispersive X-ray spectroscopy (EDX) detector. X-ray photoelectron spectroscopy (XPS) was performed with a Phoibos 150 analyser (SPECS GmbH, Berlin, Germany) in ultra-high vacuum conditions (base pressure 4×10^{-10} mbar) with a monochromatic aluminium $K\alpha$ X-ray source (1486.74 eV). The energy resolution as measured by the FWHM of the Ag 3d_{5/2} peak for a sputtered silver foil was 0.8 eV. All the samples for HRTEM and ADF-STEM were prepared by using a mechanical process. [1] HRTEM and ADF-STEM images have been obtained by using a FEI Tecnai F20 field emission gun microscope with a 0.19 nm point-to-point resolution at 200 kV equipped with an embedded Quantum Gatan Image Filter for EELS analyses. High resolution HAADF, EELS-STEM analyses were conducted in a FEI Titan 80-300 STEM at 300 kV and Titan G3 50-300 PICO at 80kV in Ernst Ruska-Centre Juelich. [22-23] Images have been analyzed by means of Gatan Digital Micrograph software. Atomic supercell modelling was performed by the Eje-Z, Rhodius and JMOL software packages with the corresponding crystal phase parameters of each species obtained from ICSD, which were verified by HRTEM and STEM-EELS

mapping. [24-26] Specifically, to further identify the crystal phases via HRTEM, HAADF and probe the spatial distribution of these components in the integrated electrodes, we created crystal models based on the single crystal data found in the Inorganic Crystal Structure Database (ICSD). With these crystal models, the diffraction patterns visualized from different zone axes of each phase could be simulated. Then, the simulated diffraction pattern was compared with the power spectrum (FFT) obtained on the atomic resolution HRTEM and HAADF experimental images for the identification of the crystal phases in the composite electrodes.

5.2.4 Photo-electrochemical Measurements

Photocurrent (j , mA cm⁻²) vs. potential (E , V) curves were taken using an undivided three-electrode cell. The working, counter and reference electrodes were the composite hematite nanowires (1 cm² geometric area), a Pt wire and a Ag/AgCl (3M KCl) electrode (Metrohm, $E = 0.203$ vs. NHE), respectively. The electrolyte was a 1 M NaNO₃ + 1M HNO₃ solution (pH = 1.01). The electrolyte was purged with N₂ during the experiments. CV was taken using a computer-controlled potentiostat (VMP3, BioLogic Science Instruments). Potential was scanned from 0.30 V vs. Ag/AgCl to 1.60 V vs. Ag/AgCl, with a scan rate of 20 mV s⁻¹. The photocurrent density is referred to the geometric area. All potentials were corrected at 80% for the ohmic drop, which was determined using the automatic current interrupt (CI) method implemented by the potentiostat, [13] and are converted with respect to the reversible hydrogen electrode (RHE): E (V vs. RHE) = E (V vs. Ag/AgCl) + 0.0592×pH + 0.203. Light illumination was performed using a 150 W AM 1.5G solar simulator (Solar Light Co., 16S-300-002 v 4.0) with an incident light intensity set at 1 Sun (100 mW cm⁻²), as measured using a thermopile (Gentec-EO, XLPF12-3S-H2-DO) coupled with an optical power meter (Gentec-EO UNO). In the PEC characterization, the light came from the front side (electrode-electrolyte interface, front side illumination). PEIS data were acquired with an alternate current (AC) perturbation of 5 mV in amplitude and a 100 mHz to 1 MHz frequency range, both in the dark and under illumination, and under selected direct current (DC) potentiostatic conditions (0.30 to

1.60 V vs Ag/AgCl). Nyquist plots (imaginary vs. real components of impedance, Z_{Im} vs. Z_{Re}) were fitted to the corresponding equivalent circuits using Z-fit (BioLogic Associates). Fitted capacitances and resistances are referred to the electrode geometric area (1 cm × 1cm). Error bars stem from the goodness of the EIS data fittings.

5.3 Result and Discussion

5.3.1 Pristine CoFe PBA for OER Processed by Chemical Etching Characterized by SEM and TEM

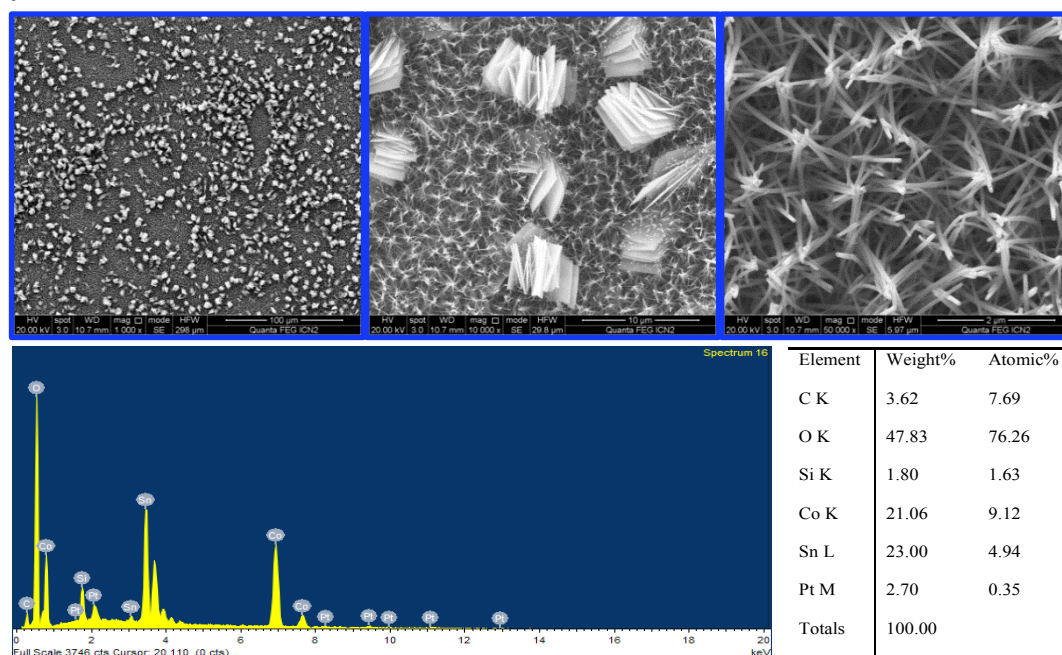


Figure 5.1 SEM images and EDX data of CoO_x nano arrays.

Before the investigation of CoFe PBA combining with hematite based nanowires as photoanodes for water splitting, we investigated the structure and the electrochemical properties of the pristine CoFe PBA for OER processed by chemical etching. Firstly, CoO_x films were grown on FTO glass substrates via a hydrothermal process. [13] Specifically, 77.5 mg $\text{Co}(\text{NO}_3)_2 \cdot 6\text{H}_2\text{O}$ and 80.8 mg $\text{CO}(\text{NH}_2)_2$ were dissolved in 10 mL MilliQ water and then transferred into a 20 mL Teflon-lined autoclave with two pieces of FTO substrates immersed into the reaction solution. The autoclave was maintained at 120 °C for 10 h and then cooled down to room temperature in air. After the reaction, the samples were rinsed with MilliQ water several times. As shown in **Figure 5.1**, the CoO_x films present at the surface of FTO substrate with nanowires or

nanoflakes arrays morphology. The corresponding EDX data demonstrated the Co and O content in the nanowires and nanoflakes.

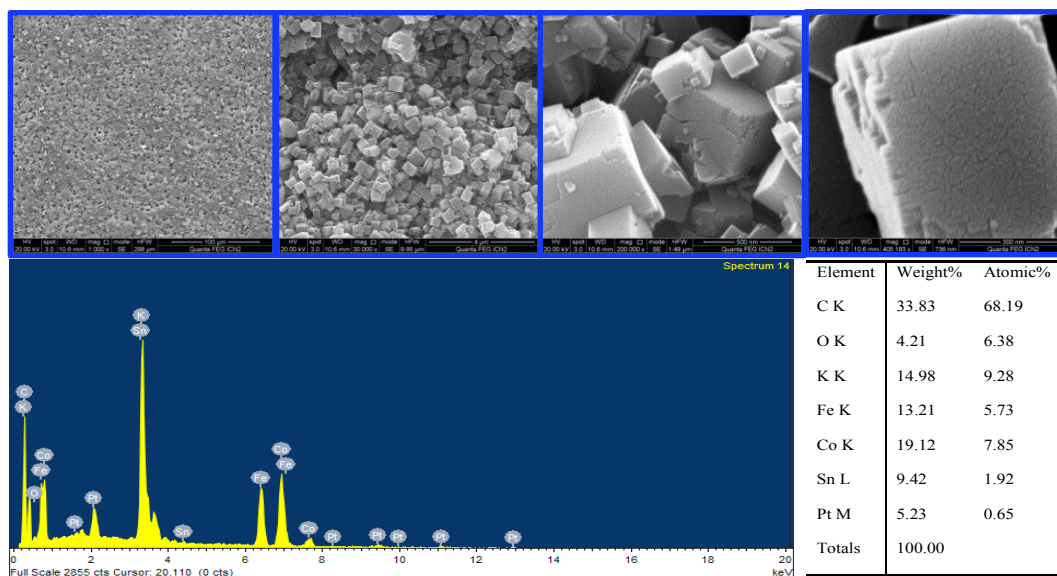


Figure 5.2 SEM images and corresponding EDX data of CoFe PBA on FTO substrate.

The obtained CoO_x nano arrays were then subjected to a chemical etching process with $\text{K}_3\text{Fe}(\text{CN})_6$ aqueous solution. [13] All electrodes were immersed in 20 mL concentrated H_2SO_4 solution ($\text{pH} = 1$) for at least 3 hours to remove any remaining traces of CoO_x . The obtained CoFe PBA electrodes exhibit nanocube morphology, as displayed in **Figure 5.2**. The presence of C, N, Fe and Co is confirmed in this sample by EDX.

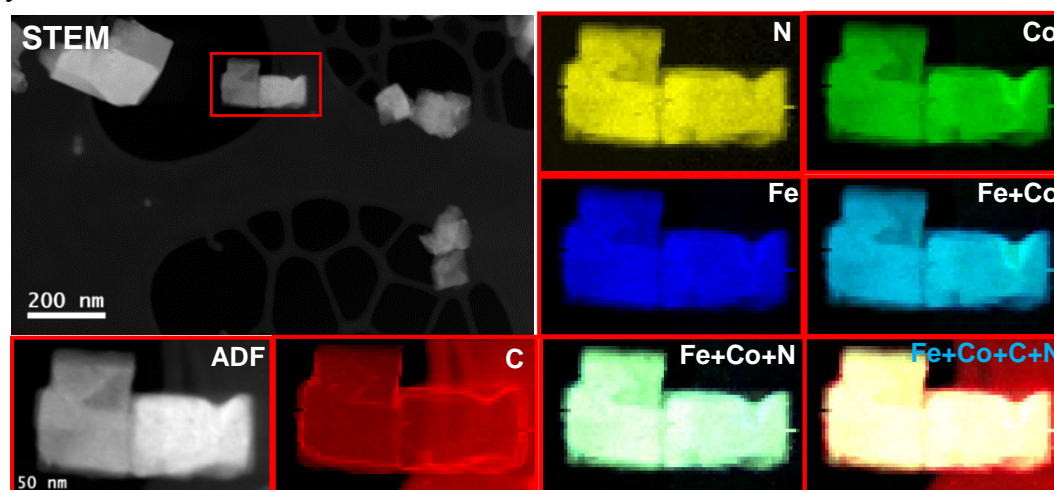


Figure 5.3 EELS chemical composition maps obtained from the red rectangle area of the STEM-ADF micrograph. Individual C (red), N (yellow), Co (green), Fe (blue) elemental maps and their composites.

The extra C signal on the right side of the map area is derived from the carbon support (we used holey carbon grids).

The spatial elemental distribution of C, N, Fe and Co in CoFe PBA samples were investigated via nanoscale STEM EELS SI maps. We used K-edges for O, C and N and L-edges for Co and Fe maps during the EELS studies. As shown in **Figure 5.3**, the C, N, Fe and Co elements are homogeneously distributed through the nanocubes matrix, indicating the pure CoFe PBA presented in the nanocubes.

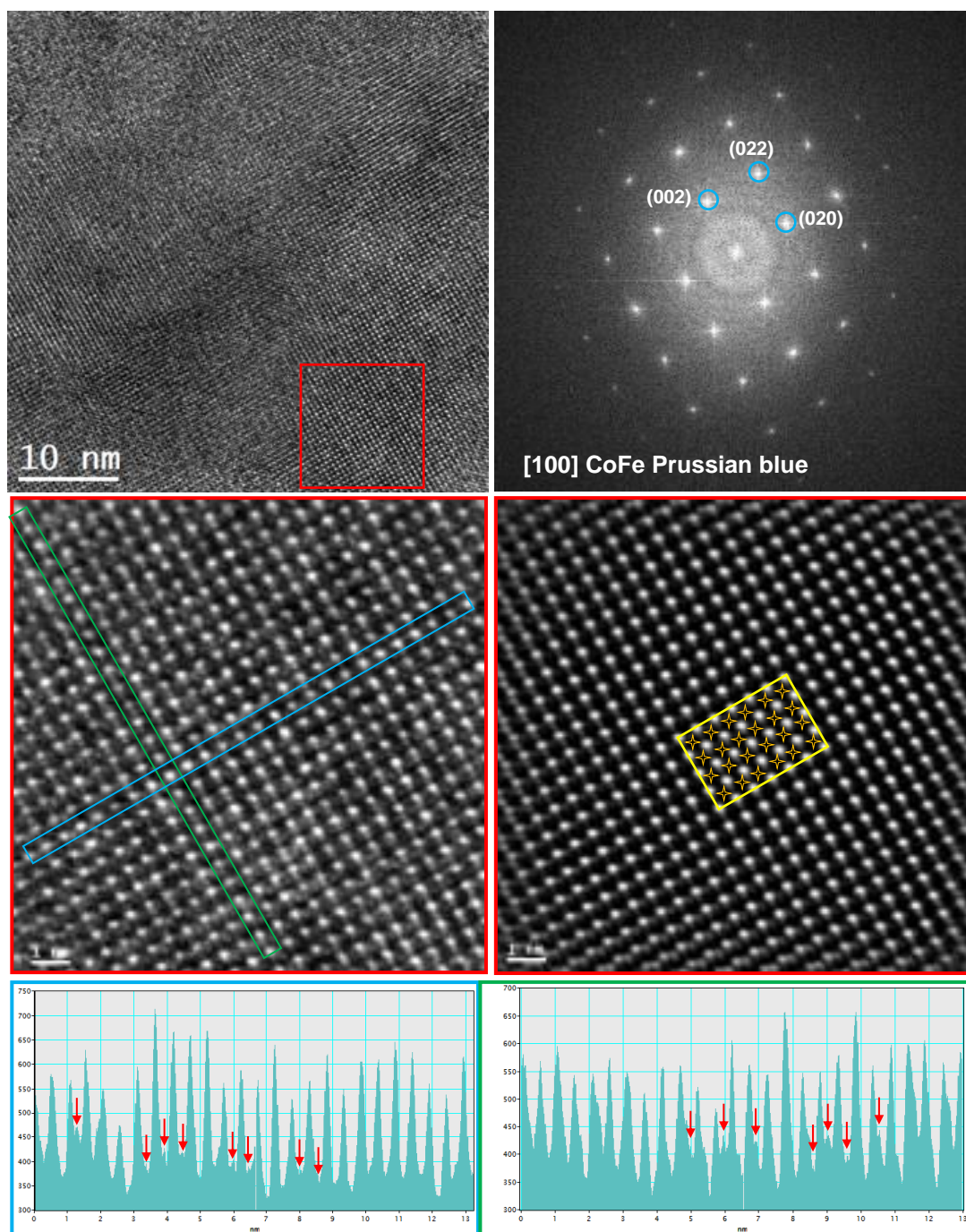


Figure 5.4 Top rows: HRTEM micrograph of the CoFe PBA sample showing a general view of the nanocube structure, the corresponding power spectrum indicates that the cubes crystallize as Cubic CoFe Prussian blue, [FM-3M]-Space group 225, with lattice parameters corresponding to $a = 1.02794$ nm, $b = 1.02794$ nm and $c = 1.02794$ nm as visualized along the [100] direction. Middle rows: atomic resolution TEM of the red rectangled area on the top left image. The periodic structure of as-prepared CoFe PBA is extracted by frequency filtering (Inset in the yellow rectangle area: the Co and Fe atomic positions correspond to the dark spots in the HRTEM image, indicated with orange stars in the center of the Co-Fe cubic lattices. The bright spots could correspond to the Wyckoff site 8 of the Fm3m space group). Bottom rows: The TEM intensity profile obtained along the (002)/left and (020)/right planes on the indigo and green squared regions in the left middle row HRTEM image, respectively.

A direct TEM observation of the local atomic structure is critical for understanding the relationship between microstructure and electrocatalysis performance. [27] However, the coordination polymers in CoFe PBA are especially susceptible to electron beam damage, even at very short exposure times, which makes difficult to reach stable atomic-level TEM observation of the Fe and Co atom arrays within the CoFe lattice. [13] Itoi and Talham succeeded in exploring ionic liquid to stabilize CoFe PBA nanoparticles for electron microscopy for the first time and gave spatial information on the local microstructure at the atomic level. [27] In the present case, the CoFe PBA sample processed by chemical etching was submitted to a 15 minutes electron beam shower at 200 kV to remove possible organic impurities and water molecules at room temperature. After this process, high resolution TEM images could still be obtained without degradation and the fringes associated with the cubic structure were clearly observed.

Figure 5.4 display HRTEM images and a general power spectrum image of as-prepared CoFe PBA at room temperature. A coherent shepherd-check pattern is related to the alternating Co atom and Fe atom arrays. The corresponding power spectrum image indicates that the nanocubes crystallize as Cubic CoFe Prussian blue, [FM-3M]-Space group 225, with lattice parameters corresponding to $a = 1.02794$ nm, $b = 1.02794$ nm and $c = 1.02794$ nm as visualized along the [100] direction. The

bottom images in **Figure 5.4** show the HRTEM intensity profiles obtained along as-prepared (002) and (020) planes. The inhomogeneous peak densities can further be related to the presence of vacancies, as expected in these non-stoichiometric compounds. [27]

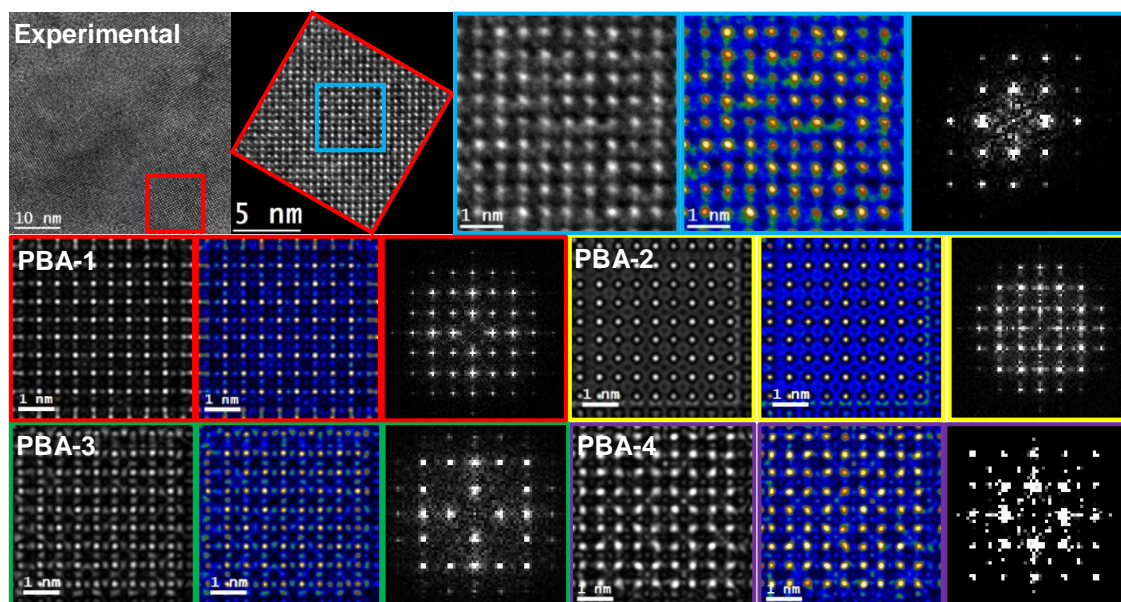


Figure 5.5 The experimental HRTEM, temperature coloured HRTEM images and power spectra of the indigo squared area are displayed in the first two rows. Simulated HRTEM images of different PBAs in the [100] projection at the optimized experimental conditions: specimen thickness (t) and defocus (Δf): PBA-1 ($t = 200 \text{ \AA}$, $\Delta f = 60 \text{ \AA}$), PBA-2 ($t = 400 \text{ \AA}$, $\Delta f = 60 \text{ \AA}$), PBA-3 ($t = 400 \text{ \AA}$, $\Delta f = 60 \text{ \AA}$), PBA-4 ($t = 500 \text{ \AA}$, $\Delta f = 0 \text{ \AA}$) are displayed in the bottom panel, with their corresponding coloured temperature HRTEM image and power spectrum.

Furthermore, we compared the simulated HRTEM, temperature colored HRTEM images and power spectrum of different PBA-1 $\{K_{0.34}Co(Fe(CN)_6)_{0.75}(H_2O)_{3.6}[F4-3M]-216\}$, PBA-2 $\{Co_3(Fe(CN)_6)_2(H_2O)-[F4-3M]-216\}$, PBA-3 $\{Co(Fe(CN)_6)_{0.667}(H_2O)_{3.333}-[F4-3M]-216\}$ and PBA-4 $\{Co_4(Fe(CN)_6)_{2.67}(H_2O)_{15.33}-[FM3-M]-225\}$ crystal models with that of the experimental result, to temporarily assign the obtained CoFe PBA sample to PBA-4 $\{Co_4(Fe(CN)_6)_{2.67}(H_2O)_{15.33}-[FM3-M]-225\}$, as displayed in **Figure 5.5**. [13] The detail electrochemical experiment about the obtained pristine CoFe PBA processed by chemical etching for OER is presented in

reference [13], demonstrating that CoFe PBA as a electrocatalyst is able to promote water oxidation under neutral, basic ($\text{pH} < 13$) and acidic conditions ($\text{pH} > 1$).

5.3.2 Optimization of the Chemical Bath Reaction Time in $\text{Fe}_2\text{O}_3/\text{CoFe}$ PBA Electrodes

The pristine hematite nanowires were subjected to a chemical bath in a glass vial with 4 mL freshly prepared mixture solution containing $\text{Co}(\text{NO}_3)_2 \cdot 6\text{H}_2\text{O} + \text{K}_3\text{Fe}(\text{CN})_6$. The glass vial was sealed and then heated at $60\text{ }^\circ\text{C}$ for different reaction times in the oven. Finally, the obtained samples were rinsed with Milli-Q water to remove any impurities and were dried in the oven at $60\text{ }^\circ\text{C}$ overnight. The chemical bath reaction time was under control to tune the thickness of the CoFe PBA on the surface of the hematite nanowires since the overloading of CoFe PBA OEC is supposed to reduce the light absorption of the hematite. As shown in **Figure 5.6**, with the extending of the chemical bath reaction time, the CoFe PBA gradually grew onto the surface of the nanowires, finally presenting a nanoparticle-shape decoration on their surface.

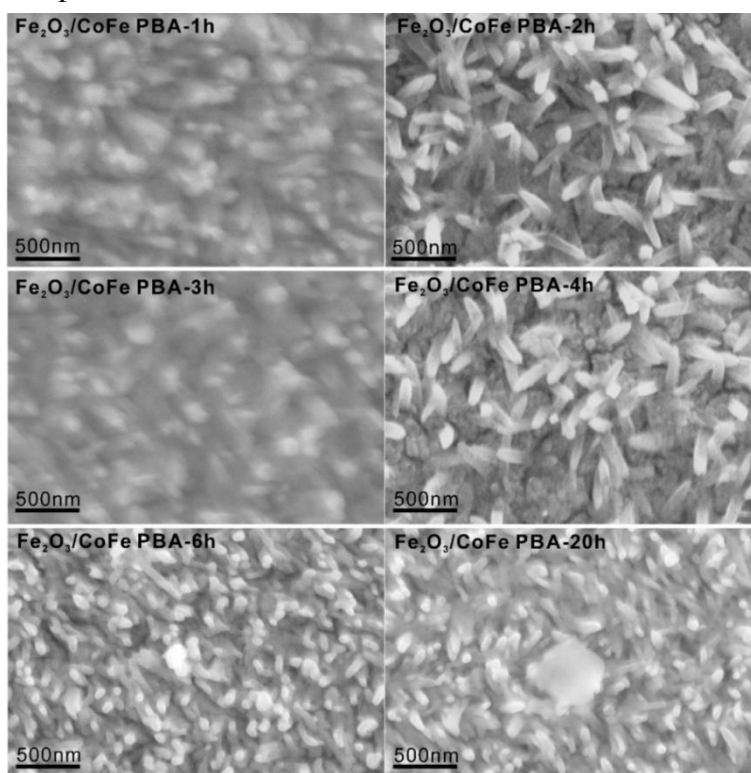


Figure 5.6 SEM images of the $\text{Fe}_2\text{O}_3/\text{CoFe}$ PBA electrodes with different chemical bath reaction time, e.g. 1 h, 2 h, 3 h, 4 h, 6 h and 20 h.

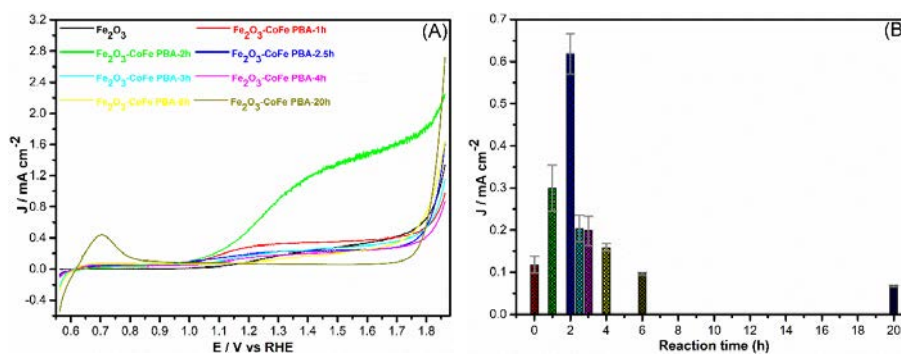


Figure 5.7 (A): CV curves of the $\text{Fe}_2\text{O}_3/\text{CoFe}$ PBA electrodes with chemical bath reaction time; (B): the photocurrent density at 1.23 V vs. RHE related to the reaction time (the error bar stemmed from the standard deviation of the statistical data collected at least for three repeated electrodes).

Figure 5.7 display the CV curves of the $\text{Fe}_2\text{O}_3/\text{CoFe}$ PBA electrodes with chemical bath reaction time the photocurrent density at 1.23 V vs. RHE related to the reaction time. As shown in **Figure 5.7 A**, the onset potential of $\text{Fe}_2\text{O}_3/\text{CoFe}$ PBA-1 h, $\text{Fe}_2\text{O}_3/\text{CoFe}$ PBA-2 h, $\text{Fe}_2\text{O}_3/\text{CoFe}$ PBA-2.5 h, $\text{Fe}_2\text{O}_3/\text{CoFe}$ PBA-3 h, $\text{Fe}_2\text{O}_3/\text{CoFe}$ PBA-4 h and $\text{Fe}_2\text{O}_3/\text{CoFe}$ PBA-6 h electrodes are lower than that of pristine Fe_2O_3 electrode. While the onset potential of $\text{Fe}_2\text{O}_3/\text{CoFe}$ PBA-20 h is much higher than that pristine Fe_2O_3 electrode, which is probably due to the overloading of the CoFe PBA on the surface of hematite nanowires. **Figure 5.7 B** reveals that $\text{Fe}_2\text{O}_3/\text{CoFe}$ PBA-2h electrodes possess the highest photocurrent response (0.62 mA cm^{-2}) at 1.23 V vs. RHE., indicating that the optimized chemical batch reaction time for the CoFe PBA coating in the case of hematite nanowires is 2h.

5.3.3 Optimization of the Chemical Bath Reaction Time in $\text{Fe}_2\text{O}_3/\text{Fe}_2\text{TiO}_5/\text{CoFe}$ PBA Electrodes

The $\text{Fe}_2\text{O}_3/\text{Fe}_2\text{TiO}_5$ composite nanowires were subjected to a chemical bath in a glass vial with 4 mL freshly prepared mixture solution containing $\text{Co}(\text{NO}_3)_2 \cdot 6\text{H}_2\text{O} + \text{K}_3\text{Fe}(\text{CN})_6$. The glass vial was sealed and then heated at $60 \text{ }^\circ\text{C}$ for different reaction times in the oven. Finally, the obtained samples were rinsed with Milli-Q water to remove any impurities and were dried in the oven at $60 \text{ }^\circ\text{C}$ overnight. The chemical bath reaction time was under control to tune the thickness of the CoFe PBA on the surface of the $\text{Fe}_2\text{O}_3/\text{Fe}_2\text{TiO}_5$ composite

nanowires since the overloading of CoFe PBA OECs is supposed to reduce the light absorption of the $\text{Fe}_2\text{O}_3/\text{Fe}_2\text{TiO}_5$ composite nanowires. As shown in **Figure 5.8**, with the extending of the chemical bath reaction time, the CoFe PBA gradually grew onto the surface of the nanowires, finally presenting crowded nanoparticles decorating their surface.

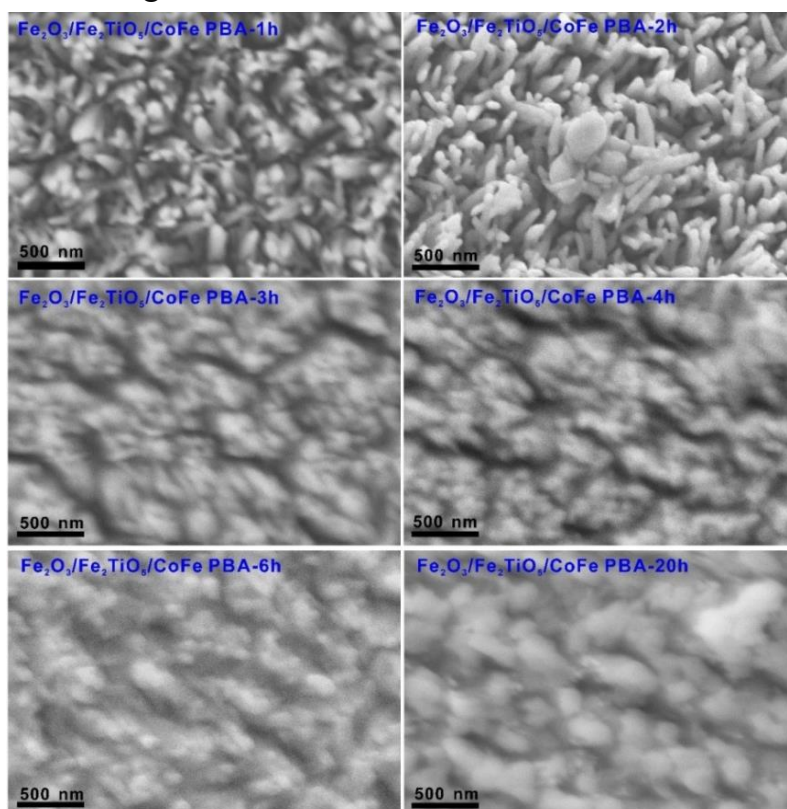


Figure 5.8 SEM images of the $\text{Fe}_2\text{O}_3/\text{Fe}_2\text{TiO}_5/\text{CoFe}$ PBA electrodes with different chemical bath reaction times, e.g. 1 h, 2 h, 3 h, 4 h, 6 h and 20 h.

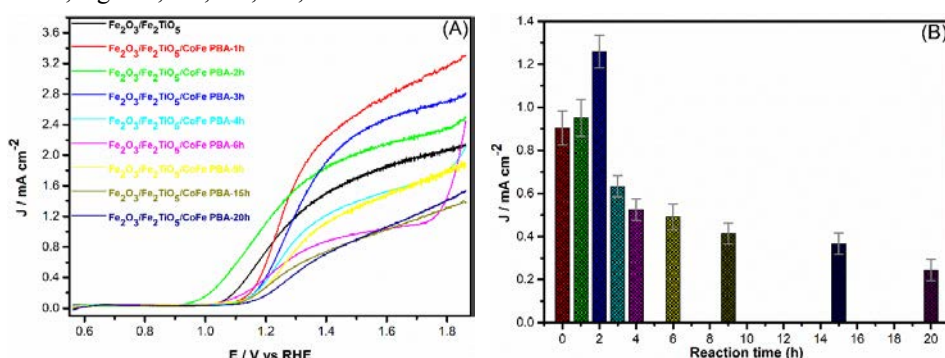


Figure 5.9 (A): CV curves of the $\text{Fe}_2\text{O}_3/\text{Fe}_2\text{TiO}_5/\text{CoFe}$ PBA electrodes with chemical bath reaction time; (B): the photocurrent density at 1.23 V vs. RHE related to the reaction time (the error bar stemmed from the standard deviation of the statistical data collected at least for three repeated electrodes).

Figure 5.9A displays the CV curves of the $\text{Fe}_2\text{O}_3/\text{Fe}_2\text{TiO}_5/\text{CoFe}$ PBA electrodes, while **Figure 5.9B** shows the photocurrent density at 1.23 V vs. RHE related to the chemical bath reaction time. As shown in **Figure 5.9A**, the onset potential of $\text{Fe}_2\text{O}_3/\text{CoFe}$ PBA-2 h is lower than that of the $\text{Fe}_2\text{O}_3/\text{Fe}_2\text{TiO}_5$ electrode. While the onset potential of $\text{Fe}_2\text{O}_3/\text{CoFe}$ PBA-1 h, $\text{Fe}_2\text{O}_3/\text{CoFe}$ PBA-2 h, $\text{Fe}_2\text{O}_3/\text{CoFe}$ PBA-3 h, $\text{Fe}_2\text{O}_3/\text{CoFe}$ PBA-4 h and $\text{Fe}_2\text{O}_3/\text{CoFe}$ PBA-6 h, $\text{Fe}_2\text{O}_3/\text{CoFe}$ PBA-9 h, $\text{Fe}_2\text{O}_3/\text{CoFe}$ PBA-15 h and $\text{Fe}_2\text{O}_3/\text{CoFe}$ PBA-20 h electrodes is much higher than that of the $\text{Fe}_2\text{O}_3/\text{Fe}_2\text{TiO}_5$ electrode. **Figure 5.9B** reveals that $\text{Fe}_2\text{O}_3/\text{Fe}_2\text{TiO}_5/\text{CoFe}$ -2h electrodes possess the highest photocurrent response (1.25 mA cm^{-2}) at 1.23 V vs. RHE, indicating that the optimized chemical bath reaction time for coating CoFe PBA in the case of $\text{Fe}_2\text{O}_3/\text{Fe}_2\text{TiO}_5$ composite nanowires is 2 h.

5.3.4 Comparison between Structure and PEC Performance in Optimized Fe_2O_3 , $\text{Fe}_2\text{O}_3/\text{Fe}_2\text{TiO}_5$ and $\text{Fe}_2\text{O}_3/\text{Fe}_2\text{TiO}_5/\text{CoFe}$ PBA Electrodes

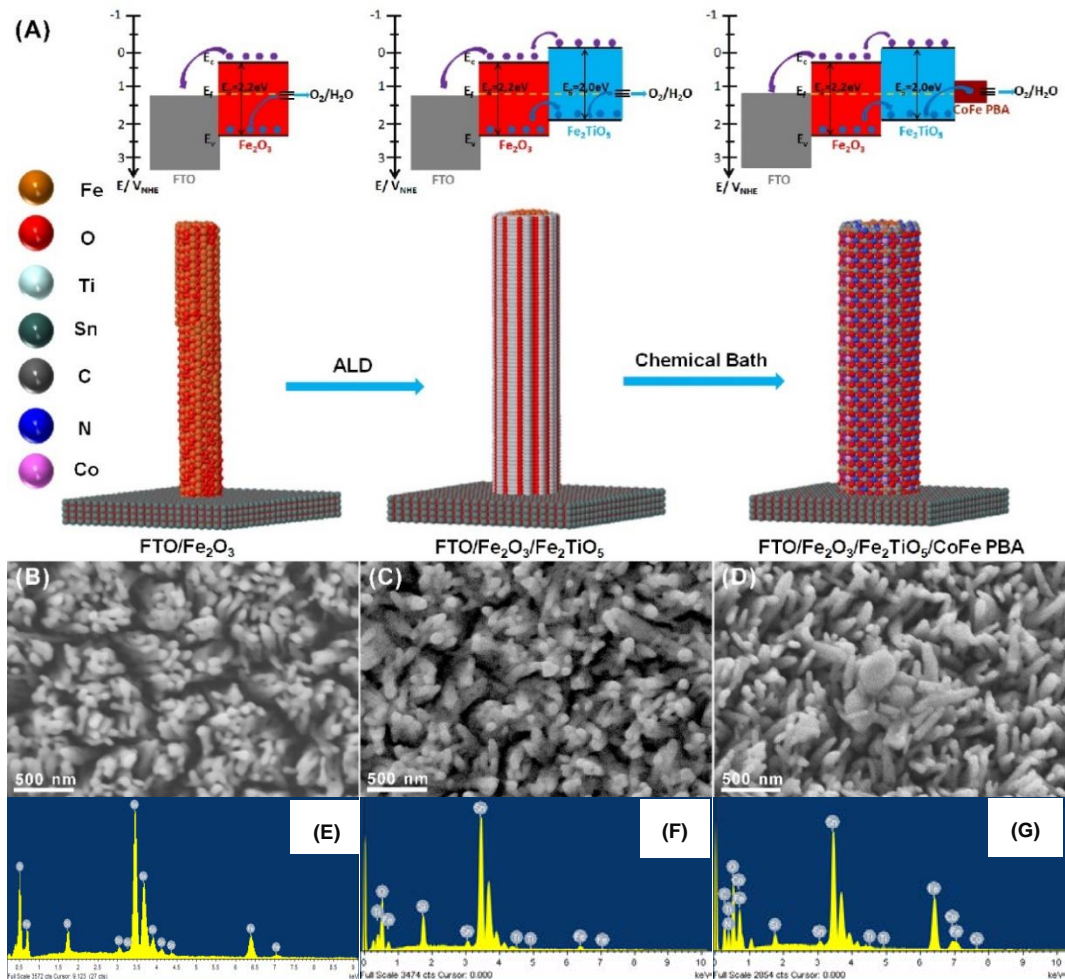


Figure 5.10 (A): Top rows: Thermodynamic scheme for the charge transfer processes at 1.23 V vs. RHE of SEI under illumination for the Fe_2O_3 , $\text{Fe}_2\text{O}_3/\text{Fe}_2\text{TiO}_5$, and $\text{Fe}_2\text{O}_3/\text{Fe}_2\text{TiO}_5/\text{CoFe}$ PBA electrodes. The black arrows indicate the bandgap of hematite and Fe_2TiO_5 . The dark blue and purple arrows refer to the hole and electron transfer processes at the multi-interfaces, respectively. For simplicity, interfacial charge transfer is considered to occur through the E_V (valence band) and/or E_C (conduction band) states directly, without the intervention of interfacial surface state. In all photoanodes, 4 electron-hole couples per visible active semiconductor are depicted. Fe_2O_3 : red; Fe_2TiO_5 : indigo; CoFe PBA: brown. Middle rows: 3D atomic supercell models illustrating the synthesis procedure for the $\text{Fe}_2\text{O}_3/\text{Fe}_2\text{TiO}_5/\text{CoFe}$ PBA photoanodes growth. SEM images of Fe_2O_3 (**B**), $\text{Fe}_2\text{O}_3/\text{Fe}_2\text{TiO}_5$ (**C**), and $\text{Fe}_2\text{O}_3/\text{Fe}_2\text{TiO}_5/\text{CoFe}$ PBA (**D**) electrodes. Bottom rows: EDS obtained on the Fe_2O_3 (**E**), $\text{Fe}_2\text{O}_3/\text{Fe}_2\text{TiO}_5$ (**F**), and $\text{Fe}_2\text{O}_3/\text{Fe}_2\text{TiO}_5/\text{CoFe}$ PBA (**G**) electrodes.

Vertically aligned Fe_2O_3 nanowires were firstly grown on a FTO substrate via the hydrothermal method, [20] the diameter of which ranges from 50 to 100 nm (**Figure 5.10 B**). Then, an ultrathin TiO_2 layer was coated onto the Fe_2O_3 nanowires by 30 ALD cycles. The surface coated TiO_2 was subsequently transformed into Fe_2TiO_5 through a post-quenching process in ambient atmosphere at 750 °C for 30 min. As displayed in **Figure 5.10 C**, the $\text{Fe}_2\text{O}_3/\text{Fe}_2\text{TiO}_5$ heterostructured nanowires are homogeneous without changing the nanowire-like architecture. Subsequently, the obtained $\text{Fe}_2\text{O}_3/\text{Fe}_2\text{TiO}_5$ composite nanowires were subjected to a chemical bath for 2h in the presence of CoFe PBA precursor at 60 °C to produce the $\text{Fe}_2\text{O}_3/\text{Fe}_2\text{TiO}_5/\text{CoFe}$ PBA heterostructured nanowires. Its SEM displayed in **Figure 5.10 D** reveals that tiny CoFe PBA nanoparticles were successfully grown onto the nanowires surface. It is important to point out that the diameter of these nanowires is almost not changed compared to that of the $\text{Fe}_2\text{O}_3/\text{Fe}_2\text{TiO}_5$ nanowires, indicating the ultrathin structure of the CoFe PBA shell. The elemental composition of the sample was primarily analysed via EDX in SEM in **Figures 5.10 E-G**, confirming the presence of hematite, Fe_2TiO_5 and CoFe PBA species in the corresponding electrodes.

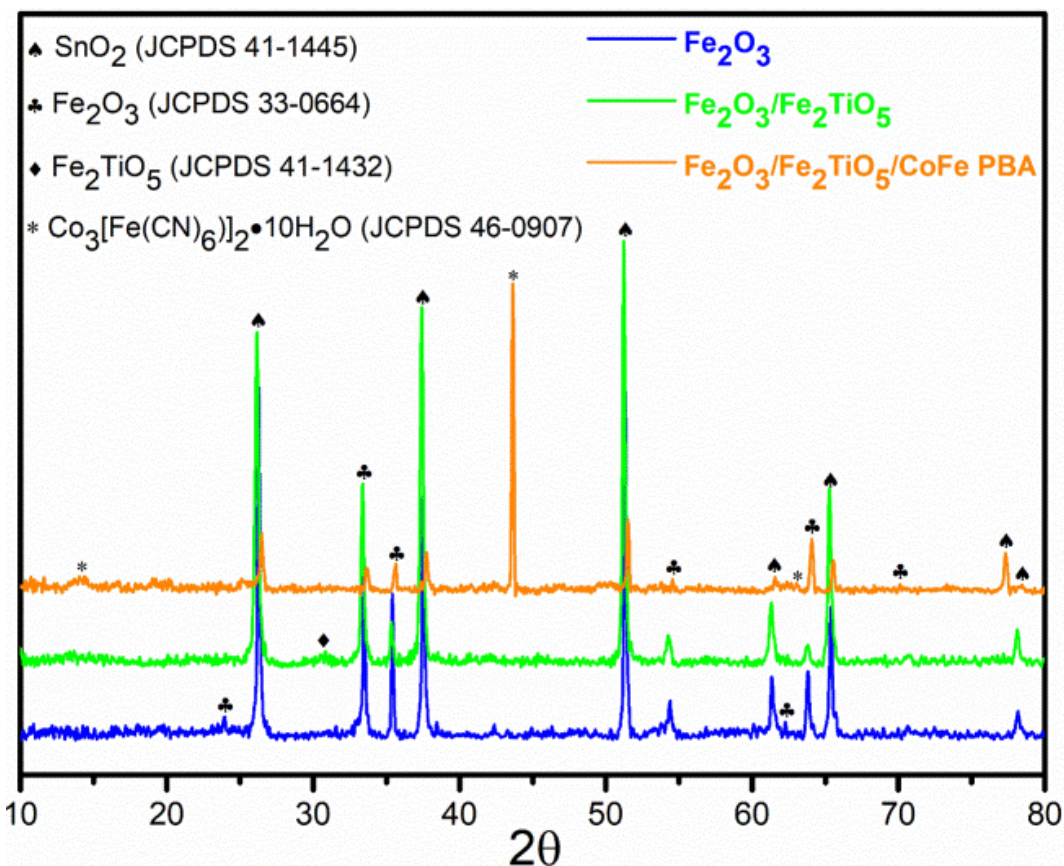


Figure 5.11 Grazing incidence XRD patterns of the Fe_2O_3 , $\text{Fe}_2\text{O}_3/\text{Fe}_2\text{TiO}_5$, and $\text{Fe}_2\text{O}_3/\text{Fe}_2\text{TiO}_5/\text{CoFe}$ PBA electrodes.

Characteristic XRD peaks of Fe_2O_3 (JCPDS no. 33-0664) and SnO_2 (JCPDS no. 41-1445, derived from FTO substrate) can be clearly observed in these electrodes shown in **Figure 5.11**. The diffraction peaks related to the pseudobrookite (Fe_2TiO_5 , JCPDS no. 41-1432) phase of $\text{Fe}_2\text{O}_3/\text{Fe}_2\text{TiO}_5$, and $\text{Fe}_2\text{O}_3/\text{Fe}_2\text{TiO}_5/\text{CoFe}$ PBA electrodes are very weak, which is attributed to the ultrathin Fe_2TiO_5 coating shell (30 ALD cycles, estimated ca. 0.81 nm). There is a sharp peak located at 44° in $\text{Fe}_2\text{O}_3/\text{Fe}_2\text{TiO}_5/\text{CoFe}$ PBA electrode, which can be assigned to the CoFe PBA, [13] revealing that the mass loading of CoFe PBA is higher than Fe_2TiO_5 . In addition, the reduced peaks intensity of SnO_2 , hematite and Fe_2TiO_5 phases in $\text{Fe}_2\text{O}_3/\text{Fe}_2\text{TiO}_5/\text{CoFe}$ PBA electrode are probably attributed to the shielding effect from the coated CoFe PBA species.

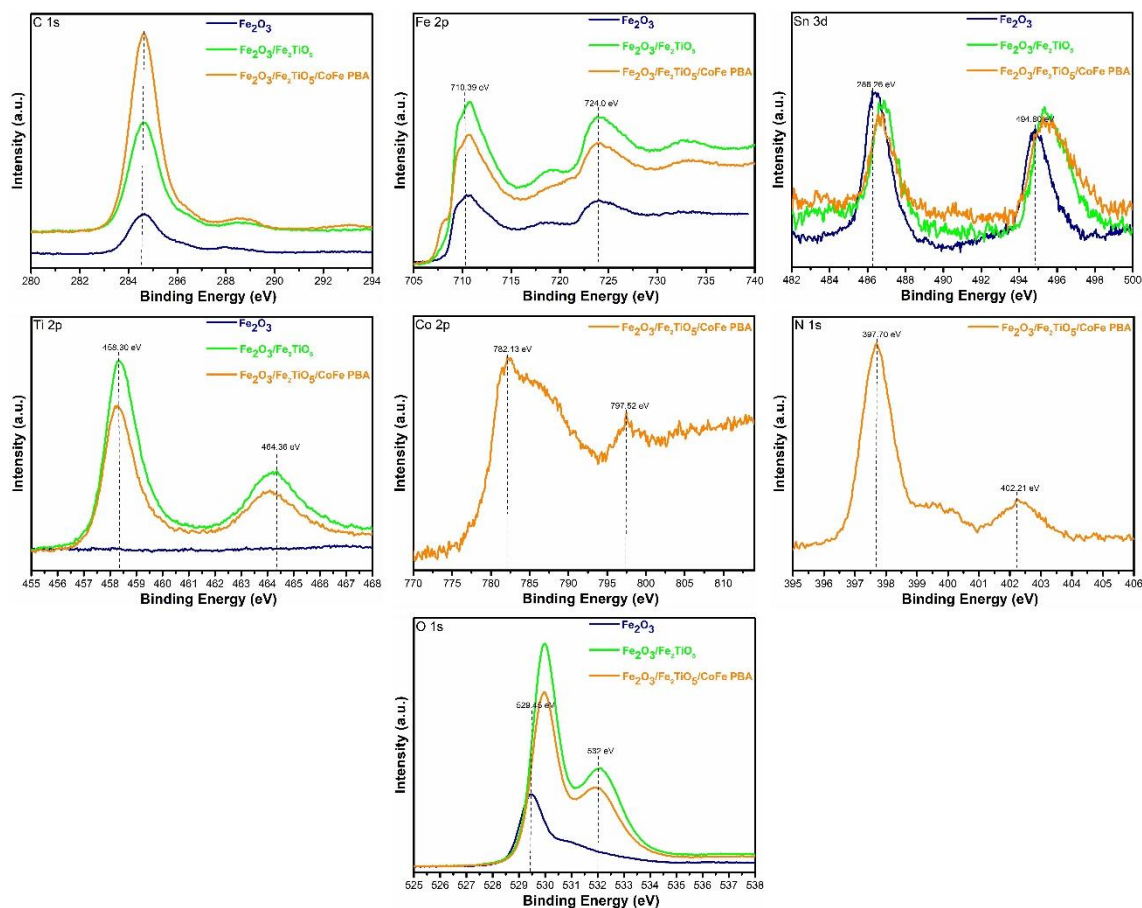


Figure 5.12 High resolution XPS spectra of C 1s, O 1s, Sn 3d, Ti 2p, Co 2p, Fe 2p and N 1s of the Fe_2O_3 , $\text{Fe}_2\text{O}_3/\text{CoFe PBA}$, $\text{Fe}_2\text{O}_3/\text{Fe}_2\text{TiO}_5$, and $\text{Fe}_2\text{O}_3/\text{Fe}_2\text{TiO}_5/\text{CoFe PBA}$ electrodes.

The surface electronic states and composition of these three representative electrodes were analysed by XPS and all binding energies were corrected for sample charging effects regarding the C 1s line at 284.6 eV. **Figure 5.12** presents the C 1s, O 1s, Sn 3d, Ti 2p, Co 2p, Fe 2p, and N 1s core level XPS scans at higher resolution over smaller energy windows. The Fe 2p_{1/2} and 2p_{3/2} peaks at the binding energies of 710.39 eV and 724.00 eV confirm the presence of the Fe element in these four electrodes. Additionally, two satellite peaks of the Fe 2p main line are present at approximately 8.1-8.5 eV lower energy than the main line, indicating the presence of Fe³⁺ species. [28-29] The Sn 3d_{3/2} and Sn 3d_{5/2} peaks at 494.80 and 486.26 eV with a splitting energy of 8.54 eV are consistent with reported values of Sn⁴⁺, indicating the diffusing of Sn elements from FTO substrate into nanowires due to the sintering treatment. [30-31] The Ti 2p_{1/2} and 2p_{3/2} peaks at 463.26 and 457.27 eV reveal the successful

coating of Fe_2TiO_5 for $\text{Fe}_2\text{O}_3/\text{Fe}_2\text{TiO}_5$ and $\text{Fe}_2\text{O}_3/\text{Fe}_2\text{TiO}_5/\text{CoFe PBA}$ electrodes. [28] The presence of Co 2p and N 1s peaks in $\text{Fe}_2\text{O}_3/\text{Fe}_2\text{TiO}_5/\text{CoFe PBA}$ electrodes, confirms the successful coating of CoFe PBA onto the $\text{Fe}_2\text{O}_3/\text{Fe}_2\text{TiO}_5$ nanowires surface. [32-33] The O 1s XPS spectrum of the Fe_2O_3 electrode has one peak, while that of $\text{Fe}_2\text{O}_3/\text{Fe}_2\text{TiO}_5$ and $\text{Fe}_2\text{O}_3/\text{Fe}_2\text{TiO}_5/\text{CoFe PBA}$ electrodes are composed of two peaks. The low binding energy at 529.45 eV is attributed to the coordination of the oxygen bound to iron atoms from the Fe_2O_3 or Fe_2TiO_5 moiety. [34] Whereas, the higher binding energy component at 532 eV O1s peak in $\text{Fe}_2\text{O}_3/\text{Fe}_2\text{TiO}_5$ and $\text{Fe}_2\text{O}_3/\text{Fe}_2\text{TiO}_5/\text{CoFe PBA}$ electrodes can be assigned to surface absorbed OH groups and the OOH bonding presence in CoFe PBA, respectively. [35]

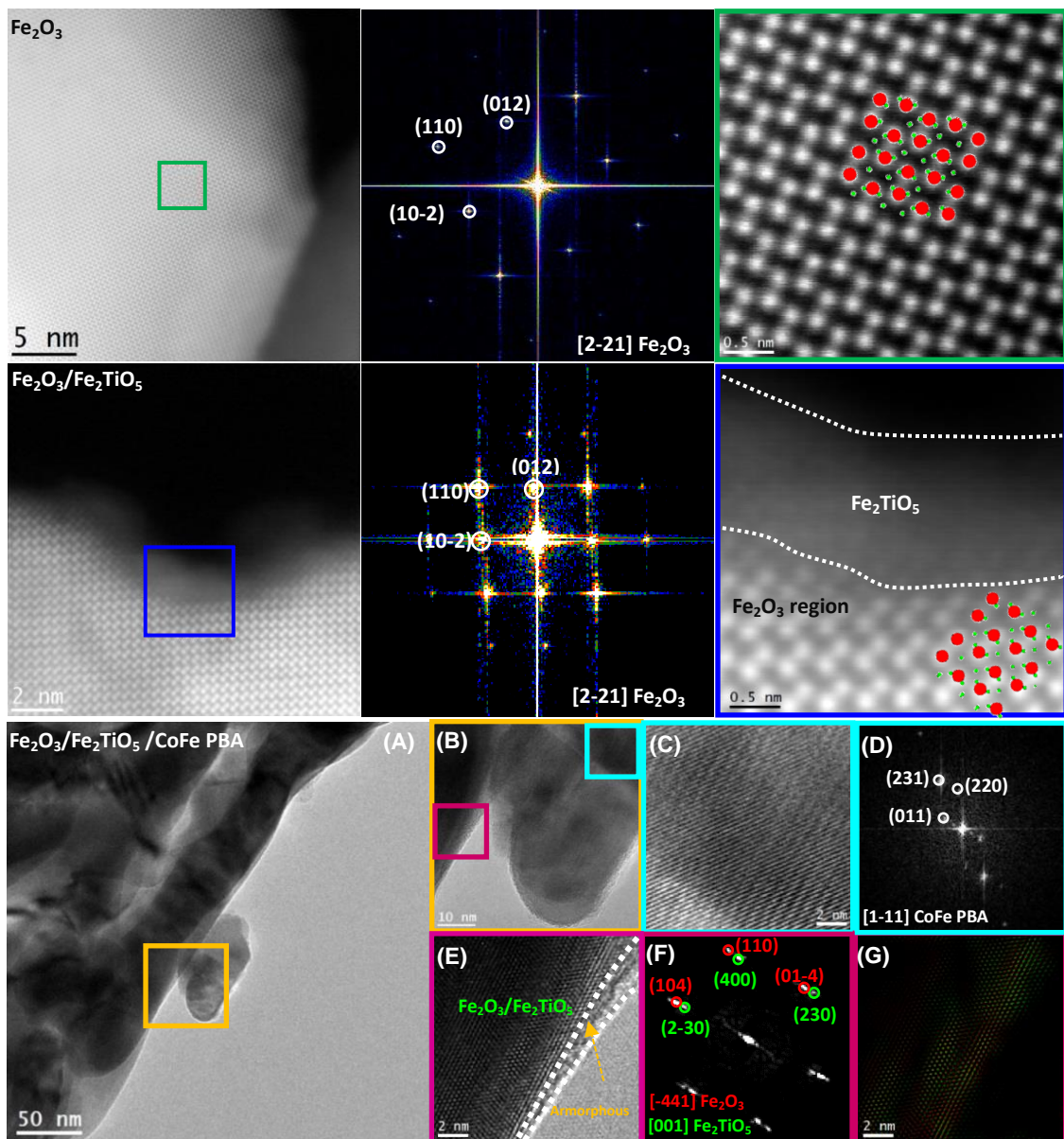


Figure 5.13 Top row: (Left) HAADF image showing the atomic ordering at the edge region of the Fe_2O_3 electrode. (Middle) the corresponding colored power spectrum (FFT) indicates that the nanowires crystallize in the hematite phase, as visualized along the [2-21] direction. (Right) atomic resolution HAADF image of the green squared region showing the Fe ordering, while O atoms are almost not visible in HAADF mode due to their weak Z-contrast. **Middle row:** (Left) HAADF image showing the atomic ordering at the edge region of the $\text{Fe}_2\text{O}_3/\text{Fe}_2\text{TiO}_5$ electrode. (Middle) the corresponding colored power spectrum indicates that the nanowires matrix is composed of hematite as visualized along the [2-21] direction. (Right) atomic resolution HAADF image of the blue squared region showing the ordering of Fe from hematite. The Fe_2TiO_5 shell is shown as a blurred ultrathin shell (ca. 1nm) on the surface of the hematite matrix since the height of the hematite-core and Fe_2TiO_5 shell are different. (The inset shows the atomic model of the Fe and O atoms visualized from [2-21] direction, Fe atoms are marked in red and O atoms are marked in green). **Bottom row:** (A): low magnification bright field TEM images showing the general morphology of the $\text{Fe}_2\text{O}_3/\text{Fe}_2\text{TiO}_5/\text{CoFe}$ PBA nanowires. (B): HRTEM detail showing the yellow squared interface area in (A). (C): Magnified HRTEM detail of the nanoparticle and (D): corresponding power spectrum indicating that the nanoparticle attached to the nanowire matrix crystallized in the cubic $\text{Co}_4(\text{Fe}(\text{CN})_6)_{2.67}(\text{H}_2\text{O})_{15.33}$ crystal structure (named as CoFe PBA), with [FM-3M]-Space group 225, and lattice parameters of $a = b = c = 1.02794$ nm. The nanoparticle is visualized along the [1-11] direction. (E): Left: HRTEM image of the nanowire edge region squared in purple in (C). The white dotted line is marking an amorphous CoFe PBA region. (F): Corresponding power spectrum (FFT) indicating that the nanowire heterostructure is mainly composed of hematite and pseudobrookite visualized along the [-441] and [001] directions, respectively. (G): Frequency filtered structural map of the hematite (red) and pseudobrookite (green), showing their atomic stacking sequence.

The HAADF images obtained on the Fe_2O_3 and $\text{Fe}_2\text{O}_3/\text{Fe}_2\text{TiO}_5$ electrodes in top and middle rows of **Figure 5.13** show the atomic ordering of the hematite matrix, while the Fe_2TiO_5 species in the $\text{Fe}_2\text{O}_3/\text{Fe}_2\text{TiO}_5$ electrode are shown as a blurred ultrathin shell on the surface of the hematite nanowires. **Figure 5.13A** display general TEM images of the $\text{Fe}_2\text{O}_3/\text{Fe}_2\text{TiO}_5/\text{CoFe}$ PBA nanowire. The crystal structure assigned to CoFe PBA species is mainly derived from the nanoparticles attached to the composite

nanowire matrix according to **Figures 5.13 B-D**. The hematite and pseudobrookite phases dominate the nanowires matrix, as identified by the HRTEM and their corresponding power spectra in **Figures 5.13 E-F**. Moreover, the corresponding frequency filtered image (**Figure 5.13 G**) illustrates the localized presence of a core hematite nanowire and an ultrathin pseudobrookite shell. Besides, **Figure 5.14** indicates that the fine CoFe PBA shell on the nanowires surface tend to be an amorphous structure, whereas, the biggish CoFe PBA nanoparticles present clearly lattice fringes denoting a good crystallinity, as displayed in **Figure 5.13 C**.

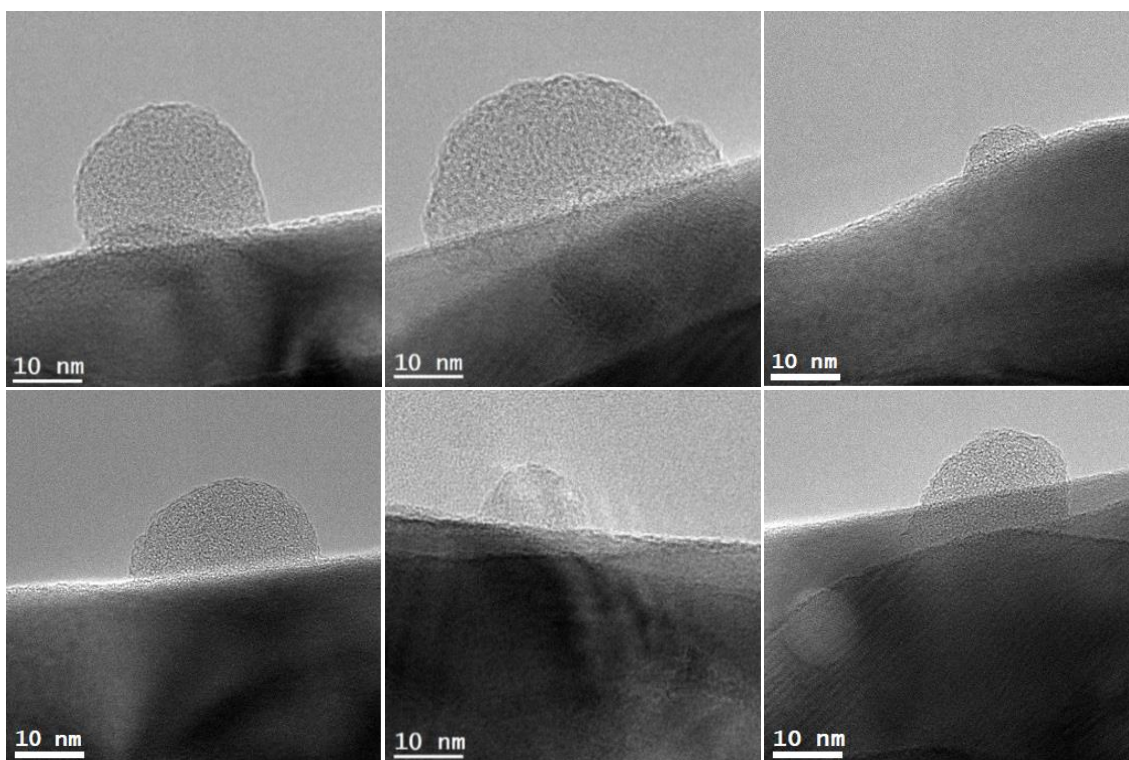


Figure 5.14 Low magnification TEM showing the nanodots-like CoFe PBA decorating the composite $\text{Fe}_2\text{O}_3/\text{Fe}_2\text{TiO}_5$ nanowires surface in the $\text{Fe}_2\text{O}_3/\text{Fe}_2\text{TiO}_5/\text{CoFe}$ PBA electrode.

It is noteworthy to mention that in addition to the CoFe PBA nanoparticles, there is also a tiny C, N, O, Co and Fe signal surrounding the nanowires matrix based on the STEM-EELS maps shown in **Figure 5.15**. The latest EELS results reveal the presence of an ultrathin CoFe PBA shell on the surface of the $\text{Fe}_2\text{O}_3/\text{Fe}_2\text{TiO}_5$ nanowires, which is consistent with the ultrathin amorphous region observed in **Figure 5.13 E**.

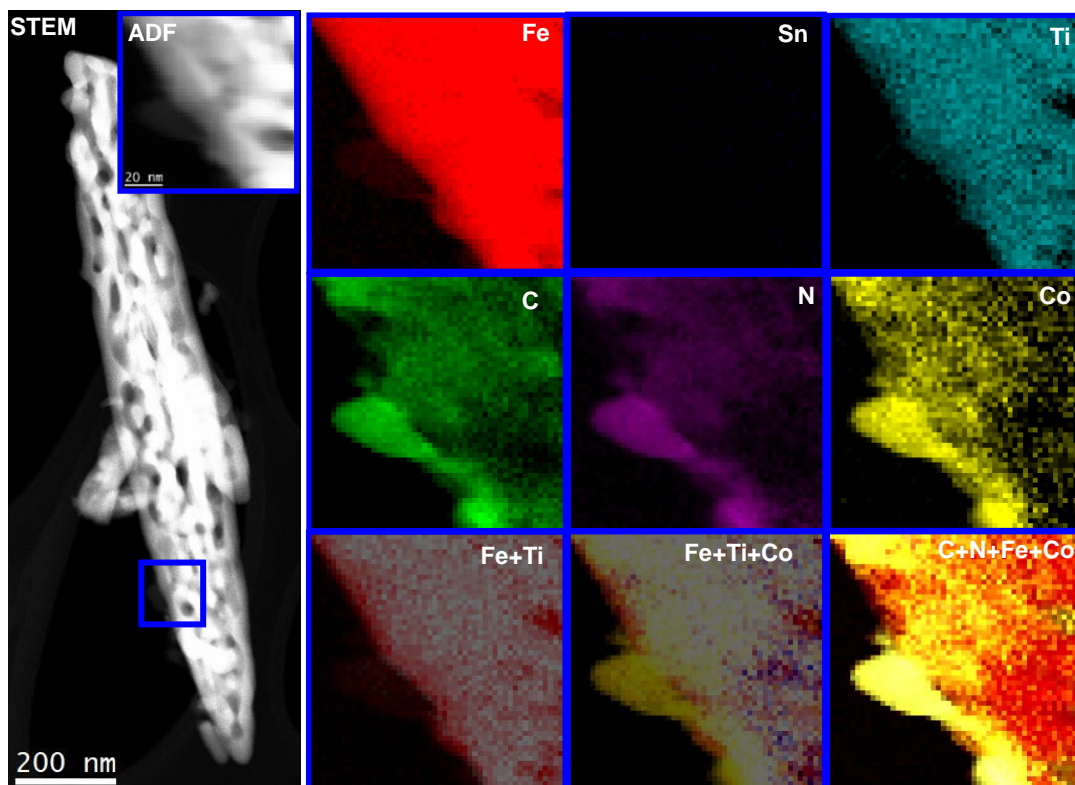


Figure 5.15 EELS chemical composition maps obtained from the blue rectangled area of the ADF-STEM micrograph of a nanowire extracted from the $\text{Fe}_2\text{O}_3/\text{Fe}_2\text{TiO}_5/\text{CoFe}$ PBA electrode. Individual Fe (red), C (green), Sn (blue), N (purple), Ti (indigo) and Co (yellow) maps and their composites.

The PEC performance measured for these photoanodes is displayed in **Figure 5.16**. CVs under dark in **Figure 5.16A** reveals that the onset potential of hematite nanowires shows a positive shift with the addition of ultrathin Fe_2TiO_5 shell, coinciding with our previous report. [20] However, that of $\text{Fe}_2\text{O}_3/\text{Fe}_2\text{TiO}_5$ nanowires is reduced with the addition of CoFe PBA, indicating the catalytic effect from CoFe PBA OECs. The CVs under illumination of pristine Fe_2O_3 nanowires (**Figure 5.16B** and the inset of **Figure 5.16A**) show a relatively low photocurrent response over the whole potential window with a photocurrent density of 0.12 mA cm^{-2} at 1.23 V vs RHE, thermodynamic potential for oxygen evolution reaction (OER). Upon introduction of the Fe_2TiO_5 , the photocurrent density increases to 0.90 mA cm^{-2} at 1.23 V vs. RHE. The $\text{Fe}_2\text{O}_3/\text{Fe}_2\text{TiO}_5/\text{CoFe}$ PBA electrode possesses a lower onset potential than the Fe_2O_3 and the $\text{Fe}_2\text{O}_3/\text{Fe}_2\text{TiO}_5$ electrodes. The optimized $\text{Fe}_2\text{O}_3/\text{Fe}_2\text{TiO}_5/\text{CoFe}$ PBA electrode exhibits a photocurrent of 1.25 mA cm^{-2} at 1.23 V vs.

RHE after chemical bath reaction at 60 °C for 2 h, which is much higher than that of the Fe₂O₃ and Fe₂O₃/Fe₂TiO₅ electrodes.

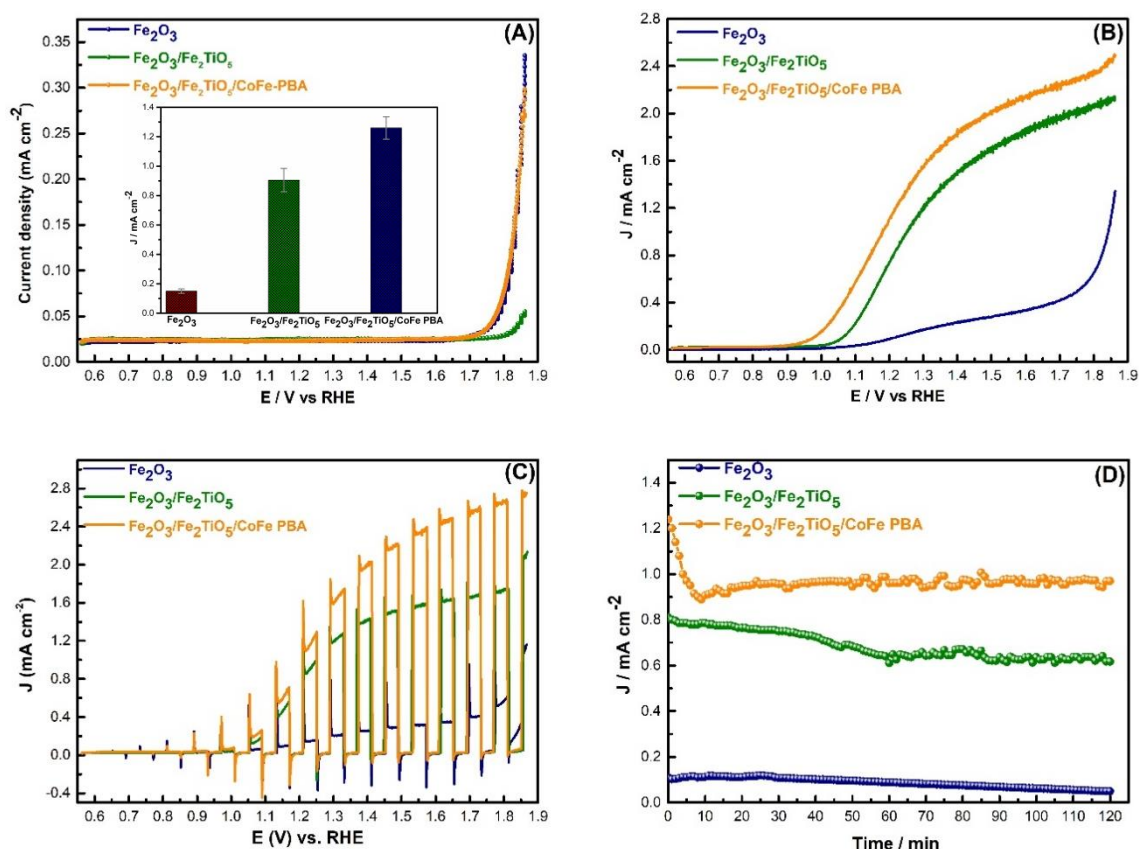


Figure 5.16 (A) Cyclic voltammetry under dark (the inset shows the statistical photocurrent response at 1.23 V vs RHE. based on at least three repeated electrodes), (B) Cyclic voltammetry under illumination, (C) chopped light photocurrent-potential curves, and (D) photoelectrochemical stability test operated at 1.23 V vs. RHE for the Fe₂O₃, Fe₂O₃/Fe₂TiO₅, and Fe₂O₃/Fe₂TiO₅/CoFe PBA electrodes. All polarization potentials reported here are relative to the reversible hydrogen electrode (RHE), and current densities are per geometric area. J (mA cm⁻²) represents the current density response under light illumination.

Additionally, it is better than the photocurrent response (0.62 mA cm⁻²) of the optimized Fe₂O₃/CoFe PBA electrode in **Figures 5.6-5.7**, indicating the advantage of combining the Fe₂O₃/Fe₂TiO₅ type II heterojunction and effective CoFe PBA OECs. Besides, the chopping light CV characterization in **Figure 5.16 C** indicates the reduction of the electron and hole recombination in the Fe₂O₃/Fe₂TiO₅/CoFe PBA electrodes, which further confirms its best photocurrent response among these three

electrodes. The photoelectrochemical stability is operated by chronoamperometric response at a constant applied working potential of 1.23 V vs. RHE, as shown in **Figure 5.16 D**. The photocurrent of the Fe_2O_3 intensively decreases from 0.12 mA cm^{-2} to 0.05 mA cm^{-2} over the course of 2 h experiment. In contrast, almost 80% of the photocurrent response has been retained for the $\text{Fe}_2\text{O}_3/\text{Fe}_2\text{TiO}_5/\text{CoFe}$ PBA electrode during the stability test and maintained a photocurrent of 0.95 mA cm^{-2} throughout. The slightly reduction of its photocurrent is probably due to the detachment of the CoFe PBA OEC from the $\text{Fe}_2\text{O}_3/\text{Fe}_2\text{TiO}_5$ nanowires, which is also observed in the report of Wang D.W. et al. [6]

5.3.5 PEC mechanism Investigation of the Optimized Fe_2O_3 , $\text{Fe}_2\text{O}_3/\text{Fe}_2\text{TiO}_5$ and $\text{Fe}_2\text{O}_3/\text{Fe}_2\text{TiO}_5/\text{CoFe}$ PBA Electrodes via PEIS

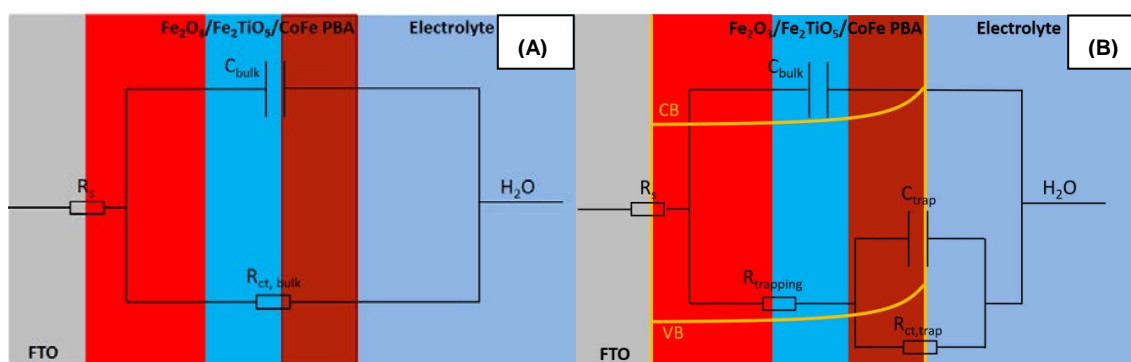


Figure 5.17 **A**: Simple Randles circuit for the charge transfer process of a composite hematite electrode under dark. **B**: Equivalent circuit (EC) for the charge transfer process of a composite hematite electrode under illumination, the semiconductor/electrolyte interface is mediated by surface states.

Figure 5.18 shows the Nyquist impedance of Fe_2O_3 , $\text{Fe}_2\text{O}_3/\text{Fe}_2\text{TiO}_5$ and $\text{Fe}_2\text{O}_3/\text{Fe}_2\text{TiO}_5/\text{CoFe}$ PBA electrodes carried out under dark at different potential, from 0.50 to 0.90 V vs. Ag/AgCl. A Bode plot represents the frequency response of a system to a sinusoidal perturbation: it is usually a combination of a magnitude plot, expressing the magnitude of the frequency response, and an angle plot, expressing the phase shift. Both quantities are plotted against a horizontal axis proportional to the logarithm of the frequency. In the Bode angle plot, each peak should be associated with a capacitance and a resistance in parallel, to which corresponds a characteristic

frequency, given by $1/RC$. [36] In this condition, each curve is composed of one arc, characterized by one peak in the Bode angle plots. [13] **Figure 5.17A** displays the equivalent circuit (EC) used to fit the EIS data obtained from 0.50 V up to 0.90 V vs Ag/AgCl under dark. [37] In this case, the R_s resistance is associated with the electric contacts of the electrode, electrolyte, etc. The parallel ($R_{ct,bulk}+C_{bulk}$) combination is associated with the dielectric properties and resistivity of the film as well as the faradic process of OER. [13]

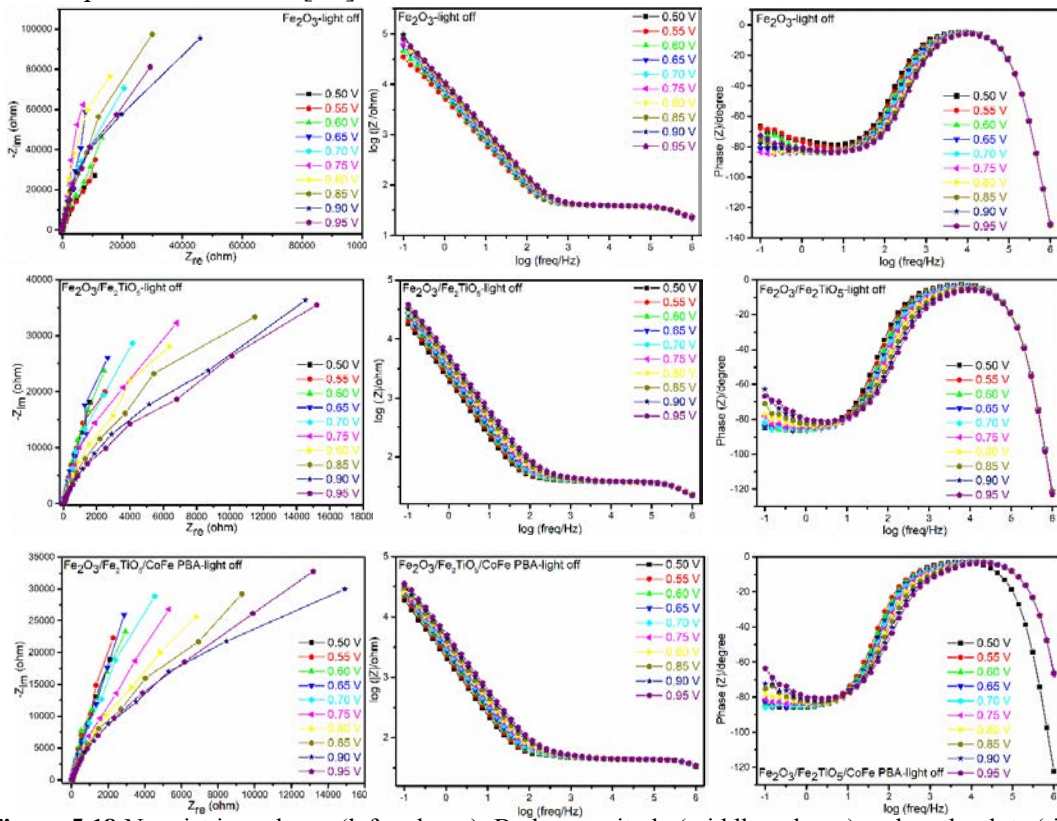


Figure 5.18 Nyquist impedance (left column), Bode magnitude (middle column) and angle plots (right column) for the Fe_2O_3 , Fe_2O_3/Fe_2TiO_5 , and $Fe_2O_3/Fe_2TiO_5/CoFe$ PBA electrodes at 0.50, 0.55, 0.60, 0.65, 0.70, 0.75, 0.80, 0.85 and 0.90 V vs Ag/AgCl reference electrode under dark (light off).

Figure 5.19 shows the Nyquist impedance of Fe_2O_3 , Fe_2O_3/Fe_2TiO_5 and $Fe_2O_3/Fe_2TiO_5/CoFe$ PBA electrodes carried out under illumination at different potential, from 0.60 to 1.20 V vs. Ag/AgCl. Differently from the Nyquist impedance of these electrodes under dark, in this case, each curve is composed of two arcs, characterized by two peaks in the Bode angle plots. [36] **Figure 5.17B** displays the equivalent circuit (EC) used to fit the EIS data obtained from 0.60 V up to 0.90 V vs. Ag/AgCl under illumination. [37] The R_s resistance is associated with the electric contacts of

the electrode, electrolyte, etc. The R_{trapping} resistance is associated with charge trapping at surface states. The C_{bulk} capacitance is associated with charge accumulation in the bulk. The $R_{\text{ct,trap}}$ resistance is associated with the charge transfer process from surface states. Finally, the C_{trap} capacitance is associated with charge accumulation on the surface states. [28]

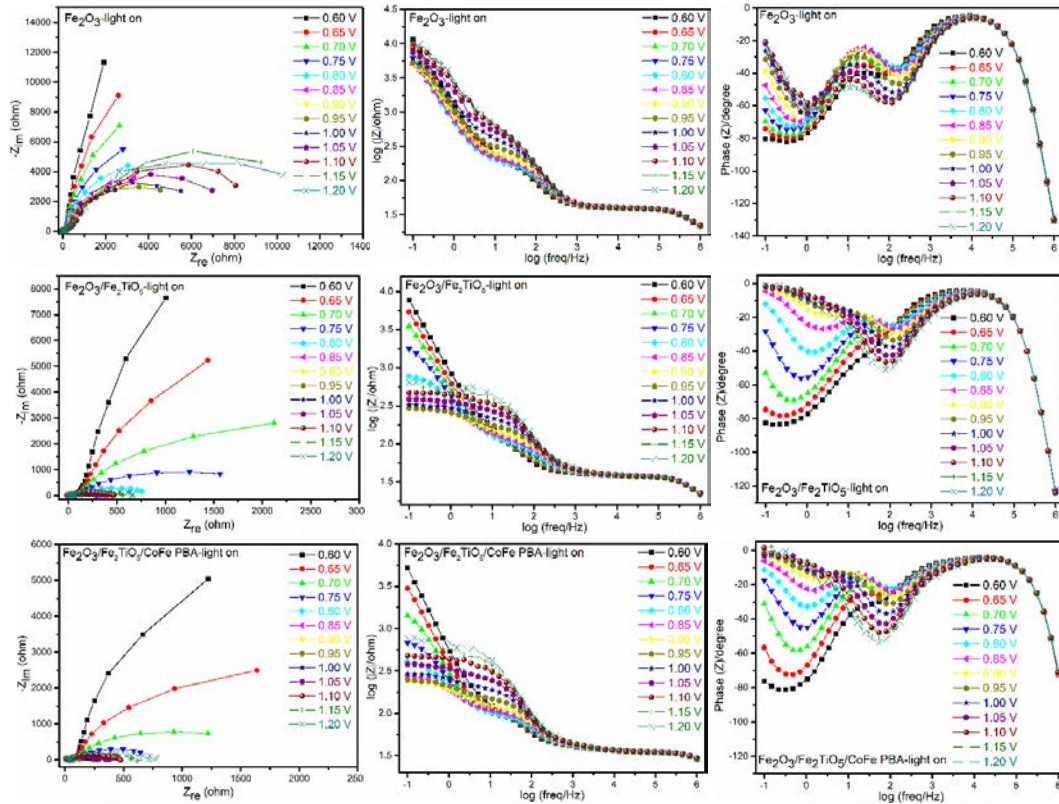


Figure 5.19 Nyquist impedance (left column), Bode magnitude (middle column) and angle plots (right column) of the Fe_2O_3 , $\text{Fe}_2\text{O}_3/\text{Fe}_2\text{TiO}_5$, and $\text{Fe}_2\text{O}_3/\text{Fe}_2\text{TiO}_5/\text{CoFe PBA}$ electrodes at 0.60, 0.65, 0.70, 0.75, 0.80, 0.85, 0.90, 0.95, 1.00, 1.05, 1.10, 1.15 and 1.20 V vs Ag/AgCl reference electrode under illumination.

Previous cyclic voltammetry and impedance spectroscopy combined with operando UV-vis experiments have related the C_{trap} to the oxidation of low valent iron-hydroxyl surface species to surface bound iron species with higher valence states on hematite photoanodes, such as $\text{Fe}=\text{O}$ intermediates. [38] Herein, CV and PEIS techniques are employed to investigate the mechanisms by which the Fe_2TiO_5 and CoFe PBA enhance the PEC performance of the hematite photoanodes. As displayed in **Figure 5.22A**, the cathodic peak in the CV curves varies with the addition of Fe_2TiO_5 and CoFe PBA, indicating the gradual change of the surface state. [39] The general

behaviour of the composite nanowires can be phenomenologically correlated with the varying of the surface state based on the aforementioned CV result and the primary PEIS in **Figures 5.18-5.19**. [20, 40-41] In particular, electrical active surface states located in the semiconductor's band gap are expected to play a vital role in PEC water splitting, therefore, a deeper investigation is required to verify their effect on the charge transportation at the interface of the semiconductor and the electrolyte. [41-42] The primary EIS under dark and illumination were fitted via the equivalent circuits in **Figure 5.17**; the obtained fitting data were plotted in **Figures 5.19-5.21**.

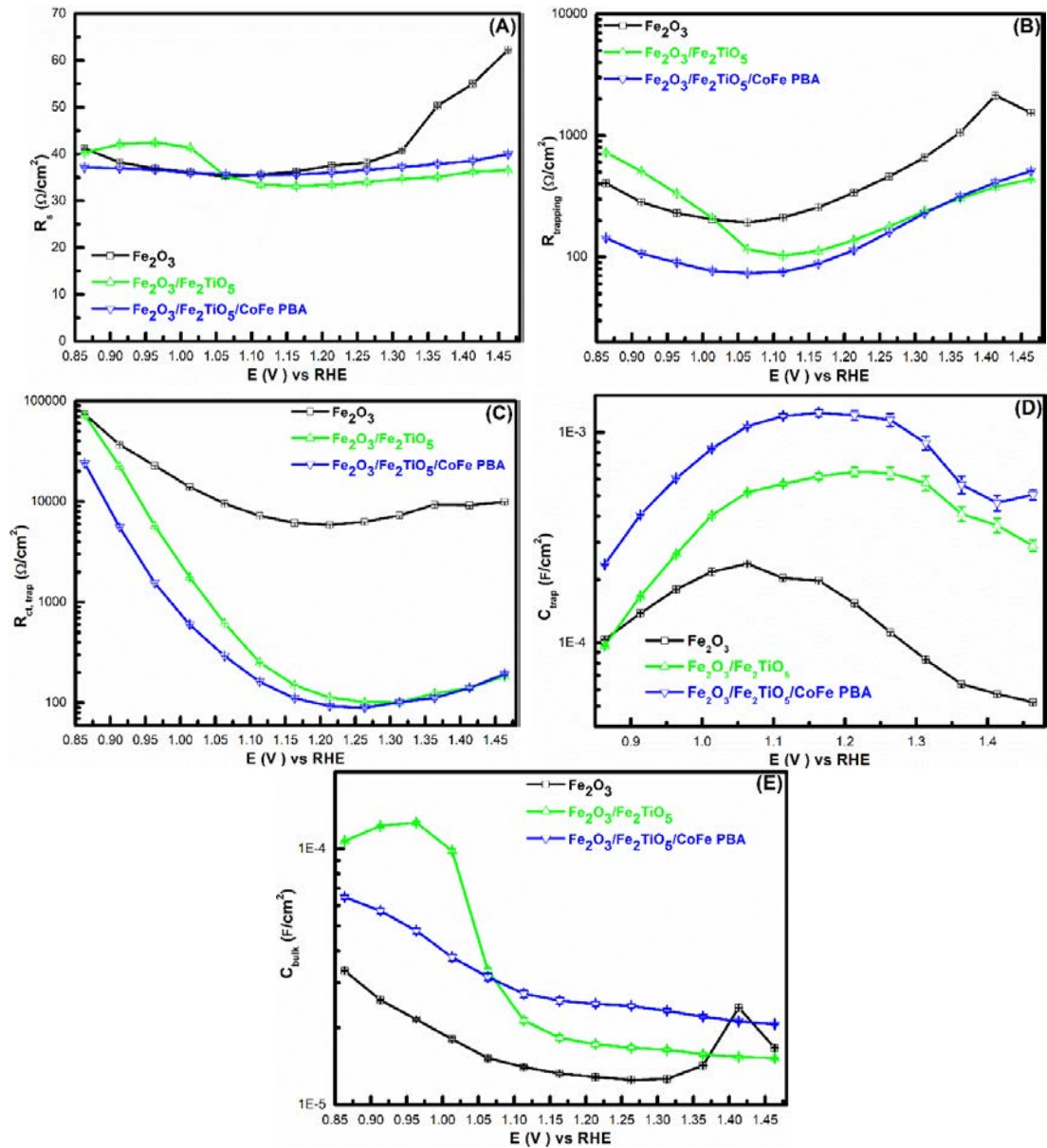


Figure 5.20 Equivalent circuit parameters obtained from fitting EIS data for the Fe₂O₃, Fe₂O₃/Fe₂TiO₅, and Fe₂O₃/Fe₂TiO₅/CoFe PBA electrodes in contact with 0.1 M NaNO₃ + 0.1 M HNO₃ electrolytes

under 1 sun illumination. R_s (A), R_{trapping} (B), $R_{\text{ct,trap}}$ (C), C_{trap} (D) and C_{bulk} (E) as a function of the applied potential. R_s , associated with the electric contacts of the electrode, electrolyte, etc. R_{trapping} , associated with charge trapping at surface states. $R_{\text{ct,trap}}$, associated with the charge transfer process from surface states. C_{bulk} , associated with charge accumulation in the bulk. C_{trap} , associated with charge accumulation on the surface states.

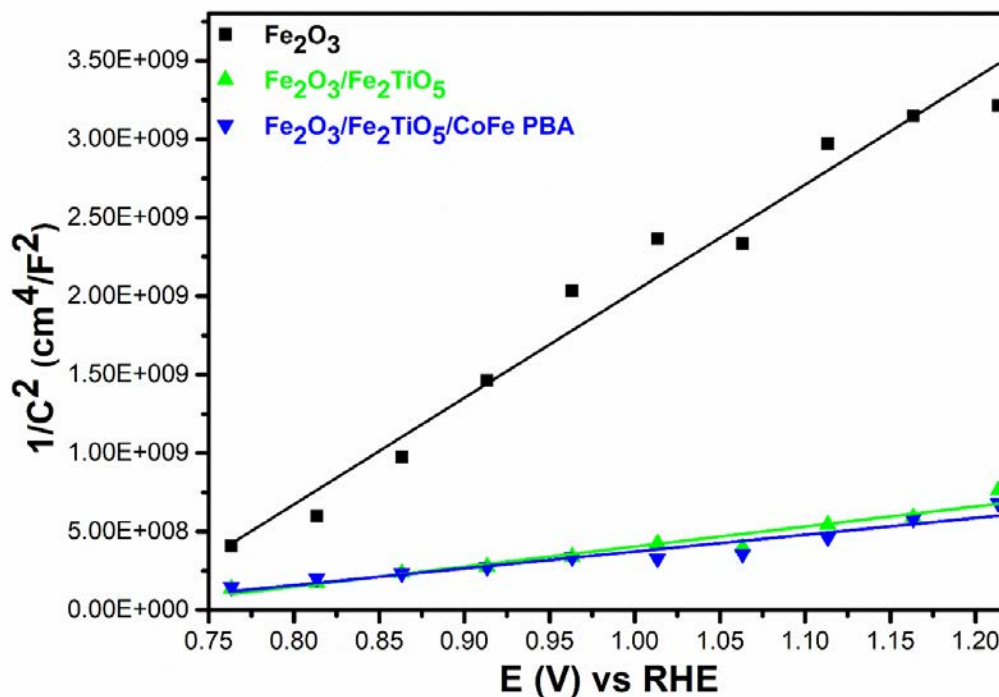


Figure 5.21 Mott-Schottky plots (C^{-2} vs. E) of the Fe_2O_3 , $\text{Fe}_2\text{O}_3/\text{Fe}_2\text{TiO}_5$, and $\text{Fe}_2\text{O}_3/\text{Fe}_2\text{TiO}_5/\text{CoFe}$ PBA electrodes. Each point was obtained upon fitting the corresponding Nyquist plot at each potential in the dark to a classic Randles circuit (i.e. resistance and capacitance in parallel). Linear fittings (obtained in the 0.75-1.20 V vs. RHE potential range) are also depicted on each case.

In order to highlight the role of the surface state in the interfacial charge transfer process, we calculated the density of surface states (DOSS) with the C_{trap} obtained by using equation (1): [28, 37]

$$N_{\text{ss}}(E) = C_{\text{trap}}(E)/q \quad (1)$$

Where $N_{\text{ss}}(E)$ is the DOSS ($\text{cm}^{-2} \text{eV}^{-1}$) as a function of the applied potential and q is the electron charge ($1.602 \times 10^{-19} \text{C}$). It is possible to observe the energy and density distribution of the surface state located below the photocurrent onset with its Fermi level pinned at the surface state. [37]

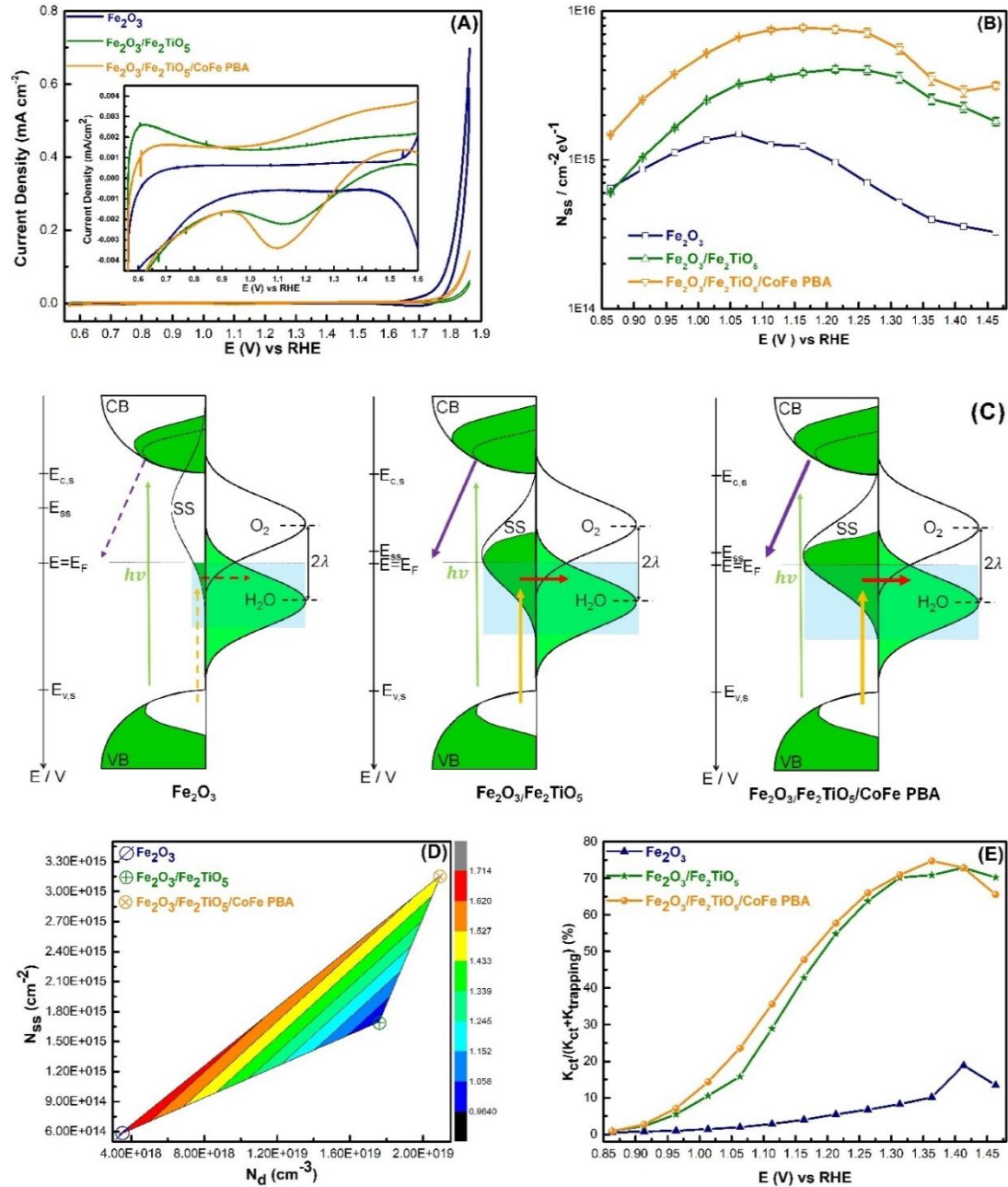


Figure 5.22 (A): CV curves scanned in dark at $20 \text{ mV} \cdot \text{s}^{-1}$ immediately after holding the electrode potential at 1.85 V vs. RHE. for 1 min under illumination. (The inset shows its magnified plot). (B): Density of surface states (DOSS) as a function of the applied potential. Error bars stem from the goodness of the EIS data fittings. (C) Kinetic scheme of the charge generation and transfer processes at SEI at 1.23 V vs RHE of these electrodes under illumination. Green and white areas refer to electron filled and empty states, respectively. The dotted lines marked region in the conduction band (CB) filled states denote photogenerated electrons with the same relative area as the empty states at the valence band (VB); the exceeding green region highlight the doping levels in these electrodes. The green arrow

refers to the charge generation process upon visible photons absorption; the yellow arrow refers to the hole trapping process at SS; the red arrow refers to the hole transfer process from SS to electrolyte; the purple arrow refers to electron transfer from CB states to the FTO substrate. The thickness and shape of the arrows reveal the relative rates of the charge transfer processes, where the dotted line represents the slowest rate (Fe_2O_3 electrode) and the thickest line represents the fastest rate ($\text{Fe}_2\text{O}_3/\text{Fe}_2\text{TiO}_5/\text{CoFe}$ PBA electrode). The light indigo shaded areas refer to the relative overlapping of the DOSS and water density of states. E : electrode potential; $E_{c,s}$: surface CB edge potential; E_F : Fermi level of the semiconductors that matches the electrode potential (E) and the $\text{O}_2/\text{H}_2\text{O}$ couple thermodynamic potential (1.23 V vs RHE); E_{ss} : center potential of the SS distribution; $E_{v,s}$: surface VB edge potential; λ : redox couple reorganization energy. **(D)**: Total surface state density (N_{ss}), donor density (N_d), and their ratio (N_{ss}/N_d) plot. N_d was estimated from the slopes of the Mott-Schottky plots in the dark, whereas N_{ss} was obtained from integration of DOSS profiles. Color bar with a unit of μm is plotted on the right Y axis for N_{ss}/N_d . **(E)**: Ratio of the charge transfer rate constant (k_{ct}) and the sum of k_{ct} and trapping rate constant ($k_{trapping}$) at different potential.

As displayed in **Figure 5.22B**, the N_{ss} of these photoanodes follows the order: $\text{Fe}_2\text{O}_3 < \text{Fe}_2\text{O}_3/\text{Fe}_2\text{TiO}_5 < \text{Fe}_2\text{O}_3/\text{Fe}_2\text{TiO}_5/\text{CoFe}$ PBA across the entire SS dominated region (0.86 V to 1.46 V). The extended SS distribution from 0.86 V to 1.46 V in the Fe_2O_3 electrodes probably spans inside the CB and triggers a deleterious Fermi level pinning at SS, which could be responsible for its low photocurrent response. [28] Moreover, the potential of the DOSS peak of the composite photoanodes shifts to more positive values, e.g., 1.05 V, 1.15 V and 1.15 V for the Fe_2O_3 , $\text{Fe}_2\text{O}_3/\text{Fe}_2\text{TiO}_5$ and $\text{Fe}_2\text{O}_3/\text{Fe}_2\text{TiO}_5/\text{CoFe}$ PBA electrodes, respectively. Besides, the shape of these DOSS curves is consistent with the CV curves of these electrodes scanned in the cathodic direction in dark at 20 mV s^{-1} immediately after holding the electrodes' potential at 1.85 V vs. RHE. for 1 min under illumination in **Figure 5.22A**, indicating the suitable utilization of an electrical circuit for EIS fitting. [38-39, 46] Consequently, the ultrathin Fe_2TiO_5 and CoFe PBA coatings essentially worked together to regulate the density and energy level of the surface state of hematite nanowires. Since the SS lie inside the bandgap and the hole transfer occurs from the top of the VB ($E_{v,s}$), then

under a certain electrode polarization (E), the hole transfer rate constant (k_{ct}) will be proportional to equation (2): [43-44]

$$k_{ct} = \int_{E_{v,s}}^E N_{ss}f(E)D_{H_2O}(E)dE \quad (2)$$

in which. $f(E)$ is the Fermi-Dirac distribution that indicates the fraction of occupied SS and $D_{H_2O}(E)$ is the water density of states ($cm^{-2}eV^{-1}$). Given that the inelastic hole trapping process mediated by SS is fast enough, [43] the photocurrent response is proportional to k_{ct} , [45] depending upon the overlapping between the filled SS and the filled water density of states. Hence, there is a direct correlation between the percentage of available filled surface states (larger DOSS) near the thermodynamic potential for OER, and the observed photocurrent response at 1.23 V vs. RHE due to the required isoenergetic hole transfer process at the SEI, as illustrated in **Figure 5.22C**. [20, 28, 43]

A combined comparison of the N_{ss} , N_d and N_{ss}/N_d ratio is presented in **Figure 5.22D**. The pristine Fe_2O_3 electrodes display a relatively high N_{ss}/N_d ratio but poor PEC performance, indicating that a large N_{ss}/N_d ratio does not ensure a good photoactivity due to the lack of donors and conductivity in the Fe_2O_3 electrode. For the Fe_2O_3/Fe_2TiO_5 electrode, even though, the N_d is enhanced via Ti doping, it does not enable a high photocurrent response because the N_{ss}/N_d is relatively low. In the case of the $Fe_2O_3/Fe_2TiO_5/CoFe$ PBA electrode, a relatively high N_{ss}/N_d ratio corresponds to a scenario in which N_{ss} and N_d are both numerous enough to enable a larger photocurrent response. Furthermore, the charge transfer efficiency at the SEI is estimated through (equation (3)): [20, 28, 45, 47]

$$\text{Transfer efficiency}(\%) = \frac{k_{ct}}{k_{ct}+k_{trapping}} = \frac{R_{trapping}}{R_{ct,trap}+R_{trapping}} \quad (3)$$

where k_{ct} and $k_{trapping}$ are the charge transfer and trapping rate constants, respectively. The charge transfer efficiency calculated based on the fitted resistance from PEIS is shown in **Figure 5.22E**. Typically, the surface electron-hole recombination in the $Fe_2O_3/Fe_2TiO_5/CoFe$ PBA electrodes has been suppressed due to the couple effect

from type II heterojunction and the catalytic property of the OECs. Specifically, in the case of the $\text{Fe}_2\text{O}_3/\text{Fe}_2\text{TiO}_5/\text{CoFe}$ PBA electrode, over 60 % of the holes are being transferred into the electrolyte at 1.23 V vs RHE, which is almost 10 times higher than that of pristine Fe_2O_3 . Taken as a whole, the calculated charge transfer efficiency of these electrodes coincide with the steady-state current-voltage relationship (**Figure 5.16B**), indicating the correct utilization of the electrical circuit for PEIS data fitting to illustrate the charge transfer at the SEI. [37]

5.4 Summary

Cheap and stable water-oxidation catalysts (OECs) in acidic electrolyte are a key component for a functional photoelectrochemical (PEC) water splitting device. The state-of-the-art OECs in acid electrolyte usually feature expensive noble metals such as ruthenium and iridium (Ir)-based species, which are typically too expensive to be implemented broadly in affordable hematite photoanodes. Herein, an alternative earth-abundant CoFe PBA is combined with Fe₂O₃/Fe₂TiO₅ core-shell type II heterojunction nanowires as photoanodes for PEC water splitting. The observed photocurrent is improved from 0.12 mA cm⁻² to 1.25 mA cm⁻² at 1.23 V vs RHE upon the integration of ultrathin Fe₂TiO₅ layer and CoFe PBA OECs coating; the value is 10 times higher than that of pristine Fe₂O₃ nanowires in acidic electrolyte (pH=1.01). Further investigation of the PEC mechanisms via PEIS demonstrates that the tuned energy level and density of surface state and the enhanced charge transfer efficiency together contribute to its excellent PEC performance in acid electrolyte.

References

- [1] N. S. Lewis, Toward cost-effective solar energy use, *Science*, **2007**, 315, 798-801.
- [2] S. Dahl, I. Chorkendorff, Solar-fuel generation: towards practical implementation, *Nat. Mater.*, **2012**, 11, 100-101.
- [3] A.J. Bard, M. A. Fox, Artificial photosynthesis: solar splitting of water to hydrogen and oxygen, *Acc. Chem. Res.*, **1995**, 28, 141-145.
- [4] K. Sivula, R.V.D. Krol, Semiconducting materials for photoelectrochemical energy conversion, *Nat. Rev. Mater.*, **2016**, 1, 15010.
- [5] R. E. Blankenship, D. M. Tiede, J. Barber, G. W. Brudvig, G. Fleming, M. Ghirardi, M. R. Gunner, W. Junge, D. M. Kramer, A. Melis, T. A. Moore, C. C. Moser, D. G. Nocera, A. J. Nozik, D. R. Ort, W. W. Parson, R. C. Prince, R. T. Sayre, Comparing photosynthetic and photovoltaic efficiencies and recognizing the potential for improvement, *Science*, **2011**, 332, 805-809.
- [6] W. Li, S. W. Sheehan, D. He, Y.M. He, X.H. Yao, R. L. Grimm, G. W. Brudvig, D. W. Wang, Hematite-based solar water splitting in acidic solutions: Functionalization by mono- and multilayers of iridium oxygen-evolution catalysts, *Angew. Chem. Int. Ed.* **2015**, 54, 11428-11432.
- [7] F. H. Saadi, A. I. Carim, W. S. Drisdell, S. Gul, J. H. Baricuatro, J. Yano, M. P. Soriaga, N. S. Lewis, Operando spectroscopic analysis of CoP films electrocatalyzing the hydrogen-evolution reaction, *J. Am. Chem. Soc.* **2017**, 139, 12927-12930.
- [8] Q. S. Yin, C. L. Hill, Water splitting: Passing the acid test, *Nat. Chem.*, **2018**, 10, 6-7.
- [9] M. Blasco-Ahicart, J. Soriano-López, J. J. Carbó, J. M. Poblet, J. R. Galan-Mascaros, Polyoxometalate electrocatalysts based on earth-abundant metals for efficient water oxidation in acidic media, *Nat. Chem.*, **2018**, 10, 24-30.
- [10] R. Frydendal, E. A. Paoli, I. Chorkendorff, J. Rossmeisl, I. E. L. Stephens, Toward an active and stable catalyst for oxygen evolution in acidic media: Ti-stabilized MnO₂, *Adv. Energy Mater.* **2015**, 5, 1500991.
- [11] S. Kumari, B. P. Ajayi, B. Kumar, J. B. Jasinski, M. K. Sunkara, J. M. Spurgeon, A low-noble-metal W_{1-x}Ir_xO_{3-δ} water oxidation electrocatalyst for acidic media via rapid plasma synthesis, *Energy Environ. Sci.*, **2017**, 10, 2432-2440.
- [12] I. A. Moreno-Hernandez, C. A. MacFarland, C. G. Read, K. K. Papadantonakis, B. S. Brunshwig, N. S. Lewis, Crystalline nickel manganese antimonate as a stable water-oxidation catalyst in aqueous 1.0 M H₂SO₄, *Energy Environ. Sci.*, **2017**, 10, 2103-2108.
- [13] L. J. Han, P. Y. Tang, Á. Reyes-Carmona, B. Rodriguez-Garcia, M. Torrens, J. R. Morante, J. Arbiol, J. R. Galan-Mascaros, Enhanced activity and acid pH stability of prussian blue-type oxygen evolution electrocatalysts processed by chemical etching, *J. Am. Chem. Soc.*, **2016**, 138, 16037-16045.
- [14] B. Rodríguez-García, A. Reyes-Carmona, I. Jiménez-Morales, M. Blasco-Ahicart, S. Cavaliere, M. Dupont, D. Jones, J. Rozière, J.R. Galán-Mascarós, F. Jaouen, Cobalt hexacyanoferrate supported on Sb-doped SnO₂ as a non-noble catalyst for oxygen evolution in acidic medium, *Sustain. Energy Fuels*, **2018**, 2, 589-597.

- [15] Z.L. Wang, G.J. Liu, C.M. Ding, Z. Chen, F.X. Zhang, J.J. Shi, C. Li, Synergetic effect of conjugated Ni(OH)₂/IrO₂ cocatalyst on titanium-doped hematite photoanode for solar water splitting, *J. Phys. Chem. C*, **2015**, 119, 19607-19612.
- [16] W. Li, D. He, S.W. Sheehan, Y.M. He, J.E. Thorne, X.H. Yao, G.W. Brudvig, D.W. Wang, Comparison of heterogenized molecular and heterogeneous oxide catalysts for photoelectrochemical water oxidation, *Energy Environ. Sci.*, **2016**, 9, 1794-1802.
- [17] C. H. Cui, M. Heggen, W. D. Zabka, W. Cui, J. Osterwalder, B. Probst, R. Alberto, Atomically dispersed hybrid nickel-iridium sites for photoelectrocatalysis, *Nature Commun.*, **2017**, 8, 1341.
- [18] K. Sivula, F. L. Formal, M. Grätzel, Solar water splitting: progress using hematite (α -Fe₂O₃) photoelectrodes, *ChemSusChem*, **2011**, 4, 432-449.
- [19] F. L. Formal, E. Pastor, S. D. Tilley, C. A. Mesa, S. R. Pendlebury, M. Grätzel, J. R. Durrant, Rate law analysis of water oxidation on a hematite surface, *J. Am. Chem. Soc.* **2015**, 137, 6629-6637.
- [20] P. Y. Tang, H. B. Xie, C. Ros, L. J. Han, M. Biset-Peiró, Y. M. He, W. Kramer, A., Perez-Rodriguez, E. Saucedo, J. Galan-Mascaros, T. Andreu, J. R. Morante, J. Arbiol, Enhanced photoelectrochemical water splitting of hematite multilayer nanowire photoanodes by tuning the surface state via bottom-up interfacial engineering, *Energy Environ. Sci.*, **2017**, 10, 2124- 2136.
- [21] C. Ros, T. Andreu, M. Dolores Hernández-Alonso, G. Penelas-Pérez, J. Arbiol, J. R. Morante, Charge transfer characterization of ALD-grown TiO₂ protective layers in silicon photocathodes, *ACS Appl. Mater. Interfaces*, **2017**, 9, 17932-17941.
- [22] M. Heggen, M. Luysberg, K. Tillmann, FEI Titan 80-300 STEM, *Journal of large-scale research facilities*, **2016**, 2, 42.
- [23] J. Barthel, L. Houben, K. Tillmann, FEI Titan G3 50-300 PICO, *Journal of large-scale research facilities*, 2015, 1, 34.
- [24] M. D. L. Mata, R. Leturcq, S. R. Plissard, C. Rolland, C. Magen, J. Arbiol, P. Caroff, Twin-induced InSb nanosails: a convenient high mobility quantum system, *Nano Lett.*, **2016**, 16, 825-833.
- [25] S. Bernal, F. J. Botana, J. J. Calvino, C. Lopez-Cartes, J. A. Perez-Omil and J. M. Rodriguez-Izquierdo, The interpretation of HREM images of supported metal catalysts using image simulation: profile view images, *Ultramicroscopy*, **1998**, 72, 135-164.
- [26] R. R. Zamani, M. Ibanez, M. Luysberg, N. Garcia-Castello, L. Houben, J. D. Prades, V. Grillo, R. E. Dunin-Borkowski, J.R. Morante, A. Cabot, J. Arbiol, Polarity-driven polytypic branching in Cu-based quaternary chalcogenide nanostructures, *ACS Nano*, **2014**, 8, 2290-2301.
- [27] M. Itoi, T. Jike, D. Nishio-Hamane, S. Udagawa, T. Tsuda, S. Kuwabata, K. Boukheddaden, M. J. Andrus, D. R. Talham, Direct observation of short-range structural coherence during a charge transfer induced spin transition in a CoFe prussian blue analogue by transmission electron microscopy, *J. Am Chem Soc.* **2015**, 137, 14686-14693.
- [28] D. M. Satoca, M. Bartsch, C. Fabrega, A. Gen, S. Reinhard, T. Andreu, J. Arbiol, M. Niederberger and J. R. Morante, What do you do, titanium? Insight into the role of titanium oxide as a water oxidation promoter in hematite-based photoanodes, *Energy Environ. Sci.*, **2015**, 8, 3242-3254.

- [29] P. Y. Tang, L. J. Han, A. Gen, Y. M. He, X. Zhang, L. Zhang, J. R. Galán-Mascarós, J. R. Morante and J. Arbiol, Synergistic effects in 3D honeycomb-like hematite nanoflakes/branched polypyrrole nanoleaves heterostructures as high-performance negative electrodes for asymmetric supercapacitors, *Nano Energy*, **2016**, 22, 189-201.
- [30] Z. M. Zhang, C. T. Gao, Y. X. Li, W. H. Han, W. B. Fu, Y. M. He and E. Q. Xie, Enhanced charge separation and transfer through Fe₂O₃/ITO nanowire arrays wrapped with reduced graphene oxide for water-splitting, *Nano Energy*, **2016**, 30, 892-899.
- [31] Z. M. Zhang, C. T. Gao, Z. M. Wu, W. H. Han, Y. L. Wang, W. B. Fu, X. D. Li and E. Q. Xie, Toward efficient photoelectrochemical water-splitting by using screw-like SnO₂ nanostructures as photoanode after being decorated with CdS quantum dots, *Nano Energy*, **2016**, 19, 318-327.
- [32] F. S. Hegner, D. Cardenas-Morcoso, S. Gimenez, Nuria Lopez, J. R. Galan-Mascaros, Level alignment as descriptor for semiconductor/catalyst systems in water splitting: The case of hematite/cobalt hexacyanoferrate photoanodes, *ChemSusChem*, **2017**, 10, 4552-4560.
- [33] F. S. Hegner, I. Herraiz-Cardona, D. Cardenas-Morcoso, N. López, J.R. Galán-Mascarós, S. Gimenez, Cobalt hexacyanoferrate on BiVO₄ photoanodes for robust water splitting, *ACS Appl. Mater. Interfaces*, **2017**, 9, 37671-37681.
- [34] A. Brauna, Y. L. Hu, F. Boudoiea, D. K. Bora, D. D. Sarmad, M. Grätzel and C. M. Eggleston, The electronic, chemical and electrocatalytic processes and intermediates on iron oxide surfaces during photoelectrochemical water splitting, *Catal. Today*, **2016**, 260, 72-81.
- [35] F. Y. Ning, M. F. Shao, S. M. Xu, Y. Fu, R. K. Zhang, M. Wei, D. G. Evans and X. Duan, TiO₂/graphene/NiFe-layered double hydroxide nanorod array photoanodes for efficient photoelectrochemical water splitting, *Energy Environ. Sci.*, **2016**, 9, 2633-2643.
- [36] F. Malara, A. Minguzzi, M. Marelli, S. Morandi, R. Psaro, V. D. Santo, A. Naldoni, α -Fe₂O₃/NiOOH: An effective heterostructure for photoelectrochemical water oxidation, *ACS Catal.* **2015**, 5, 5292-5300.
- [37] B. Klahr, S. Gimenez, F. Fabregat-Santiago, T. Hamann, J. Bisquert, Water oxidation at hematite photoelectrodes: the role of surface states, *J. Am. Chem. Soc.* **2012**, 134, 4294-4302.
- [38] B. Klahr, T. Hamann, Water oxidation on hematite photoelectrodes: insight into the nature of surface states through in situ spectroelectrochemistry, *J. Phys. Chem. C*, **2014**, 118, 10393-10399.
- [39] O. Zandi, T. W. Hamann, Determination of photoelectrochemical water oxidation intermediates on hematite electrode surfaces using operando infrared spectroscopy, *Nat. Chem.*, **2016**, 8, 778-783.
- [40] B. Iandolo, A. Hellman, The role of surface states in the oxygen evolution reaction on hematite, *Angew. Chem. Int. Ed.* **2014**, 126, 13622-13626.
- [41] M. Sachsenhauser, I. D. Sharp, M. Stutzmann, J. A. Garrido, Surface state mediated electron transfer across the n-type SiC/electrolyte interface, *J. Phys. Chem. C*, **2016**, 120, 6524-6533.
- [42] M. R. Nellist, F. A. L. Laskowski, J.J. Qiu, H. Hajibabaei, K. Sivula, T. W. Hamann, S. W. Boettcher, Potential-sensing electrochemical atomic force microscopy for in operando analysis of water-splitting catalysts and interfaces, *Nat. Energy*, **2018**, 3, 46-52.

- [43] T. L. Villarreal, R. Gómez, M. Neumann-Spallart, N. Alonso-Vante, P. Salvador, Semiconductor photooxidation of pollutants dissolved in water: A kinetic model for distinguishing between direct and indirect interfacial hole transfer. I. Photoelectrochemical experiments with polycrystalline anatase electrodes under current doubling and absence of recombination, *J. Phys. Chem. B*, **2004**, 108, 15172-15181.
- [44] B. Klahr, S. Gimenez, F. Fabregat-Santiago, J. Bisquert, T. W. Hamann, Electrochemical and photoelectrochemical investigation of water oxidation with hematite electrodes, *Energy Environ. Sci.*, **2012**, 5, 7626-7636.
- [45] K. G. Upul Wijayantha, S. Saremi-Yarahmadi and L. M. Peter, Kinetics of oxygen evolution at α -Fe₂O₃ photoanodes: a study by photoelectrochemical impedance spectroscopy, *Phys. Chem. Chem. Phys.*, **2011**, 13, 5264-5270.
- [46] O. Zandi, T. W. Hamann, Enhanced water splitting efficiency through selective surface state removal, *J. Phys. Chem. Lett.*, **2014**, 5, 1522-1526.
- [47] E. A. Ponomarev and L. M. Peter, A comparison of intensity modulated photocurrent spectroscopy and photoelectrochemical impedance spectroscopy in a study of photoelectrochemical hydrogen evolution at p-InP, *J. Electroanal. Chem.*, **1995**, 397, 45-52.

Chapter 6

Advanced TEM Characterization of 2D Materials for Water Splitting

6.1 Introduction

Transition metal dichalcogenide materials (TMDs) are two-dimensional (2D) materials, which are typically composed of two atomic layers of close-packed chalcogenide atoms separated by one close-packed transition metal atomic layer. TMDs display plenty of intriguing physical and chemical properties with a wide range of promising applications. [1-6] Traditionally, monolayer TMDs are obtained via top-down methods, such as mechanical exfoliation, [2, 7-8] chemical [9] and electrochemical exfoliation, [10] and direct sonication [11] to separate the stacked thick layers of the TMDs. Nevertheless, the obtained TMD layers are typically microscale flakes with poor uniformity in thickness, ranging from a monolayer to tens of layers. To correct this deficiency, several bottom-up methods have been recently developed to synthesize large-area TMD thin layers directly onto SiO₂/Si substrates, including the sulphurisation of pre-deposited Mo [12] or Mo oxide layers, [13] the decomposition of thiomolybdates, [14] and chemical vapour deposition (CVD) through a gas-phase reaction of MoO_{3-x} and sulphur.[15] However, compared to mechanically exfoliated samples, CVD grown monolayer TMDs typically have a much lower carrier mobility, [14-15] due to growth process imperfections that induce various structural defects in the material. [16] It is well established that structural defects in graphene, including point defects, grain boundaries (GB) and edges have an important influence on its mechanical, optical, thermal, and electrical properties. For instance, GBs have been shown to weaken mechanical strength [17] as well as degrade the electronic performance in the case of graphene. [18-19] Meanwhile, structural defects in 2D materials also provide exciting opportunities to tailor the local properties with new functionalities. [20-24] Examples include the generation of regulated magnetic phases in graphene with vacancies, [20] and local enhancement of optical excitations at the edges of graphene. [21] Compared to one atomic layer graphene, structural defects in MoS₂ have rarely been explored because of the increased complexity of the three-dimensional structure and the binary element system involved. [22-24]

Similarly, TMDs have emerged as a fascinating new class of electrocatalysts for the hydrogen evolution reaction (HER) in water splitting due to their atomically thin nature for exposing nearly all of the catalytically active sites. [25-26] 2D TMD can serve as a promising alternative to noble metals thanks to its fascinating advantages such as low cost, earth abundance, and good stability. [27-28] Plenty of researchers have attempted to identify active sites in 2D TMDs for HER applications. [28-36] To date, structural defects, such as edges, [28-32] doped heteroatoms, [33] defects [34] or basal planes [35-36], have been intensively explored for HER and identified as the active sites. For instance, T. F. Jaramillo et al. engineered the surface structure of MoS₂ to preferentially expose edge sites to efficiently improve catalysis. This was achieved by successfully synthesizing contiguous large-area thin films of a highly ordered double-gyroid MoS₂ continuous network with a silica template; the high surface curvature of this catalyst mesostructured exposes a large fraction of edge sites, which along with its high surface area, leads to excellent activity for electrocatalytic hydrogen evolution. [29] L.Y. Cao et al. systematically investigated HER performance edge sites, sulphur vacancies, and grain boundaries, which possess intrinsic turnover frequencies (Tafel slopes) of 7.5 s⁻¹ (65-75 mV/dec), 3.2 s⁻¹ (65-85 mV/dec), and 0.1 s⁻¹ (120-160 mV/dec), indicating the better catalytic performance of edge sites. [31] On the contrary, X.L. Zheng et al. reported the activation and optimization of the basal plane of monolayer 2H-MoS₂ for HER by introducing sulphur (S) vacancies and strain via argon plasma treatment and utilization of a gold nanocone substrate. Their theoretical and experimental results demonstrated that the S-vacancies are new catalytic sites in the basal plane, and the hydrogen adsorption free energy can be further manipulated by straining the surface with S-vacancies, which leads to optimized HER catalytic activity. [35] M. Chowalla et al. found that the activity of 2H basal planes of monolayer MoS₂ nanosheets can be made comparable to state-of-the-art catalytic properties of metallic edges and the 1T phase by improving the electrical coupling between the substrate and the catalyst so that electron injection from the electrode and transport to the catalyst active site is

facilitated. [36] Therefore, in the application of TMDs for water splitting, it is critical to directly correlate their specified atomic structure with its electrochemical performance.

6.2 Experimental Section

Part of the scanning transmission electron microscopy (STEM) measurements were performed at the SuperSTEM Laboratory, UK, on a Nion UltraSTEM100TM aberration-corrected dedicated STEM. The Nion UltraSTEM has a cold field emission gun with a native energy spread of 0.35 eV and was operated at 60 kV acceleration voltage. The beam was set up to a convergence semi-angle of 30 mrad with an estimated beam current of ~100 pA. Under these operating conditions, the estimated probe size is ~1.1 Å, providing the perfect tool for atom-by-atom chemical analysis. The other scanning transmission electron microscopy (STEM) measurements were performed using a FEI Titan 50-300 PICO operated at 80 kV equipped with a high-brightness electron gun, a monochromator unit, and a C_s probe corrector at Ernst Ruska-Centre for Microscopy and Spectroscopy with Electrons (ER-C), Germany. Additionally, a C_s - C_c achro-aplanat image corrector and a post-column energy filter system were also on hand. [37] High Angle Annular Dark Field (HAADF) imaging was employed to produce atomically resolved images whose intensity was approximately proportional to the square of the average atomic number Z of the material under investigation. This chemically-sensitive ‘Z-contrast’ mode is ideally suited to directly identify the nature of individual atoms. HAADF imaging was complemented by further chemical fingerprinting through Electron Energy Loss Spectroscopy (EELS). All the HAADF images presented here were filtered by exact wiener filter with sigma from 2-5 and 50 iterations in MEM (Maximum Entropy Methods) with 4th order Gaussian filter functions of STEM-CELL software. The GPA was obtained via Cosine Mask with a suitable size and 1 binning base on the GPA algorithm. [38-39] The supplementary analyses performed by means of HRTEM were conducted in a FEI Tecnai F20, installed at the Institut Català de Nanociència i

Nanotecnologia (ICN2), which was equipped with a field emission gun and operated at 200 kV.

6.3 Result and Discussion

6.3.1 Structural Defects in 2D MoS₂

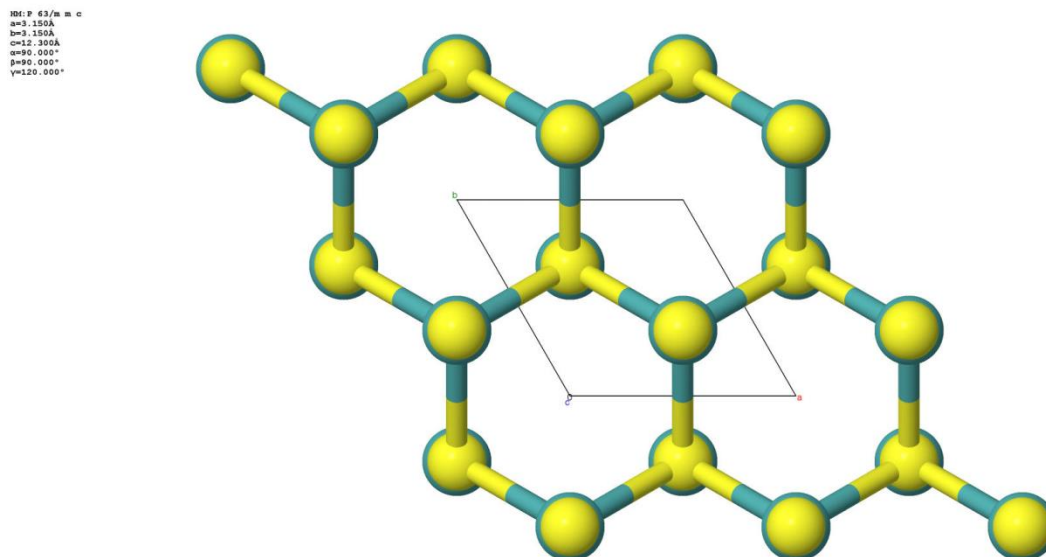


Figure 6.1 The crystal parameters and the corresponding crystal model of 2H MoS₂ based on the ICSD database. (Yellow balls represent S atoms and indigo balls represent Mo atoms).

As displayed in **Figure 6.1**, when 2H MoS₂ is viewed from a [0001] direction, it has a hexagonal ring atomic ordering formed by the S and Mo atoms.

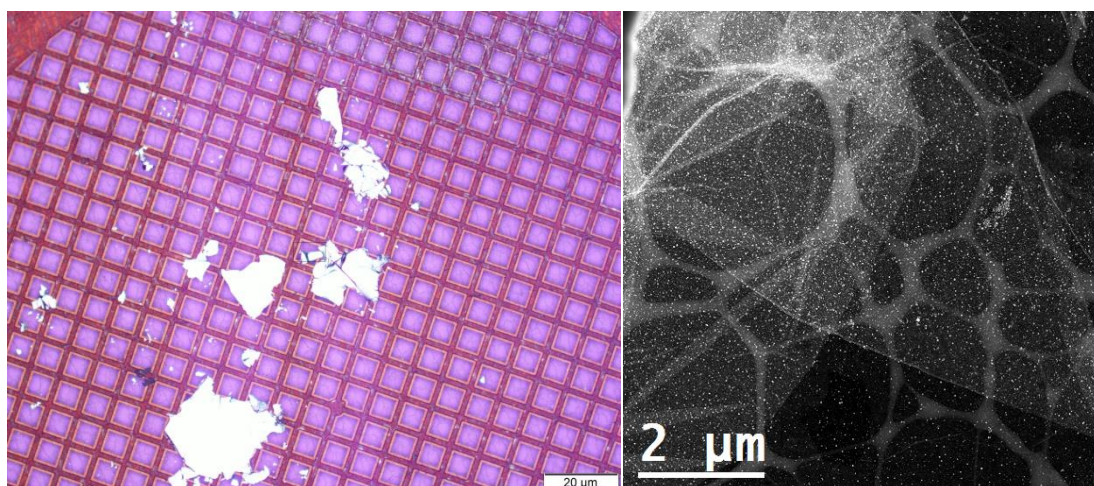


Figure 6.2. Left: the optical image shows the general view of represented MoS₂ materials, Right: the low magnification ADF-STEM image shows the membrane-like 2D MoS₂ with the Au nanoparticles catalyst embedded into it.

The as-grown MoS₂ film was transferred onto a TEM grid. The optical image in **Figure 6.2 (left)** shows an optical micrograph of the 2D MoS₂ sample with Au nanoparticles as the catalyst. The continuous film is composed of multiple adjacent polycrystalline crystals. [40] The detail structure 2D MoS₂ sample was studied using annular dark field (ADF) imaging in scanning transmission electron microscopy mode (STEM). The ADF image intensity is proportional to the number of atomic layers for thin samples, providing an easy and accurate way to measure the thickness of thin samples without the need for image simulation. [41] A general ADF-STEM image from clean region is shown in right image of **Figure 6.2** with brighter Au nanoparticles and membrane-like MoS₂.

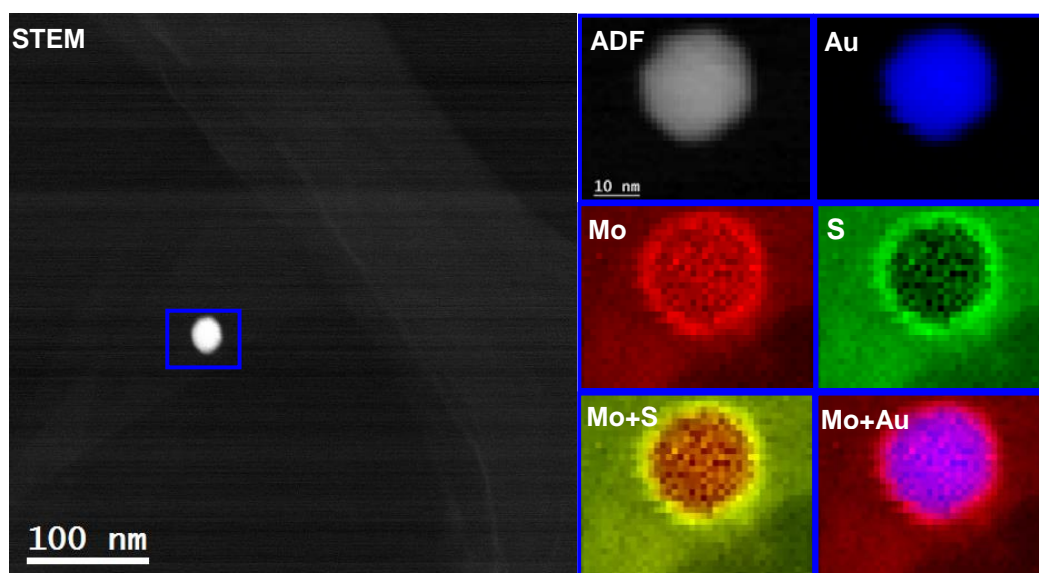


Figure 6.3 Left: low magnification EELS chemical composition maps obtained from the blue rectangular area of the STEM-ADF micrograph. Right: Individual Au (Blue), Mo (Red) and S (Green) maps and their composite.

Additionally, we performed STEM-EELS maps for Au, Mo and S elements based on their M (2206 eV, Au), L (2472 eV, Mo) and K (2520 eV, S) edges signals, respectively. As shown in **Figure 6.3**, the Au signal dominated in the nanoparticle region, while the Mo and S signals are homogeneously distributed in the membrane region and form a shell structure around the Au nanoparticles, indicating the Au nanoparticles is covered by MoS₂ layers. It is well established that HAADF image intensity is directly correlated with the atomic number of the imaged atoms, allowing

chemical identification via quantitative analysis of the image at various defect sites, as shown in the following discussion. [41]

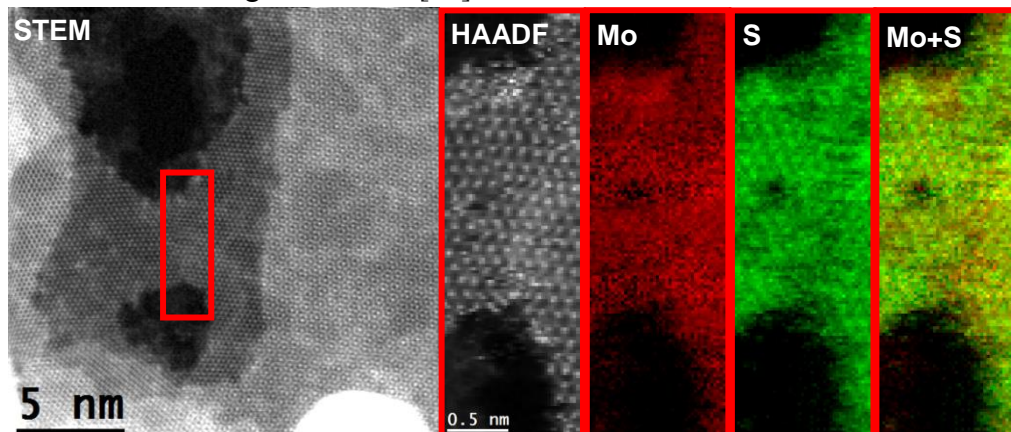


Figure 6.4 High magnification EELS chemical composition maps obtained from the red rectangled area on the HAADF-STEM micrograph. Individual Mo (red), S (green) maps and their composite.

We also performed atomic-scale STEM-EELS maps at the interface of the MoS₂ membrane. It can be seen from **Figure 6.4** that the Mo and S atoms are relatively homogeneously distributed in the membrane region. It should be pointed out that from the EELS elemental maps, the S sublattice is almost atomically visible in the S mapping, while the Mo sublattice is not so clearly visible, which is probably due to the short dwell time to avoid damaging the structure with the electron beam during the SI acquisition.

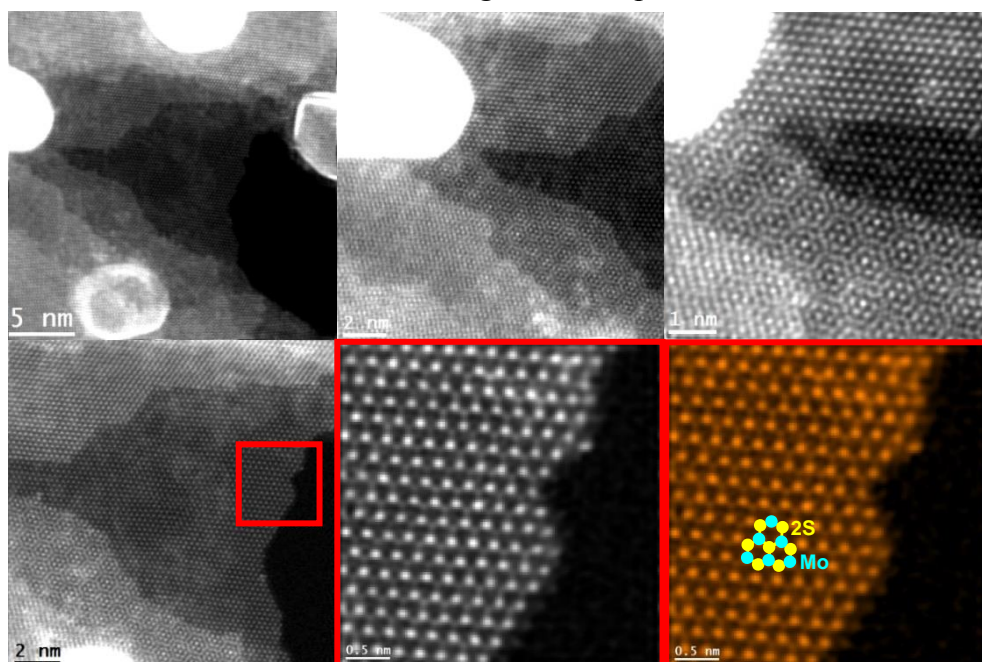


Figure 6.5 **Top rows:** low magnification HAADF STEM images of Au nanoparticles and MoS₂ nanoflakes showing their distribution. **Bottom rows:** left: atomic resolution HAADF STEM image displaying the edge region of the MoS₂ monolayer. Middle: atomic resolution HAADF-STEM image of the red squared region showing the hexagonal ordering of Mo and 2S atoms. Right: False color atomic resolution HAADF STEM image enhancing the contrast of Mo and 2S with inset showing the monolayer 2H MoS₂ atomic model.

As shown in the top rows of **Figure 6.5**, there are several layers of MoS₂ species overlapping, Au nanoparticles and MoS₂ nano-cavities after chemically etching part of the Au nanoparticles. The atomic resolution HAADF-STEM images in the bottom rows show hexagonal rings composed of alternating Mo and S2 atom columns.

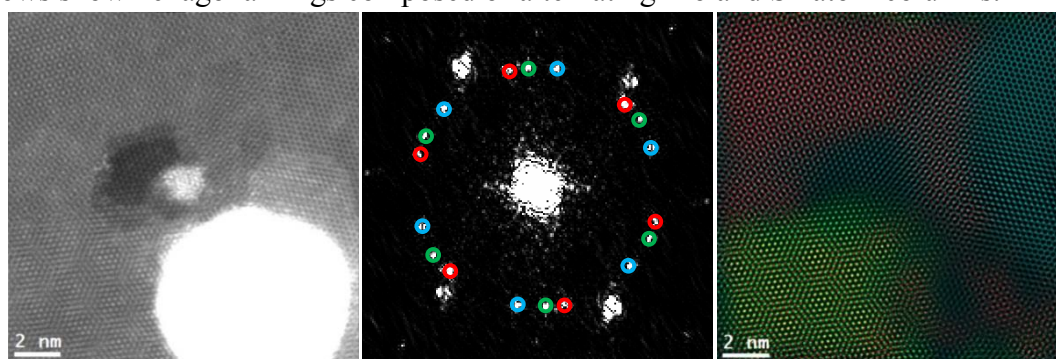


Figure 6.6 Left: atomic resolution HAADF STEM image showing the grain boundary formation around an Au nanoparticle. Middle: the power spectrum indicates 3 sets of MoS₂ diffraction patterns with rotation angles of 9.1° and 24.8°. Right: the RGB frequency filtered image after spot mask filtering using the 3 sets of diffraction spots, indicating that the Au nanoparticle indeed acts as the nucleation site for the formation of these three grains.

It can be seen from **Figure 6.6** that this region is composed of an Au nanoparticle and three crystalline domains of MoS₂ according to the atomic HAADF and the FFT images. Additionally, these three MoS₂ domains possess rotation angles of 9.1° and 24.8°. Combing the HRTEM results, EELS-STEM and atomic HAADF images, we can therefore speculate that the Au nanoparticle indeed acts as the nucleation site for the formation of these three MoS₂ grains during the CVD growth stage.

As aforementioned, the edge region of MoS₂ is supposed to be the active site for HER according to some previous reports. It is therefore critical to identify the atomic ordering in the edge region of the MoS₂ membrane and directly correlate the atomic structure with their HER performance. The knock-on damage can be reduced by lowering the primary electron energy below its threshold energy, which is approximately 66 keV for MoS₂.

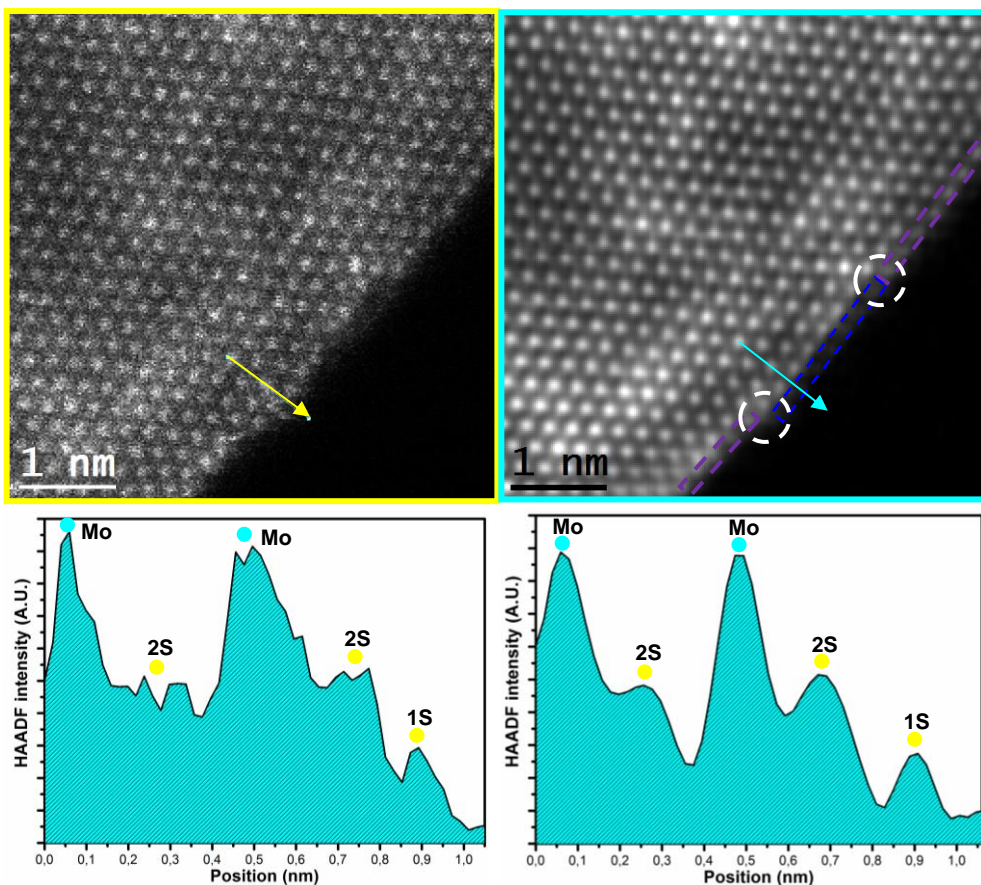


Figure 6.7 Left column: (top) original raw atomic resolution HAADF STEM image showing the edge structure, and (bottom) the profile of the atomic intensity along the yellow arrow direction at the HAADF STEM image. Right column: (top) filtered atomic resolution HAADF STEM image showing the edge structure, and (bottom) the profile of the atomic intensity along the indigo arrow direction at the filtered HAADF STEM image.

In this case, the effect of knock-on damage on the samples was drastically reduced by employing 60 keV primary energy for STEM-HAADF image acquisition. As displayed in **Figure 6.7**, even though the original raw HAADF STEM image quality is somehow blurred by the supported carbon derived from the lacey Cu grid, the

atomic structure can still be identified by filtering the noise of the HAADF STEM images. [42] After processing by a wiener filter, the atomic contrast was enhanced and the signal noise was reduced, evidenced by the disappearance of the serrated HAADF STEM intensity peaks corresponding to the Mo and S atoms. Based on the filtered HAADF STEM image, the edge part of the MoS₂ membrane seems to be dominated by a Mo terminated edge (purple squared region) and a 50% S terminated edge (blue square region). [41, 43] Kink sites present at the connection region (marked by white dotted circles) of Mo terminated and 50% S terminated edges. [43] According to W. Zhou's report, the Mo terminated and 50% S terminated edges tend to form under Mo-rich or S-deficient conditions. [41]

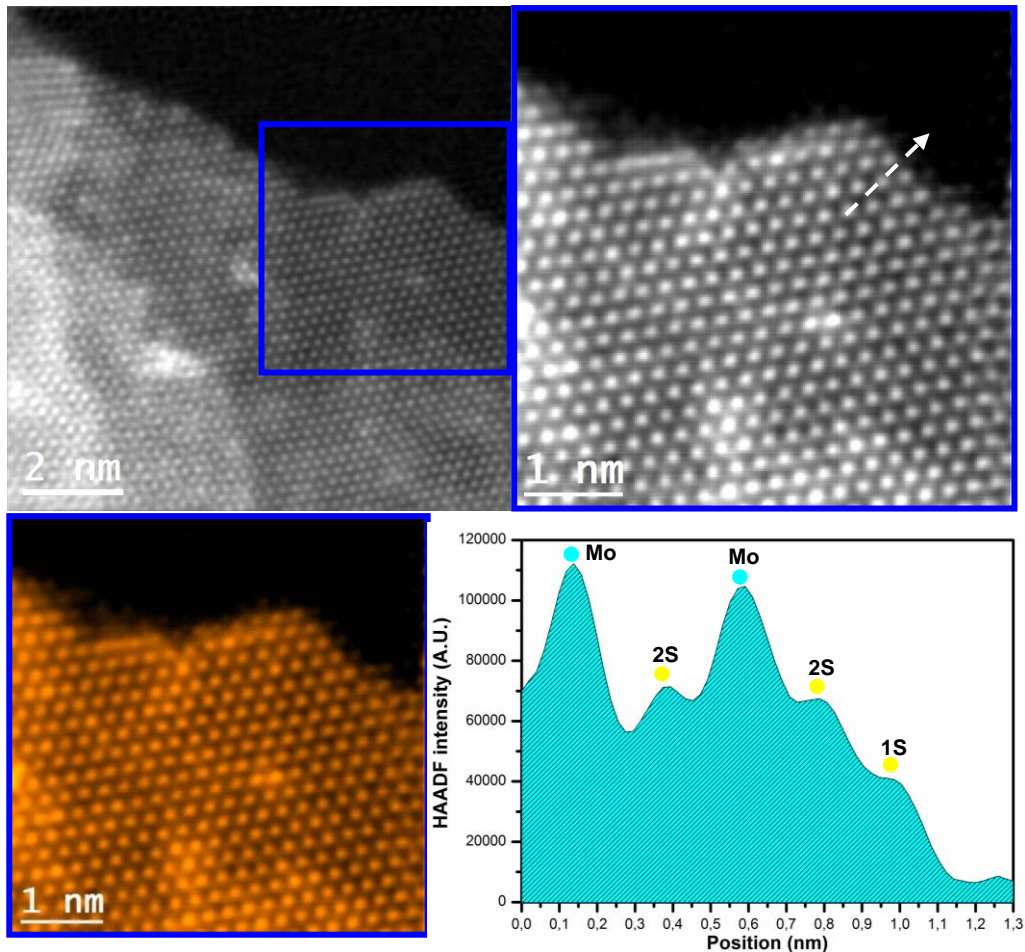


Figure 6.8 Top: Low magnification HAADF STEM (left) and atomic resolution HAADF STEM (right) images showing the detailed structure at the edge region. Bottom: orange false color atomic resolution HAADF STEM (left) along with the profile of the atomic intensity (right) along the white dotted arrow direction in top right atomic resolution HAADF STEM image confirming that the 50% S terminated

edge dominates the edge region.

In the other edges displayed in **Figure 6.8**, 50% S terminated edges dominated the edge region with other types of terminations. The observed 50% S-covered Mo-edge is supposed to be energetically stable compared to the regular Mo-edge under the thermodynamic range of the S chemical potential. [44] Above all, even at the straight segments of the Mo-terminated edge, two different kinds of atomic configurations can be observed: namely the regular Mo-edge with bare Mo termination, and the 50% S-covered Mo-edge with one additional S atom for each Mo atom on the edge. The step edges provide additional Mo and S sites with unsaturated bonds, which could be correlated with its HER performance.

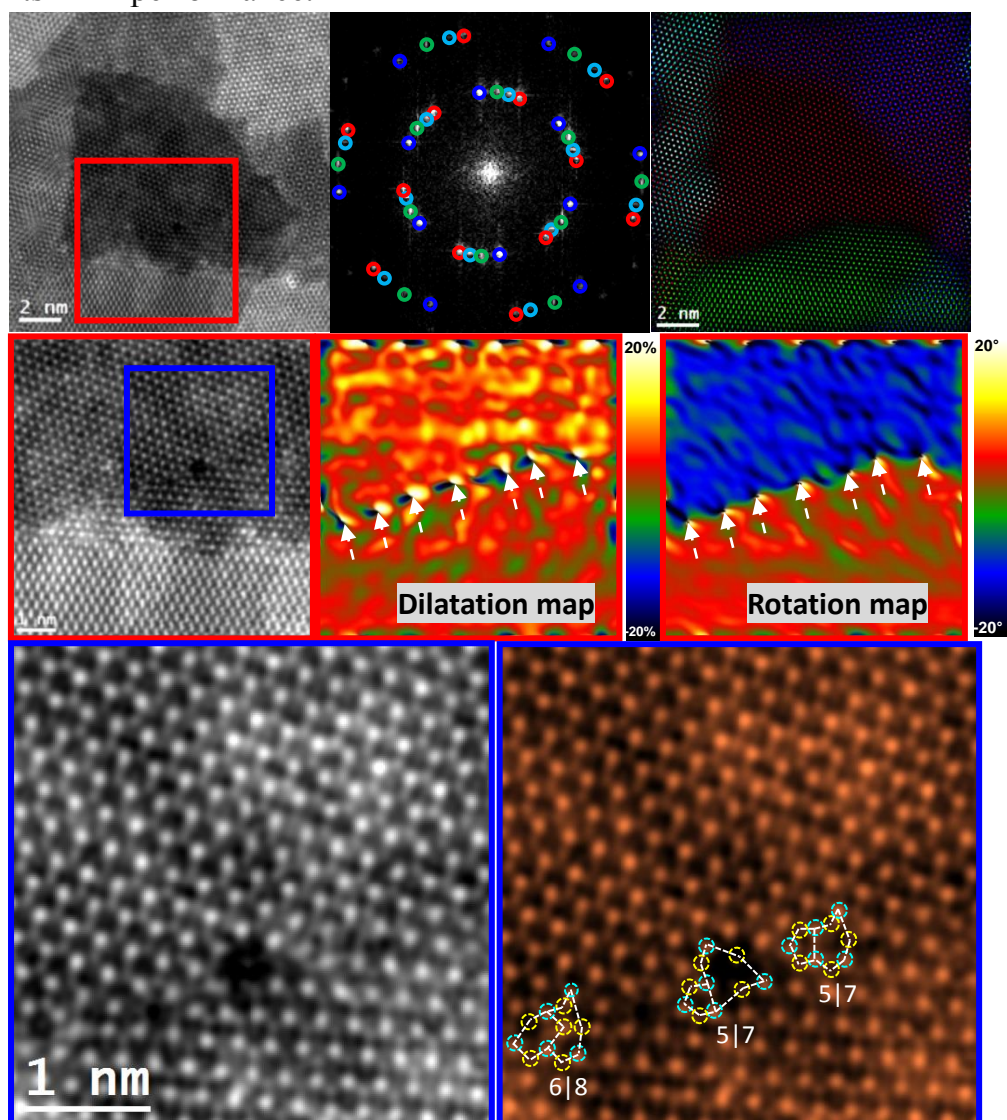


Figure 6.9 Top rows: Low magnification HAADF STEM images showing the detailed structure at edge and grain boundary region between two layers (18.5° rotation). **Middle rows:** Left: Dilatation map after applying GPA to the MoS₂ (1000) plane. Right: Rotation map of the MoS₂ (1000) plane, indicating the dislocation core position. **Bottom rows:** atomic resolution HAADF STEM of the grain boundary region and the orange colored HAADF STEM image showing the grain boundary, which is composed of a dislocation with five- and seven-fold rings (5|7) and a dislocation with six- and eight-fold rings (6|8), Mo atoms are marked with indigo dotted circles and S atoms are marked with yellow dotted circles.

On the other hand, the peculiar bonding characteristics between Mo and S in the monolayer MoS₂ render different kinds of dislocation cores in the grain boundary (GB) region, including not only the topologically conventional one with five- and 7-fold (5|7) rings, but also new core structures with 4|4, 4|6, 4|8, and 6|8 fold rings. [41] In order to map the dislocation cores present at the grain boundary in this film, we used GPA, developed by Hytch et al. [45-46] The middle rows of **Figure 6.9**, show the dilatation map and the rotation map obtained by applying the GPA algorithm to the (1000) MoS₂ plane, where the white arrows indicate the position of the core dislocation. Furthermore, the atomic HAADF images at the grain boundary region in the bottom rows of **Figure 6.9** reveal that the grain boundary in this case is composed of a dislocation with five- and seven-fold rings (5|7) and a dislocation with six- and eight-fold rings (6|8).

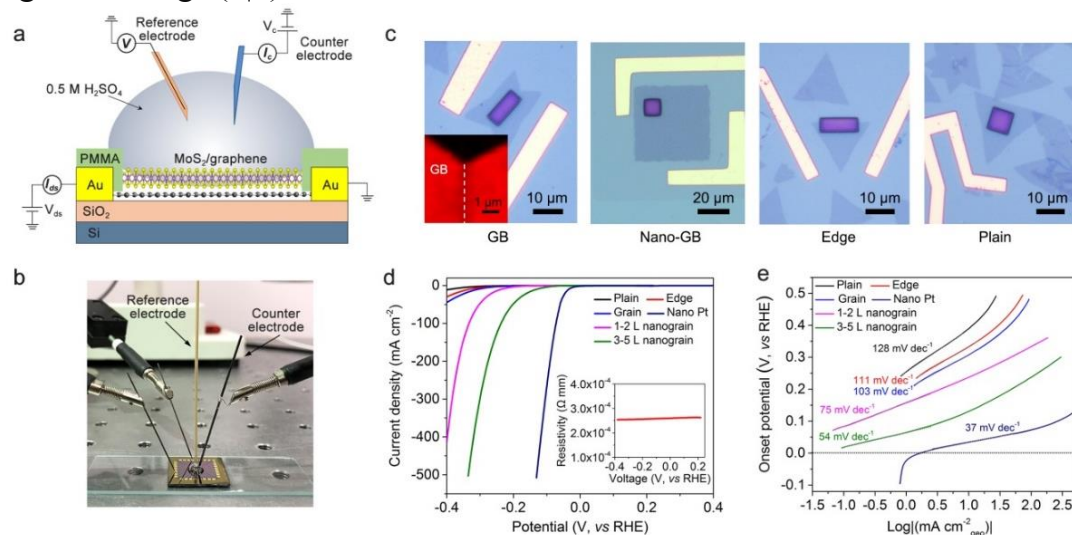


Figure. 6.10 Identification of the HER activity of GBs in the micro-electrochemical cell. a, Schematic illustration of the micro-electrochemical cell performing the HER measurement of GB on graphene supporting, in which graphene serves as vertical electron injector. b, Photograph of the micro-electrochemical cell. c, Optical images of the MoS₂ devices including basal plane, single edge, single GB and nano-GB films with 1-2 L, in which electrochemical windows are opened on PMMA passivation film. d-e, The polarization curves of the current density (d) and the corresponding Tafel plots (e) of the MoS₂ devices (the window size of about 80 μm² for each device), respectively.

In order to identify the catalytic activities of the single grain boundary (GB) and nano-GB in HER, we developed a four-electrode micro-electrochemical cell, as displayed in **Figure 6.10a**. **Figure 6.10b** shows the photograph of such cell, in which the graphite counter electrode and micro-reference electrode are used. **Figure 6.10c** show the optical images of the typical devices made up of graphene supported MoS₂ basal plane, single edge, single GB, and nano-GB films, respectively. **Figures 6.10d-e** show the polarization curves and the corresponding Tafel slopes of various active sites of MoS₂ in 0.5 M H₂SO₄ solution, respectively. We find that the single GB device delivers a better catalytic activity than the one with edge, and both are much better than the basal plane one, echoing our first-principles results set forth above. Additionally, nano-GB MoS₂ films, with ultra-high density of grain boundaries, show superior HER performances. And the superior HER performance of the nano-GB film suggests that the inert plane of MoS₂ can be intrinsically activated by GBs.

6.3.2 Core-Shell MoO₂/MoS₂ Nanoflakes

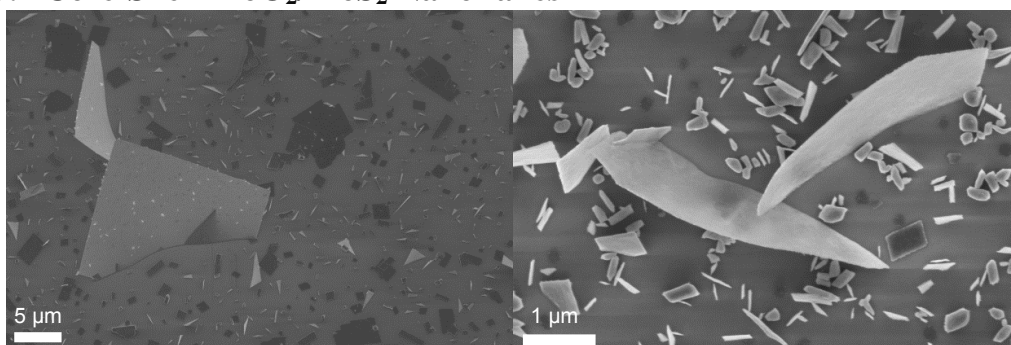


Figure 6.11 General SEM images of core-shell MoO₂/MoS₂ nanoflakes.

As displayed in **Figure 6.11**, the $\text{MoO}_2/\text{MoS}_2$ samples exhibit a nanoflake structure, which is free-standing grown onto a Si wafer substrate. The free-standing vertical nanoflakes were cut by FIB to obtain a cross-section of the sample. The detailed crystalline structure and the chemical composition information were investigated by atomic HAADF, STEM-EELS maps and GPA, as follows.

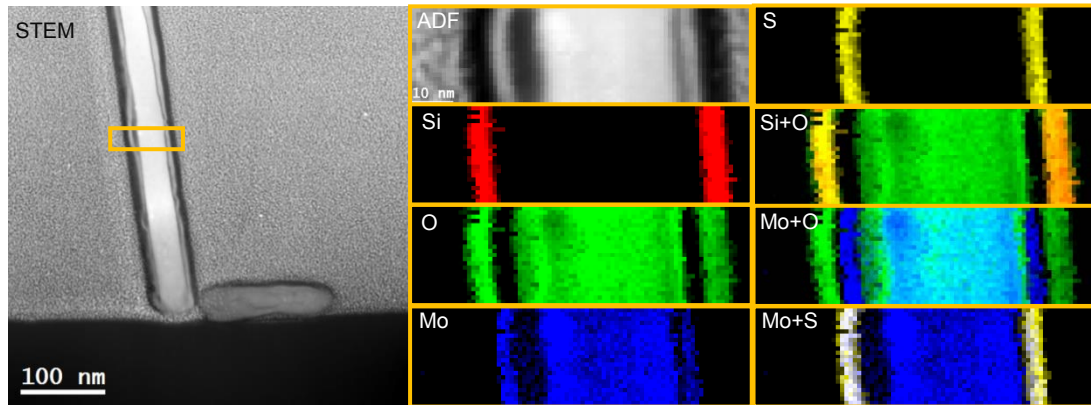


Figure 6.12 EELS chemical composition maps obtained from the yellow rectangled area of the STEM-ADF micrograph. Individual Si (red), O (green), Mo (blue) and S (yellow) elemental maps and their composites.

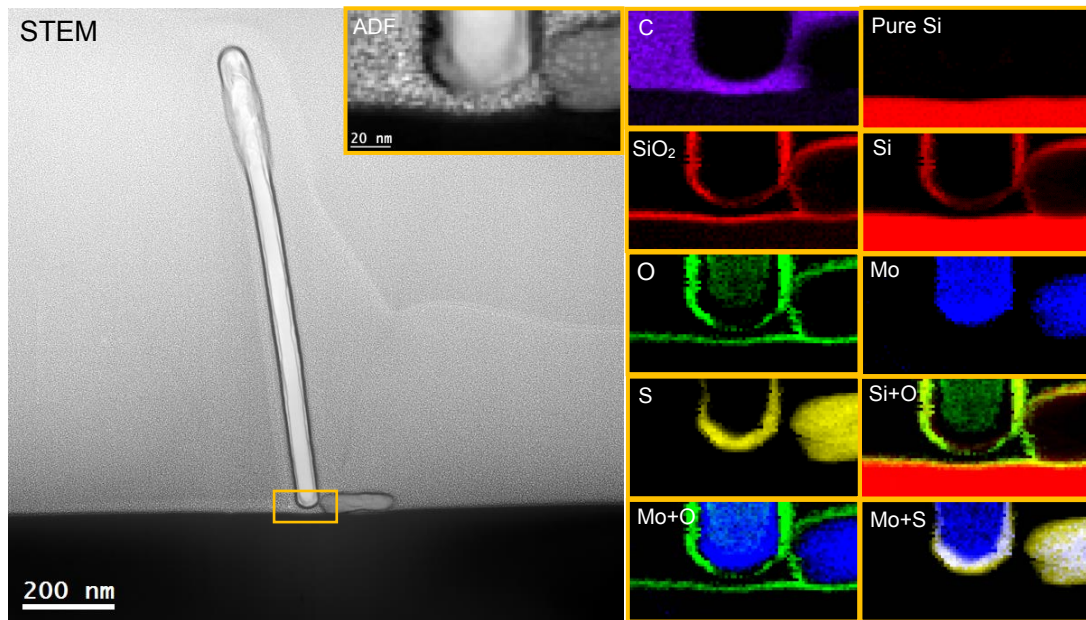


Figure 6.13 EELS chemical composition maps obtained from the yellow rectangled area of the STEM-ADF micrograph. The right top two rows: C (purple) elemental mapping, Si signal derived from Si and SiO_2 by MLLS fitting with the energy range from 98 eV to 150 eV and all Si elemental maps. Other maps in the right panel are individual O (green), Mo (blue) and S (yellow) maps and their

composites.

EELS-STEM maps were obtained at the interface of the Si substrate and nanoflake region in the FIB cut vertical cross section. MLLS fitting were employed to distinguish the Si element signal from the pure Si and SiO₂ species. **Figure 6.12** reveals that there is an ultrathin MoS₂ layer as a shell at the surface of the MoO₂ matrix, which will be further confirmed below in the section on atomic HAADF analysis.

It is worth noting that tiny Si and O signals were found between the core-shell MoO₂-MoS₂ nanoflakes and the Si substrate (**Figure 6.13**), suggesting the presence of an ultrathin SiO₂. Due to its intrinsically poor electrical conductivity, the presence of SiO₂ between the substrate and the nanoflakes catalyst may block the electron flowing from the Si substrate into the nanoflakes catalyst.

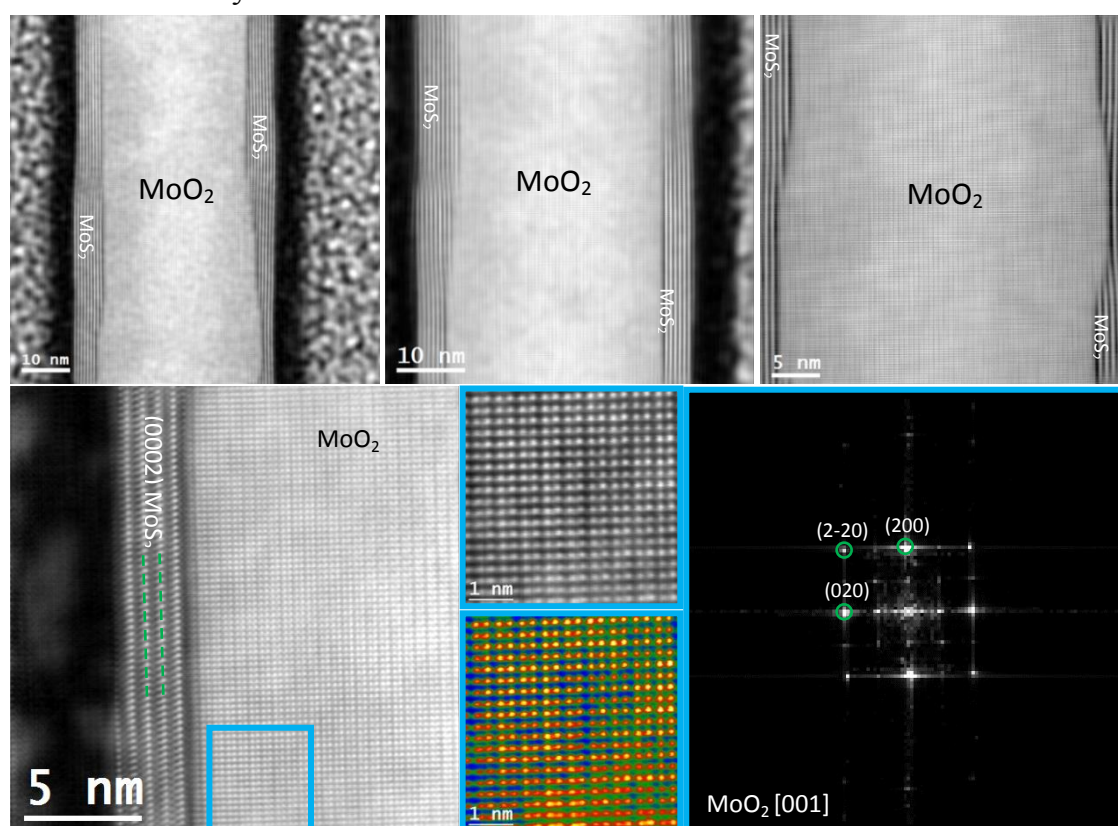


Figure 6.14 Atomic-resolution HAADF STEM images obtained along the vertical direction of the cross-section of the MoO₂/MoS₂ sample. Top rows: Several HAADF STEM images taken from the middle region of the selected nanoflakes showing the relative homogenous distribution of MoS₂ on the

surface of the MoO₂ flake core. Bottom rows: Atomic-resolution HAADF STEM image, raw and temperature colored HAADF STEM magnified detail of the squared region and the corresponding FFT corresponding to Monoclinic MoO₂, with lattice parameters of a = 0.5610 nm, b = 0.4843 nm and c = 0.5526 nm as visualized along the [001] direction.

The detailed structural information of the MoO₂/MoS₂ samples was investigated by atomic HAADF in an aberration-corrected scanning transmission electron microscope. As displayed in the top of **Figure 6.14**, there are several fingerprint-like layers of MoS₂ on the surface of core MoO₂ in the middle region of the selected nanoflakes, which demonstrates the relative homogenous distribution of MoS₂ on the surface of the MoO₂ flake core. The atomic resolution HAADF STEM images in the bottom of **Figure 6.14**, demonstrate that the fingerprint like layers correspond to the (0002) planes of the 2H phase MoS₂. The atomic HAADF in the indigo rectangle shows the ordering of the Mo atom columns and the power spectrum confirms that the core region crystallized in the monoclinic MoO₂ crystal structure, with lattice parameters of a = 0.5610 nm, b = 0.4843 nm and c = 0.5526 nm as visualized along the [001] direction.

The sulphurization process at different regions of the MoO₂/MoS₂ nanoflake was also investigated by atomic HAADF STEM images. The left image in **Figure 6.15** shows the general view of a cross-section obtained on one of the nanoflakes from the MoO₂/MoS₂ sample. The magnified HAADF images in the middle column show the sulfurization process at different regions of the MoO₂/MoS₂ nanoflake. We can observe that the sulfurization process at the top region of the MoO₂/MoS₂ nanoflake was more effective and penetrated more deeply than at the bottom region, which is evidenced by the magnified HAADF STEM images of the squared marked area shown in the right column of **Figure 6.15**. Specifically, in the top region of the nanoflakes, the MoS₂ thickness is c.a. 50 nm, while in the middle region of the nanoflakes, the MoS₂ content ranges from 3-8 monolayers. As the MoS₂ thickness in the bottom region of the nanoflakes is much thinner than that at the top region, the interface of MoO₂ and MoS₂ is hard to distinguish.

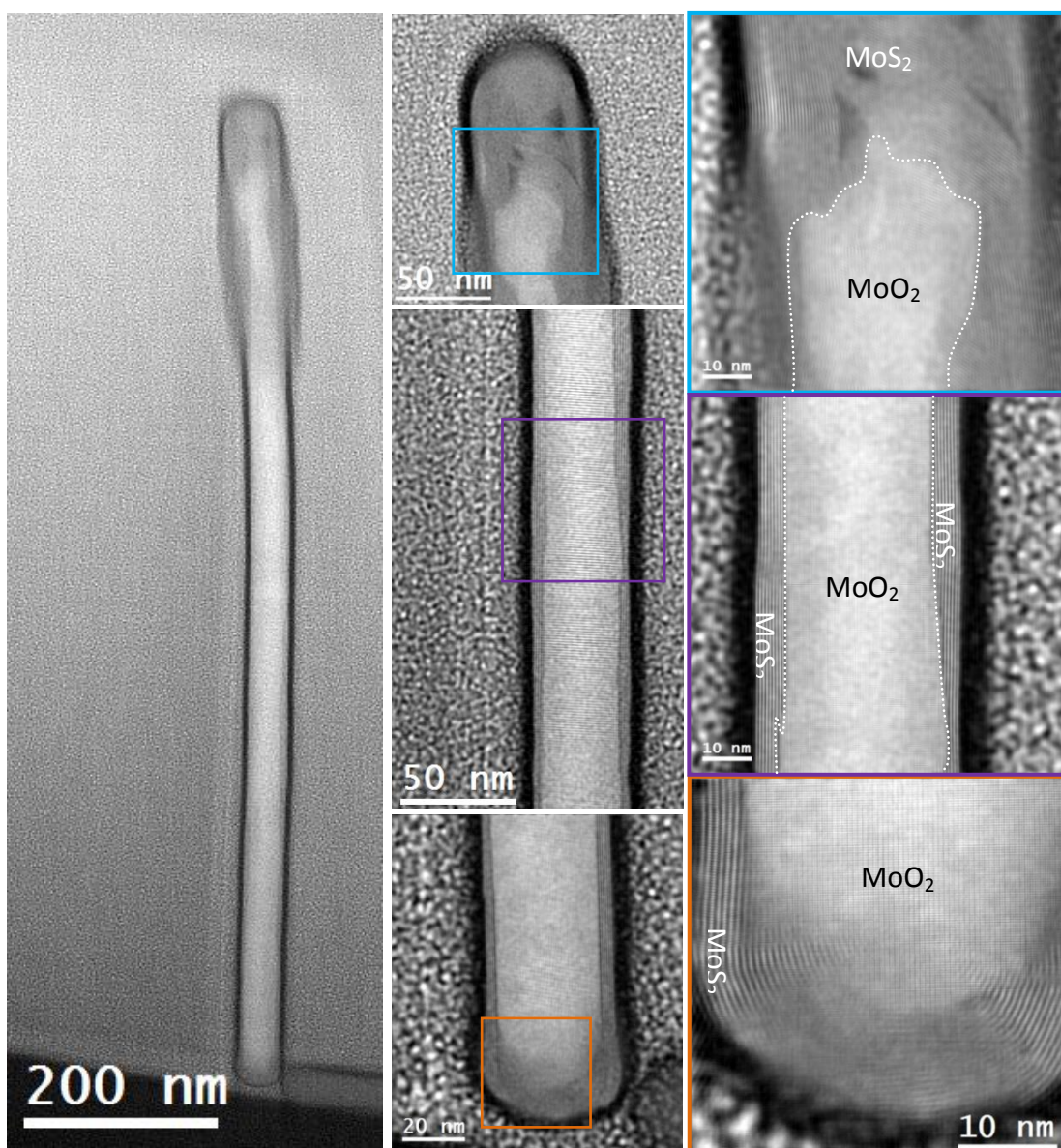


Figure 6.15 HAADF STEM micrograph obtained along the vertical direction in a cross-section in one of the MoO₂/MoS₂ nanoflakes.

X.L. Zheng et al. reported the activation and optimization of the basal plane of the 2H-MoS₂ monolayer for HER by introducing strain via utilization of a gold nanocone substrate. [35] Herein, it was thought interesting to measure the strain induced by the lattice mismatch between MoS₂ shell and MoO₂ core. **Figure 6.16**, shows the dilatation and rotation maps obtained by applying the GPA algorithm to the (200) MoO₂ plane. It can be seen that the MoO₂ matrix is compressed by ca. 10 %, while the MoS₂ is expanded by ca. 10 %, confirming that there is a large amount of strain in the MoS₂ shell region. [46]

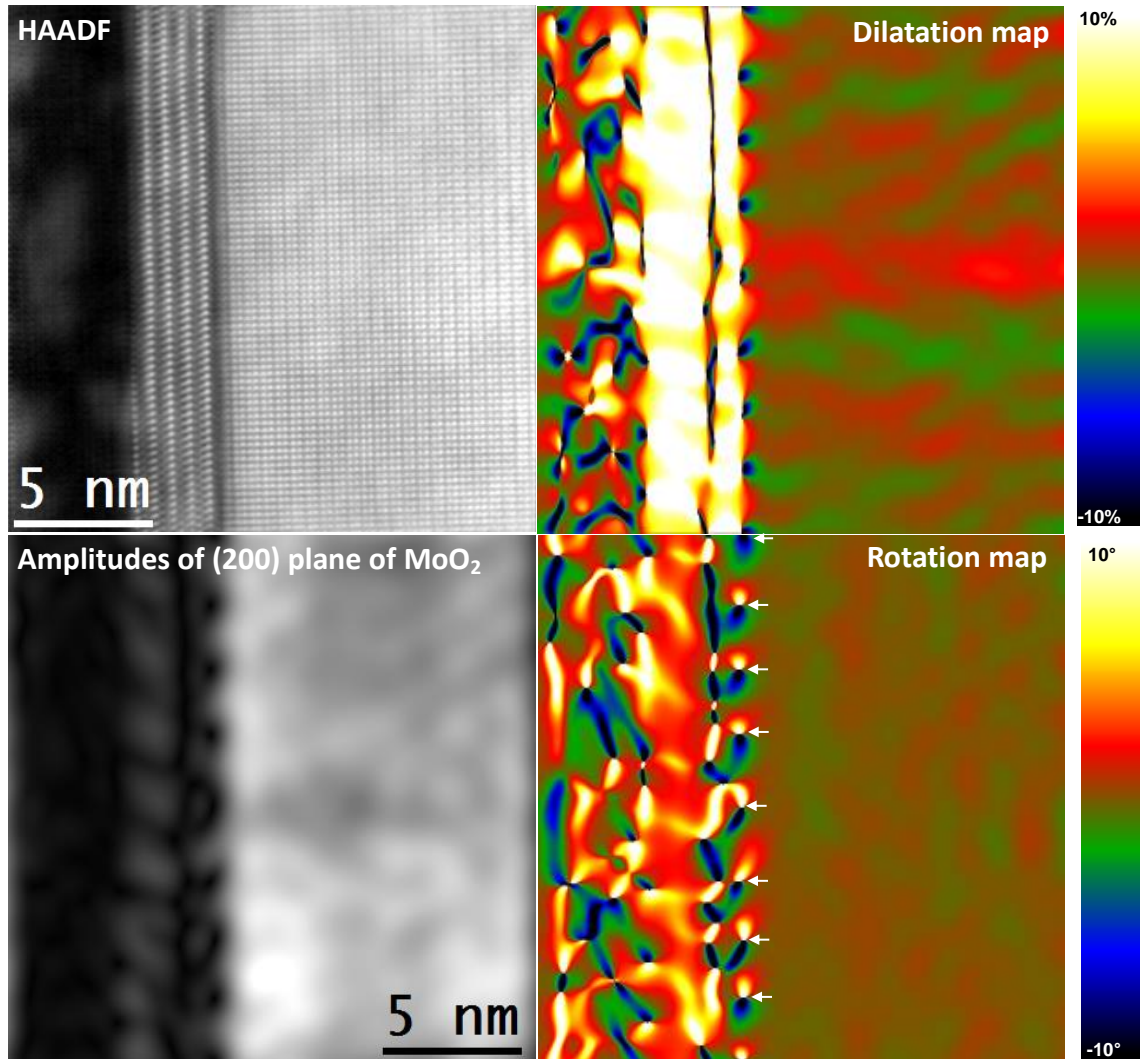


Figure 6.16 HAADF STEM image of the cross-section of a MoO₂/MoS₂ nanoflake. Amplitude of the (200) plane of MoO₂. Dilatation map after applying GPA to the (200) plane of the MoO₂ region displayed in temperature color (scale codes included on the right side of the panel). Rotation map of the (200) MoO₂ plane, showing symmetric rotation through the left side interface of the nanoflake. (White arrows indicated the location of misfit dislocations.)

6.3.3 Semiconductor and Metallic Phases of MoTe₂

Table 6.1 shows the crystallographic data of 2H and 1T' phase MoTe₂. It is well established that 2H MoTe₂ is a semiconductor, while in contrast to the 2H phase MoTe₂, the 1T' phase MoTe₂ exhibits semi-metallic characteristics with a slight band overlap near the Fermi level. [47] Thus, it is of great importance to distinguish them via atomic resolution (S)TEM.

Table 6.1 Crystallographic data of 2H and 1T' phase MoTe₂.

	2H MoTe ₂	1T' MoTe ₂
Structure	Hexagonal	Monoclinic
Space group	P6 ₃ /mmc	P 2 ₁ /m
a (nm)	0.352085	0.63274
b (nm)	0.352085	0.34755
c (nm)	1.39664	1.38100
α (degree)	90	90
β (degree)	90	93.887
γ (degree)	120	90

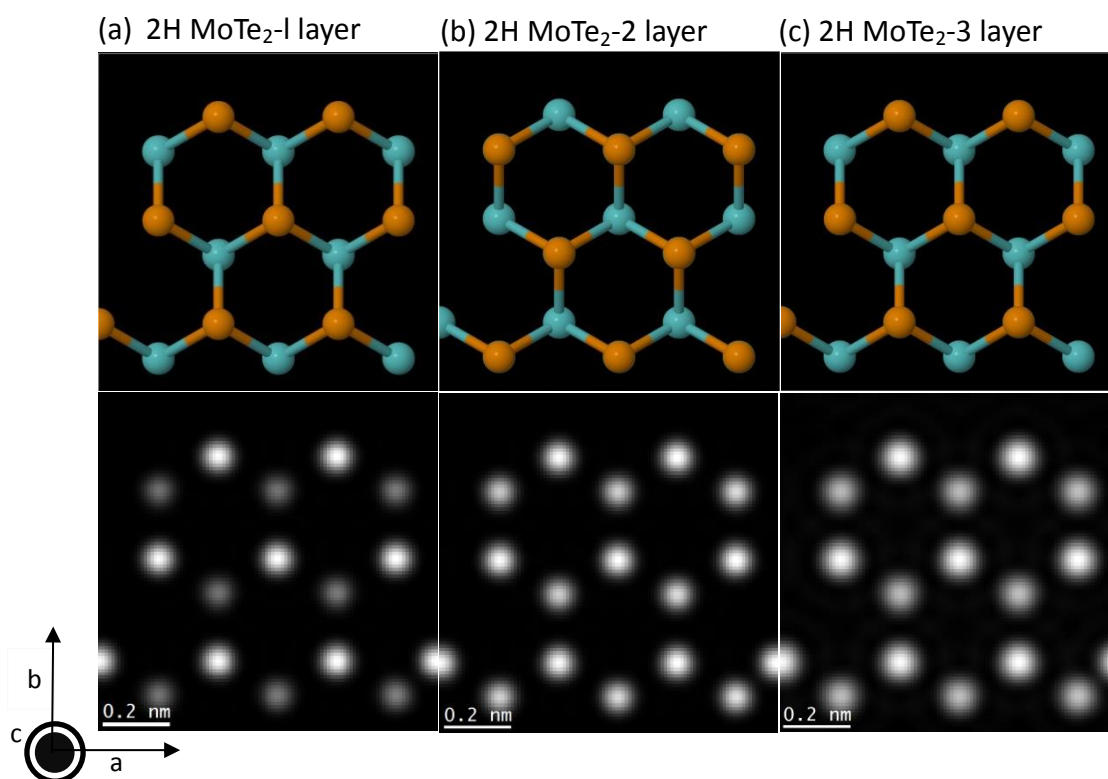


Figure 6.17 HAADF-STEM image simulation of the 2H-MoTe₂ phase with different layer thicknesses. Top row: Atomic model configurations with top view (along the [001] zone axis) of the 2H-MoTe₂ lattice at (a) monolayer, (b) bilayer and (c) trilayer. Bottom row: Simulated HAADF-STEM images of 2H-MoTe₂ at monolayer, bilayer and trilayer thicknesses.

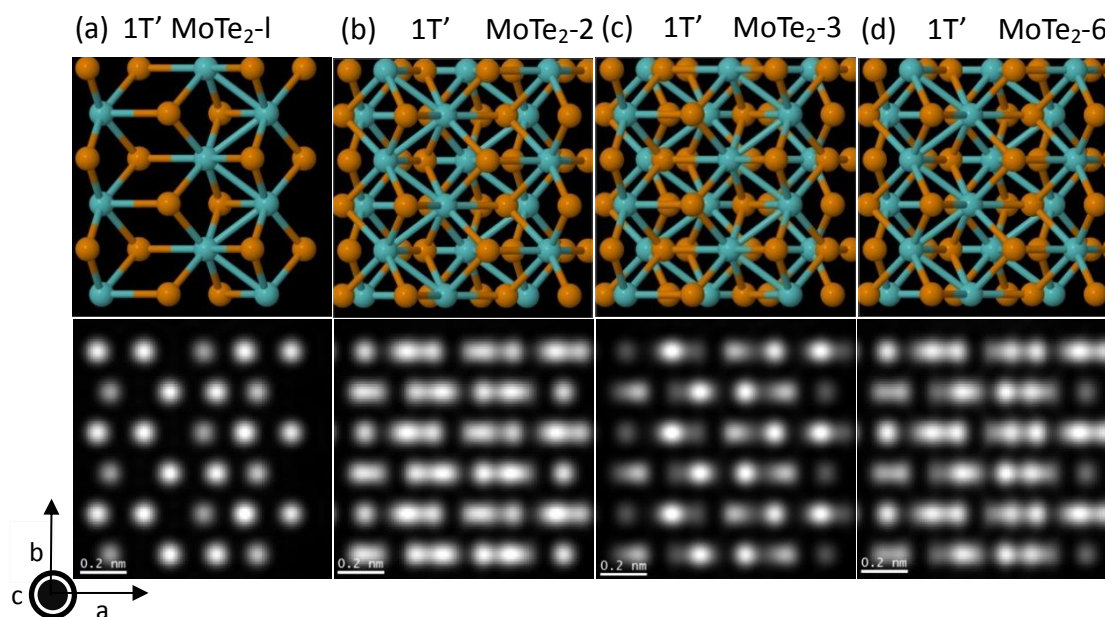


Figure 6.18 HAADF-STEM image simulation of the 1T'-MoTe₂ phase with different layer thicknesses. Top row: Atomic model configurations with top view (along the [001] zone axis) of the 1T'-MoTe₂ lattice at (a) monolayer, (b) bilayer, (c) trilayer and (d) 6 layers. Bottom row: Simulated HAADF-STEM images of 1T'-MoTe₂ at monolayer, bilayer, trilayer and 6 layers thicknesses.

Before conducting the HAADF-STEM experiments for the MoTe₂ samples, we performed HAADF simulation for these two MoTe₂ phases. The atomic models were created with Rhodius software. [48] With the created atomic model, the HAADF image simulations were carried out by using STEM CELL. [38] We used a 60 keV electron beam with a convergence angle of 25 mrad, neglecting aberrations (defocus, astigmatism and higher order aberrations are set to 0). The collection angle was set from 80 to 250 mrad. As displayed in **Figure 6.17**, the atomic ordering maintained as hexagonal rings with varying MoTe₂ thickness in the case of 2H MoTe₂. In contrast, the atomic ordering changes with the varying of MoTe₂ thickness in the case of 1T' MoTe₂, which makes the distinguishing of these two phases even more difficult, as displayed in **Figure 6.18**.

Figure 6.19 shows typical HAADF images of the 2H phase. The FFT in the right images of **Figure 6.19** represents the hexagonal crystals, and the measured inter-planar spacings are consistent with the literature for 2H MoTe₂.

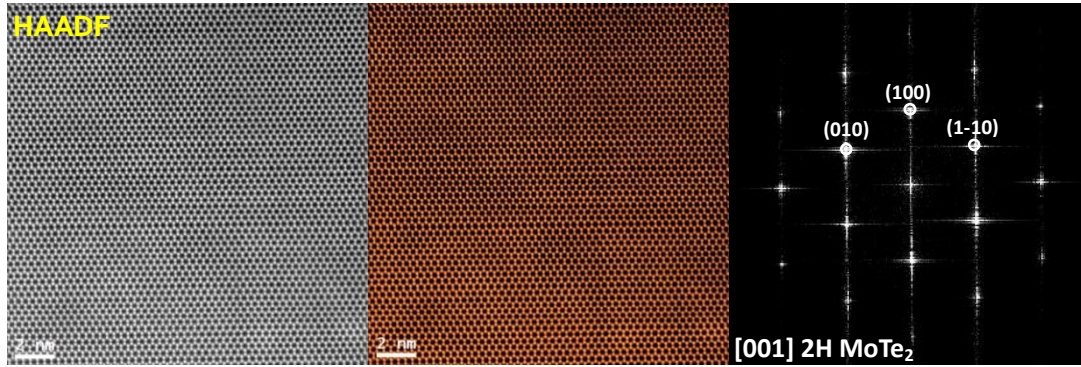


Figure 6.19 (Left): the atomic resolution HAADF STEM image, (Middle): orange colored atomic resolution HAADF STEM image showing the hexagonal atomic ordering. (Right) The corresponding FFT spectrum indicates that the membrane crystallized in hexagonal MoTe₂, [P63/MMC]-space group 194, with crystal parameters of $a=b=0.3521$ nm, $c=1.396$ nm and $\alpha=\beta=90^\circ$, $\gamma=120^\circ$ as visualized from [0001] direction.

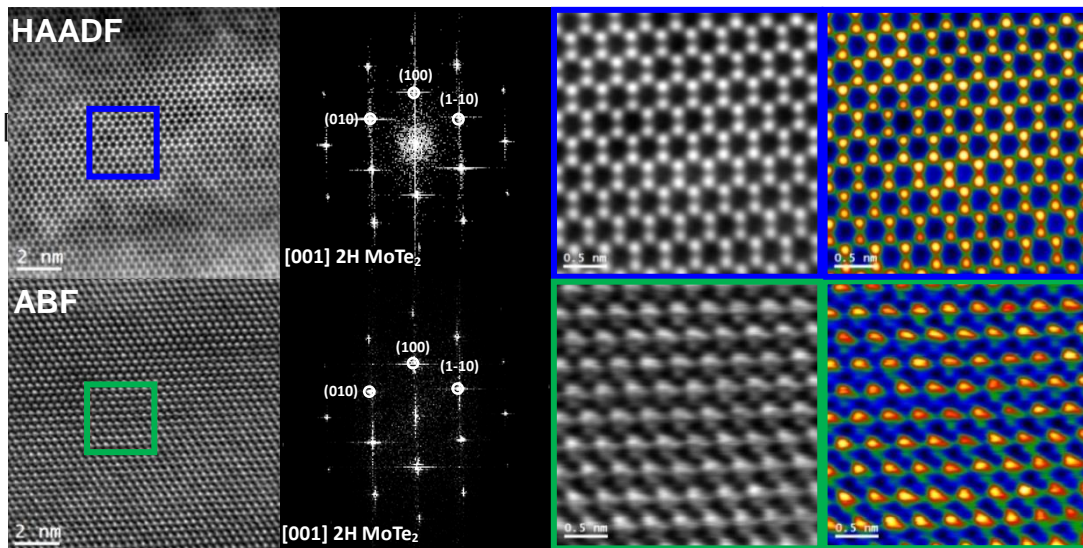


Figure 6.20 **Top row:** Left: the atomic resolution HAADF STEM image shows hexagonal atomic ordering. The corresponding FFT spectrum indicates the membrane crystallized in 2H MoTe₂, as visualized from [001] direction. Right: the atomic resolution HAADF STEM images and the temperature colored atomically HAADF STEM images of the blue squared region show the ordering of Mo and Te atoms. **Bottom row:** Left: the ABF STEM image shows the hexagonal atomic ordering. The corresponding power spectrum also indicates that the membrane crystallized in the 2H MoTe₂ crystal phase, as visualized along the [001] direction. Right: ABF STEM images and the temperature colored counterparts of the green squared region showing the ordering of Mo and Te atoms.

The schematic hexagonal atomic models and simulated HAADF images in **Figure 6.17** agree well with the atomic HAADF-STEM image in **Figure 6.20**. Here, despite the difference in the atomic numbers ($Z_{\text{Mo}}=42$, $Z_{\text{Te}}=52$), the similar atomic contrast in the Mo and Te atomic positions in the HAADF and ABF images in **Figure 6.20** indicate that the 2H phase exists in a few layers with the known stacking sequence of Mo and Te layers. [49]

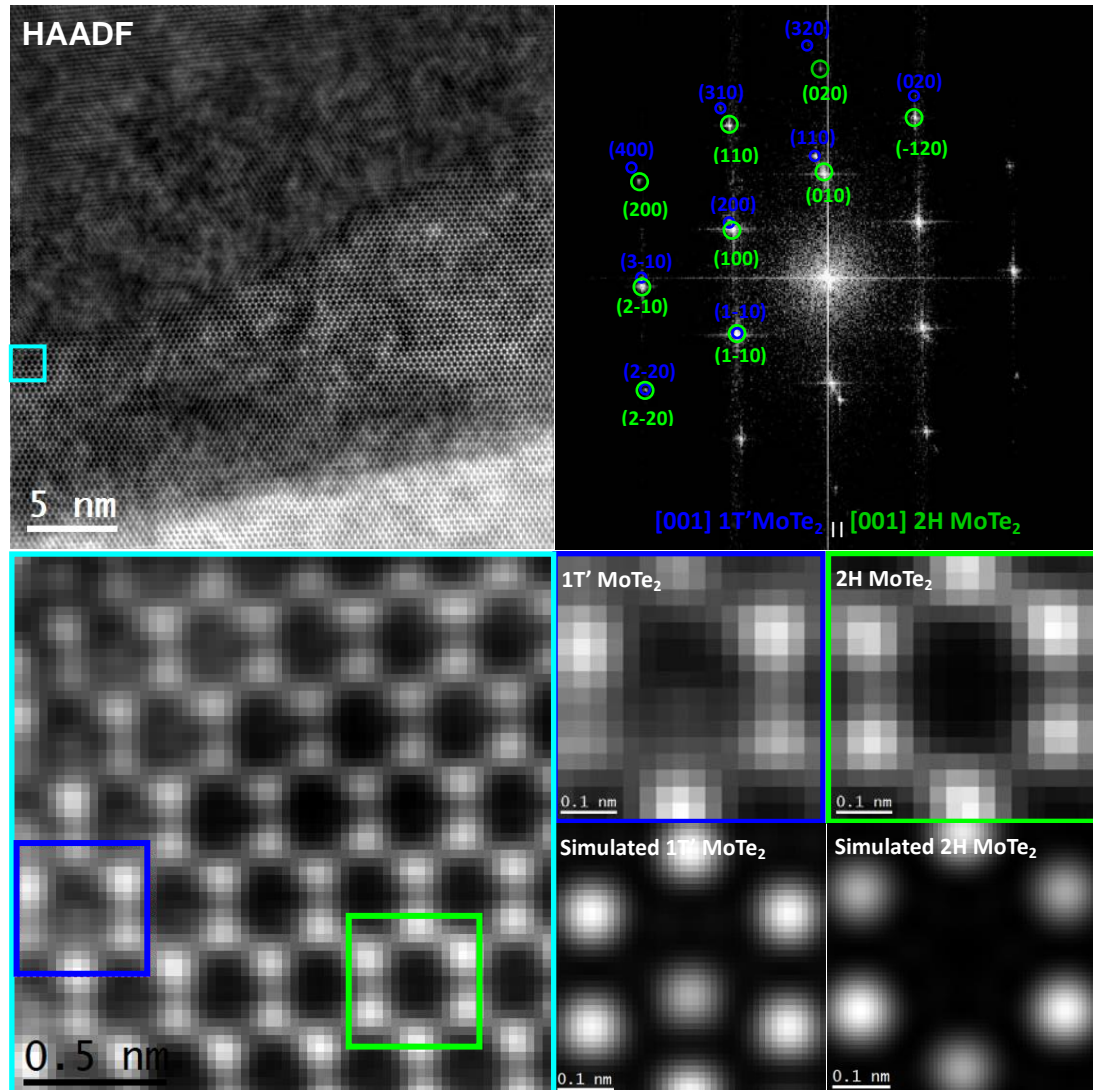


Figure 6.21 **Top row**: Left: the HAADF STEM image of the thin edge part shows two separated regions. Right: the power spectrum obtained in the membrane indicates that there are two different crystal regions, one crystallized in the 1T' MoTe₂ as visualized from [001] direction, while the second region crystallized in the 2H MoTe₂ as visualized from [001] direction. **Bottom row**: Left: the atomic resolution HAADF STEM image of the interface squared in cyan. Middle: experimental atomic resolution HAADF STEM image of the 2H MoTe₂ in the green squared region and simulated atomic

resolution HAADF STEM image of the 2H phase for comparison. Right: experimental atomic resolution HAADF STEM image of the 1T' MoTe₂ in the blue squared region and simulated atomic resolution HAADF STEM image of the 1T' MoTe₂ for comparison.

We then moved to the identification of coplanar semiconductor-metal interface composed of 2H and 1T' MoTe₂. It is worth noting that the [001] zone axis of 1T' MoTe₂ is 3.9° off the [001] zone axis of 2H MoTe₂, which makes observation of the atomic structure of 1T' MoTe₂ and 2H MoTe₂ from [001] direction at the same time difficult. We were able to obtain the atomic resolution HAADF STEM images at the interface between the 2H MoTe₂ and 1T' MoTe₂ crystal domains. As displayed in **Figure 6.21**, by carefully comparing the experimental HAADF and simulated HAADF STEM images, the top region can be assigned to the 1T phase, while the bottom region belongs to the 2H phase.

6.3.4 Vacancy Generation in PtSe₂ by means of Argon Plasma Treatment

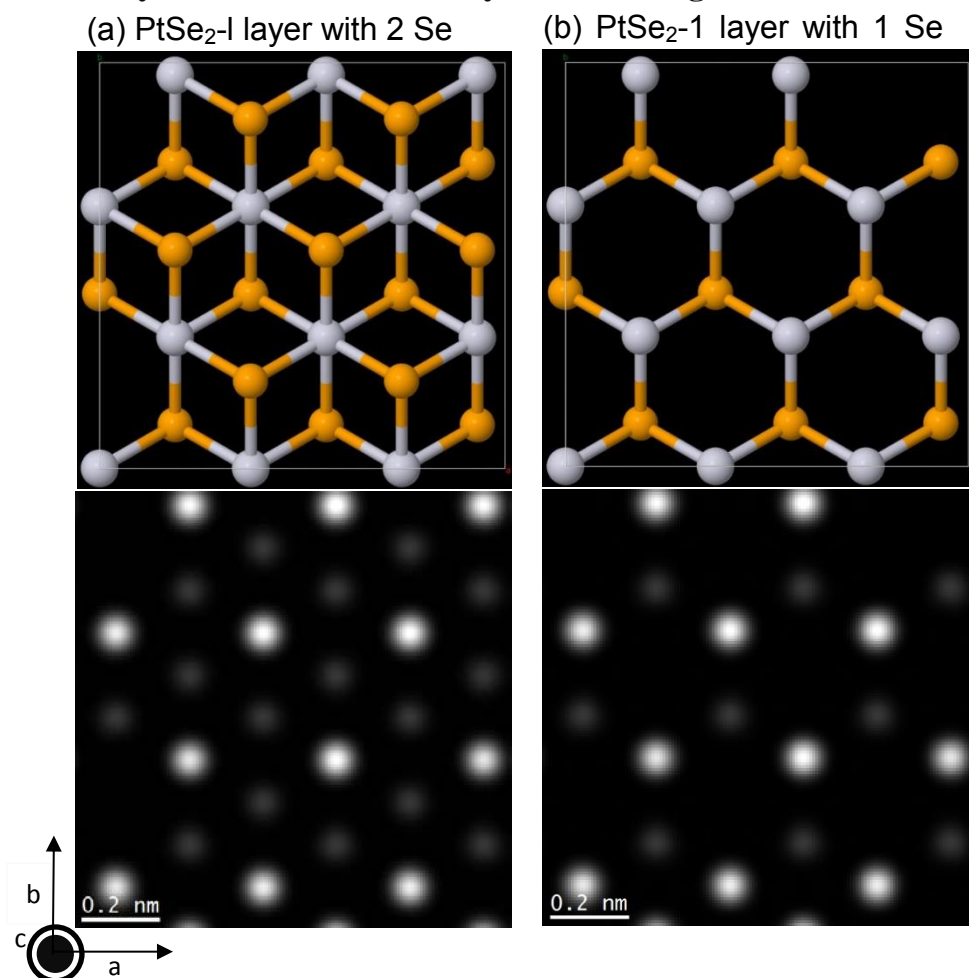


Figure 6.22 Atomic resolution HAADF-STEM image simulation of the PtSe₂ structure with different

Se atomic arrangement. **Top row:** Top view atomic model configurations (along the [0001] zone axis) of (a) monolayer PtSe₂ with 2 Se atoms, (b) monolayer PtSe₂ with 1 Se atom (top Se atom has been removed to create the Se vacancy). **Bottom row:** Corresponding simulated HAADF-STEM images of PtSe₂.

In the case of PtSe₂ samples, before conducting the HAADF-STEM experiments, we also performed HAADF STEM image simulations for primary PtSe₂ and PtSe₂ with Se vacancies. The atomic models were created with Rhodius software. [48] With the created atomic models, the HAADF STEM image simulations were carried out using STEM CELL. [38] We used an 80 keV electron beam with a convergence angle of 21.5 mrad, neglecting aberrations (defocus, astigmatism and higher order aberrations are set to 0). The collection angle was set from 80 to 250 mrad. As displayed in **Figure 6.22**, the atomic ordering maintained as hexagonal rings with a Se atom inside in the case of the primary PtSe₂. In contrast, there is no Se atom inside the hexagonal ring in the case of PtSe₂ when the structure has a Se vacancy.

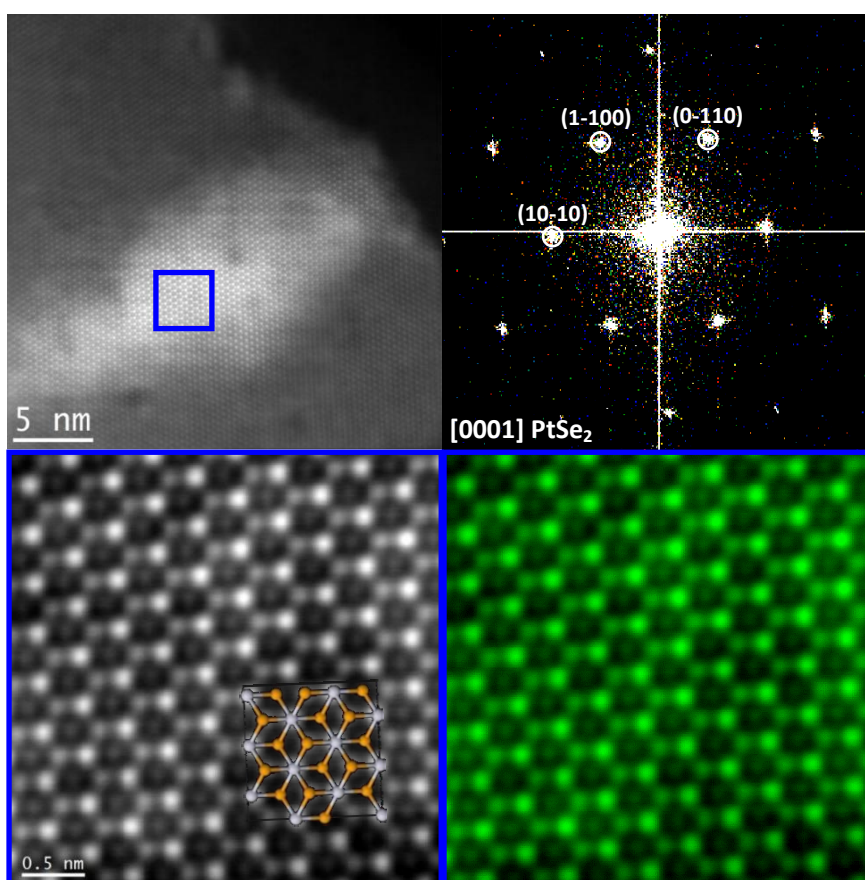


Figure 6.23 Atomic HAADF images and power spectrum of the pristine PtSe₂ membrane.

The low magnification atomic resolution HAADF STEM image in the top left of **Figure 6.23** shows the general structure of the PtSe₂ membranes. The corresponding FFT spectrum in the top right of **Figure 6.23** indicates that the membrane has a hexagonal PtSe₂ crystal structure, with [P3-M1]-Space group 164, and lattice parameters of $a = b = 0.3727$ nm, $c = 0.5082$ nm, and $\alpha = \beta = 90^\circ$, $\gamma = 120^\circ$ as visualized along the [0001] direction. Magnified detail of the atomic resolution HAADF STEM image of the blue squared region shows the atomic ordering of the Pt and Se atoms with the superposed monolayer PtSe₂ atomic model with two Se atoms (silver ball: Pt atom; orange ball: Se atom). The green colored atomic resolution HAADF STEM image of the blue squared region enhances the contrast of the Pt and Se atoms, confirming there are two layers of Se atoms that sandwich the Pt atoms, which is consistent with the simulated HAADF STEM image of the PtSe₂ monolayer with 2 Se atoms in **Figure 6.22**.

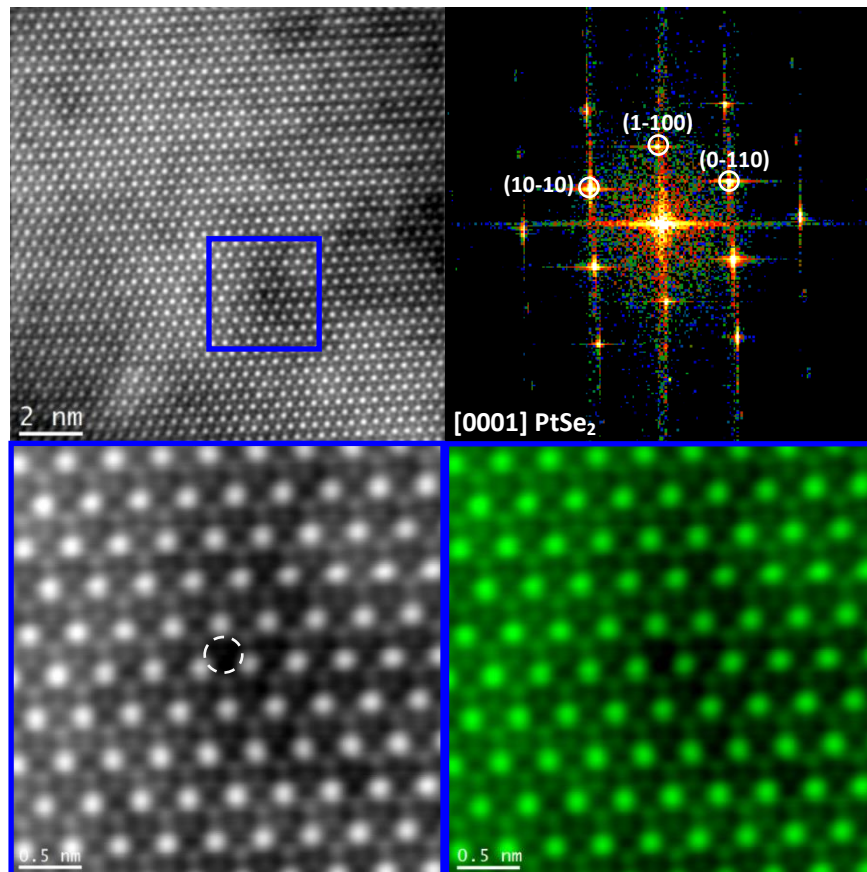


Figure 6.24 Atomic HAADF STEM images and power spectrum of the PtSe₂ membrane after being treated by Ar plasma for 5s.

The low magnification atomic resolution HAADF image in the left top of **Figure 6.24** shows the general structure of the PtSe₂ membrane after being treated by an Ar plasma for 5s. The corresponding FFT spectrum in the top right of **Figure 6.24** indicates that the membrane still maintains the hexagonal PtSe₂ crystal structure, with [P3-M1]-Space group 164, and lattice parameters of $a = b = 0.3727$ nm, $c = 0.5082$ nm, and $\alpha = \beta = 90^\circ$, $\gamma = 120^\circ$ as visualized along the [0001] direction. Magnified detail of the atomic resolution HAADF STEM image of the blue squared region showing the atomic ordering of Pt and Se atoms, where the Se vacancy is marked by a dotted white circle. The false colored (green) atomic resolution image further enhances the contrast of Pt and Se atoms, confirming the presence of a Se vacancy in the PtSe₂ membrane.

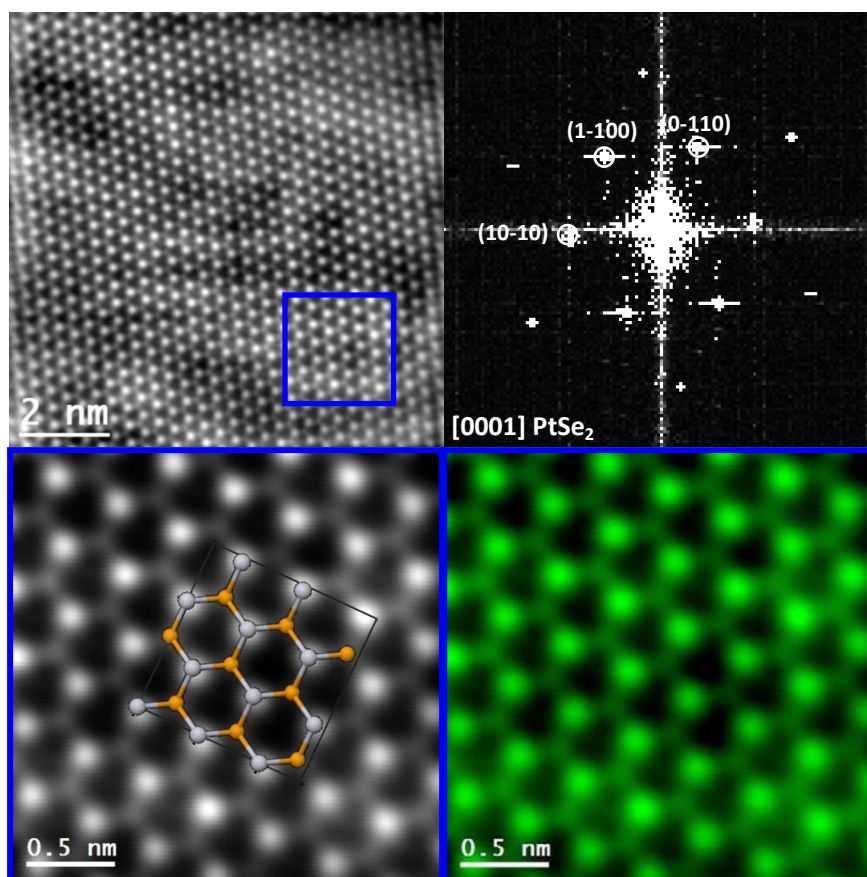


Figure 6.25 Atomic resolution HAADF STEM images and power spectrum of the PtSe₂ membrane after being treated by Ar plasma for 2 min.

The low magnification atomic resolution HAADF image in the top left of **Figure 6.25** shows the general structure of the PtSe₂ membrane after being treated by an Ar

plasma for 2 min. The corresponding power spectrum in the top right of **Figure 6.25** indicates that the membrane still maintains the hexagonal PtSe_2 crystal structure, with [P3-M1]-Space group 164, and lattice parameters of $a = b = 0.3727$ nm, $c = 0.5082$ nm, and $\alpha = \beta = 90^\circ$, $\gamma = 120^\circ$ as visualized along the [0001] direction. Magnified detail of the atomic resolution HAADF STEM image of the blue squared region showing the atomic ordering of the Pt and Se atoms, which have no Se atoms inside the hexagonal ring composed of Mo and Se atoms. The atomic model of a PtSe_2 monolayer with one Se atom (silver balls: Pt atoms; orange balls: Se atoms) is superposed onto it, confirming it is full of Se atom vacancies in the plane of the PtSe_2 membrane.

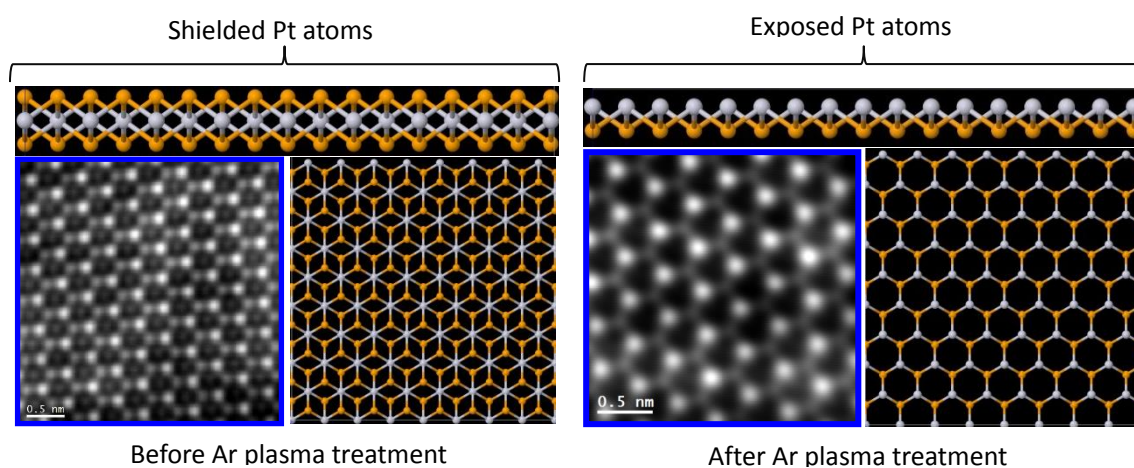


Figure 6.26 Schematic showing the creation of Se vacancies in order to enhance the exposition of Pt atoms for HER in water splitting applications.

As displayed in **Figure 6.26**, the created Se vacancies in the plane of 2D PtSe_2 is supposed to enhance the exposure area of Pt atoms to the electrolyte and thus enhance the HER performance. In this way, the detailed atomic structure of the as-prepared 2D materials can be directly correlated with the HER performance, which may provide some clues for rational designing of highly active and cost-effective 2D material for HER in water splitting application.

6.4 Summary

In conclusion, with aberration-corrected dedicated STEM, we have investigated the structural defects of MoS₂, such as atomic termination in the edge region and grain boundary. The strain presented in the MoO₂/MoS₂ core-shell nanoflakes was systematically investigated and could be related to the tuned HER performance. Furthermore, the coplanar phase transmission of 2H and 1T' phases in the MoTe₂ sample was demonstrated by comparing the experimental atomic resolution HAADF STEM images with the simulated ones. Additionally, the presence of Se atom vacancies, which increase when extending the Ar plasma treatment time was demonstrated via comparing the experimental atomic HAADF STEM with its simulated images. The creation of Se atom vacancies in 2D PtSe₂ membranes is supposed to enhance the exposure of Pt atoms to electrolyte and thus enhance the HER performance. In fact, as Pt is one of the most active catalysts for HER, a way to reduce its cost would be by maximizing its surface area. In this way, we could dream on nanoengineering a perfect 2D Pt monolayer, which in fact it has not been possible till now. By using PtSe₂ monolayers as templates, we have demonstrated that the Ar plasma can be used to peel or remove the top Se surface, leaving a perfect Pt monolayer fully exposed to the electrolyte.

References

- [1] K. F. Mak, C. Lee, J. Hone, J. Shan, T. F. Heinz, Atomically thin MoS₂: A new direct-gap semiconductor. *Phys. Rev. Lett.* **2010**, 105, 136805.
- [2] B. Radisavljevic, A. Radenovic, J. Brivio, V. Giacometti, A. Kis, Single-layer MoS₂ transistors. *Nat. Nanotechnol.* **2011**, 6, 147-150.
- [3] Z. Yin, H. Li, H. Li, L. Jiang, Y. Shi, Y. Sun, G. Lu, Q. Zhang, X. Chen, H. Zhang, Single-layer MoS₂ phototransistors. *ACS Nano*, **2011**, 6, 74–80.
- [4] Z. Zeng, Z. Yin, X. Huang, H. Li, Q. He, G. Lu, F. Boey, H. Zhang, Single-layer semiconducting nanosheets: High-yield preparation and device fabrication, *Angew. Chem., Int. Ed.* **2011**, 50, 11093-11097
- [5] Q. H. Wang, K. Kalantar-Zadeh, A. Kis, J. N. Coleman, M. S. Strano, Electronics and optoelectronics of two-dimensional transition metal dichalcogenides, *Nat. Nanotechnol.* **2012**, 7, 699-712.
- [6] K. F. Mak, K. He, J. Shan, T. F. Heinz, Control of valley polarization in monolayer MoS₂ by optical helicity. *Nat. Nanotechnol.* **2012**, 7, 494-498.
- [7] K. S. Novoselov, D. Jiang, F. Schedin, T. J. Booth, V. V. Khotkevich, S. V. Morozov and A. K. Geim, Two-dimensional atomic crystals, *Proc. Natl. Acad. Sci.*, **2005**, 102, 10451-10453.
- [8] A. Splendiani, L. Sun, Y. Zhang, T. Li, J. Kim, C.Y. Chim, G. Galli and F. Wang, Emerging photoluminescence in monolayer MoS₂, *Nano Lett.*, **2010**, 10, 1271-1275.
- [9] G. Eda, H. Yamaguchi, D. Voiry, T. Fujita, M. Chen and M. Chhowalla, Photoluminescence from chemically exfoliated MoS₂, *Nano Lett.*, **2011**, 11, 5111-5116.
- [10] Z. Zeng, Z. Yin, X. Huang, H. Li, Q. He, G. Lu, F. Boey and H. Zhang, Single-layer semiconducting nanosheets: High-yield preparation and device fabrication, *Angew. Chem., Int. Ed.*, **2011**, 50, 11093-11097.
- [11] J. N. Coleman, M. Lotya, A. O'Neill, S. D. Bergin, P. J. King, U. Khan, K. Young, A. Gaucher, S. De, R. J. Smith, I. V. Shvets, S. K. Arora, G. Stanton, H.-Y. Kim, K. Lee, G. T. Kim, G. S. Duesberg, T. Hallam, J. J. Boland, J. J. Wang, J. F. Donegan, J. C. Grunlan, G. Moriarty, A. Shmeliov, R. J. Nicholls, J. M. Perkins, E. M. Grievson, K. Theuwissen, D. W. McComb, P. D. Nellist and V. Nicolosi, Two-dimensional nanosheets produced by liquid exfoliation of layered materials, *Science*, **2011**, 331, 568-571.
- [12] Y. Zhan, Z. Liu, S. Najmaei, P. M. Ajayan and J. Lou, Large-area vapor-phase growth and characterization of MoS₂ atomic layers on a SiO₂ substrate, *Small*, **2012**, 8, 966-971.
- [13] X. Wang, H. Feng, Y. Wu and L. Jiao, Controlled synthesis of highly crystalline MoS₂ flakes by chemical vapor deposition, *J. Am. Chem. Soc.*, **2013**, 135, 5304-5307.
- [14] K.K. Liu, W. Zhang, Y.H. Lee, Y.C. Lin, M.T. Chang, C.Y. Su, C.S. Chang, H. Li, Y. Shi, H. Zhang, C.S. Lai and L.J. Li, Growth of large-area and highly crystalline MoS₂ thin layers on insulating substrates, *Nano Lett.*, **2012**, 12, 1538-1544.

- [15] Y. H. Lee, X. Q. Zhang, W. Zhang, M. T. Chang, C. T. Lin, K. D. Chang, Y. C. Yu, J. T. W. Wang, C. S. Chang, L.J. Li and T.W. Lin, Synthesis of large-area MoS₂ atomic layers with chemical vapor deposition, *Adv. Mater.*, **2012**, 24, 2320-2325.
- [16] F. Banhart, J. Kotakoski, A.V. Krasheninnikov, Structural defects in graphene. *ACS Nano*, **2011**, 5, 26-41.
- [17] Y. Wei, J. Wu, H. Yin, X. Shi, R. Yang, M. D. Dresselhaus, The nature of strength enhancement and weakening by pentagon-heptagon defects in graphene. *Nat. Mater.* **2012**, 11, 759-763.
- [18] Q. Yu, L.A. Jauregui, W. Wu, R. Colby, J. Tian, Z. Su, H. Cao, Z. Liu, D. Pandey, D. Wei, T. F. Chung, P. Peng, N.P. Guisinger, E.A. Stach, J. Bao, S.S. Pei, Y. P. Chen, Control and characterization of individual grains and grain boundaries in graphene grown by chemical vapour deposition. *Nat. Mater.* **2011**, 10, 443-449.
- [19] O.V. Yazyev, S. G. Louie, Electronic transport in polycrystalline graphene. *Nat. Mater.* **2010**, 9, 806-809.
- [20] J.H. Chen, L. Li, W.G. Cullen, E.D. Williams, M.S. Fuhrer, Tunable kondo effect in graphene with defects. *Nat. Phys.* **2011**, 7, 535-538.
- [21] W. Zhou, S. J. Pennycook, J.C. Idrobo, Localization of inelastic electron scattering in the low loss energy regime. *Ultramicroscopy*, **2012**, 119, 51-56.
- [22] X. Zou, Y. Liu, B.I. Yakobson, Predicting dislocations and grain boundaries in two-dimensional metal-disulfides from the first principles. *Nano Lett.* **2013**, 13, 253-258.
- [23] H. P. Komsa, J. Kotakoski, S. Kurasch, O. Lehtinen, U. Kaiser, A. V. Krasheninnikov, Two-dimensional transition metal dichalcogenides under electron irradiation: Defect production and doping. *Phys. Rev. Lett.* **2012**, 109, 035503.
- [24] A. M. V. D. Zande, P. Y. Huang, D. A. Chenet, T. C. Berkelbach, Y. You, G.H. Lee, T. F. Heinz, D. R. Reichman, D. A. Muller, J. C. Hone, Grains and grain boundaries in highly crystalline monolayer molybdenum disulfide. *Nat. Mater.*, **2013**, 12, 554-561.
- [25] S. Manzeli, D. Ovchinnikov, D. Pasquier, O. V. Yazyev, A. Kis, 2D transition metal dichalcogenides. *Nat. Rev. Mater.*, **2017**, 2, 17033.
- [26] D. Voiry, J. Yang, M. Chhowalla, Recent strategies for improving the catalytic activity of 2D TMD nanosheets toward the hydrogen evolution reaction. *Adv. Mater.* **2016**, 28, 6197-6206.
- [27] Y.Y. Liu, J.J. Wu, K. P. Hackenberg, J. Zhang, Y. M. Wang, Y.C. Yang, K. Keyshar, J. Gu, T. Ogitsu, R. Vajtai, J. Lou, P. M. Ajayan, B. C. Wood, B. I. Yakobson, Self-optimizing, highly surface-active layered metal dichalcogenide catalysts for hydrogen evolution, *Nat. Energy*, **2017**, 2, 17127.
- [28] T. F. Jaramillo, K. P. Jørgensen, J. Bonde, J. H. Nielsen, S. Horch, I. Chorkendorff, Identification of active edge sites for electrochemical H₂ evolution from MoS₂ nanocatalysts. *Science*, 2007, 317, 100-102.
- [29] J. Kibsgaard, Z. Chen, B. N. Reinecke, T. F. Jaramillo, Engineering the surface structure of MoS₂ to preferentially expose active edge sites for electrocatalysis. *Nat. Mater.* **2012**, 11, 963-969.

- [30] Q. Ji, Y. Zhang, Y. Zhang, Z. Liu, Chemical vapour deposition of group-VIB metal dichalcogenide monolayers: engineered substrates from amorphous to single crystalline. *Chem. Soc. Rev.* **2015**, 44, 2587-2602.
- [31] G. Q. Li, D. Zhang, Q. Qiao, Y. F. Yu, D. Peterson, A. Zafar, R. Kumar, S. Curtarolo, F. Hunte, S. Shannon, Y. M. Zhu, W.T. Yang, L.Y. Cao, All the catalytic active sites of MoS₂ for hydrogen evolution. *J. Am. Chem. Soc.* **2016**, 138, 16632-16638.
- [32] J. F. Xie, H. Zhang, S. Li, R. X. Wang, X. Sun, M. Zhou, J. F. Zhou, X.W. Lou, Y. Xie, Defect-Rich MoS₂ Ultrathin nanosheets with additional active edge sites for enhanced electrocatalytic hydrogen evolution. *Adv. Mater.* **2013**, 25, 5807-5813.
- [33] X.P. Dai, K.L. Du, Z.Z. Li, M.Z. Liu, Y.D. Ma, H. Sun, X. Zhang, Y. Yang, Co-doped MoS₂ nanosheets with the dominant CoMoS phase coated on carbon as an excellent electrocatalyst for hydrogen evolution. *ACS Appl. Mater. Interfaces*, **2015**, 7, 27242-27253.
- [34] G. L. Ye, Y.J. Gong, J.H. Li, B. Li, Y.M. He, S. T. Pantelide, W. Zhou, R. Vajtai, P. M. Ajayan, Defects engineered monolayer MoS₂ for improved hydrogen evolution reaction. *Nano Lett.* **2016**, 16, 1097-1103.
- [35] H. Li, C. Tsai, A. L. Koh, L.L. Cai, A. W. Contryman, A. H. Fragapane, J.H. Zhao, H.S. Han, H. C. Manoharan, F. Abild-Pedersen, J. K. Nørskov, X. L. Zheng Activating and optimizing MoS₂ basal planes for hydrogen evolution through the formation of strained sulphur vacancies. *Nat. Mater.* **2016**, 15, 48-53.
- [36] D. Voiry, R. Fullon, J. Yang, C. D. C. C. E. Silva, R. Kappera, I. Bozkurt, D. Kaplan, M. J. Lagos, P. E. Batson, G. Gupta, A. D. Mohite, L. Dong, D.Q. Er, V. B. Shenoy, T. Asefa, M. Chhowalla, The role of electronic coupling between substrate and 2D MoS₂ nanosheets in electrocatalytic production of hydrogen. *Nat. Mater.* **2016**, 15, 1003-1009.
- [37] Juri Barthel, Lothar Houben, Karsten Tillmann, FEI Titan G3 50-300 PICO, *Journal of Large-Scale Research Facilities*, 1, 34.
- [38] V. Grillo, E. Rotunno, STEM CELL: A software tool for electron microscopy: Part I-simulations, *Ultramicroscopy*, **2013**, 125, 97-111.
- [39] V. Grillo, F. Rossi, STEM CELL: A software tool for electron microscopy. Part 2 analysis of crystalline materials, *Ultramicroscopy*, **2013**, 125, 112-129.
- [40] S. Najmaei, Z. Liu, W. Zhou, X. Zou, G. Shi, S. Lei, B. I. Yakobson, J. C. Idrobo, P. M. Ajayan, J. Lou, Vapor phase growth and grain boundary structure of molybdenum disulfide atomic layers. *Nat. Mater.*, **2013**, 12, 754-759.
- [41] W. Zhou, X.L. Zou, S. Najmaei, Z. Liu, Y.M. Shi, J. Kong, J. Lou, P.M. Ajayan, B. I. Yakobson, J.C. Idrobo, Intrinsic structural defects in monolayer molybdenum disulphide, *Nano Lett.* **2013**, 13, 2615-2622.
- [42] M. D. L. Mata, C. Magen, J. Gazquez, M. I. B. Utama, M. Heiss, S. Lopatin, F. Furtmayr, C. J. Fernandez-Rojas, B. Peng, J. R. Morante, R. Rurali, M. Eickhoff, A. F. I. Morral, Q. H. Xiong, J. Arbiol, Polarity assignment in ZnTe, GaAs, ZnO, and GaN-AlN nanowires from direct dumbbell analysis, *Nano Lett.*, **2012**, 12, 2579-2586.

- [43] L. P. Hansen, Q. M. Ramasse, C. Kisielowski, M. Brorson, E. Johnson, H. Topsøe, S. Helveg, Atomic-scale edge structures on industrial-style MoS₂ nanocatalysts, *Angew. Chem. Int. Ed.* **2011**, 50, 10153-10156.
- [44] H. Schweiger, P. Raybaud, G. Kresse, H. Toulhoat, Shape and edge sites modifications of MoS₂ catalytic nanoparticles induced by working conditions: A theoretical study. *J. Catal.* **2002**, 207, 76-87.
- [45] M.J. Hÿtch, E. Snoeck, R. Kilaas, Quantitative measurement of displacement and strain fields from HREM micrographs, *Ultramicroscopy*, **1998**, 74, 131-146.
- [46] M. D. L. Mata, C. Magén, P. Caroff, J. Arbiol, Atomic scale strain relaxation in axial semiconductor III-V nanowire heterostructures. *Nano Lett.* **2014**, 14, 6614-6620.
- [47] D. H. Keum, S. Cho, J. H. Kim, D. H. Choe, H. J. Sung, M. Kan, H. Y. Kang, J. Y. Hwang, S. W. Kim, H. J. Yang, K. J. Chang, Y. H. Lee, Bandgap opening in few-layered monoclinic MoTe₂, *Nat. Phys.*, **2015**, 11, 482-487.
- [48] S. Bernal, F.J. Botana, J.J. Calvino, C. Lopez-Cartes, J.A. Perez-Omil, J.M. Rodríguez-Izquierdo, The interpretation of HREM images of supported metal catalysts using image simulation: profile view images, *Ultramicroscopy*, **1998**, 72, 135-164.
- [49] J. H. Sung, H. Heo, S. Si, Y. H. Kim, H. R. Noh, K. Song, J. Kim, C.S. Lee, S.Y. Seo, D.H. Kim, H. K. Kim, H. W. Yeom, T.H. Kim, S.Y. Choi, J. S. Kim, M.H. Jo, Coplanar semiconductor-metal circuitry defined on few-layer MoTe₂ via polymorphic heteroepitaxy, *Nat. Nanotechnol.*, **2017**, 12, 1064-1070.

Chapter 7

General Conclusions and Outlook

In this dissertation, we designed and comprehensively investigated one dimensional (nanowires) and two dimensional (nanoflakes) materials for supercapacitors and water splitting applications. Various chemical and physical technologies, including the hydrothermal method, electrochemical-deposition, sputtering, atomic layer deposition and chemical bath, were employed to design smart nanoflakes and nanowire composites for specific energy applications. The structural characterization was achieved by the utilization of XRD, XPS, Raman spectrum; UV-Vis, SEM, EDS and specially (S)TEM advanced techniques, mainly aberration-corrected HAADF, ABF and EELS. The charge transfer and reaction kinetic mechanisms of different composites were investigated via employing the impedance spectrum (EIS). The analyses combining (S)TEM and EIS techniques allowed a better understanding of the growth mechanisms, the surface state tuning mechanisms and the formation of structural defects in our composite materials. We could carefully engineer several types of nanostructures, namely hematite/PPY nanoflakes for supercapacitor applications and ITO/Fe₂O₃/Fe₂TiO₅/FeNiOOH, Fe₂O₃/Fe₂TiO₅/CoFe PBA and 2D materials (nanosheets and nanoflakes) for water splitting applications. We started our study focusing on the design of core-shell Fe₂O₃/PPy nanoflakes for supercapacitor applications. Then, we moved to the smart design of composite nanowires based on hematite, where different materials were combined as photoanodes for the water splitting application. Finally, we used aberration-corrected (S)TEM to investigate the structural defects presented in the 2D materials for the HER application. In the following part, we present the main general conclusions achieved in this dissertation.

7.1 General Conclusions

In **Chapter 3**, we have optimized the hydrothermal reaction in order to replicate the nanoflakes-like structure for hematite backbone from MnO₂ nanoflakes. We have controlled the mass loading of PPy on the surface of the hematite nanoflakes via controlling the electrodeposition charge of PPy. SEM, EDX, XRD, XPS, Raman spectroscopy, HRTEM and STEM-EELS were employed to investigate their structural evolution and growth mechanism. We have discussed the PPy nanoleaves growth

mechanism onto the hematite nanoflakes. As a proof-of-concept experiment for optimized core-branch $\text{Fe}_2\text{O}_3@\text{PPy}$ synthesis, we have conducted systematic electrochemical characterization, including CV and EIS for different core-branch $\text{Fe}_2\text{O}_3@\text{PPy}$ electrodes. Then, we have used the optimized $\text{Fe}_2\text{O}_3@\text{PPy}$ electrode as negative electrode and as-prepared MnO_2 as the positive electrode to assemble an ASC device. Thanks to the detailed experimental and characterization techniques presented in **Chapter 3**, we could draw the following conclusions:

- The best hydrothermal reaction time for producing hematite nanoflakes is 30 min at 120 °C, which transfer the MnO_2 nanoflakes into hematite nanoflakes without damaging its nanostructure. It was concluded that the hydrothermal time needs to be optimized when the chemical transition and the morphology evolution occur simultaneously.
- The optimized PPy deposition charge is 0.3C in core-branch $\text{Fe}_2\text{O}_3@\text{PPy}$ electrodes, which improve the electrical conductivity without blocking the electrolyte ion accessibility at the same time.
- The mechanism of PPy growth on the hematite nanoflakes was investigated via combining SEM and TEM. The PPy growth mechanism is slightly different from the previously reported PPy growth mechanism on metal substrates.
- Benefiting from the stability of the honeycomb-like hematite nanoflakes and the high conductivity of the PPy nanoleaves, the resultant core-branch $\text{Fe}_2\text{O}_3@\text{PPy}$ exhibits an ultrahigh capacitance of 1167.8 F g⁻¹ at 1 A g⁻¹ in 0.5 M Na₂SO₄ aqueous solution.
- The assembled bi-metal oxides asymmetric supercapacitor ($\text{Fe}_2\text{O}_3@\text{PPy}//\text{MnO}_2$) gives rise to a maximum energy density of 42.4 W h kg⁻¹ and a maximum power density of 19.14 kW kg⁻¹ with an excellent cycling performance of 97.1% retention after 3000 cycles at 3 A g⁻¹.

In **Chapter 4**, several technologies, such as sputtering, hydrothermal treatment,

atomic layer deposition and photo-electrochemical deposition were employed to obtain the composite hematite nanowires used as photoanodes for water splitting in alkaline electrolyte. We have optimized the synthesis conditions, including the ITO thickness, TiO_2 thickness, FeNiOOH deposition charge and the post-sintering temperature of the $\text{ITO}/\text{Fe}_2\text{O}_3/\text{Fe}_2\text{TiO}_5/\text{FeNiOOH}$ electrodes. The charge transfer and the reaction kinetic mechanism were investigated by PEIS for the representative composite nanowire electrodes. Thanks to the detailed experimental and characterization techniques presented in this chapter, we could draw the following conclusions:

- The optimized ITO thickness for $\text{ITO}/\text{Fe}_2\text{O}_3$ electrode is 105 nm, which supply enough Sn atoms to diffuse into the hematite nanowires matrix and maintain the ordering of hematite nanowires morphology at the same time.
- The optimized ALD TiO_2 deposition is 30 cycles, ensuring the formation of an ultrathin Fe_2TiO_5 layer at the surface of the hematite nanowires. This layer enables the formation of $\text{Fe}_2\text{O}_3/\text{Fe}_2\text{TiO}_5$ type II heterojunction and avoids the formation of a deleterious heterojunction, such as $\text{Fe}_2\text{O}_3/\text{Fe}_2\text{TiO}_5/\text{TiO}_2$.
- The optimized sintering time is 750 °C for 30 min in the case of the $\text{ITO}/\text{Fe}_2\text{O}_3/\text{Fe}_2\text{TiO}_5$ electrode.
- The optimized FeNiOOH deposition charge onto $\text{ITO}/\text{Fe}_2\text{O}_3/\text{Fe}_2\text{TiO}_5$ electrode is 10 mC, ensuring the OER catalyst effect from FeNiOOH and avoiding the reduced light absorption in hematite nanowires.
- The obtained $\text{ITO}/\text{Fe}_2\text{O}_3/\text{Fe}_2\text{TiO}_5/\text{FeNiOOH}$ nanowires display photocurrents that are more than an order of magnitude higher than those of pristine Fe_2O_3 nanowires (from 0.205 mA cm^{-2} to 2.2 mA cm^{-2} at 1.23 V vs. RHE in 1 M NaOH electrolytes and 1 Sun).
- The surface states (SS) are finely regulated via the atomic addition of the Fe_2TiO_5 layer and the FeNiOOH nanodots, while the upgrading of the back contact conductivity and the high charge donor densities originate from the epitaxial

relationship and enhanced Sn doping contributed from the ITO underlayer.

- The excellent OER performance is attributed to the interfacial coupling effect of the ITO underlayer (Sn doping and back contact conductivity promoter), the atomic level Fe_2TiO_5 coating (Ti doping, surface state density and energy level modulation) and the FeNiOOH nanodot electrocatalyst (regulating surface state energy level).

In **Chapter 5**, we have optimized the chemical bath conditions for the synthesis of CoFe PBA supported onto $\text{Fe}_2\text{O}_3/\text{Fe}_2\text{TiO}_5$ nanowire-based electrodes. Several technologies, such as the hydrothermal method, the atomic layer deposition and the chemical bath were employed to obtain the composite nanowire based on hematite as photoanodes for water splitting in acidic electrolyte. The charge transfer and reaction kinetic mechanism were investigated by PEIS for the representative composite nanowire electrodes. In this way, we could draw the following conclusions:

- SEM, HRTEM, STEM-EELS, atomic modelling and image simulation were employed for the illustration of the structure of the pure CoFe PBA oxygen evolution catalyst (OEC), which could be related to the OEC performance.
- The optimized chemical bath for $\text{Fe}_2\text{O}_3/\text{CoFe}$ PBA electrode is 2 h at 60 °C, exhibiting 0.61 mA cm^{-2} at 1.23V vs. RHE in 1 M $\text{NaNO}_3+1\text{M HNO}_3$ electrolyte (pH=1.01).
- The optimized chemical bath for $\text{Fe}_2\text{O}_3/\text{Fe}_2\text{TiO}_5/\text{CoFe}$ PBA electrode is 2 h at 60 °C, exhibiting 1.25 mA cm^{-2} at 1.23 V vs. RHE in 1 M $\text{NaNO}_3+1\text{M HNO}_3$ electrolyte (pH=1.01).
- The PEC mechanism studied via PEIS demonstrates that the tuned energy level and the density of surface states and the enhanced charge transfer efficiency together contribute to its excellent PEC performance in acidic electrolyte.

In **Chapter 6**, we moved the characterization of the structural defects, phase transition

and vacancy distribution in 2D nanomaterials for HER with advanced aberration-corrected dedicated STEM, including HAADF, ABF, EELS-STEM, GPA, atomic modelling and HAADF image simulation. In this way, we could draw the following conclusions:

- We identified that the edge region of the MoS₂ membrane is dominated by Mo-terminated edges and 50% S-terminated edge; while there are grain boundaries in the basal plane, which are composed of dislocations with five- and seven-fold rings (5|7) and dislocations with six- and eight-fold rings (6|8).
- Core-shell MoO₂/MoS₂ nanoflakes were investigated by atomic HAADF and EELS-STEM. Their GPA investigation reveals that there is plenty of strain at the interface of MoO₂ and MoS₂, which may be responsible for its enhanced HER performance.
- 2H and 1T' phases MoTe₂ were investigated via HAADF and ABF methodologies. Comparing the experimental and the simulated results, the coplanar existence of 2H and 1T' MoTe₂ was confirmed.
- Via comparing the atomic resolution HAADF and the simulated HAADF images, the increase of Se vacancies density in the top PtSe₂ plane with the extending of Ar plasma treatment is demonstrated, which could be responsible for the improved HER performance because of the enhanced exposure of the Pt atoms.

7.2 Outlook

Our systematic investigation about the manipulation of composite nanowires for water splitting application via atomic modification of the surface of hematite have been validated for tuning the surface state of hematite and thus enhance the corresponding OER properties. Exploring the ability of different materials to tune the surface states of hematite could be of great interest. Systematic in-depth investigation is still needed, covering huge sets of second modification materials onto hematite, in order to elucidate the general rule for controlling the surface state tune direction.

On the other hand, it is well established that the $\text{Fe}^{\text{IV}}=\text{O}$ intermediate at the surface of hematite is indeed acting as the active site for driving the OER in water splitting. Nonetheless, previous mechanism investigations of hematite photoanodes are limited in obtaining macroscopic information of the $\text{Fe}^{\text{IV}}=\text{O}$ intermediate via in-situ spectroscopies, like UV-Vis, in-situ infrared spectroscopy and PEIS, but without spatially disclosing the location of the active sites (at atomic scale). The shortage of an accurate spatial identification of the OER active sites ($\text{Fe}^{\text{IV}}=\text{O}$) in hematite photoanodes currently hinders the clear determination of the OER mechanism of hematite photoanodes for water splitting. Such a spatial identification of the $\text{Fe}^{\text{IV}}=\text{O}$ intermediate under different conditions (potential bias and/or water vapour) would be highly desirable. Fortunately, we believe that the advances in in-situ TEM techniques allow more detailed analyses, unveiling the structural, chemical, morphological features during the catalysis process. Therefore, an enriched knowledge about the active site of hematite for water splitting can be developed via employing the cutting-edge state-of-the-art in-situ TEM in the near future.

List of Publications

- [10] Junshan Li, Zhishan Luo, Yong Zuo, Junfeng Liu, Ting Zhang, **Pengyi Tang**, Jordi Arbiol, Jordi Llorca, Andreu Cabot, NiSn Bimetallic Nanoparticles as Stable Electrocatalysts for Methanol Oxidation Reaction, *Applied Catalysis B: Environmental*, 2018, 234,10-18.
- [9] Qin Shi, Sebastián Murcia-López, **Pengyi Tang**, Cristina Flox, Joan R Morante, Zhaoyong Bian, Hui Wang, Teresa Andreu, Role of tungsten doping on the surface states in BiVO₄ photoanodes for water oxidation: tuning the electron trapping process, *ACS Catal.*, 2018, 8, 3331-3342.
- [8] Xuan Zhang, Jiangshui Luo, **Pengyi Tang**, Joan Ramon Morante, Jordi Arbiol, Cailing Xu, Qingfeng Li, Jan Fransaer, Ultrasensitive binder-free glucose sensors based on the pyrolysis of in situ grown Cu MOF, *Sensors and Actuators B: Chemical*, 2018, 254, 272-281.
- [7] Sebastián Murcia-López, Marilena Moschogiannaki, Vassilios Binas, Teresa Andreu, **Pengyi Tang**, Jordi Arbiol, Jordi Jacas Biendicho, George Kiriakidis, Joan Ramon Morante, Insights into the Performance of Co_xNi_{1-x}TiO₃ Solid Solutions as Photocatalysts for Sun-Driven Water Oxidation, *ACS Appl. Mater. Interfaces*, 2017, 9, 40290-40297.
- [6] Mauro Epifani, Saulius Kaciulis, Alessio Mezzi, Davide Altamura, Cinzia Giannini, **Pengyi Tang**, Joan Ramon Morante, Jordi Arbiol, Pietro Siciliano, Elisabetta Comini, Isabella Concina, Solvothermal Synthesis, Gas-Sensing Properties and Solar Cell-Aided Investigation of TiO₂-MoO_x nanocrystals, *ChemNanoMat*, 2017, 3, 798-807.
- [5] Félix Urbain, **Pengyi Tang**, Nina M Carretero, Teresa Andreu, Luís G Gerling, Cristóbal Voz, Jordi Arbiol, Joan Ramon Morante, Prototype reactor for highly selective solar-driven CO₂ reduction to synthesis gas using nanosized earth-abundant catalysts and silicon photovoltaics, *Energy & Environmental Science*, 2017, 10, 2256-2266.

[4] **Pengyi Tang**, HaiBing Xie, Carles Ros, LiJuan Han, Martí Biset-Peiró, Yongmin He, Wesley Kramer, Alejandro Perez-Rodriguez, Edgardo Saucedo, Jose Galan-Mascaros, Teresa Andreu, Joan Ramon Morante, Jordi Arbiol, Enhanced Photoelectrochemical Water Splitting of Hematite Multilayer Nanowires Photoanode with Tuning Surface State via Bottom-up Interfacial Engineering, *Energy & Environmental Science*, 2017, 10, 2124-2136. (Front Cover)

[3] Lijuan Han, **Pengyi Tang**, Álvaro Reyes-Carmona, Bárbara Rodríguez-García, Mabel Torréns, Joan Ramon Morante, Jordi Arbiol, Jose Ramon Galan-Mascaros, Enhanced activity and acid pH stability of Prussian blue-type oxygen evolution electrocatalysts processed by chemical etching, *Journal of the American Chemical Society*, 2016, 49, 16037-16045.

[2] Mauro Epifani, **Pengyi Tang**, Aziz Genç, Joan Ramon Morante, Jordi Arbiol, Raul Diaz, Susanne Wicker, The Ethylhexanoate Route to Metal Oxide Nanocrystals: Synthesis of CoO Nanooctahedra from CoII 2-Ethylhexanoate, *European Journal of Inorganic Chemistry*, 2016, 24, 3963-3968.

[1] **Pengyi Tang**, Li-Juan Han, Aziz Genç, Yong-Min He, Xuan Zhang, Lin Zhang, José Ramón Galán-Mascarós, Joan Ramon Morante, Jordi Arbiol, Synergistic Effects in 3D Honeycomb-like Hematite Nanoflakes/Branched Polypyrrole Nanoleaves Heterostructures as High-Performance Negative Electrodes for Asymmetric Supercapacitors, *Nano Energy*, 2016, 22, 189-201.

